University of Wisconsin Milwaukee
UWM Digital Commons

Theses and Dissertations

May 2020

A Feasibility Study of Microbialites as Paleomagnetic Recorders

ji-in jung
University of Wisconsin-Milwaukee

Follow this and additional works at: https://dc.uwm.edu/etd

Part of the Atmospheric Sciences Commons, Geology Commons, and the Geophysics and Seismology Commons

Recommended Citation

jung, ji-in, "A Feasibility Study of Microbialites as Paleomagnetic Recorders" (2020). *Theses and Dissertations*. 2389.
https://dc.uwm.edu/etd/2389

This Thesis is brought to you for free and open access by UWM Digital Commons. It has been accepted for inclusion in Theses and Dissertations by an authorized administrator of UWM Digital Commons. For more information, please contact open-access@uwm.edu.

A FEASIBILITY STUDY OF MICROBIALITES AS PALEOMAGNETIC RECORDERS

by

Ji-In Jung

A Thesis Submitted in

Partial Fulfillment of the

Requirements for the Degree of

Master of Science

in Geosciences

at

The University of Wisconsin-Milwaukee

May 2020

ABSTRACT

A FEASIBILITY STUDY OF MICROBIALITES AS PALEOMAGNETIC RECORDERS

by

Ji-In Jung

The University of Wisconsin-Milwaukee, 2020
Under the Supervision of Associate Professor Julie A. Bowles

Microbialites are carbonate organosedimentary deposits formed by benthic microbial communities that trap and bind detrital sediments, and/or inorganic and biologically influenced calcification. Any ferromagnetic particles incorporated into the microbialite structure have the potential to preserve variations in Earth's magnetic field. A paleomagnetic record in microbialites would be useful for reconstructing the geomagnetic field because it may record at a high temporal resolution based on estimated growth rates, thus preserving relatively short-period variations of the Earth's magnetic field. In addition, microbialites can be found in the geologic record going back ~3.5 Ga, hence potentially providing information on very ancient variations in the geomagnetic field.

The purpose of this study is to evaluate whether microbialites are capable of reliably recording the Earth's magnetic field by using paleomagnetic studies and rock magnetic methods on ancient and modern microbialites. This thesis is designed to answer the associated sub-questions: 1) Do microbialites carry a magnetization that is stable in time? What are the spatial variations in magnetization within the microbialite structure? (Chapter 3: Microbialite Magnetism and Stability); 2) Do microbialites accurately record Earth's magnetic field direction? (Chapter 4: Paleomagnetic Directional Analysis); 3) What are the magnetic carriers in the microbialites? (Chapter 5: Magnetic Properties of Microbialites); and 5) What is the magnetization process or the

origin of the magnetization? (Chapter 6: Microbialite Magnetization Processes). To answer these questions, microbialites from four locations were collected: 1) Living and lithified hypersaline microbialites from the Great Salt Lake (GSL), Utah, U.S.A.; 2) living and lithified freshwater microbialites from Laguna Bacalar (LB), Quintana Roo, Mexico; 3) an ancient lacustrine environment microbialite from the Eocene Green River formation (GR), Wyoming, U.S.A; and 4) a marine, lower Cambrian Bayan Gol formation (BG) stromatolite, South Western Mongolia.

Samples' spatial and temporal variations in magnetic susceptibility (χ) and natural remnant magnetization (NRM) intensity were measured (Chapter 3) for assessing stability, reliability of the recorded magnetization, and to better understand magnetization processes. Microbialites were subjected to a stepwise alternating field (AF) or thermal demagnetization, to isolate a characteristic remanent magnetization (ChRM) which is compared with the expected field direction (Chapter 4). To identify the magnetic mineralogy (Chapter 5) seven tests were conducted: (1) S-ratio, (2) isothermal remanent (IRM) unmixing, (3) Lowrie-Fuller test, (4) 3D IRM technique, (5) Curie temperature, (6) hysteresis loops, and (7) first order reversal curve (FORC) experiments. To understand the microbialite magnetization processes, three more tests were conducted: (8) NRM intensity was compared to an anhysteretic remanent magnetization (ARM), (9) Anisotropy of Magnetic Susceptibility (AMS), (10) low-temperature test for biogenic magnetite.

Results demonstrate that microbialites contain ferromagnetic materials that carry a stable magnetization. However, χ measurements show that magnetic mineralogy changes as living samples are removed from their environments (Chapter 3). With the exception of the GR microbialite, all microbialites record a direction close to the expected field directions (Chapter 4). Based on the tests (1) - (7), all microbialites show a predominant coercivity component around 30-50 mT, which is interpreted to be magnetite. The two ancient microbialites additionally have

significant contributions from higher coercivity components, including hematite, which do not contribute significantly to NRM (Chapter 5). The major magnetization processes are interpreted as a detrital remanent magnetization with the possible additional presence of biomagnetization based on the tests (8) and (9).

Microbialites appear to have a high potential for paleomagnetic reconstruction. However, in order to use microbialites as paleomagnetic recorders, magnetization intensity should be more than 1.00E-07Am^2/kg. For paleomagnetic reconstruction, samples should be collected from the middle of the structure, or the directional deviations should be averaged out in a layer. For an assessment of magnetic mineralogy from living microbialites, environmental and laboratory setting such as water current, humidity, temperature, and pH conditions should be considered.

TABLE OF CONTENTS

ABSTRACT ii

TABLE OF CONTENTS v

LIST OF FIGURES ix

LIST OF TABLES xii

LIST OF ABBREVIATIONS xiii

ACKNOWLEDGMENTS xvi

Chapter 1: Introduction 1
- 1.1 Motivation and goals 1
- 1.2 Background 3
  - 1.2.1 The Earth's Magnetic Field and Paleomagnetism 3
  - 1.2.2 Microbialites 6

Chapter 2: Geologic Setting, Field Methods, and Laboratory Sample Preparation 10
- 2.1 Geologic Setting and Field Methods 10
  - 2.1.1 Great Salt Lake 11
  - 2.1.2 Laguna Bacalar 15
  - 2.1.3 Green River Formation 18
  - 2.1.4 Bayan Gol Formation 20
- 2.2 Laboratory Sample Preparation 23
  - 2.2.1 Great Salt Lake 25
  - 2.2.2 Laguna Bacalar 25
  - 2.2.3 Green River Formation 26
  - 2.2.4 Bayan Gol Formation 26
  - 2.2.5. Naming Convention 27
- 2.3. Magnetic Measurement 28
- 2.4. Laboratory Instrumentation 29

Chapter 3: Microbialite Magnetism and Stability 30
- 3.1 Introduction 30
- 3.2 Background 30
- 3.3 Methods 32
  - 3.3.1 Spatial Variations in Magnetization Intensity and Magnetic Susceptibility 32
  - 3.3.2 Temporal Variations in Magnetization Intensity and Magnetic Susceptibility 32
- 3.4. Results 34

3.4.1 Spatial Variations 34
3.4.1.1 Great Salt Lake 34
3.4.1.2 Laguna Bacalar 36
3.4.1.3 Green River Formation 37
3.4.1.4 Bayan Gol Formation 38
3.4.2 Temporal Variations 41
3.4.2.1 Great Salt Lake 43
3.4.2.2 Laguna Bacalar 44
3.5 Summary/Discussion 45

Chapter 4: Paleomagnetic Directional Analysis 47
4.1 Introduction 47
4.2 Methods 48
4.2.1 Demagnetization Techniques 48
4.2.2 Samples 49
4.2.3 Statistical Data Analysis 50
4.2.4 Expected Field Values: Observations and Models 53
4.2.4.1 IGRF 54
4.2.4.2 CALSxK.n 54
4.2.4.3 GAD 55
4.2.4.4 APWP 55
4.2.4.5 Sedimentary Paleomagnetic Data 56
4.3. Results and Interpretation 57
4.3.1 Great Salt Lake 57
4.3.2 Laguna Bacalar 62
4.3.3 Green River Formation 66
4.3.4 Bayan Gol Formation 68
4.4 Discussion 70
4.4.1 Is a Microbialite Capable of Recording Earth's Magnetic Field Direction? 70
4.4.2 Deposition on a Sloping Bed 70
4.4.3 Water Current 72
4.4.4 Timing of Magnetization 72
4.5 Conclusion 73

Chapter 5: Magnetic Properties of Microbialite 74
5.1 Introduction 74
5.2 Methods 75
5.2.1 S-ratio 75
5.2.2 IRM Unmixing 76
5.2.3 Lowrie-Fuller Test 78
5.2.4 3D IRM Technique 79

5.2.5 Curie Temperature 80
5.2.6 Hysteresis Loops and Day plot 81
5.2.7 First-Order Reversal Curves (FORC) 86
5.3 Results 88
5.3.1 S-ratio 88
5.3.2 IRM Unmixing 91
5.3.3 Lowrie-Fuller Test 100
5.3.4 3D IRM Technique 102
5.3.5 Curie Temperature 105
5.3.6 Hysteresis Loops and Day plot 111
5.3.7 First-Order Reversal Curves (FORC) 117
5.4 Summary/Discussion 120
5.4.1 Great Salt Lake 120
5.4.2 Laguna Bacalar 121
5.4.3 Green River Formation 121
5.4.4 Bayan Gol Formation 121
5.4.5 Ancient vs Modern Microbialites 122

Chapter 6: Microbialite Magnetization Processes 125
6.1 Introduction 125
6.2 Methods 127
6.2.1 ARM vs NRM 127
6.2.2 Anisotropy of Magnetic Susceptibility (AMS) 128
6.2.3 Low-Temperature Test for Biogenic Magnetite 133
6.3. Results 134
6.3.1 ARM vs NRM 134
6.3.2 Anisotropy of Magnetic Susceptibility (AMS) 138
6.3.3 Low-Temperature Test for Biogenic Magnetite 141
6.4. Summary/Discussion 142
6.4.1 DRM 142
6.4.2 Biomagnetism 143

Chapter 7: Conclusion 144
7.1. General Observations and Summary 144
7.2. Assessment as a Paleomagnetic Recorder 146

REFERENCES 148

Appendix A: Sample Photos and Coordinates 156

Appendix B: Magnetic Susceptibility and NRM Intensity Mappings 163

Appendix C: IRM Unmixing Curves 165

Appendix D: Lowrie-Fuller Tests 167

Appendix E: 3D IRM Technique 171

Appendix F: Curie Temperature 176

Appendix G: FORCs Measurements 179

Appendix H: MPMS measurements 180

LIST OF FIGURES

Chapter 1: Introduction

Figure 1.1: Types of magnetic behavior with an applied field 4
Figure 1.2: Illustration of magnetic domain states 6
Figure 1.3: Classification of microbialites 7
Figure 1.4: Stromatolite diversity over geologic time scales 9

Chapter 2: Geologic Setting, Field Methods, and Laboratory Sample Preparation

Figure 2.1: Global map showing the locations of four microbialite samples 10
Figure 2.2: Classification of microfabric structure of Great Salt Lake microbialites 12
Figure 2.3: Photos of Great Salt Lake sampling locations 14
Figure 2.4: Photos of Laguna Bacalar sampling locations 17
Figure 2.5: Photos of Green River formation sampling location 19
Figure 2.6: Photos of Bayan Gol formation sampling location 21
Figure 2.7: Photos of sample preparation 23
Figure 2.8: Photos of the microbialite samples 24

Chapter 3: Microbialite Magnetism and Stability

Figure 3.1: Diagram of four hypothetical of model for magnetic stability test 33
Figure 3.2: NRM intensity and susceptibility mapping of GSL18_0101_A, B, C, D, E 35
Figure 3.3: NRM intensity and susceptibility mapping of GSL19_0201_A 36
Figure 3.4: NRM intensity and susceptibility mapping of LB19_0104 37
Figure 3.5: NRM intensity and susceptibility mapping of GR18_0101_A 39
Figure 3.6: NRM intensity and susceptibility mapping of BG14_0101_A 40
Figure 3.7: NRM intensity and susceptibility variations of GSL18 samples over time 42
Figure 3.8: NRM intensity variations of LB19 samples over time 44

Chapter 4: Paleomagnetic Directional Analysis

Figure 4.1: GSL18_0301's magnetic vectors on stereonet 58
Figure 4.2: GSL19_0103's magnetic vectors on stereonet & vector endpoint diagram 60
Figure 4.3: GSL18 and19 samples' magnetic vectors on stereonet 61
Figure 4.4: LB19 samples' magnetic vectors on stereonet 66
Figure 4.5: LB19 samples' vector endpoint diagram 65
Figure 4.6: GR18_0101's magnetic vectors on stereonet & vector endpoint diagram 67
Figure 4.7: BG14_0101's vector endpoint diagram 68
Figure 4.8: BG14_0101's magnetic vectors on stereonet 69
Figure 4.9: Illustration of magnetic vector depositions on a sloping surface 71

Chapter 5: Magnetic Properties of Microbialites

Figure 5.1: Illustration of IRM acquisition directions for the 3D-IRM technique 80

Figure 5.2: Illustration of a hysteresis loop and backfield remanence curve 82
Figure 5.3: Illustration of theoretical Day plot 84
Figure 5.4: S-ratio mapping of BG14_0101 90
Figure 5.5: IRM unmixing curves of GSL18 specimens 92
Figure 5.6: IRM unmixing curves of GSL19 specimens 94
Figure 5.7: IRM unmixing curves of LB19 specimens 96
Figure 5.8: IRM unmixing curves of GR18 specimens 97
Figure 5.9: IRM unmixing curves of BG14 specimens 99
Figure 5.10: ARM decay & IRM acquisition and decay diagram for Lowrie-Fuller test 101
Figure 5.11: Diagram of IRM component decays by 3D IRM technique 105
Figure 5.12: Curie temperature of GSL18_0202 106
Figure 5.13: Curie temperature of LB19_0201 108
Figure 5.14: Curie temperature of GR18_0101 109
Figure 5.15: Curie temperature of BG14_0101 110
Figure 5.16: Sample's magnetic behaviors with an applied field 111
Figure 5.17: Hysteresis loops of GSL18 specimens 112
Figure 5.18: Hysteresis loops of LB19 specimens 113
Figure 5.19: Hysteresis loops of GR18 specimens 114
Figure 5.20: Hysteresis loops of BG14 specimens 115
Figure 5.21: Day plot of microbialite specimens 116
Figure 5.22: FORC diagram of GSL18 and LB19 specimens 117
Figure 5.23: FORC diagram of GR18 specimens 118
Figure 5.24: FORC diagram of BG14 specimens 119

Chapter 6: Microbialite Magnetization Processes
Figure 6.1: Illustration of plausible microbialite magnetization processes 125
Figure 6.2: Illustration of an AMS coordinate system and an anisotropy ellipsoid 129
Figure 6.3: Classification of AMS fabric using bootstrap confidence ellipses 131
Figure 6.4: Verwey transition of a biogenic magnetite 134
Figure 6.5: Diagram of NRM vs ARM intensity 135
Figure 6.6: NRM/ARM mapping of GSL18_0301, GSL19_0202, and BG14_0101 137
Figure 6.7: NRM/ARM mapping of GR18_0101 138
Figure 6.8: AMS results of GSL18_0301 139
Figure 6.9: AMS results of GR18_0101 140
Figure 6.10: AMS results of BG14_0101 141
Figure 6.11: MPMS measurement of LB19_0305 142

Appendix A: Sample Photos and Coordinates
Figure A.1: Sample photos and lab coordinate of GSL18_0301_A, B, C, D, E 156
Figure A.2: Sample photos and lab coordinate of GSL19_0103_A 157
Figure A.3: Sample photos and lab coordinate of GSL19_0201_A 158

Figure A.4: Sample photos and lab coordinate of GSL19_0202_A 159
Figure A.5: Sample photos and lab coordinate of LB19_0104 160
Figure A.6: Sample photos and lab coordinate of GR18_0101_A 161
Figure A.7: Sample photos and lab coordinate of BG14_0101_A 162

Appendix B: NRM intensity and Magnetic Susceptibility Mappings
Figure B.1: NRM intensity and susceptibility mapping of GSL19_0103_A 163
Figure B.2: NRM intensity and susceptibility mapping of GSL19_0202_A 164

Appendix C: IRM Unmixing Curves
Figure C.1: IRM unmixing curves of GSL18 specimens 165
Figure C.2: IRM unmixing curves of LB19 specimens 166

Appendix D: Lowrie-Fuller Tests
Figure D.1: ARM decay & IRM acquisition and decay diagram of GSL18 specimens 167
Figure D.2: ARM decay & IRM acquisition and decay diagram of GSL19 specimens 168
Figure D.3: ARM decay & IRM acquisition and decay diagram of LB19 specimens 169
Figure D.4: ARM decay & IRM acquisition and decay diagram of GR18 specimens 170

Appendix E: 3D IRM Technique
Figure E.1: GSL18 specimens' IRM component decays by 3D IRM technique 171
Figure E.2: GSL19 specimens' IRM component decays by 3D IRM technique 172
Figure E.3: LB19 specimens' IRM component decays by 3D IRM technique 173
Figure E.4: GR18 specimens' IRM component decays by 3D IRM technique 174
Figure E.5: BG14 specimens' IRM component decays by 3D IRM technique 175

Appendix E: Curie Temperature
Figure E.1: Curie temperature of GSL18_0202 176
Figure E.2: Curie temperature of LB19_0201 177
Figure E.3: Curie temperature of GR18_0101 178
Figure E.4: Curie temperature of BG14_0101 179

Appendix G: FORC measurements
Figure G.1: FORC diagram of high coercivity BG14 specimens 180
Figure G.2: FORC diagram of low coercivity BG14 specimens 181

Appendix H: MPMS measurements
Figure H.1: MPMS measurement of specimen LB19_0305_01 182
Figure H.2: MPMS measurement of specimen LB19_0305_02 183

LIST OF TABLES

Chapter 1: Introduction
Table 1.1: Occurrences of modern living microbialites 8

Chapter 2: Geologic Setting, Field Methods, and Laboratory Sample Preparation
Table 2.1: Four microbialite sample locations, types, environments, and ages 11
Table 2.2: Detailed samples' location, sites, location, description, and orientation 22

Chapter 3: Microbialite Magnetism and Stability
Table 3.1: NRM intensity and magnetic susceptibility values of GSL18 specimens 42
Table 3.2: NRM intensity and CSD values of LB19 specimens 44

Chapter 4: Paleomagnetic Directional Analysis
Table 4.1: Demagnetization types and steps applied on each specimen 52
Table 4.2: GAD inclinations of the four sampling sites 55
Table 4.2: APWP directions of the four sampling sites 56

Chapter 5: Magnetic Properties of Microbialites
Table 5.1: IRM unmixing types and steps applied on each specimen 77
Table 5.2: S-ratio of GSL18_0301 specimens 88
Table 5.3: S-ratio of LB19_0301 specimens 88
Table 5.4: S-ratio of GR18_0101 specimens 89
Table 5.5: S-ratio of BG14_0101 specimens 90
Table 5.6: IRM unmixing statistics of GSL18 specimens 92
Table 5.7: IRM unmixing statistics of GSL19 specimens 94
Table 5.8: IRM unmixing statistics of LB19 specimens 96
Table 5.9: IRM unmixing statistics of GR18 specimens 98
Table 5.10: IRM unmixing statistics of BG14 specimens 99
Table 5.11: MDF of ARM decay, IRM decay and acquisition for Lowrie-Fuller test 101
Table 5.12: Blocking temperature of soft, medium, hard minerals (3D IRM technique) 104
Table 5.13: Curie temperatures of GSL18 specimens by different smoothing window 107
Table 5.14: Curie temperatures of GR18 specimens by different smoothing window 109
Table 5.15: Curie temperatures of BG14 specimens by different smoothing window 111
Table 5.16: Parameters (M_{rs}, M_r, H_c, H_{cr}, X_{hf}) measured by magnetic hysteresis loops 116
Table 5.17: Summary of the magnetic properties of microbialite samples 124

LIST OF ABBREVIATIONS

AMS	Anisotropy of Magnetic Susceptibility
A/H	Azimuth and Hade
AF	Alternating Field
APWP	Apparent Polar Wonder Path
ARM	Anhysteretic Remanent Magnetization
asl	Above Sea Level
BCM	Biologically Controlled Mineralization
BG	Bayan Gol Formation
BIM	Biologically Induced Mineralizatioon
cal	Calibrated Dates
CALSxK.n	Continous Models of Archaeomagnetic and Lake Sediment Data for the Past x Thousand Years Version.n
ChRM	Characteristic Remanent Magnetization
CRM	Chemical Remanent Magnetization
DP	Dispersion Parameter (mT)
DP.sd	Dispersion Parameter standard deviation (mT)
DRM	Detrital Remanent Magnetization
err(H)	Hysteresis Loop Error Curve as a Function of an Applied Field (H)
FC	Field Cooled
FORC	First-Order Reversal Curve
Ga	Giga-Annum (billion year)
GAD	Geocentric Axial Dipole
GR	Green River Formation
GSL	Great Salt Lake
H	Magnetic Field
H_c	Coercivity
H_{cr}	Coercivity of remanence
$H_{cr_IRMunmixing}$	Coercivity Defined from IRM unmixing data
$H_{cr_Lowrie\text{-}Fuller}$	Coercivity Defined by the Lowrie-Fuller test
IGRF	International Geomagnetic Reference Field
IRM	Isothermal Remanent Magnetization
$IRM_{-0.3T}$	IRM Acquired in 0.3T Backfield
IRM_{1T}	IRM Acquired in 1T Forward field

$IRM_{-1000mT}$	IRM Stepwise Acquisition Measurements Starting with 1000mT Backfield
IRM_{0mT}	IRM Stepwise Acquisition Measurements Starting with 0mT
ka	Kilo-annum (thousand year)
kyr	kiloyear (thousand year)
lat	Latitude
LB	Laguna Bacalar
lon	Longitude
M	Magnetization
$M^-(H)$	Lower Branch of a Hysteresis Loop
$M^+(H)$	Upper Branch of a Hysteresis Loop
MAD	Maximum Angular Deviation
Ma	Mega-Annum (million year)
MC	Mean Coercivity (mT)
MC.sd	Mean Coercivity Standard Deviation (mT)
MD	Multi-Domain
MDF	Median Destructive Field
M_{inv}	Magnetization of Inverted Lower Branch of a Hysteresis Loop
MPMS	Magnetic Properties Measurement System
M_{rem}	Remanent Magnetization
M_{rh}	Symmetry Parameter of a Hysteresis Loop
M_{rs}	Saturation Remanent Magnetization
M_s	Saturation Magnetization
MTB	Magnetotactic Bacteria
M_{tot}	Total Magnetization
Myr	Million Years
N	Vector Sum of Unit Vectors
NRM	Natural Remanent Magnetization
OATZ	Oxic-Anoxic interface or Transition Zone
P	Relative Proportion
P.sd	Relative Proportion Standard Deviation
PSD	Pseudo-Single Domain
R	Resultant Vector
S	Skewness
S-ratio	Saturation Ratio
S.sd	Skewness Standard Deviation
S/D	Strike and Dip

SD	Single-Domain
sIRM	Saturated Remanent Magnetization
SP	Superparamagnetic
SQUID	Superconducting Quantum Interface Device
$\mathbf{T_b}$	Unblocking Temperature
$\mathbf{T_{b_soft}}$	Unblocking Temperature of Soft Fragment (coercivity>100mT)
$\mathbf{T_{b_hard}}$	Unblocking Temperature of Hard Fragment (coercivity>1T)
$\mathbf{T_{b_medium}}$	Unblocking Temperature of Medium Fragment (coercivity>300mT)
$\mathbf{T_c}$	Curie Temperature
$\mathbf{T_{c_cooling}}$	Curie Temperature from cooling curve
$\mathbf{T_{c_heating}}$	Curie Temperature from heating curve
TRM	Thermal Remanent Magnetization
$\mathbf{T_v}$	Verwey Transition
$\mathbf{V_1}$	Maximum Eigenvector
$\mathbf{V_2}$	Intermediate Eigenvector
$\mathbf{V_3}$	Minimum Eigenvector
VRM	Viscous Remanent Magnetization
ZFC	Zero Field Cooled
$\boldsymbol{\alpha_{95}}$	95 Confidence Ellipse of the Mean Direction
$\boldsymbol{\kappa}$	Precision Parameter
τ_1	Maximum eigenvalue
τ_2	Intermediate eigenvalue
τ_3	Minimum eigenvalue
χ	Magnetic Susceptibility
χ**(T)**	Magnetic Susceptibility as a Function of Temperature
χ_{hf}	High-Field Susceptibility

ACKNOWLEDGMENTS

First and foremost, I sincerely thank my advisor Dr. Julie Bowles. Without her support and encouragement, this work would not have been possible. I thank her for providing me a very cool project, patiently teaching me, answering all the questions that I asked, and willing to devote her time to fieldwork in Utah and lab work in Minnesota. Thanks for being a true advisor and my scientific role model. I would also like to thank the entire faculty and staff of the Department of Geosciences at the University of Wisconsin-Milwaukee (UWM), especially to my committee members Dr. Tim Grundl and Dr. Mark Harris for taking time for my thesis and for their thoughtful comments.

Funding for my masters thesis was generously provided by the assistantships from the UWM Department of Geosciences, and this project is supported by a grant from UWM's Research and Creative Activities Support (RACAS) program. Also, I would like to thank the National Institute for International Education, South Korea, for supporting the Korean Government scholarship for my masters study.

Many people aided microbialite sample collection and rock magnetic experiments. Bayan Gol stromatolite samples were provided by Dr. Steve Dornbos, UWM. Thanks to Jaimi Butler and Bonnie Baxter of Westminster College for assistance with sampling at the Great Salt Lake. Thanks to Dr. Tim Grundl, UWM, for help with sampling at Laguna Bacalar. Thanks to Eli Sutula and Josh Marquardt, UWM, for data collection. Thanks to the Institute of Rock Magnetism (IRM) for allowing to conduct multiple magnetic experiments.

Thank you to all my fellow graduate students, especially Chase Glenister, Gayantha Loku Kodikara, Jordan Ludyan, and Sebastian Fearn. I would never forget various discussions that we

made, including planetary sciences, paleomagnetism, and other global issues. Thanks to Dr. Yongjae Yu from Chungnam National University for seeing my potential and encouraging me. Many thanks to Han Gyeol Suh, UWM, for helping and supporting me while I finished my thesis in this COVID-19 situation. Lastly, I thank my family for continuous love and support.

Chapter 1: Introduction

1.1 Motivation and goals

The Earth's magnetic field changes in both time and space (i.e., secular variation), and these variations originate in the convection of the liquid outer core. To understand geodynamics of the ancient Earth and the magnetic field interactions with the complex Earth system over time, paleomagnetists seek the accurate recovery of the ancient geomagnetic field in the geologic record. Remanent magnetization in natural materials such as volcanic and sedimentary rocks as well as archeological materials have been used for ancient magnetic field reconstruction and geodynamo modeling.

This thesis addresses the feasibility of microbialites as paleomagnetic recorders. Paleomagnetic records in microbialites would be very useful for reconstructing the geomagnetic field for three reasons: 1) microbialites may record at high temporal resolution based on estimated growth rates (0.05~50 mm/year) (Berelson et al., 2011; Brady et al., 2009) thus preserving relatively short-period variations of Earth's magnetic field; 2) microbialites can be found in the geologic record going back ~3.5 Ga and may thus provide information on very ancient variations in Earth's magnetic field if they are preserved without significant metamorphism; and 3) microbialites have relatively wide environmental distribution.

Microbialites may incorporate ferromagnetic particles and a remanent magnetization by abiogenic processes (e.g. detrital remanent magnetization) and/or biogenic processes (e.g. magnetotactic bacteria, biologically induced biomineralization). However, natural remanent magnetization (NRM) intensity and direction may differ if acquired by different magnetization processes, and secondary magnetizations may also obscure the primary magnetization. Therefore, in order to properly interpret microbialites as a paleomagnetic recorder, it is important to

understand the magnetic stability of microbialites, their magnetic properties and the magnetization process. Limited prior studies have shown that ancient microbialites carry a magnetization (Vanyo & Awramik, 1982; Muraszko, 2014), but did not evaluate the magnetization timing, the process(es) by which the magnetization is acquired, or variations within the microbialite structure.

The goals of this research are to answer the following questions: 1) Do microbialites carry a magnetization that is stable in time? (Chapter 3); 2) What are the spatial variations in magnetization within the microbialite structure? (Chapter 3); 3) Do microbialites accurately record Earth's magnetic field direction? (Chapter 4); 4) What are the magnetic carriers in the microbialites? (Chapter 5); and 5) What is the magnetization process or the origin of the magnetization? (Chapter 6). Microbialite samples from four locations were collected: 1) Living and lithified hypersaline thrombolites from the Great Salt Lake, Utah, U.S.A.; 2) living and lithified freshwater microbialites from Laguna Bacalar, Quintana Roo, Mexico; 3) an ancient lacustrine environment stromatolite from the Eocene Green River formation, Wyoming, U.S.A; and 4) a marine, lower Cambrian Bayan Gol formation stromatolite, South Western Mongolia.

The rest of Chapter 1 provides the background of paleomagnetism (Section 1.2.1) and microbialites (Section 1.2.2). Chapter 2 lays out the geologic settings of four microbialite samples and laboratory methods. It also includes methods of magnetic measurements and instrumentation. The following four chapters discuss the four sub-aims of the thesis. Chapter 3 "Microbialite Magnetism and Stability" focus on whether microbialites can have stable magnetism by measuring magnetization over time. It also contains the contents of spatial variations in the microbialite structure. In Chapter 4 "Paleomagnetic Directional Analysis", directions extracted from ancient and modern microbialite samples from different localities are compared with their expected field values. Chapter 5 "Magnetic Properties of Microbialites" displays rock magnetic results to infer

the magnetic mineralogy and domain states of microbialites. With additional rock magnetic methods, the magnetization processes of samples are evaluated in Chapter 6 "Magnetization Processes of Microbialites". The last chapter presents summary observations and an assessment statement of microbialites as paleomagnetic recorders.

1.2 Background

1.2.1. The Earth's Magnetic Field and Paleomagnetism

The geomagnetic field is represented by a vector, so a magnetic field on any position on Earth's surface can be described with the vector's intensity and direction (declination and inclination). As a result, a magnetization of a rock records intensity, inclination, and declination of a field, from which we can reconstruct the Earth's ancient magnetic field.

Rocks are typically assemblages of ferromagnetic minerals (e.g., magnetite) dispersed within a matrix of diamagnetic (e.g., calcite, quartz) and paramagnetic minerals (e.g., fayalite). Diamagnetism and paramagnetism are types of induced magnetism that are present only in an applied field, while ferromagnetism has an induced component, but is also a permanent magnetism even in the absence of a magnetic field. Paleomagnetism is based on the assumption that these ferromagnetic particles carry the record of ancient magnetic fields.

The relationship between the magnetic field and a magnetism of a rock can be simply written as:

$$\mathrm{M_{tot}} = \chi \mathrm{H} + \mathrm{M_{rem}}$$

Where M_{tot} is total magnetization, and M_{rem} is remanent magnetization. Any information on ancient fields is carried by M_{rem}, which is held by ferromagnetic minerals. In the presence of an applied field, H, an induced magnetization may also be present, and is proportional to the material's

susceptibility (χ). Diamagnetic and paramagnetic materials have weakly negative and positive χ, respectively (Figure 1.1.A and B). However, when a ferromagnetic mineral is exposed to magnetizing field, the magnetization of ferromagnetic minerals will not go back to zero in the absence of a field, and it requires an opposing field to be removed. As a function of applied field, this material's magnetization will trace out a hysteresis loop (Figure 1.1.C). Often (but not always), the (positive) magnetic susceptibility of ferromagnetic minerals is much stronger than diamagnetic or paramagnetic minerals.

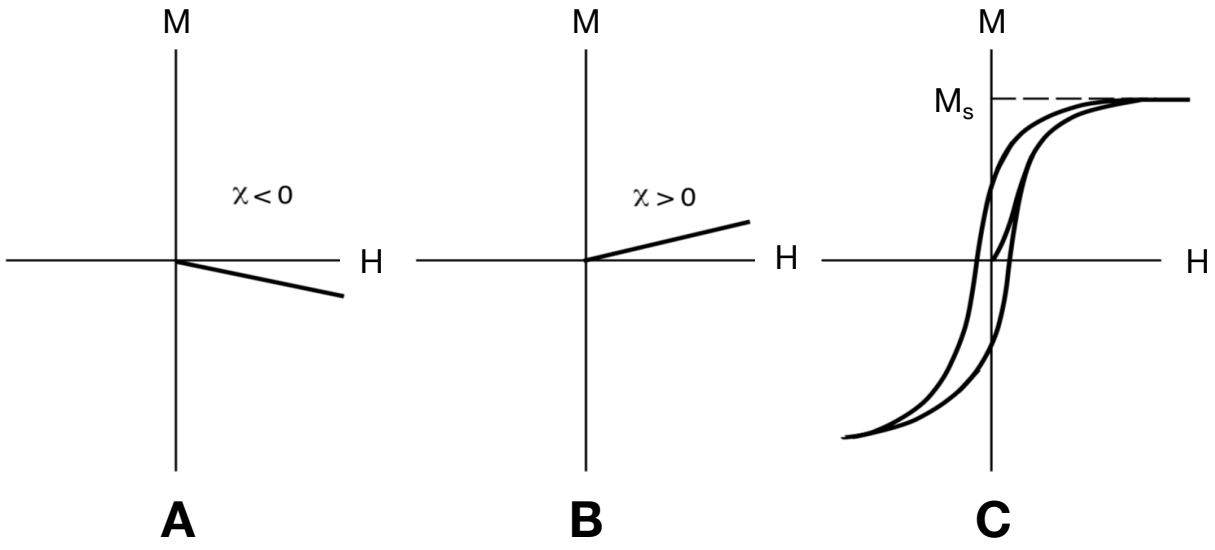

Figure 1.1. Magnetization (M), versus applied field (H) for a diamagnetic (A), paramagnetic (B) and ferromagnetic (C) materials (Modified from Butler, 2004).

Almost any rock will have a permanent (remanent) magnetization acquired in nature (i.e., a natural remanent magnetization, NRM). However, the NRM may record the geomagnetic field by different natural processes. 1) Thermal remanent magnetization (TRM) is produced by cooling from above the Curie temperature (T_c) in a presence of a magnetic field, and this is the main processes for igneous and metamorphic rocks. 2) Detrital remanent magnetization (DRM) is produced when magnetized detrital grains partially align with an applied field in the water column

and/or at the sediment/water interface, and therefore this is the major process for sedimentary rocks. 3) Viscous remanent magnetization (VRM) is gradually acquired during exposure to a weak magnetic field, and this is typically a secondary magnetization resulting from the change of the geomagnetic field long after the formation of the rock. 4) Chemical remanent magnetization (CRM) can also be a secondary remanent magnetization, formed by growth of ferromagnetic grains below the Curie temperature. 5) Isothermal remanent magnetization (IRM) can be acquired once a rock is exposed to a very high magnetic field; in nature, lightening can produce an IRM. In addition to these natural processes, there is another way to artificially magnetize rocks. 6) Anhysteretic remanent magnetization (ARM) can be produced when a rock sample is subjected to an alternating biased field in the laboratory.

Once the NRM is acquired in rocks by these magnetization processes, the stability over time is partly related to magnetic domain state. Within a single magnetic crystal, magnetic domain is an area with uniform magnetization. The size and number of domains depends on the grain size and mineral composition. This is because the ferromagnetic particles' internal magnetization structure is a function of the minimization of all magnetic and thermal energies, some of which vary with grain size. For example, a magnetite particle less than ~40 nm in diameter will have uniform magnetization throughout, and it is called single domain (SD) (Figure 1.2.A). For larger particles (greater than a few microns), in order to minimize the net energy, the grains will have multiple competing regions of uniform magnetization, with boundaries between them. This state is called multidomain (MD) (Figure 1.2.B), and this phase is relatively easier to demagnetize compared to SD. The magnetic particles with grain sizes between SD and MD, can show flower, vortex or other non-uniform magnetizations, and this state is called pseudo-single domain (PSD). When the thermal energy of very small magnetite particles (< 20nm) exceeds magnetic energy barriers, they

show very unstable magnetization, and these particles are called superparamagnetic (SP) grains. In general, magnetic remanence and stability decreases with increasing grain size from SD to MD, and purely SP grains have no remanence.

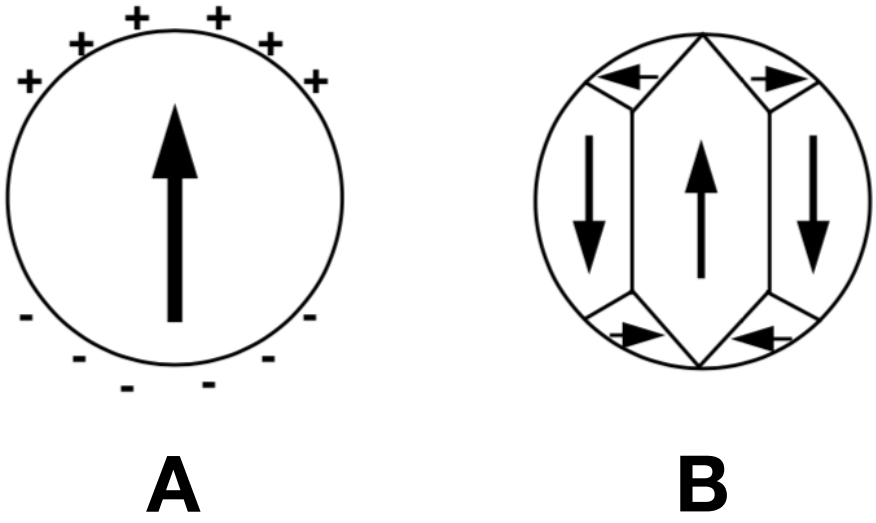

Figure 1.2. Illustration of magnetic domain states: (A) single-domain and (B) multidomain phase (From Butler, 2004).

One measure of ferromagnetic particle stability is its coercivity. Coercivity is a measure of the material to resist demagnetization. Ferromagnetic materials with high coercivity are called magnetically hard, and low coercivity materials are called magnetically soft. For the same mineral composition, SD materials will have higher coercivity than MD materials. Different mineraologies also have different coercivity ranges. Magnetically hard materials (e.g., hematite) are typically more stable than magnetically soft substances (e.g., magnetite) and are more difficult to demagnetize.

1.2.2. Microbialites

Microbialites are organosedimentary deposits accreted by a combination of benthic microbial community trapping and binding detrital sediment and/or mineral precipitation, and abiogenic

precipitation (cementation) (Riding, 2011a). Microbialites can be subdivided by different fabric structures (Figure 1.3): stromatolite (laminated structure), thrombolite (a clotted structure lacking lamination), dendrolite (dendritic structure), leolite (aphanitic structure), and all categories can be intergradational.

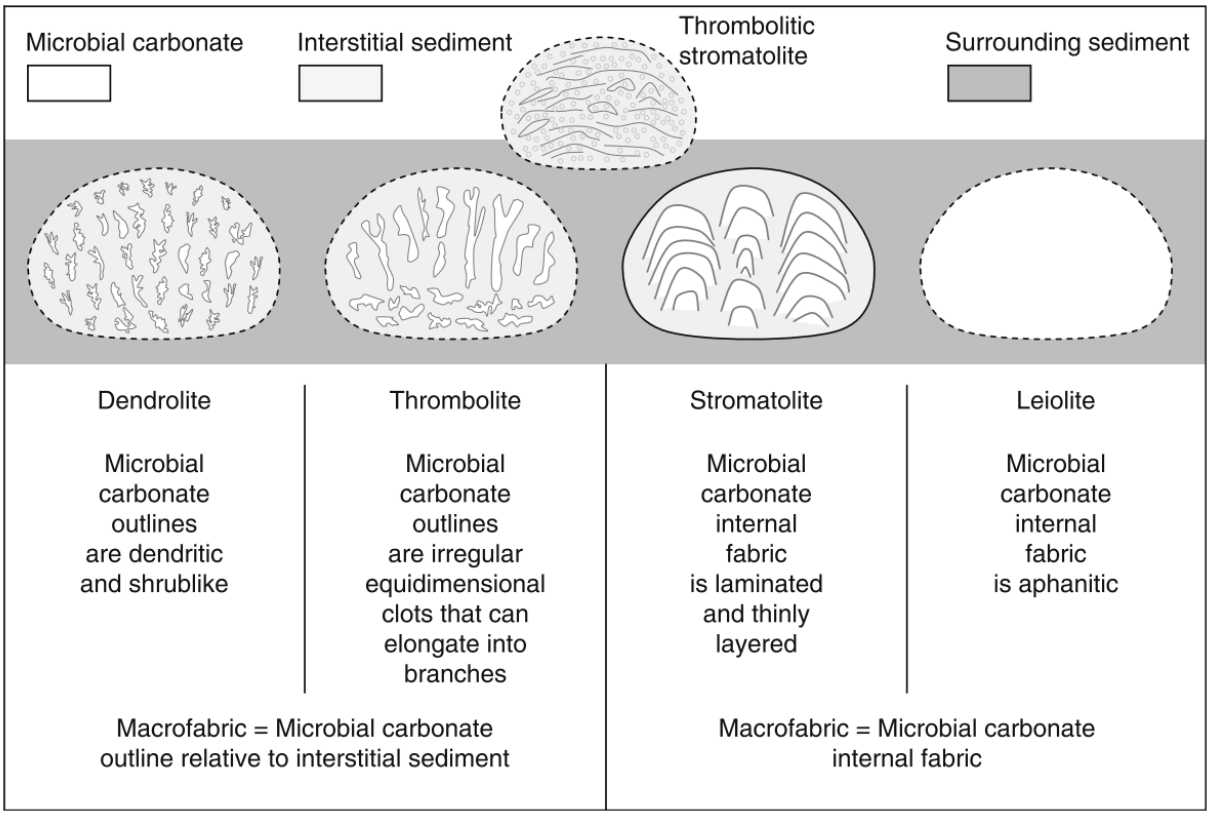

Figure 1.3. The classification of microbialites based on their fabric structures (From Riding, 2011a)

Stromatolites are a type of microbial carbonate rock (biogenic) with or without interlayered abiogenic precipitates. They are layered, lithified, authigenic microbial structures (domed or columnar) that developed at the sediment-water interface in marine (high salinity), freshwater, and evaporitic environments (Riding, 2011a). Most extant classic stromatolites are found in Shark Bay, Australia, and Exuma Cays, Bahamas (highly saline marine environments). Stromatolite micro- and macrofabrics commonly intergrade with those of dendrolites and thrombolites. While stromatolites are laminated microbialites, thrombolites have unlayered and/or internal lamination

with clotted features. Including thrombolites, other modern microbial rocks are found in subtropical marshes and shorelines, tidal flats, high-salinity lakes, alkaline freshwater lakes, and acidic hydrothermal environments (Table 1.1).

Table 1.1 Occurrences of modern living microbialites

Location	Environment	References
Shark Bay (Australia)	High-Salinity Marine	Burns et al., 2009; Burns, Goh, Allen, & Neilan, 2004; Chivas, 1990
Exuma Cays (Bahamas)	High-Salinity Marine	Edgcomb et al., 2014; Tarhan, Planavsky, Laumer, Stolz, & Reid, 2013
Great Salt Lake (Utah, US)	High-Salinity Lake	Pedone & Folk, 1996; Halley, 1976
Pavilion Lake (BC, Canada)	Alkaline Freshwater Lake	Brady et al., 2009
Kelly Lake (BC, Canada)	Alkaline Freshwater Lake	Ferris, Thompson, Beveridge, Ferris, & Thompson, 2016
Yellowstone (Wyoming, US)	Acidic Hydrothermal Environments	Berelson et al., 2011; Pepe-Ranney, Berelson, Corsetti, Treants, & Spear, 2012
Chetumal Bay (Belize)	Tidal Flats	Rasmussen, Macintyre, & Prufert, 1993
Laguna Bacalar (Cancun, Mexico)	Freshwater Lagoon	Castro et al., 2014; Castro, 2014; Gischler, Gibson, & Oschmann, 2008; Johnson, Beddows, Flynn, & Osburn, 2018

The geological record of stromatolites goes back to at least 3.5 billion years ago (Grotzinger & Knoll, 2002), and their peak diversity abundance was around 1.25 billion years ago (Riding, 2006) (Figure 1.4). In the history of stromatolites, the process dominating the formation has varied between biogenic (e.g. lithified microbial carbonate), abiogenic precipitated crust (i.e. sparry crust), and/or a hybrid mixture of the two (Riding, 2011b). However, the definition of stromatolite is still debatable in terms of encompassing both biogenic and abiogenic origins because it is difficult to find ancient samples more than 1 billion year old (Riding, 2011b). It has been observed that more abiogenic processes were dominant in Archean stromatolites, and mixed and more biogenic processes are observed to the present (Riding, 2011b). Grazing and metazoan competition have been suggested as a major factor contributing to the decline of stromatolite diversity after

their acme, but other factors such as seawater chemistry and atmospheric composition could affect their diversity (Riding, 2006). After the end of the Precambrian and into the early Phanaerozoic, thrombolites became the predominant type of microbialites.

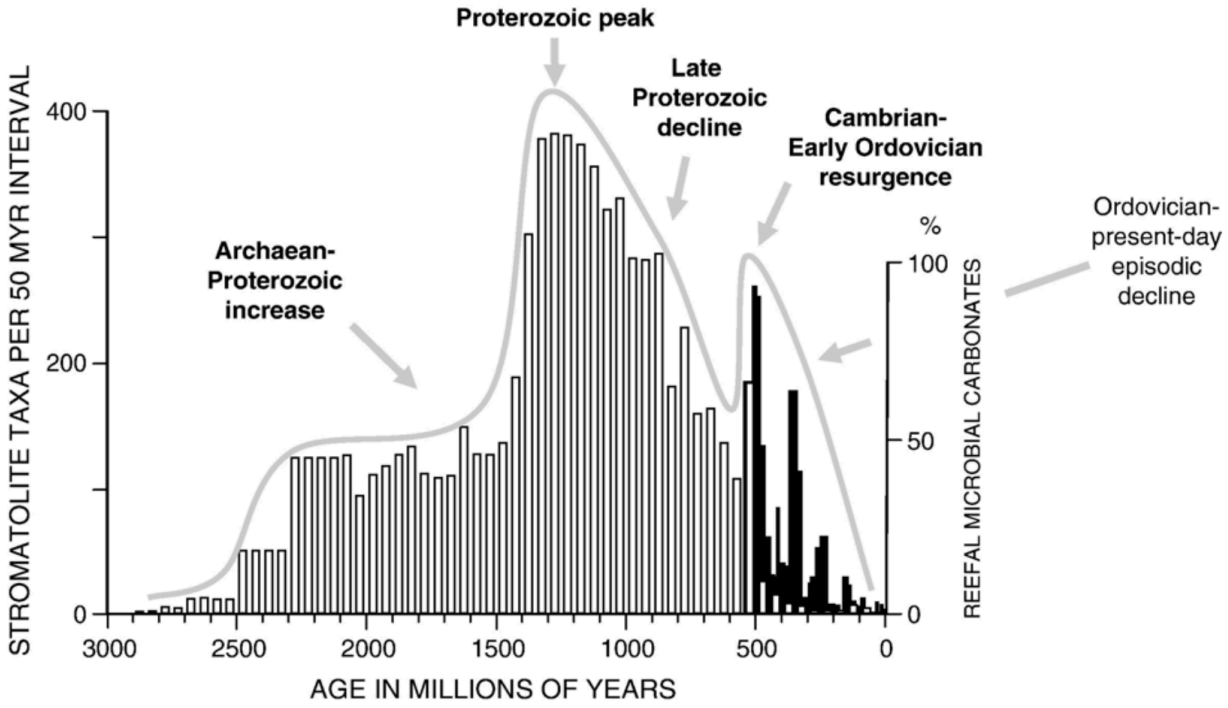

Figure 1.4. Stromatolite diversity (white columns) and reefal carbonate abundance (black columns) over geologic time scale (From Riding, 2006)

Chapter 2: Geologic Settings, Field Methods, and Laboratory Sample Preparation

2.1. Geologic Setting and Field Methods

Living and lithified modern and Pleistocene microbialite samples were collected at Great Salt Lake (GSL), Utah, U.S.A. in June 2018 and August 2019. Living and lithified modern and Holocene microbialites were retrieved from Laguna Bacalar (LB), Quintana Roo, Mexico, in January 2019. Two ancient microbialites were collected from the Green River (GR) formation near Boar's Tusk, Wyoming, U.S.A., in June 2018, and the lower Cambrian Bayan Gol (BG) formation, Southwestern Mongolia in 2014 (Figure 2.1, Table 2.1).

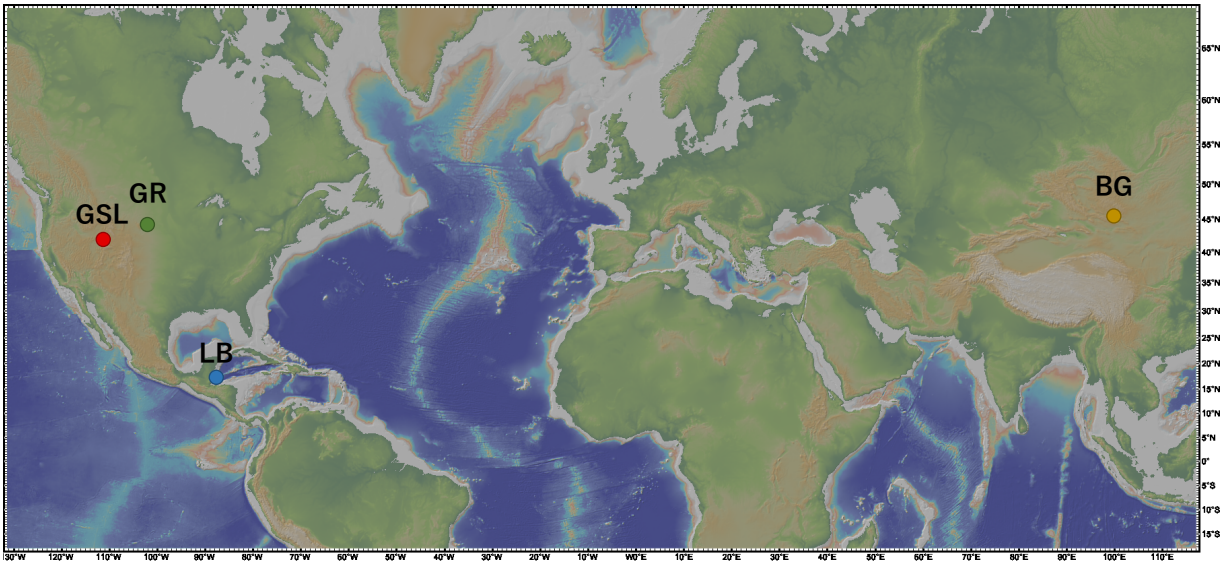

Figure 2.1. Global map showing the locations of four microbialite samples: Laguna Bacalar (LB), Quintana Roo, MX; Great Salt Lake (GSL), Utah; Green River formation (GR), Wyoming; Bayan Gol formation (BG), South Western Mongolia. Figure made with GeoMapApp (www.geomapapp.org) (Ryan et al., 2009).

Table 2.1. Table of the microbialite sample locations, types, environments, and ages.

Sampling Site	Location (Lon, Lat)	Type and Description	Environment	Age
Great Salt Lake (GSL), Utah, U.S.A.	N 41.15°, W 112.5°	Living and lithified microbialites	Hypersaline Lacustrine	Living Modern Pleistocene
Laguna Bacalar (LB), Quintana Roo, Mexico	N 18.6°, W 88.45°	Unlithified laminated sediments and Lithified porous microbialites	Freshwater Lacustrine	Living Modern Holocene
Green River Formation (GR), Wyoming, U.S.A.	N 41.97°, W 109.25°	Fossilized dome style gently convex microbialites	Lacustrine	Eocene
Bayan Gol formation (BG), Salaany Gol, Mongolia	N 46.42°, E 96.19°	Fossilized dome style steeply convex stromatolite	Marine	Cambrian ~530Ma

2.1.1. Great Salt Lake

The Great Salt Lake (GSL) is an endorheic hypersaline lake located in northwestern Utah, and it is the evaporative remanent of freshwater Pleistocene Lake Bonneville. The average salinity in the south arm of the GSL, where samples were collected, is approximately 120 g/L but fluctuates over a range of 50 to 285 g/L (Rupke & Mcdonald, 2012).

Currently, modern microbial deposits cover 1000 km^2 (Baskin, 2014), and these lacustrine microbialites are predominately located around the lake margin and show a heterogeneous but non-random spatial distribution and macrofabric (Figure 2.2). Climate driven water level fluctuations and tectonics were key roles in the microbial deposits' distributions (Bouton et al., 2016). The macrofabrics of microbialites (e.g. laminated cauliflower, cow-pie, oncoid, flat ridge and dome-style) can be distinguished along the shore to lake transect (Figure 2.2 ; Bouton et al., 2016).

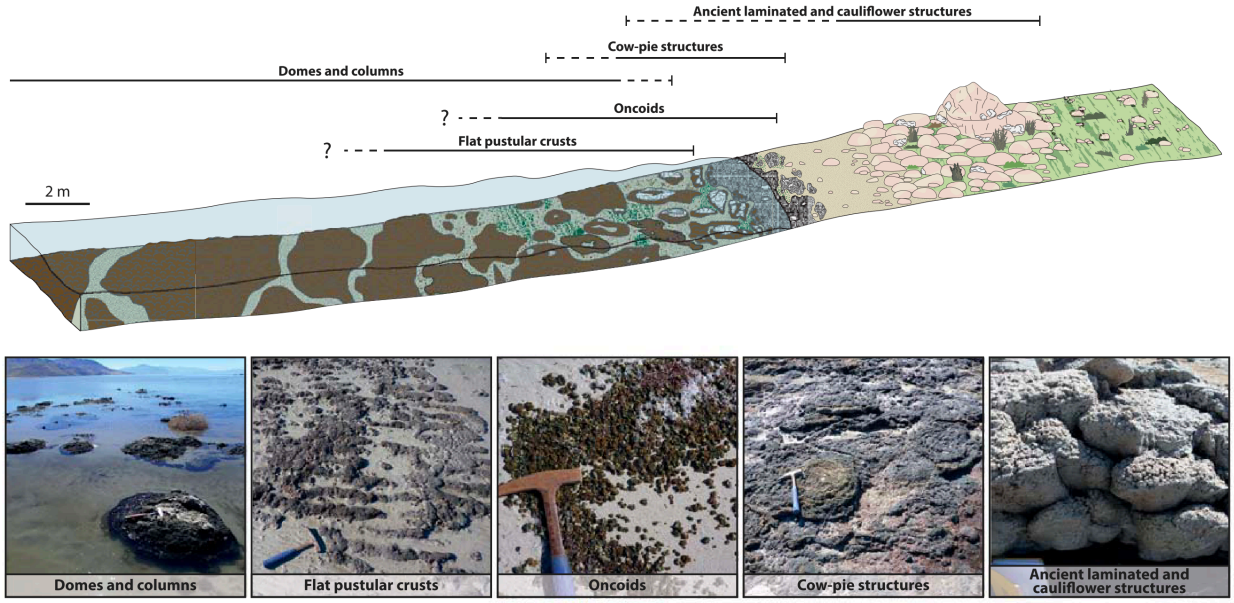

Figure 2.2. The classification of macrofabric structures of GSL microbialites which can be observed along the shore-to-lake transect both the emersed and submersed area (From Bouton et al., 2016).

In August 2018, living and lithified microbialite samples were obtained from four sites along the northwest margin of Antelope Island (Figure 2.3.A, B). Eight living and one lithified (Site 3) samples representing different morphologies were taken from four sites. Site 1 and Site 2 were low-relief, rounded 'cow-pie'-like features (Figure 2.3.D; GSL18_0101-04, GSL18_0201-02). Site 4 included some similar structures (GSL18_0402), as well as some more similar to flat, ridge-like crusts which form parallel to wave action (GSL18_0401). At Site 3, a larger dome-style feature (Figure 2.3.E; GSL18_0301) protruded above the waterline, which has fallen significantly in recent years. This feature was no longer living, and a lithified section was removed. An orientation tag was affixed to the living, underwater samples from sites 1, 2, and 4 with an underwater epoxy. Unfortunately, the epoxy did not adhere well to the microbial surface, and the tags all ultimately fell off in transport. These living microbialite samples were sealed in Whirlpak bags with lake water and kept at ambient temperatures until opened several weeks later. Temperature fluctuations

during transport and storage were likely similar to those experienced by the microbialites in the shallow waters of the GSL.

In August 2019, lithified microbialite samples were collected from two sites near Lakeside at 1283 m asl (Site 1) and 1285 m asl (Site 2), respectively. The age of the samples is estimated about ~12.5 kyr based on ^{14}C ages of nearby tufa and microbialite samples collected from Lakeside (~1283 m asl) (Godsey et al., 2005; Pedone & Dickson, 2000; Newell et al., 2017). At Site 1, fossil microbialite deposits were collected from the monk's head structure layer (Figure 2.3.G). These samples were porous, and clasts (approximately 0.5 to 5 mm in diameter) were interbedded in the microbialite inner structure. Two core samples (GSL19_0101, GSL19_0102) were obtained by drilling with a diamond bit, and two hand samples (GSL19_0103, GSL19_0104) were collected by hammering. Microbialites located at Site 2 were ancient cauliflower structures and two hand samples (GSL19_0201, GSL19_0201) were collected. Azimuth/hades of core samples were recorded, and strike/dips were marked on hand samples before removing from the sites.

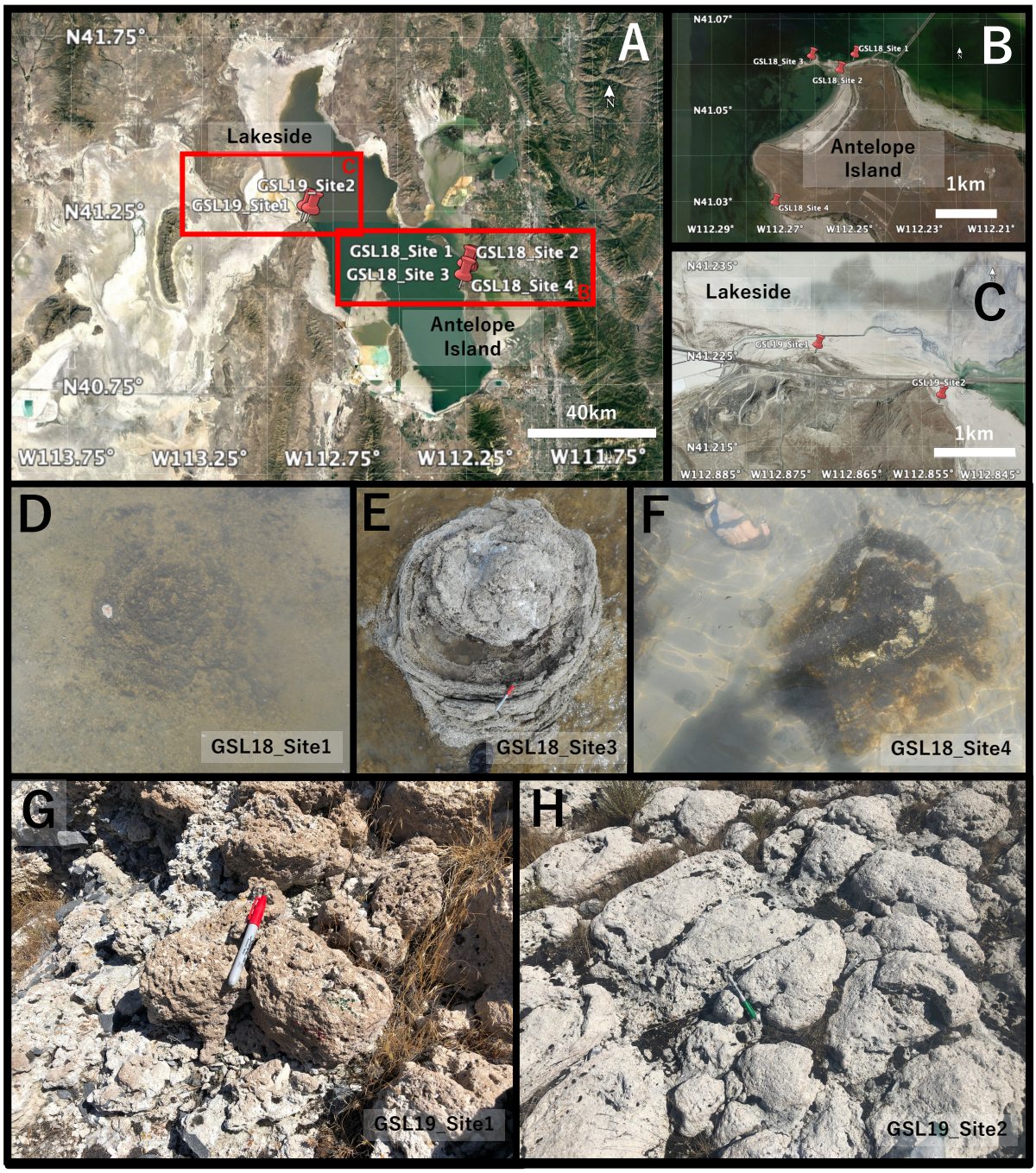

Figure 2.3. Satellite image of the sampling locations of microbialites at Great Salt Lake (GSL) (A). Closer look of GSL18 study localities at the Antelope Island area (B) and GSL 19 sampling sites at Lakeside (C). Imagery from July 2019, ©2019 Google, Image Landsat/Copernicus. (D) Cow-pie structure microbialite under water from GSL18_Site1. (E) Lithified domal microbialite mound protruding above the water line at GSL18_Site3. (F) Partially collapsed dome style microbialites sampled at GSL_Site4. (G) Monk's head structure and (H) cauliflower structure of microbialites collected at GSL19 Site 1 and 2, respectively.

2.1.2. Laguna Bacalar

Laguna Bacalar is a 40 km long (north to south) and 2 km wide narrow NNE-trending freshwater lagoon located in the state of Quintana Roo, Mexico. It is surrounded by Cenozoic limestone and the carbonate platforms mostly consist of limestone, dolomite and evaporates. The water chemistry is supersaturated with $CaCO_3$ as a result of degassing of karstic waters (Castro, 2014; Gischler et al., 2008), and thus, compared with the rest of the lagoon, the carbonate concentration is much higher in the southwest, where cenotes are located (Gischler et al.,2008).

Microbialites are predominantly found starting from the northern end of Xul-Ha cenote to the southern end of the town of Bacalar (Figure 2.4.A), formed by carbonate precipitation fed by karst aquifer circulation through cenotes (Gischler et al., 2008). Both thrombolitic and stromatolitic meso-structure domal morphologies are observed in the Laguna Bacalar microbialites (Castro, 2014), and the bulk of the microbialites formed in late Holocene. ^{14}C dating of the microbialites results in anomalously old ages of 9 to 8 cal kyr BP, likely due to the incorporation of "old" carbon from the karst system (Gischler et al.,2008).

The Laguna Bacalar microbialite growth rate is largely related to the ambient carbonate saturation state, and the texture depends on accretion rates and sediment depositions (Castro, 2014). While internally-laminated Laguna Bacalar microbialites (stromatolites) were formed during the period of low sedimentation with the upward migration of cyanobacteria, the clotting fabrics (thrombolites) were formed during the period of high sedimentation as a result of binding, trapping of micritic peloids by cyanobacteria (Castro, 2014). Laguna Bacalar microbialite growth is not significantly inhibited by grazing animals (Castro, 2014). This lack of disturbance may create favorable conditions for the preservation of DRM.

Samples were taken from three different sites (Figure 2.4.A, B). Microbialites from Site 1 (Figure 2.4.C) are unlithified deposits in a layered giant domal structure and were soft and easily penetrated. Eight surface samples were collected in 2 cm^3 plastic cubes directly from the field (LB19_0101). One domal structure hand sample (15 cm x 13 cm; LB19_0102; Figure 2.4.F) was collected, transported back to the lab, and then subsampled (see Section 2.2.2). Microbialites were additionally sampled with a small plastic core (16 cm long, 5 cm wide; LB19_0103) by push coring, rotating to the left. A large core (35 cm long, 7.5 cm wide; LB19_0104) was also collected by push coring, rotating to the right. Their surface directions were marked by bradding non-magnetic nails, and these cores were preserved at room temperature for two days filled with the lake water, then frozen for two days. Microbialites from Site 2 (East Coast; Figure 2.4.D, G) were lithified but very porous, and three core samples (LB19_0201-03) were obtained using an electric drill with a 1" diamond coring bit. At Site 3 (Figure 2.4.E, the rapids), giant coalesced microbialites have soft surfaces including living cyanobacteria layers (~ 2cm) and lithified but porous microbialites underneath (~15cm) (Figure 2.4.H). One hand sample (LB19_0305) and six surface layer specimens were collected in 2 cm^3 plastic cubes (LB19_0304). Three cores (LB19_0301-03) were collected from lithified parts with the electric drill. Living and unlithified samples were frozen after collection (within 3 hours for LB19_0101, 0201, 0202, 0203, 0304; within 2 days for LB19_0102,0103,0101) for 1 to 3 days prior to transportation. During the approximately 20 hours transportation back to the lab, all the samples warmed back to room temperature before being re-frozen.

The Site 1's water was quiet and stagnant. The water flows were turbulent for the east coast (Site 2). The rapids (Site 3) had fast currents overall, but for the sampling area at Site 3, the current was flowing moderately to the south.

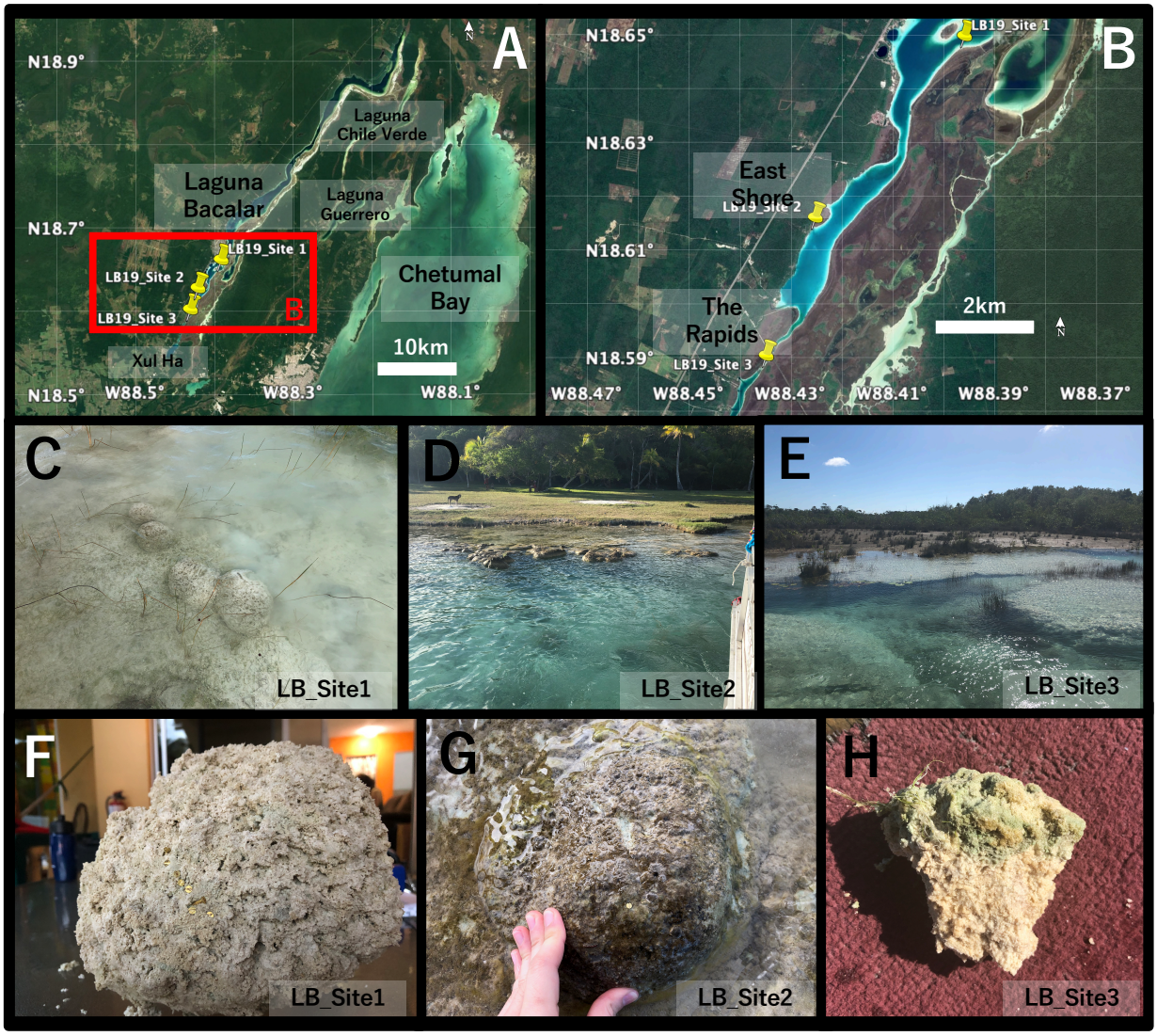

Figure 2.4. Satellite image of the sampling locations of microbialites at Laguna Bacalar (LB) (A). Closer look of LB19 study localities and three sampling sites (B). Imagery from April 2018, ©2019 Google, Image Landsat/Copernicus. Unlithified domal structure microbialite under water from LB19_Site1 (C), and the collected hand sample LB19_0102 (F). Microbialite mounds exposed along the east shore at LB19_Site2 (D) and top view of one microbialite body (G). Giant microbialites from the rapids at LB19_Site3 (E). Piece of a microbialite from site 3, which shows cyanobacteria layer at the top and lithified porous microbialite underneath (H).

2.1.3. Green River Formation

The Green River Formation is located in southwestern Wyoming, northwestern Colorado and northeastern Utah. During the Eocene period, four depositional basins were involved in three connected lakes including Lake Gosiute (Green River Basin), Lake Unita (the Unita and Piceance Creek Basin), and Fossil Lake (Fossil Basin) (Figure 2.5.A). These basins were later separated by chains of anticlinal uplifts. The Green River (GR) formation preserves ancient paleolake systems (the Goiute Lake) from the early to middle Eocene (52-50 Ma) (Frantz et al., 2014), which was the warmest period of the Cenozoic and a period of high atmospheric CO_2.

It is also well characterized by the extensive development of lacustrine microbialites (Awramik & Buchheim, 2015; Seard et al., 2013). It contains a diverse occurrence of microbialites: giant, multi-meter size, columnar stromatolites, as well as centimeter size microbialites considered to be near-shore deposits (Figure 2.5.B). Calcium rich spring water and faults were considered to play key roles in the development of Green River microbialites (Surdam et al., 1980)

The study area is located at approximately 51 km north of Rock Spring Wyoming and 4.5 km east of the Boar's Tusk (Figure 2.5.C, D). Two hand samples (GR18_0101, GR18_0201) situated in the Rife Bed (Figure 2.5.B) were marked with strike and dip in the field and removed using a hammer and chisel. The sampled microbialites (about 30 x 60 cm wide and 15 cm high) have a dome shape and are characterized by nearly horizontal internal laminations (Figure. 2.5.E). The approximate depositional age for the microbialites located in the Rife Bed is between 50.70 Ma to 51.30 Ma (Smith et al., 2008).

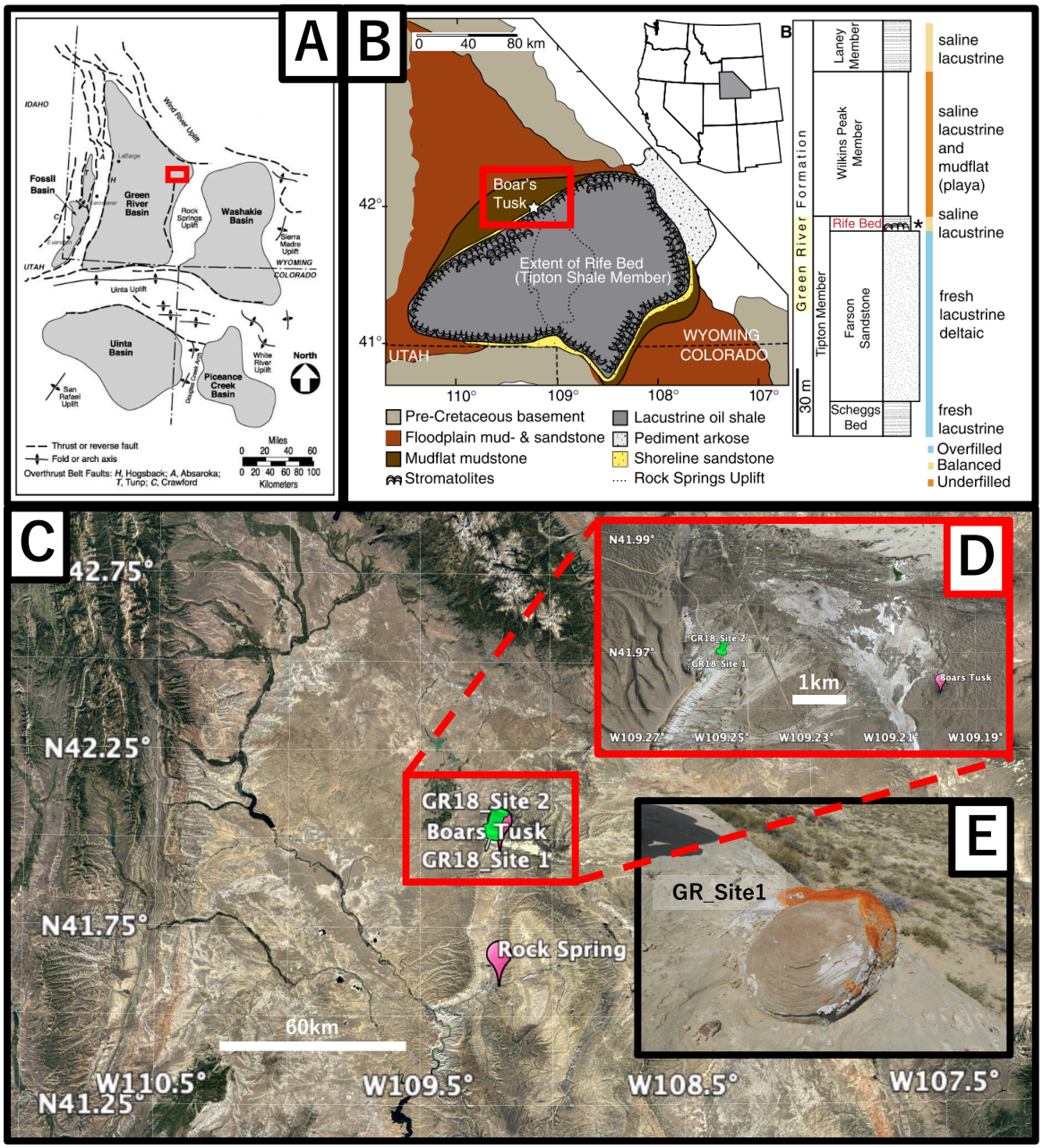

Figure 2.5. (A) Location map of the major Eocene basins in which the Green River Formation was deposited: Green River, Washakie, Unita, Piceance Creek and Fossil basins (modified from Leggitt and Cushman, 2001). (B) Map showing the location of the Boar's Tusk outcrop and the extent of the Rife Bed and surrounding depositional environments at the time when the stromatolites were forming near the shoreline of Paleolake Gosiute (modified from Frantz et al., 2014). (C) Satellite image of the sampling locations at Green River Formation (GR) in this study. (D) Closer look of sampling sites and the location of the Boar's Tusk. Imagery from July 2019, ©2019 Google, Image Landsat/Copernicus. (E) Sample GR18_0101 at Site 1, with red strike/dip line marked before removal.

2.1.4. Bayan Gol Formation

The Bayan Gol Formation is located in western Mongolia, and it consists of early Cambrian mixed carbonate-siliciclastic deposits (Khomentovsky & Gibsher 1996). It preserves ancient shallow marine environments between the Siberian craton and the Baydaric microcontinent (Lindsay et al. 1996). The formation is made up of intercalated carbonate and siliciclastic layers, with a gradual shift from limestone to siltstone and sandstone, representing a shoreline with an increasing siliclasic influx over time (Lindsay et al. 1996).

The BG14 sample is a stromatolite limestone head from lower Cambrian stromatolites in the middle of Unit 18 (Khomentovsky & Gibsher, 1996) of the Bayan Gol section (Figure 2.6). The sample (Figure. 2.6.B) was collected by Dr. Steve Dornbos and was only oriented with respect to up. The sample displays parallel (but not horizontal) internal layering (Figure. 2.8. BG14_0101A), consistent with draping growth over a rounded substrate.

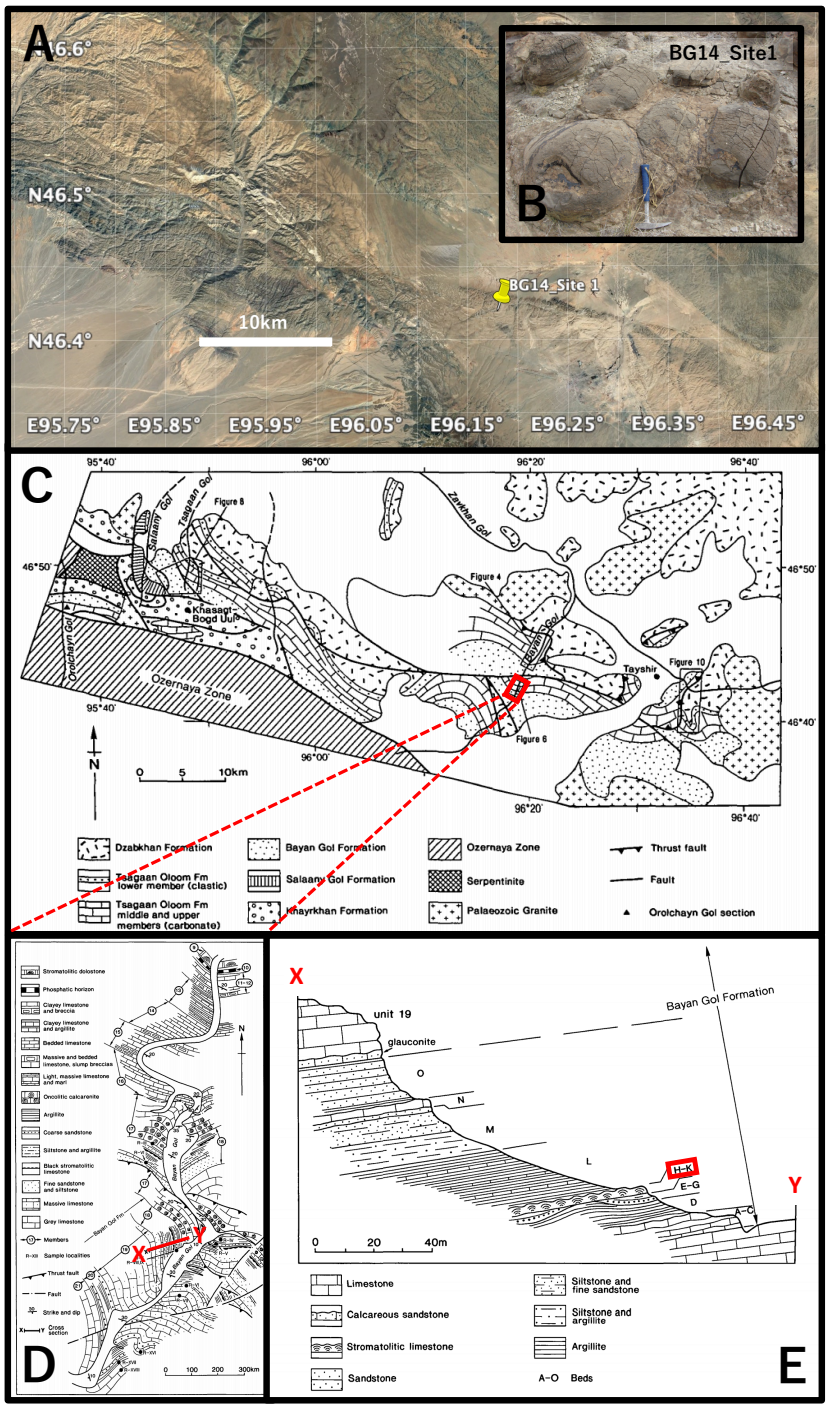

Figure 2.6. (A) Satellite image of the sampling locations at the Bayan Gol Formation (BG). Imagery from April 2019, ©2019 Google, Image Landsat/Copernicus. (B) Image of the dome-style structure stromatolite sample in the field (courtesy of S. Dornbos). (C) Geology map of the Zavkhan zone in Mongolia, and the red square on the map is where the BG14 samples were collected (modified from Khomentovsky & Gibsher 1996). (D) Geology map for upper part of Bayan Gol ravine (location shown on red square on c) and (E) Cross-section "X-Y" through the Bayan Gol Formation. BG14 samples were collected from "Stromatolitic limestone" unit (modified from Khomentovsky & Gibsher, 1996).

Table 2.2. Table of the microbialite samples locations, sites, latitude and longitude of sample locations, sample ID, description of their status, features, status of living or lithified, and orientation. S/D and A/H stand for strike/dip and azimuth/hade respectively

Location/ Site	Latitude	Longitude	Sample ID	Description	Features	Status	Orientation
GSL18/Site 1	41.06054	-112.24909	GSL18_0101	Hand Sample	Lithified cow-pie structure	Living	n/a
			GSL18_0102	Hand Sample	Lithified cow-pie structure	Living	n/a
			GSL18_0103	Hand Sample	Lithified cow-pie structure	Living	n/a
			GSL18_0104	Hand Sample	Lithified cow-pie structure	Living	n/a
GSL18/Site 2	41.05709	-112.25351	GSL18_0201	Hand Sample	Lithified cow-pie structure	Living	n/a
			GSL18_0202	Hand Sample	Lithified cow-pie structure	Living	n/a
GSL18/Site 3	41.06014	-112.26168	GSL18_0301	Hand Sample	Lithified dome style thrombolite	Modern	103° /-1° (S/D)
GSL18/Site 4	41.02802	-112.27246	GSL18_0401	Hand Sample	Lithified flat ridge style crusts	Living	n/a
			GSL18_0402	Hand Sample	Lithified collapsed dome-style	Living	n/a
GSL19/Site 1	41.21402	-112.85211	GSL19_0101	Drilled Core	Fossilized monk-head structure	Modern	138° /5° (A/H)
			GSL19_0102	Drilled Core	Fossilized monk-head structure	Modern	190° /14° (A/H)
			GSL19_0103	Hand Sample	Fossilized monk-head structure	Modern	321° /16° (S/D)
			GSL19_0104	Hand Sample	Fossilized monk-head structure	Modern	166° /80° (S/D)
GSL19/Site 2	41.15964	-112.86058	GSL19_0201	Hand Sample	Fossilized cauliflower structure	Modern	12° /24° (S/D)
			GSL19_0201	Hand Sample	Fossilized cauliflower structure	Modern	260° /47° (S/D)
LB19/Site 1	18.64766	-88.39658	LB19_0101	Surface Cube	Unlithified giant dome style	Living	0° /0° (S/D)
			LB19_0102	Hand Sample	Unlithified whole microbialite	Living	5° /0° (S/D)
			LB19_0103	Small Push Core	Unlithified giant dome style	Living	0° /7° (A/H)
			LB19_0104	Large Push Core	Unlithified giant dome style	Living	0° /0.5° (A/H)
LB19/Site 2	18.61383	-88.42595	LB19_0201	Drilled Core	Lithified porous microbialite	Modern	0° /n.a. (A/H)
			LB19_0202	Drilled Core	Lithified porous microbialite	Modern	0° /8° (A/H)
			LB19_0203	Drilled Core	Lithified porous microbialite	Modern	0° /3° (A/H)
LB19/Site 3	18.55834	-88.43537	LB19_0301	Drilled Core	Lithified porous microbialite	Modern	5° /0.5° (A/H)
			LB19_0302	Drilled Core	Lithified porous microbialite	Modern	13° /0° (A/H)
			LB19_0303	Drilled Core	Lithified porous microbialite	Modern	5° /0° (A/H)
			LB19_0304	Surface Cube	Unlithified cyanobacteria layer	Living	0° /0° (S/D)
			LB19_0305	Hand Sample	Unlithified cyanobacteria layer	Living	0° /0° (S/D)
			LB19_0306	Surface	Unlithified cyanobacteria layer	Living	0° /0° (S/D)
GR18/Site 1	41.96862	-109.2508	GR18_0101	Hand Sample	Fossilized dome style laminated	Eocene	37° /10.4° (S/D)
GR18/Site 2	41.9687	-109.25103	GR18_0201	Hand Sample	Fossilized dome style laminated	Eocene	357° /44° (S/D)
BG14/Site 1	46.4213	96.18608	BG14_0101	Hand Sample	Fossilized dome style laminated	Cambrian	Up only

2.2. Laboratory Sample Preparation

In the lab, there were four different subsampling processes for unoriented/oriented living microbialites; lithified/fossilized microbialite hand samples; push core samples for unlithified microbialites; and drill cores of fossil microbialites. Lithified/fossilized hand samples were used to map out the spatial variations in magnetic signatures or properties in the structures. They were sliced perpendicular to the laminations or growth directions (Figure 2.7.A), and then each slice was further gridded and subsampled maintaining their directions (Figure 2.7.B). With the exception of the lithified core samples, the subsampled specimens were immobilized in 2 cm^3 plastic cubes using tissue or bubble wrap. The empty cubes have an approximate magnetization range of ~2.00E-08 Am^2/kg. Non-living specimens were preserved at room temperature 20° C in the magnetically shielded room.

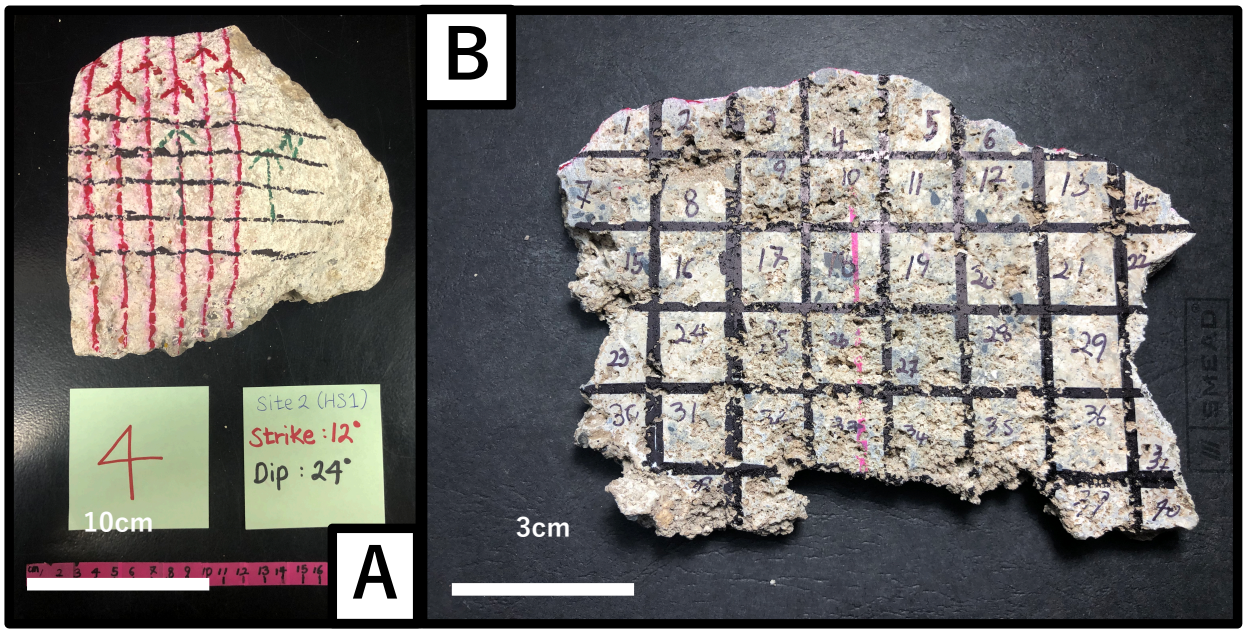

Figure 2.7. (A) Hand sample GSL19_0201. Red lines represent the strike direction, and a gap between each line is approximately 1.5 to 2 cm. Sample was sliced along the red lines and perpendicular the dip direction (B) Sample slice GSL19_0201A after it was cut. Grid lines created on the cut surface of the slice indicate where final cuts were made.

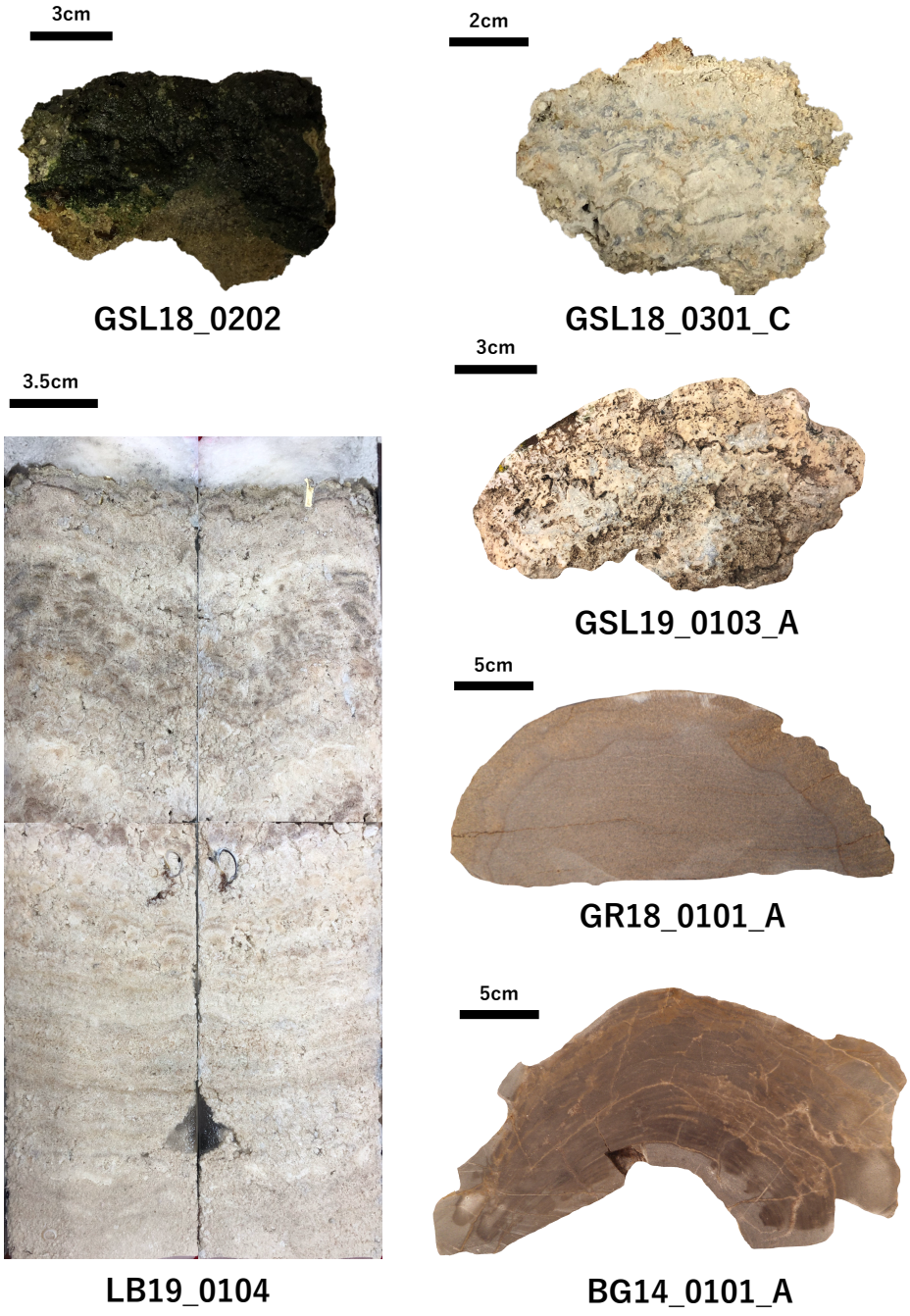

Figure 2.8. (GSL18_0202) Living microbialite hand sample from Great Salt Lake, exhibiting cyanobacteria layer on the top. (GSL18_0301_C) Slice C of lithified hand sample from Great Salt Lake Site 3. Wavy laminations are displayed. (GSL19_0103_A) Slice A of the hand sample GSL19_0103, which shows very unclear laminations or clotted features, interbedded with clasts and many pores. (LB19_0104) Long push core sample from LB site. It displays stromatalitic structures on the bottom parts and more thrombolitic structures on the top parts. (GR18_0101_A) Slice A of hand sample from Green River Site1. The domal structure has gently convex laminations with micritic textures. (BG14_0101_A) Slice A of stromatolite hand sample from Bayan Gol Formation Site 1.

2.2.1. Great Salt Lake

After living microbialites sampled in 2018 were removed from their original containers and water, samples did not hold together easily. They were slippery on the surface where the living cyanobacteria layers are located and tended to fall apart when handled (Figure 2.8. GSL18_0202). However, fifteen specimens were subsampled and immobilized in the cubes with bubble wrap. These specimens were then preserved under refrigeration at ~4° C.

The lithified and oriented hand sample microbialites (GSL18_0301, GSL19_0103, GSL19_0201, GSL19_0202) were sliced approximately 1.5 cm thick, perpendicular to the laminations. The modern microbialite sample exposed above the water surface collected at Antelope Island displays wavy laminations with disturbed features, and high porosity resulting from the incorporation biological debris (i.e., caddisfly larvae). However, Pleistocene microbialites from the Lakeside area (Figure 2.8. GSL19_0103_A) had domal structure overall but barely show internal laminations with many pores. In addition, clasts are interbedded inside of the structures. Each slice was further subdivided into a grid of approximately 1.5 cm x 1.5 cm wide specimens and immobilized in the cubes with tissues. The two core samples (GSL19_0101, GSL19_0102) are approximately 2.0 - 2.5 cm long, and the cores were not subsampled further.

2.2.2. Laguna Bacalar

The long push core into an unlithified microbialite displayed stromatolitic texture at the bottom and fingerlike clotted (thrombolitic) features towards the top (Figure 2.8. LB19_0104). In the lab, all push cores were split longitudinally while frozen using a tile saw with a new blade. The long push core was first cut cross-wise in half. The split cores were subsampled the next day with 2 cm^3 plastic cubes, after the cores had warmed to room temperature and softened. From the

large push core, 2 specimens from each half were collected every 2 cm for a total of 4 (columns) x 9 (rows) = 36 specimens. From the smaller push core, one specimen from each half was taken every 2 cm for a total of 2 (columns) x 4 (rows) = 8 specimens. One unlithified domal structure hand sample (15 cm x 13 cm; LB19_0102) was collected, transported back to the lab, and then subsampled 2 days after collection from the site. After subsampling, specimens were kept frozen. The drilled core samples were cut approximately to 2 cm long for better processing.

2.2.3. Green River Formation

The microbialites have a dome shape and are characterized by nearly horizontal internal laminations (Figure 2.8. GR18_0101A). In the lab, a ~1.1 cm slice perpendicular to laminations was removed from the center of sample GR18_0101. The slice was then gridded (1.1 cm x 1.1 cm; x and y axis) and subdivided into smaller, approximately cubic specimens. In total, 104 specimens were subsampled.

2.2.4. Bayan Gol Formation

The BG14_0101 (Figure 2.8. BG14_0101_A) stromatolite sample displays parallel (but not horizontal) internal layering, consistent with draping growth over a rounded substrate. A ~1 cm-thick slice was made perpendicular to laminations. The slice was then gridded and cut into ~1cm x 1 cm cubic specimens, and a total of 73 specimens were subsampled.

2.2.5. Naming Convention

In order, specimen names start with sample location, year, field site, and the order of sample removal from the field. For example, GSL18_0101 stands for a sample taken from the Great Salt Lake in 2018 at site location 1, and the first sample that was sampled from that site. Detailed descriptions about the sample status, such as hand samples, cube samples, push cores, or drill cores, are listed on the Table 2.2.

Specimens were subsampled from the samples, and they are numbered starting from 00. Some of the lithified microbialite samples were sliced and subsampled. For sliced samples from hand samples, the first and the second slices were denoted A and B. For instance, GSL18_0301A_01-09 are nine specimens that were subsampled from the first slice of the first sample collected from the site 3 from 2018 Great Salt Lake microbialites. For drill core samples, the specimens were denoted in alphabetical order from the bottom up. LB19_0301A-E are five samples from the same core LB19_0301. In push core samples, each column of cubes was indicated by letter and the specimens in each column were numbered starting from the bottom to the top. For example, LB19_0104A_01 is the lowest specimen from the column A of LB19_0104 push core. Since the spatial variations in magnetization in microbialites structures are important, the detailed descriptions and specimen coordinates from the slices are illustrated in Appendix A.

2.3. Magnetic Measurements

Multiple magnetic measurements and experiments were conducted on samples with four aims, which will be explained in the next four chapters. Magnetic susceptibility and NRM intensity were measured over time to check the magnetic stability of samples. Samples were also measured spatially at relatively high resolution to better understand magnetic distribution within the structure (Chapter 3). Some or all specimens from each microbialite were subjected to a stepwise alternating field (AF) or thermal demagnetization to isolate a characteristic remanent magnetization (ChRM) and compare with the current magnetic field or the estimated ancient field direction with statistical analysis (Chapter 4). To evaluate and understand magnetic properties of microbialites (Chapter 5), acquisition and AF demagnetization of IRMs and ARMs were used to calculate the S-ratio; unmix the coercivity spectra; and conduct a Lowrie-Fuller domain test. Thermal demagnetization of a triaxial IRM (Lowrie, 1990) provides information on both the blocking temperature and coercivity distribution of the magnetic minerals. Susceptibility as a function of temperature measurements, $\chi(T)$, were used to identify Curie temperature. Magnetic hysteresis loops and first order reversal curves (FORC) were measured and provide some information on the coercivities, grain sizes and domain states, and mineral compositions. Finally, in part to assist in distinguishing between a DRM or biomagnetism process (Chapter 6), an NRM was acquired and normalized by ARM, and anisotropy of magnetic susceptibility (AMS) was measured on some specimens to determine the magnetic fabrics. Four specimens were measured at low temperatures (10-300 K) to evaluate the possible presence of a signature associated with biogenic magnetite (Moskowitz et al., 1993). In this protocol, the sample is field-cooled (FC) in a 2.5 T field from 300 K to 10K. The field is then turned off and the remanence is measured on warming to 300 K. The sample is then cooled in zero

field (ZFC) back to 10K. A 2.5 T IRM is applied and the remanence is again measured on warming to 300 K.

2.4. Laboratory Instrumentation

Remanence measurements were made using a 2G Enterprises 755SRMS Superconducting Rock Magnetometer housed inside the shielded room at the University of Wisconsin-Milwaukee. Magnetic susceptibilities (including χ(T) and AMS) were acquired using an Agico MFK1-FA Multifunction Kappabridge susceptibility bridge. χ(T) was measured using a CS4 furnace insert and samples were measured under flowing Ar gas in order to deter oxidation of samples. AMS measurements were conducted in a 976 Hz applied field with 200 Am^{-1} peak intensity, using the spinning specimen method. Alternating field (AF) demagnetization and ARM acquisition (150 mT AF; 0.05 mT bias field) were processed with an ASC D-2000 AF demagnetizer. During stepwise AF-demagnetization, specimen orientation was alternated between +X/+Y/+Z and -X/-Y/-Z directions to identify possible unwanted bias field inside the AF demagnetizing device. The stepwise thermal demagnetization was processed by an ASC Thermal Demagnetizer, and IRM was acquired with an ASC Impulse Magnetizer. At the University of Minnesota Institute for Rock Magnetism, hysteresis loops and FORC measurements were conducted on a Princeton Measurement vibrating sample magnetometer, and the low temperature (20-300 K) remanence measurements were made on a Quantum Designs Magnetic Properties Measurement System (MPMS2).

Chapter 3: Microbialite Magnetism and Stability

3.1. Introduction

The magnetic studies of microbialites are challenging because the materials are mostly diamagnetic (i.e., carbonate rock) with low concentrations of ferromagnetic minerals. Yet, recent work has proved cave speleothems (also laminated carbonate rocks) can preserve short-period variations in the recent geomagnetic field (e.g., Bourne et al., 2015; Lascu & Feinberg, 2011; Trindade et al., 2018). While relatively little paleomagnetic work has been done with microbialites, there have been some endeavors to utilize microbialites for paleomagnetic studies (Vanyo and Awramik, 1982; Muraszko, 2014). However, no studies have attempted to look at high-resolution variations in magnetization and magnetic properties within microbialites. In this chapter, NRM intensity and magnetic susceptibility of microbialites are mapped out at a 1.0 cm to 3.5 cm spatial resolution scale. In addition, to help assess whether magnetizations recorded in lithified microbialites contain primary magnetization, the magnetic susceptibility (χ) and NRM intensity of living microbialites and cyanobacteria layers are measured over time. NRM measurements are limited by the sensitivity of the cryogenic SQUID magnetometer (~1.00E-12 Am^2 moment sensitivity limit), and susceptibility measurements are limited by the sensitivity of the MFK1 Kappabridge susceptibility bridge (~2.00E-08 SI or ~2.00E-13 m^3).

3.2. Background

Mapping out the magnetic susceptibility and NRM intensity of slices from microbialite samples is useful for understanding the magnetic mineral distributions in the structure. NRM is controlled entirely by ferromagnetic materials, but magnetic susceptibility depends on all

diamagnetic, paramagnetic and ferromagnetic materials. However, ferromagnetism typically has the strongest signature by volume and will often dominate the magnetic susceptibility. Therefore, it is typical that NRM intensity and magnetic susceptibility are correlated.

However, this is not always the case, and for this case, the mapping can give information about the environments. When samples' NRM and susceptibility distributions do not match each other, this might represent variations in magnetization processes or environments. For example, in a freshwater system, isolated magnetic particles quickly align with the field, but in high salinity systems, flocculation effects result in lower net magnetization during the DRM processes, even though susceptibility in both cases will be similar (Tauxe et al., 2006). Also, remagnetization in the presence of a large magnetic field such as lightning can result in relatively high remanent magnetization (i.e., IRM) despite a lower magnetic susceptibility. On the other hand, superparamagnetic grain size magnetic particles can result in high susceptibility but contribute nothing to the remanent magnetization.

For modern living microbialites growing underwater, assessing magnetic stability is essential. In unlithified microbialite deposits, chemical alteration by changing of environmental conditions may result in the destruction or creation of magnetic minerals and alteration of the net magnetization (CRM). This process could be affected by fluctuating water levels, water chemistry, pH and redox conditions and/or physical rotation of magnetic particles in a low-density and porous sediment. Often, these secondary magnetizations including VRM do not fully replace the primary magnetization. Thus, it may be possible to isolate the primary magnetization through demagnetization processes. However, it will be difficult to extract the primary magnetization 1) if the fraction of NRM replaced by newly formed minerals (CRM) is significantly higher than the

primary magnetization, and/or 2) if the magnetization intensity is lower than the sensitivity of magnetometer due to very low concentration of magnetic minerals.

3.3. Methods

3.3.1. Spatial Variations in Magnetic Intensity

The two magnetic properties (i.e., NRM intensity, magnetic susceptibility) of bulk specimens were measured soon after the subsampling of microbialites: GSL18_0301, GSL19_0103, GSL19_0201, GSL19_0202, LB19_0103, LB19_0104, GR18_0101, BG18_0101. The slices of the samples were subdivided into a grid of 1.5 cm x 1.5 cm for GSL18 and 19 samples; 1.1 cm x 1.1 cm for GR18_0101; and 1 cm x 1 cm for BG18_0101. Unlithified microbialite sediments are subsampled every 3.5 cm distance apart from push cores LB19_0103 and LB19_0104 within cube specimens (2 cm x 2 cm x 2 cm). Then, measured magnetic susceptibility and NRM intensity were mass normalized and mapped out based on the gridded coordinates by cubic interpolation. Values are plotted and mapped out with a linear scale with additional log scale contour lines.

3.3.2. Temporal Variations in Magnetic Intensity and Magnetic Stability

The magnetic stability of living microbialites was assessed based on how the magnetic susceptibility and NRM changed over time. An increase or decrease in susceptibility over time suggests the formation, destruction, or transformation of one or more types of magnetic particles (i.e., diamagnetic, paramagnetic, ferromagnetic). An increase or decrease in NRM intensity over time suggests either a change in ferromagnetic mineralogy and/or the acquisition of a VRM. These variations may result from a series of complex processes such as a change of magnetic grain sizes, reorganization of domain walls in MD grains, and/or thermoviscous relaxation of SP/SD moments.

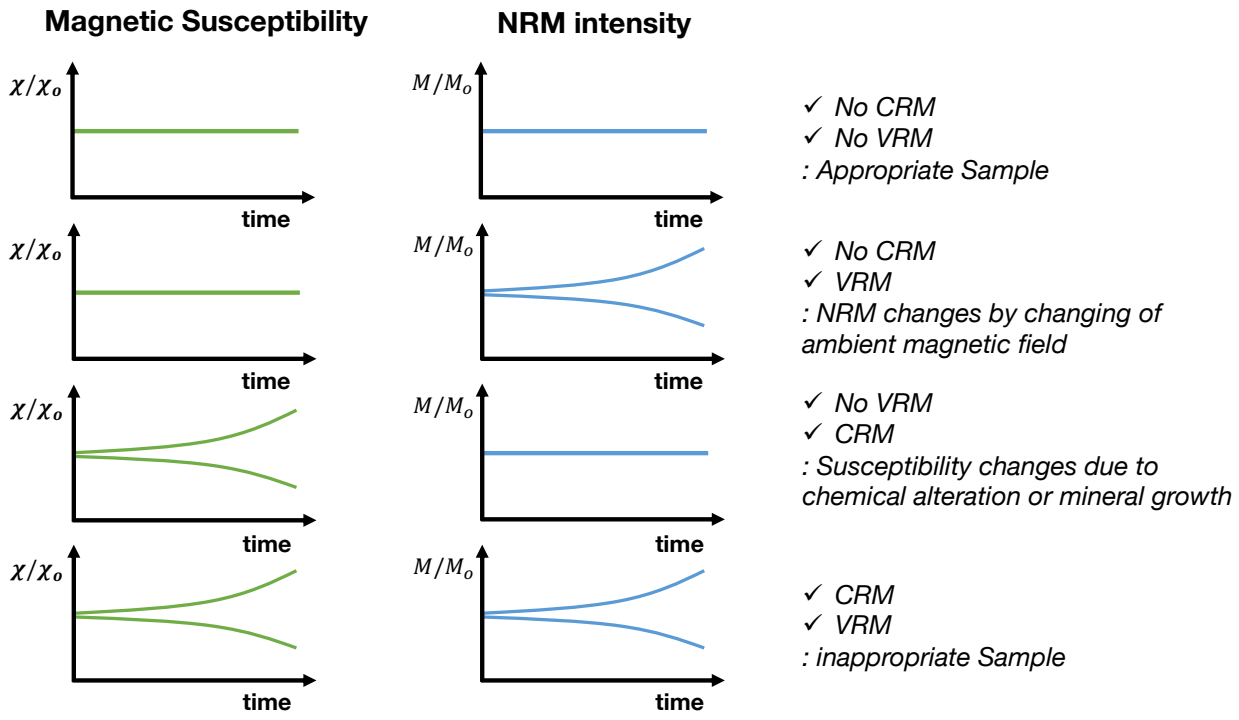

Figure 3.1. Four hypothetical models of magnetic stability results estimated by sample's magnetic susceptibility and NRM intensity measurement over time. Interpretations to right. Case 1 to 4 from the top to the bottom.

Four time-dependent patterns of NRM intensity and susceptibility behavior can be hypothesized to discuss the magnetic stability of microbialites (Figure 3.1). If a sample shows constant magnetic susceptibilities and NRM intensity over time, it indicates an appropriate sample with no considerable secondary magnetization (case 1). If NRM intensity changes over time with stable susceptibility, it suggests that the sample is affected by a secondary VRM and should be preserved in a magnetically shielded room (case 2). If a sample shows a variation of magnetic susceptibility with constant NRM intensity value, there is a high possibility that the sample is chemically altered by some change in environmental factors such as pH, temperature, redox state, and water chemistry. If newly-formed minerals are ferromagnetic, they will carry a CRM (case 3). The worst case would be a sample with both unstable NRM and susceptibility, and this indicates

that a sample is likely not to be an accurate recorder of the geomagnetic field at the time of original growth (case 4).

Living microbialites samples from the Great Salt Lake and Laguna Bacalar were analyzed based on this hypothesis. Eight specimens of GSL18 microbialites were preserved in the refrigerator (4℃) for 15 days and then out of the refrigerator (20°C) in a magnetically shielded space for another 25 days. Seven additional GSL18 specimens were kept only at room temperature in a shielded space for 25 days. LB19_0101, 0102, 0304 specimens were kept frozen (< 0°C) for 7 days. During the ~60 minutes required to measure the LB19 specimens, they were placed in an ice box. The NRM intensity and magnetic susceptibility of LB19 push cores (LB19_0103, LB19_0104) were remeasured after approximately 3 months of storage at room temperature in magnetically shielded room.

3.4. Results

3.4.1. Spatial Variations

3.4.1.1. Great Salt Lake

The NRM intensity and susceptibility of five slices (A, B, C, D, E) of sample GSL18_0301 were contoured (Figure 3.2) at the sampling resolution of approximately 1.5 cm. If the magnetization process and distribution of magnetic grains are more or less uniform, we would expect each sample 'slice' to be the same, and we would expect similar magnetic intensities along laminations (horizontal directions). Instead, we see that magnetic particles are not uniformly distributed along the laminations, although magnetic susceptibility and NRM intensity show similar trends and patterns. Some highly magnetized spots that have both high susceptibilities and NRM intensity indicates a higher concentration of ferromagnetic particles.

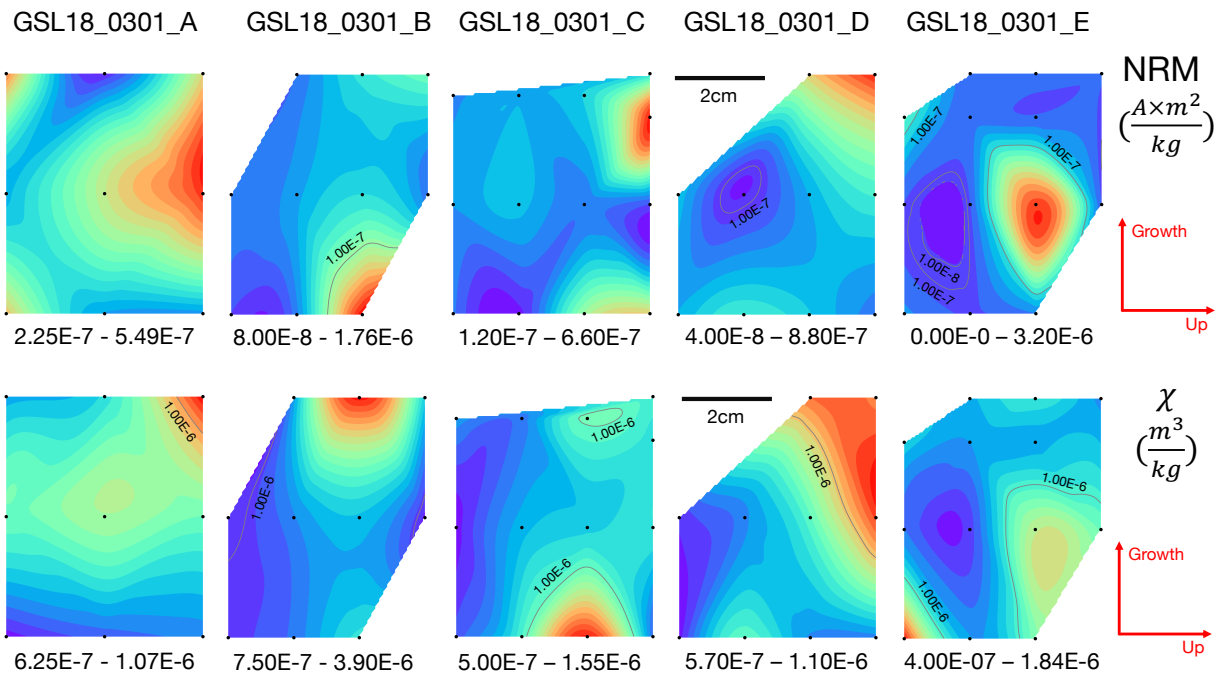

Figure 3.2. NRM intensity mapping (top) and magnetic susceptibility mapping (bottom) of GSL18_0301 sample slice A, B, C, D, E with cubic interpolation at approximately 1.5 cm spatial resolution. Color contours are on a linear scale, but labeled black contour lines show order of magnitude variations. Black dots are sample positions and the numbers below each map represent minimum and maximum value of the contour color range, where red is high and blue is low. Solid (up) red arrow indicates up in the field and growth arrows roughly represents the direction of the microbialite growth based on their laminations.

The three slices (i.e., GSL19_0103_A, GSL19_0201_A, GSL19_0202_A) of the GSL microbialites collected from Lakeside were mapped out and exhibit similar patterns to each other. All three hand samples displayed a correlation between the NRM intensity and magnetic susceptibility distribution. In addition, magnetic particles are uniformly distributed along the laminations. All three samples show highest NRM intensities (>1.00E-6 Am^2/kg) or magnetic susceptibility measurements (>1.50E-6 m^3/kg) on the surface laminations. Figure 3.3 displays the hand sample slice GSL19_0201_A (Figure 2.7. right). The microbialite's magnetization varies along the growth directions (up direction red arrows) but is consistent along the laminations (white dashed lines). Mappings of GSL19_0103_A and GSL19_0202_A are included in Appendix B.

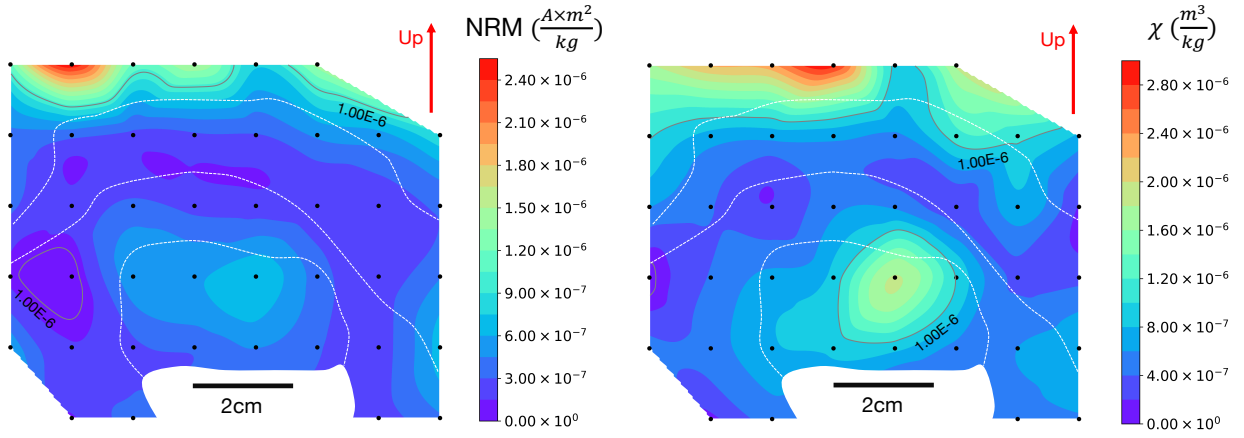

Figure 3.3. NRM intensity mapping (left) and magnetic susceptibility mapping (right) of GSL19_0201A with cubic interpolation with the approximate 1.5 cm spatial resolution. Color contours are on a linear scale, but labeled black contour lines show order of magnitude variations. Black dots are sample positions and the color bars represent NRM intensity (Am^2/kg) and magnetic susceptibility(m^3/kg) values in color range. Solid (up) red arrow indicates up in the field and is similar to the sample's growth direction. The white dashed lines roughly represent the locations of distinct laminations (see Figure 2.7 for the photo of the sample slice).

3.4.1.2. Laguna Bacalar

Data from the long push cores from LB Site 1 (LB19_0104) are mapped out in Figure 3.4. The NRM intensity mapping shows a consistent magnetization overall except for a high spot at the bottom right. Susceptibility data show a high value around 18 cm depth (parallel to the laminations), which might be an indication of a drastic change in the depositional environment (e.g., hurricane) and/or a high concentration of superparamagnetic particles. Also, note that this is the transition spot where the stromatolitic laminations had changed to thrombolitic structure.

The small push core (LB19_0104) shows a clear correlation between the susceptibility and NRM intensity. Since the core was shorter than 15 cm, the high susceptibility layer that was found from the long core was not seen in the small core sample.

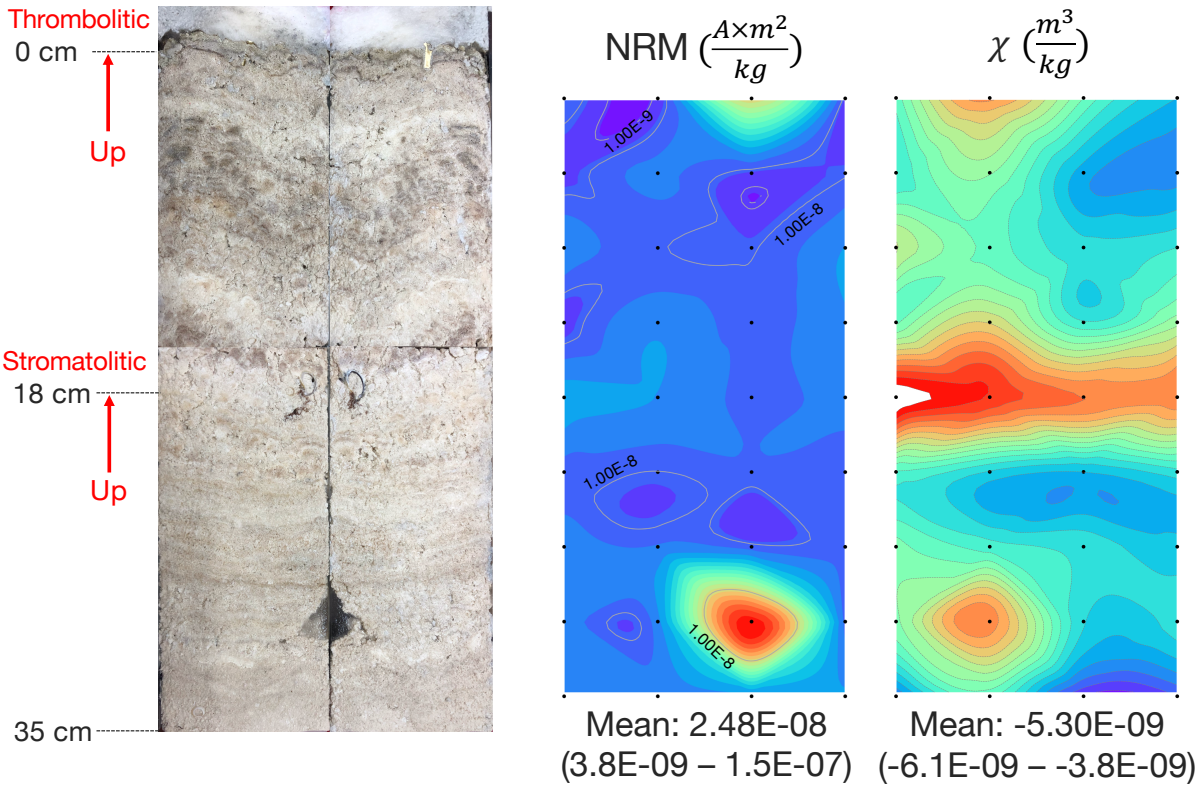

Figure 3.4. The photo of the split large push core (LB19_0104) from the unlithified living microbialite (left photo). It displays stromatolitic structures with laminations up to 18cm and thrombolitic structures from 18cm to top. The red arrow represents up direction in the field, which is roughly close to growth direction. NRM intensity mapping (middle) and magnetic susceptibility mapping (right) with cubic interpolation with approximate 3.5 cm spatial resolution. Black dots are sample positions (9 datapoints on each column x 4columns =36 datapoints). The numbers on each bottom of the mapping represent mean, minimum and maximum value of the contour color range. Color contours are on a linear scale but labeled black contour lines show order of magnitude variations. The unit of NRM intensity and magnetic susceptibility color range (color bar) are Am^2/kg and m^3/kg, respectively.

3.4.1.3. Green River Formation

For the Eocene Green River Formation microbialites (Figure 3.5), high NRM intensity was found in two discrete spots in the lower center part of the structure. This might indicate the presence of an IRM due to exposure to high field (e.g., lightening), or perhaps CRM acquisition by fluid alteration. However, these same spots show little-to-no variation in susceptibility, meaning consistent magnetic concentration or mineralogy, suggesting no additional growth of magnetic minerals, which make a CRM origin unlikely.

These spots show high NRM/ARM ratio, while most other regions show lower NRM/ARM ratio (see Section 6.3.1), and the directions of these two highly magnetized spots point the same direction (see Section 4.3.3). Also, based on IRM unmixing, S-ratio, and the 3D IRM technique, there is no mineralogical difference between the two high NRM spots and the rest of low NRM area (see Section 5.3). These results suggest that these two highly magnetized spots are due to an induced IRM instead of CRM.

3.4.1.4. Bayan Gol Formation

The Bayan Gol Formation Cambrian stromatolite shows roughly constant magnetic susceptibilities along the laminations. The NRM intensity shows a low value in the middle layers compared to outer or bottom layers (Figure 3.6). Susceptibility distributions indicate a uniform deposition rate of magnetic mineral at any given time, but NRM acquisition or preservation appears to be less uniform. The IRM unmixing, S-ratio, and the 3D IRM technique displayed mineralogical differences along the laminations (Chapter 5), but the NRM appears to be attributed to a single magnetic phase throughout.

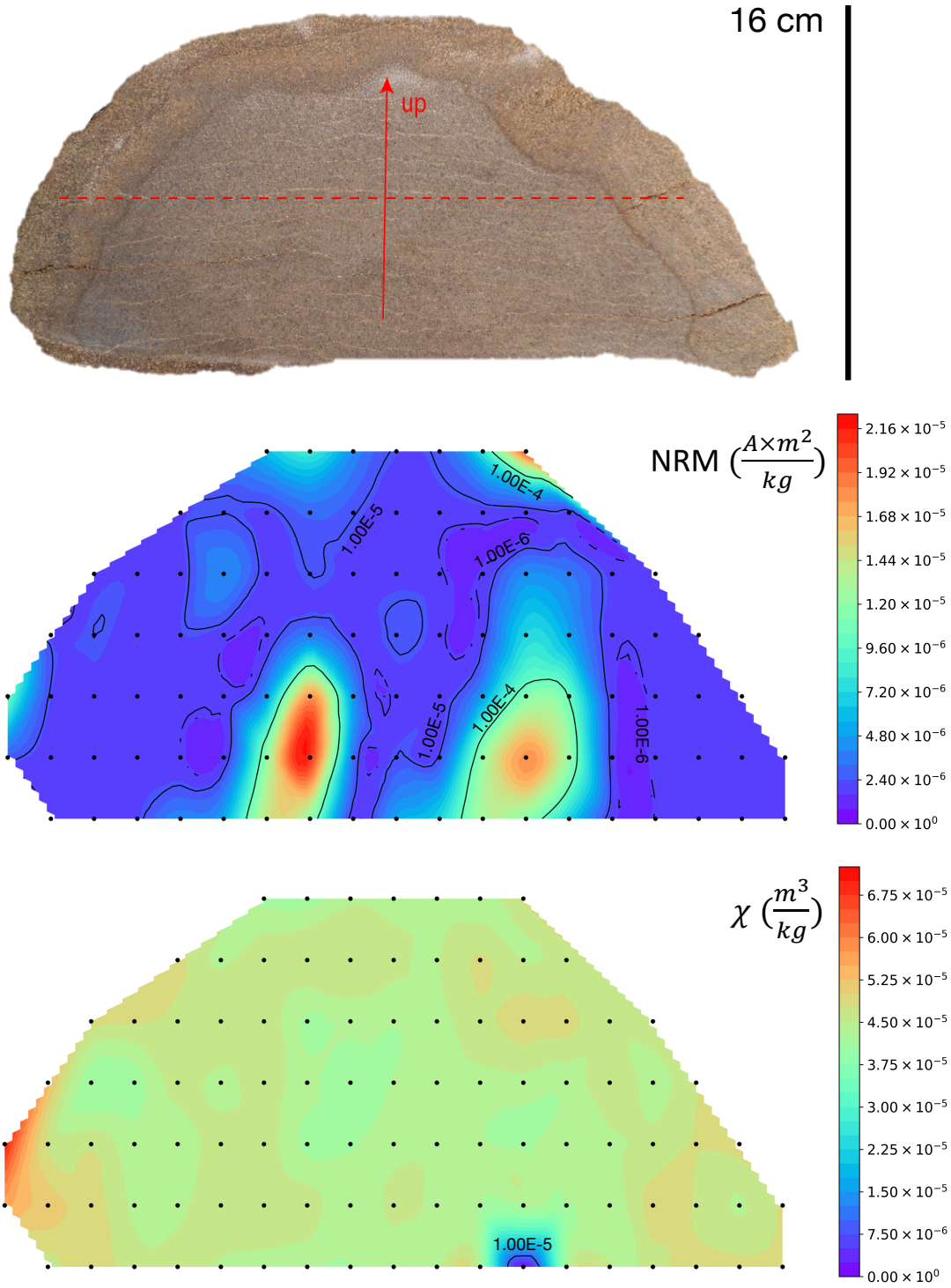

Figure 3.5. (top) Photograph of GR18_0101 sample slice A prior to sub-sampling. Solid red arrow indicates up. Dashed red line shows approximate orientation of laminations. Remanent magnetization intensity (middle) and magnetic susceptibility (bottom) mapping of the slice by cubic interpolation. Black dots are positions for real sample data. Color contours are on a linear scale but labeled black contour lines show order of magnitude variations. The unit of NRM intensity and magnetic susceptibility color range (color bar) are Am^2/kg and m^3/kg, respectively.

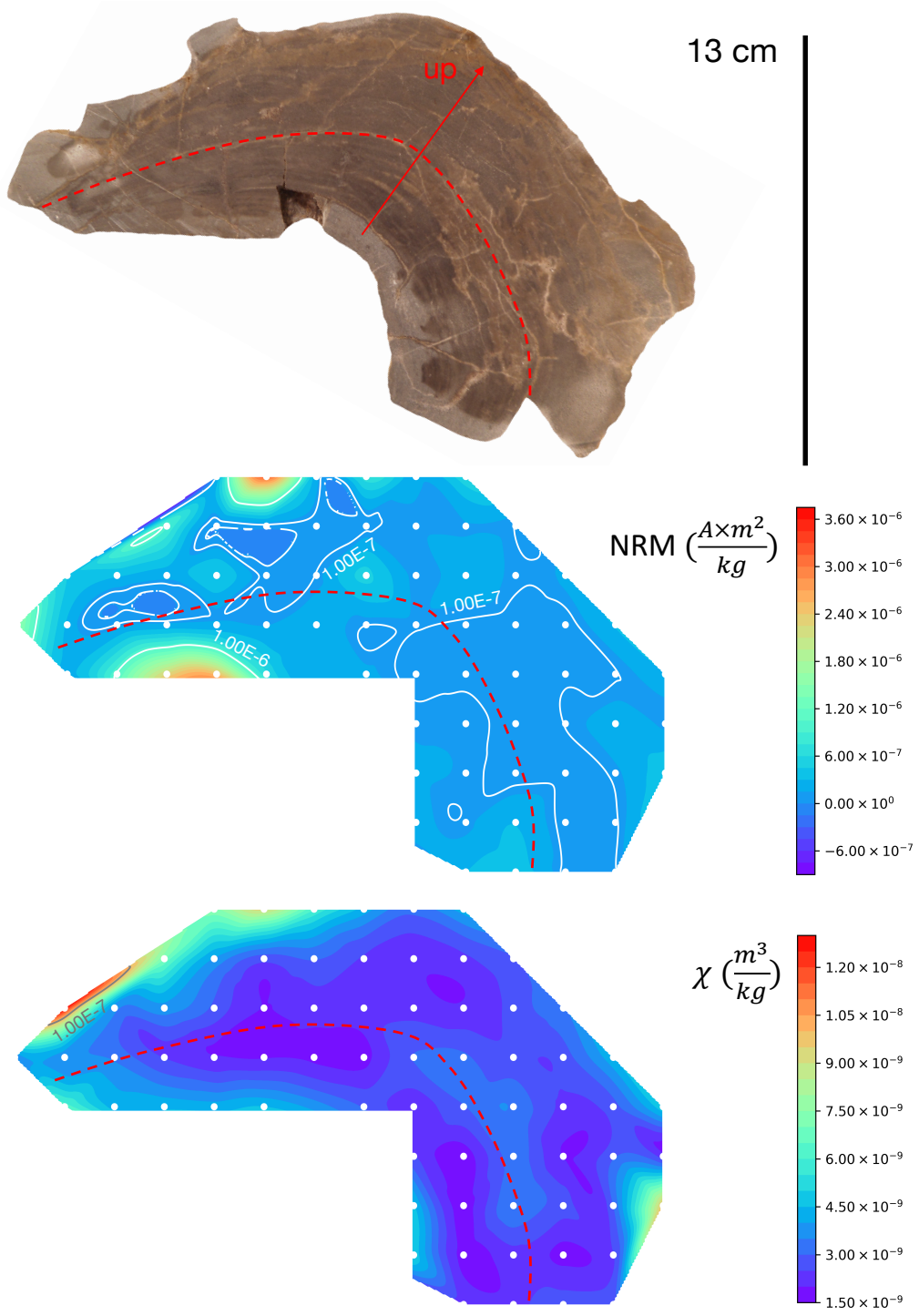

Figure 3.6. (top) Photograph of BG14_0101 sample slice A prior to sub-sampling. Solid red arrow indicates up. Dashed red line shows approximate orientation of laminations. Remanent magnetization intensity (middle) and magnetic susceptibility (bottom) mapping of the slice by cubic interpolation. White dots are positions for real sample data. Color contours are on a linear scale but labeled white (middle) or black contour (bottom) lines show order of magnitude variations. The unit of NRM intensity and magnetic susceptibility color range (color bar) are Am^2/kg and m^3/kg, respectively.

3.4.2. Temporal Variations in Magnetic Intensity

3.4.2.1. Great Salt Lake

The measurement trends of GSL living microbialites at stored at low temperatures showed a decrease of magnetic susceptibility over time (Figure 3.7. top left 0 to 14 days). However, specimens stored at room temperature clearly showed an increase in susceptibility (Figure 3.7. top left 14 to 40 days, bottom left). This suggests that temperature changes may influence chemical stability and promote the growth of paramagnetic and/or superparamagnetic in addition to ferromagnetic grains. Ten out of 15 specimens varied by <30% of the initial value. Specimens which have very weak (< 2.00E-07 m^3/kg) or negative magnetic susceptibilities (i.e., diamagnetic) displayed susceptibility changes of more than 30% from the initial value and with a lot of scatter.

NRM results showed that over 13 days nearly all samples had unchanged directions (Figure 3.7 right) and intensity changed by less than 10% from the initial NRM intensity value (Figure 3.7. middle), except for one sample (GSL18_0402_03). This sample increased in intensity by more than 230% after seven days (not shown in Figure 3.7), accompanied by a change in direction (purple circle in the bottom right stereonet plot on Figure 3.7). The initial direction of this specimen could be recovered after 20 mT AF-demagnetization, which implies the change of the intensity was due to VRM.

Table 3.1. GSL18 specimen-average initial magnetic susceptibility (m^3/kg) and NRM intensity (Am^3/kg)

Specimen ID	χ_0	NRM_0	Specimen ID	χ_0	NRM_0
GSL18_0101_00	4.78E-07	2.42E-07	**GSL18_0202_01**	6.56E-07	9.08E-07
GSL18_0101_01	-6.76E-08	7.17E-07	**GSL18_0202_02**	1.94E-06	1.82E-06
GSL18_0102_00	1.67E-07	2.52E-07	**GSL18_0202_03**	7.80E-07	1.02E-05
GSL18_0104_00	-7.63E-08	2.50E-07	**GSL18_0401_01**	3.51E-09	1.97E-06
GSL18_0201_00	5.97E-07	4.84E-07	**GSL18_0402_01**	1.22E-06	1.58E-06
GSL18_0202_00	4.71E-07	4.52E-07	**GSL18_0402_02**	1.36E-06	4.19E-07
GSL18_0401_00	1.92E-07	9.65E-07	**GSL18_0402_03**	8.78E-07	2.62E-07
GSL18_0402_00	5.06E-07	5.62E-07			

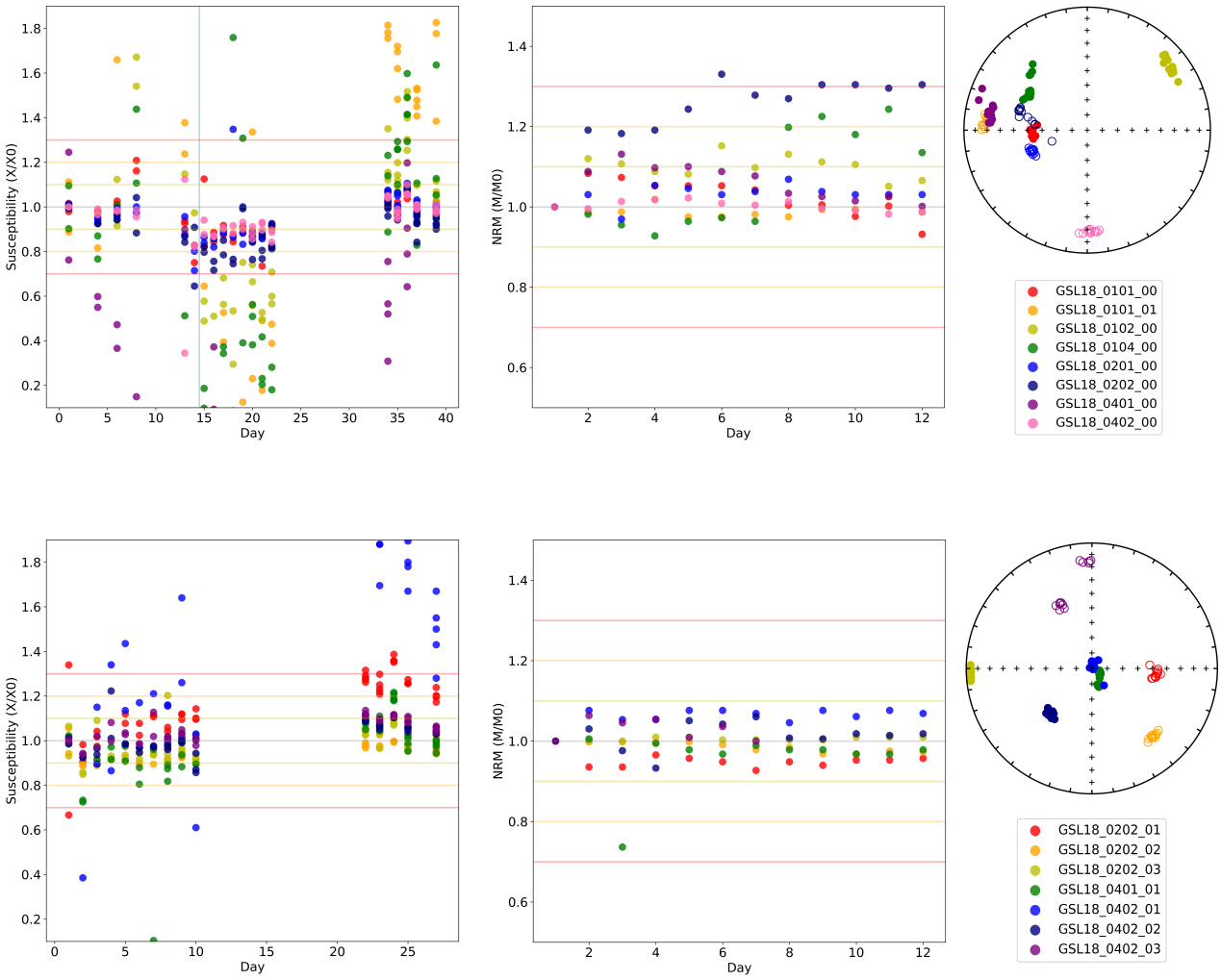

Figure 3.7. Bulk magnetic susceptibility measurements of the eight GSL18 specimens (top left) over 40 days (14 days at 4°C and the other 26 days at 20°C), and the vertical light blue on the panel is the transition from refrigerated to room temperature. Seven additional specimens (bottom left) over 26 days only at room temperature. Associated NRM intensity (middle) and directional (right) variations over 13 days (middle). Note that samples are unoriented so directions have no geomagnetic meaning. Magnetic susceptibility (χ/χ_0) and NRM (M/M_0) intensity were normalized to mean value of its initial step. The horizontal yellow, orange, red lines represent a change of 10%, 20% and 30% from the initial value.

3.4.2.2. Laguna Bacalar

LB19_0101, 0102, 0304 –unlithified microbialites with cyanobacteria layer: The same-day replicate susceptibility measurement of the surface specimens of living microbialites (LB19_0101, 0102, 0304) with cyanobacteria layers showed a high degree of scatter. This is likely because LB19 microbialites contain a relatively large amount of diamagnetic materials and a small amount of para- or ferromagnetic particles compared with other microbialites. Also, as frozen specimens warmed while measuring, the variations in temperature can lead to susceptibility variations in para-and ferromagnetic materials.

The NRM intensity of the samples were measured over seven days. The NRM intensity values exhibit no clear trend over time, but with variations of ±50%, except sample LB19_0304_01 which had an increase of > 400% on day 4 only. Directions changed slightly for most of the samples, possibly due to imperfect immobilization of samples that may have warmed/softened inside sample boxes while other samples were being measured (Figure 3.8. bottom). Yet, directions of specimens magnetized more than 1.25E-07 Am^2/kg were consistent, suggesting that some of the directional variability may be due to low measurement signal:noise ratios.

LB19_0103,0104 –unlithified microbialites push core samples: NRM and magnetic susceptibility were measured on specimens from push core samples LB19_0103 and 0104. Measurements were first made at room temperature directly after subsampling. Measurements were repeated after 42 days of storage at room temperature in the shielded room, but specimens had become desiccated and disaggregated during this time. The NRM intensity changed slightly, decreasing from an average of 1.48E-07 Am^2/kg to 1.25E-07 Am^2/kg, but at least some of decrease may be due to the disaggregated state of the sample, which can result in a partial randomization of moments inside the sample cube. Measurement circular standard deviation (CSD) values increased

from an average of 2.95 to 26.6. These high values indicate that the measurements are unreliable, reflecting a very weak magnetization, a disaggregated sample, or a sample that is not properly immobilized during measurement.

Table 3.2. The average initial value of LB19 specimen's NRM intensity (Am^2/kg) and the mean CSD value.

ID	NRM_0	CSD	ID	NRM_0	CSD	ID	NRM_0	CSD
LB19_0101_01	1.55E-08	2.70	**LB19_0102_01**	2.72E-08	4.12	**LB19_0304_01**	4.16E-09	7.74
LB19_0101_02	1.28E-08	2.79	**LB19_0102_02**	2.31E-08	2.44	**LB19_0304_02**	4.75E-08	1.78
LB19_0101_03	2.25E-08	1.73	**LB19_0102_03**	1.18E-07	0.70	**LB19_0304_03**	1.38E-08	3.60
LB19_0101_04	1.44E-08	2.26	**LB19_0102_04**	2.70E-08	1.84	**LB19_0304_04**	9.79E-09	5.22
LB19_0101_05	1.30E-08	2.94	**LB19_0102_05**	8.53E-08	0.61	**LB19_0304_05**	1.10E-06	0.75
LB19_0101_06	1.70E-08	1.50	**LB19_0102_06**	1.38E-07	2.90	**LB19_0304_06**	1.73E-08	3.12
LB19_0101_07	1.07E-08	4.13	**LB19_0102_07**	1.77E-08	2.21			
LB19_0101_08	2.75E-08	1.74	**LB19_0102_08**	5.71E-08	6.51			
			LB19_0102_09	2.66E-08	1.61			

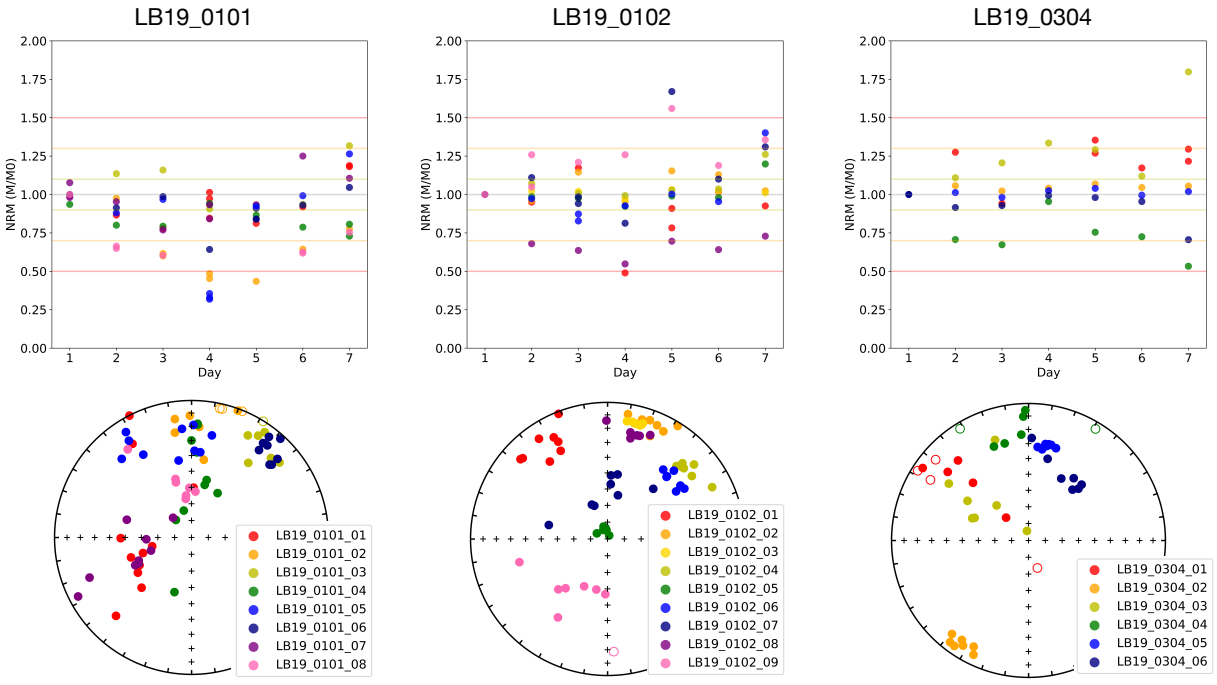

Figure 3.8. NRM changes of unlithified microbialites with living cyanobacteria layers from Laguna Bacalar over 7 days. The NRM intensity over time (top) and their magnetic components on equal area stereographic projection (bottom) of eight, nine, and six surface specimens subsampled from living microbialite bodies LB19_0101 (left), LB19_0102 (middle) LB19_0304 (right) were plotted. While measuring, specimens were kept frozen (< 0°C). NRM (M/M_0) intensity were normalized to mean value of its initial step. The horizontal yellow, orange, red lines represent a value change of 10%, 30% and 50% from the initial value.

By contrast, magnetic susceptibility is not influenced by the disaggregated state of the sample, and χ decreased from -3.79E-08 to -1.83E-06. This loss of magnetic susceptibility suggests the destruction of ferromagnetic minerals or oxidation to a less magnetic form.

3.5. Summary/ Discussion

Although microbialites possess a high proportion of diamagnetic minerals and relatively low concentration of ferromagnetic minerals, all microbialites have permanent magnetic signatures. The NRM and susceptibility intensity mapping present inhomogeneous magnetic distribution on microbialites from Antelope island, but more homogenous continuity along laminations on microbialites from Lakeside. The LB long push core displays a layer with the signature of high susceptibility but no variations in NRM intensity. This might result from a hurricane event and/or be related to the change of growth structure mode (from stromatolitic to thrombolitic). The GR microbialite displays high NRM intensity in two spots, but homogenous susceptibility distribution, which might be interpreted as IRM. The BG stromatolite's susceptibility mapping displays homogenous continuity along the laminations, but a more inhomogeneous distribution of NRM. This might represent the deposition of additional ferromagnetic materials (but no contribution to NRM) or paramagnetic minerals in addition to the NRM recorded by a single magnetic phase.

Living microbialite samples from GSL and LB show that magnetic mineralogy changes as the samples are removed from the environments based on the magnetic stability experiment. Some of the living microbialites from GSL showed relatively unstable magnetization over time (range of change more than 30%), and the storage temperature affects the magnetic susceptibility. The LB samples showed stable magnetization over time under low temperatures. However, when the samples dried out, they showed decreased magnetic susceptibility. The reduction of magnetic

susceptibility can be explained by the destruction of ferromagnetic minerals, or transformation to a less magnetic form. Therefore, environmental and laboratory setting such as humidity, temperature, and pH conditions should be contemplated before reconstructing modern microbialites magnetism. In addition, this would seem to call into question of the timing of the magnetization in the ancient microbialites if *in situ* environmental changes can modify magnetic mineralogy.

Chapter 4: Paleomagnetic Directional Analysis

4.1 Introduction

To reconstruct the past geomagnetic field, paleomagnetists have used the remanent magnetization directions recorded in igneous rocks, archaeological artifacts, and sediments. Volcanic rocks and archaeological materials that carry a thermoremanent magnetization (TRM) are typically more strongly magnetized compared with sediments, but the records are discontinuous in nature. The detrital remanent magnetization (DRM) recorded in sediments, by contrast, gives the potential of providing long, continuous records of paleosecular variations. However, DRM arises from a combination of many complicated processes, and several processes may adversely impact the accuracy of the DRM. These processes should be contemplated and, if possible, corrected for. The issues include errors caused by compaction, dewatering, bedding slope, slumping, water current flows, bioturbation, and diagenesis. In addition, the time lag between sedimentation and consolidation may result in an offset between the time of magnetization acquisition and physical deposition.

Microbialites may hold certain critical advantages over typical lake or marine sediments for paleosecular variation studies. The absence of bioturbation and a high growth rate (0.5 mm to 1cm/ year; Berelson et al., 2011; Brady et al., 2009) in microbialites may result in preservation of paleofield information at high temporal resolution. Thus, if microbialites are confirmed as accurate paleomagnetic recorders, one of the most important paleomagnetic advantages is a continuous, high-resolution NRM record which can answer some of the lingering questions related to the fine-scale temporal behavior of the geomagnetic field, especially in deep time.

Pilot studies of microbialite magnetism have shown that microbialites can carry a magnetization in a direction approximately consistent with the expected field. Vanyo and Awramik (1982) extracted a paleomagnetic direction via alternating field (AF) demagnetization from a single specimen of late Proterozoic (~850 Ma) stromatolite 'Anabaria juvensis' in order to understand sinusoidal growth patterns of ancient stromatolites. Thermal demagnetization of Jurassic stromatolites from Poland have shown them to carry a stable magnetization, including a record of a polarity reversal suggested from previous studies on other types of rocks (Muraszko, 2014). Recent work has also proved that cave speleothems (also laminated carbonate rocks) can preserve short-period variations in the recent geomagnetic field (e.g., Bourne et al., 2015; Lascu & Feinberg, 2011; Trindade et al., 2018).

In this chapter, with the goal of evaluating whether microbialites accurately record the magnetic field, the paleomagnetic directions of living, modern, and ancient microbialites were compared with expected field values or other paleomagnetic measurements.

4.2. Methods

4.2.1 Demagnetization Technique

The measurement of a microbialite's net NRM may include more than the remanence acquired when they are formed. The NRM may also include secondary magnetizations acquired after deposition. It is assumed that the original (primary) magnetization is a DRM and/or biomagnetization. There may also be additional secondary magnetizations such as VRM or CRM. As a result, the raw NRM should go through a demagnetization process in an effort to isolate the characteristic remanent magnetization (ChRM), which is typically assumed to be the original

primary magnetization. This demagnetization process may be efficient in removing a low-coercivity VRM, but a CRM is less likely to be removed completely.

In general, there are two types of demagnetization techniques: thermal demagnetization and alternating field (AF) demagnetization. The basis of thermal demagnetization is the relationship between relaxation time and temperature. As thermal energy increases, magnetic relaxation time decreases, allowing grains to "unblock" and release or change their magnetization. The NRM is a sum of components carried by minerals that have different blocking temperatures (T_b), and a (thermo)viscous overprint is often carried by the lowest T_b grains. The stepwise heating therefore can remove this overprint and isolate the most stable component at higher T_b (i.e., ChRM). Although thermal demagnetization is a common method, it is also more likely to produce chemical changes in the sample as it is heated. The AF demagnetization is an appropriate demagnetization method for a sample which should not be heated and/or which does not likely carry a TRM, such as sedimentary rocks. In AF demagnetization, an alternating field is applied to a specimen under no external field, and minerals which have lower coercivities (lower stability) will be demagnetized first, leaving the higher coercivity minerals. As with thermal demagnetization, viscous overprints are often removed at low alternating fields.

4.2.2 Samples

Lithified Microbialites: In order to compare the magnetic direction recorded by microbialites to expected field values, fully-oriented samples are required. Fossil microbialites marked with field arrows (azimuth and hade, strike and dip, and/or up direction) were subsampled, maintaining the directions with newly coordinated lab arrows. These sub-samples are referred to here as 'specimens'. Selected specimens were either AF demagnetized or thermally demagnetized

(Table 4.1). Specimens subsampled from the lithified hand sample from Antelope Island, GSL18_0301 (55 specimens); Lakeside hand samples, GSL19_0103 (10 specimens) and GSL19_0202 (25 specimens); the Green River sample, GR18_0101 (103 specimens); and the Bayan Gol sample, BG14_0101 (37 specimens) were AF demagnetized. In addition, 10 GSL19_0103 Lakeside specimens and 37 BG14_0101 specimens were thermally demagnetized for comparison. Only five specimens from one lithified LB drilled core sample (LB19_0301) were subjected to AF-demagnetization. Other LB core specimens were too porous to be easily placed in the magnetometer sample handler.

Living or Unlithified Microbialites: Living microbialites were more challenging to work with. This is because 1) it is difficult to maintain perfect field arrows during subsampling of crumbly and loosely lithified microbialites (especially for Great Salt Lake); 2) some samples dried out when left at room temperature, resulting in some shrinkage and loss of orientation; and 3) the decrease of NRM due to oxidation or formation of CRM (especially for Laguna Bacalar microbialites). Even with these limitations, 15 unoriented specimens of living GSL microbialites collected from Antelope Island were AF-demagnetized to understand demagnetization patterns. Oriented LB cube specimens (LB19_0101, 0102, 0304) directly collected from the field sites were preserved below 0℃ before measurement and during measurement were kept within an icebox except when actively being measured. This protocol was followed to prevent sediment desiccation and reduce chemical changes. The NRM directions of specimens from push cores were obtained one day after the subsampling. However, they were allowed to dry out before AF demagnetization, resulting in loss of orientation (case 2) and chemical destruction of remanence (case 3).

4.2.3 Statistical Data Analysis

For specimens that underwent AF or thermal demagnetization, a best-fit ChRM is calculated using principal component analysis (Kirschvink, 1980) from the higher coercivity (or higher temperature) fraction, selected here by minimizing the maximum angular deviation (MAD) to under 10. When the ChRM could not be convincingly isolated, data were fit with a plane (Kirschvink, 1980).

A set of magnetic directions of a sample or site were assumed to hold a Fisher distribution (Fisher,1953). Fisher statistics are used to calculate a mean direction assuming symmetric distribution of unit vectors about the mean. 95% confidence in the mean direction is described by an ellipse, alpha 95 (α_{95}), and the dispersion of the data set is given by the precision parameter, k. High values of k are associated with low dispersion. The vector sum of N unit vectors is referred to as the resultant vector, R, where $R \leq N$. R is another measure of directional scatter or dispersion, where R close to N indicates low degrees of scatter. These statistics were calculated using PmagPy software (Tauxe et al., 2016). The 'gofish' command was utilized when specimens have both declination and inclination data, but the 'incfish' command was used when only inclination data are available. This inclination-only calculation is based on the maximum-likelihood method of McFadden and Reid (1982).

Table 4.1. Chart of demagnetization types and steps on each sample and specimen (top). Associated chart demagnetization method and steps (bottom). DM, demagnetization method; DM_ID, demagnetization method identification; CB layer, cyanobacteria layer; LM, lithified microbialites; UL deposits; unlithified sedimentary deposits

Samples ID	Specimen ID	Status/Features	DM_ID
GSL18_0101	GSL18_0101_00-01	Living CB layer + porous LM	AFD_05
GSL18_0102	GSL18_0102_00	Living CB layer + porous LM	AFD_05
GSL18_0104	GSL18_0104_00	Living CB layer + porous LM	AFD_05
GSL18_0201	GSL18_0201_00	Living CB layer + porous LM	AFD_05
GSL18_0202	GSL18_0202_00-03	Living CB layer + porous LM	AFD_05
GSL18_0401	GSL18_0401_00-01	Living CB layer + porous LM	AFD_05
GSL18_0402	GSL18_0402_00-03	Living CB layer + porous LM	AFD_05
GSL18_0301	GSL18_0301_A01-09	porous LM	AFD_04
	GSL18_0301_B01-10	porous LM	AFD_02
	GSL18_0301_C01-13	porous LM	AFD_02
	GSL18_0301_D01-10	porous LM	AFD_02
	GSL18_0301_E01-13	porous LM	AFD_02
GSL19_0101	GSL19_0101_00	LM with interbedded pebbles	AFD_05
GSL19_0103	GSL19_0103A_01-45 odd	LM with interbedded pebbles	AFD_05
	GSL19_0103A_01-45 even	LM with interbedded pebbles	TD_01
GSL19_0201	GSL19_0201A_01-42	LM with interbedded pebbles	NRM
GSL19_0202	GSL19_0202A_01-22	LM with interbedded pebbles	AFD_05
LB19_0101	LB19_0101_01-08	Living CB layer +UL deposits	AFD_02
LB19_0102	LB19_0102_01-09	Living CB layer +UL deposits	AFD_01
LB19_0103	LB19_0103_A01-04	Living CB layer +UL deposits	NRM
	LB19_0103_B01-04	Living CB layer +UL deposits	NRM
LB19_0104	LB19_0104_A01-09	Living CB layer +UL deposits	NRM
	LB19_0104_B01-09	Living CB layer +UL deposits	NRM
	LB19_0104_C01-09	Living CB layer +UL deposits	NRM
	LB19_0104_D01-09	Living CB layer +UL deposits	NRM
LB19_0201	LB19_0201_A-C	porous LM	NRM
LB19_0301	LB19_0301_A-E	porous LM	AFD_03
LB19_0302	LB19_0302_A-F	porous LM	NRM
LB19_0304	LB19_0304_01-06	Living CB layer	AFD_01
GR18_0101	GR18_0101_A001-105	Eocene dense microbialite	AFD_04
BG14_0101	BG14_0101_A01-73 odd	Cambrian dense stromatolite	AFD_05
	BG14_0101_A01-73 even	Cambrian dense stromatolite	TD_01

DM_ID	DM	Demagnetization Step
NRM	NRM	
AFD_01	Alternating Field	0.0, 2.5, 5.0, 7.5, 10.0, 15.0, 20.0, 25.0, 30.0, 35.0, 40.0 (mT)
AFD_02	Alternating Field	0.0, 2.5, 5.0, 7.5, 10.0, 12.5, 15.0, 17.5, 20.0, 25.0, 30.0, 40.0, 60.0 (mT)
AFD_03	Alternating Field	0.0, 2.5, 5.0, 7.5, 10.0, 12.5, 15.0, 17.5, 20.0, 25.0, 30.0, 35.0, 40.0, 50.0, 60.0, 70.0 (mT)
AFD_04	Alternating Field	0.0, 2.5, 5.0, 7.5, 10.0, 15.0, 20.0, 25.0, 30.0, 40.0, 50.0, 60.0, 80.0, 100 (mT)
AFD_05	Alternating Field	0.0, 2.5, 5.0, 7.5, 10.0, 15.0, 20.0, 25.0, 30.0, 40.0, 60.0, 80.0, 100, 150.0, 200.0 (mT)
TD_01	Thermal	0.0, 75.0, 100.0, 150.0, 200.0, 250.0, 300.0, 350.0, 400.0, 450.0, 475.0, 500.0, 525.0, 550.0, 575.0, 600.0, 625.0, 650.0, 675.0 (℃)

4.2.4 Expected Field Value

Modern samples (<100 yrs) may be compared to the International Geomagnetic Reference Field (IGRF). Samples less than ~10,000 years old may be compared to global field models constructed from paleomagnetic measurements. Well-dated archaeomagnetic, volcanic, and lake sediments data have been combined into a series of global models "Continuous models of Archaeomagnetic and Lake Sediment data for the past x thousand years, version n." (CALSxK.n) (e.g., Korte & Constable, 2003, Constable et al., 2016).

To assess whether or not microbialites may be accurate paleomagnetic recorders, it is necessary to compare microbialite results with independent records of the geomagnetic field. In general, estimated expected field values of a sample can be determined depending on the age of the sample. For very young samples (<100 yrs) of known age, the International Geomagnetic Reference Field (IGRF) can be used. IGRF is a global model of core field variation based on direct observations (Section 4.2.3.1). For samples aged more than 100 yrs but less than 10 kyrs, global models have been constructed using well-dated paleomagnetic data from sediments, archeological materials, and volcanics (e.g., CALSxK.n; Section 4.2.3.2). If the age of a sample is unavailable but young enough that the sample was not affected by plate motion, the Geocentric Axial Dipole (GAD) model can provide an expected average field direction (Section 4.2.3.3). When a sample is old enough to be affected by plate motions, GAD is combined with the apparent polar wonder path (APWP) (Section 4.2.3.4). If a sample is so old that there is no accurate pole path, other paleomagnetic results from other materials of a similar age and location are the best sources for comparison (Section 4.2.3.5).

4.2.4.1 IGRF - (age < 100 yrs)

The International Geomagnetic Reference Field (IGRF) gives real variations in the core field over time. The field model is produced by a collection of magnetic field data from satellites and observatories. The magnetic field (H) on the Earth's surface can be written as a gradient of a scalar potential field (i.e. magnetic potential, $\nabla\psi_m$):

$$H = \nabla\psi_m$$

The divergence of the magnetic field is zero, and the potential field satisfies the Laplace equation:

$$\nabla^2\psi_m = 0$$

For the IGRF model, the potential of the geomagnetic field is expressed in spherical harmonics as:

$$\psi_m(r,\theta,\phi,t) = \frac{a}{\mu_o}\sum_{l=1}^{\infty}\sum_{m=0}^{l}\left(\frac{a}{r}\right)^{l+1} P_l^m(\cos\theta)\left([g_l^m(t)\cos m\phi + h_l^m(t)\sin m\phi]\right)$$

where a, r, θ, ϕ are the Earth's radius (6371.2 km), the radial distance to the observation point, colatitude, and longitude, respectively. The g_l^m and h_l^m are the Gauss coefficients and these parameters were based on the 13th generation IGRF model released by the International Association of Geomagnetism and Aeronomy (IAGA) (Thébault et al., 2015). The IGRF models were used to compare with the unlithified living LB push core sample (LB19_0104) (Figure 4.11).

4.2.4.2 CALSxK.n - (100 yrs < age < 10 kyrs)

The IGRF model based on direct observation is only valid for the past ~100 years. For samples >100 years old, a set of models based on paleomagnetic data from archaeomagnetic, lake sediment, and volcanic data sets can be used for the past 10,000 years. The "Continuous models of Archaeomagnetic and Lake Sediment data for the past x thousand years, version n" (CALSxK.n)

(Korte & Constable, 2003, Constable et al., 2016) are used to compare with the direction of modern GSL samples (Figure 4.3).

4.2.4.3 GAD - (age < 10 kyrs)

When averaged over sufficient time (typically at least thousands of years), Earth's field is assumed to be represented by a geocentric axial dipole (GAD) model. This approximates the geomagnetic field by a geocentric dipole aligned with the spin axis. The GAD declination on any spot on the Earth is 0°, and the inclination can be calculated using the simple dipole formula:

$$\tan \mathrm{I} = 2 \cot \theta = \tan \lambda$$

where I, θ, λ are inclination, colatitude and latitude. The GAD inclination of the four sampling sites are listed below:

Table 4.2. List of GAD inclinations calculated based on the sampling sites' longitude and latitude

Sampling Site	Location (Lon, Lat)	GAD inclination
Great Salt Lake (GSL), Utah, U.S.A.	N 41.15°,W 112.5°	60.22°
Laguna Bacalar (LB), Quintana Roo, Mexico	N 18.6°,W 88.45°	33.94°
Green River Formation (GR), Wyoming, U.S.A.	N 41.97°,W 109.25°	60.93°
Bayan Gol formation (BG), Salaany Gol, Mongolia	N 46.42°,E 96.18°	64.55°

Because the exact age of the GSL lithified thrombolites and the LB living stromatolite are unknown, these paleomagnetic directions were compared to those expected from a geocentric axial dipole (GAD).

4.2.4.4 APWP - (age < 200 Myrs)

For samples old enough that plate motions become significant, the expected GAD field is calculated using an apparent polar wander path (APWP). By sampling materials of variable ages from a continent, the movement of the continent can be reconstructed. Although the pole was

actually fixed, the data are typically shown as the position of the theoretical magnetic pole with respect to a stationary continent, hence the term “apparent polar wander path”. The APWP can be used to reconstruct or predict the paleolatitude and paleoinclination of any point on that continent.

Table 4.3. List of APWP directions (declination, inclination) of the field sites (longitude, latitude) using the ‘apwp’ command in pmag.py package.

Sampling Site	Age	Location (Lon, Lat)	APWP declination	APWP inclination
GSL	0 – 11.6 ka	N 41.15°,W 112.5°	357.9°	60.8°
LB	0 – 12 ka	N 18.6°,W 88.45°	358.2°	33.9°
GR	~51 Ma	N 41.97°,W 109.25°	345.2°	62.2°
BG	~530 Ma	N 46.42°,E 96.18°	n/a	n/a

The expected direction based on an APWP path of the sampling sites was calculated by Pmagpy software (Tauxe et al., 2016) using ‘apwp’ command (Table 4.3). The paleolatitude and longitude were predicted based on apparent polar wander paths of Besse and Courtillot (2002), which go back 200 Myr.

4.2.3.5 Sedimentary Paleomagnetic Data

APWP or other models are typically not available for samples older than about 200 Ma due to lack of the data and low reliability of sample ages. Regional or crustal magnetic field variations might also affect the sample’s magnetic directions which can result in some deviation from the global models, even for young samples. Paleomagnetic data obtained from nearby, similar age units is therefore useful for references.

Paleomagnetic results from the annually banded Eocene Green River sediments have a mean declination of 234° and inclination of 73° (Strangway, 1973). This mean direction was an averaged over ~ 10,000 years, and the sampled site was 210 km away from the GR18_0101 sample site (latitude: N 39.96°, longitude: W 108.36°). The mean paleomagnetic inclination of the

Cambrian Bayan Gol Formation is 62 °± 4° (Evans et al., 1996), and this corresponds to a paleolatitude of 44± 5°. These samples were collected at Salaany Gol and the approximate distance from the BG14_0101 sample site was 60 km (latitude: N 46.50°, longitude: E 95.45°).

4.3. Results and Interpretation

4.3.1. Great Salt Lake

GSL18_Site 3, Antelope Island lithified sample: The specimens of the lithified GSL18_0301 sample were classified based on three laminations: outer, middle, and inner. Fisher statistics of each layer were calculated from the set of ChRM directions which passed MAD < 10 (with the best-fit line anchored to the origin). The mean declination and inclination with the circle of 95% confidence (α_{95}) of each lamination are plotted on an equal-area stereonet plot (Figure 4.1). Out of nineteen specimens from the top lamination, only seven specimens show coherent AF-demagnetization patterns and the Fisher distribution of the passed dataset displays high dispersion (low k) and a high α_{95} value. These surface specimen results were excluded from site mean value because the directions are assumed to be disturbed by surface contamination, chemical alteration or physical destruction, possibly when handling the sample. The site mean declination (356.8°) is roughly similar to the GSL GAD direction, but the mean inclination (43.9°) is not as steep as expected (GAD: 60.22°, IGRF: 60°). This could be explained by an inclination shallowing effect during the DRM process (see Section 4.4.1. Deposition on a sloping bed).

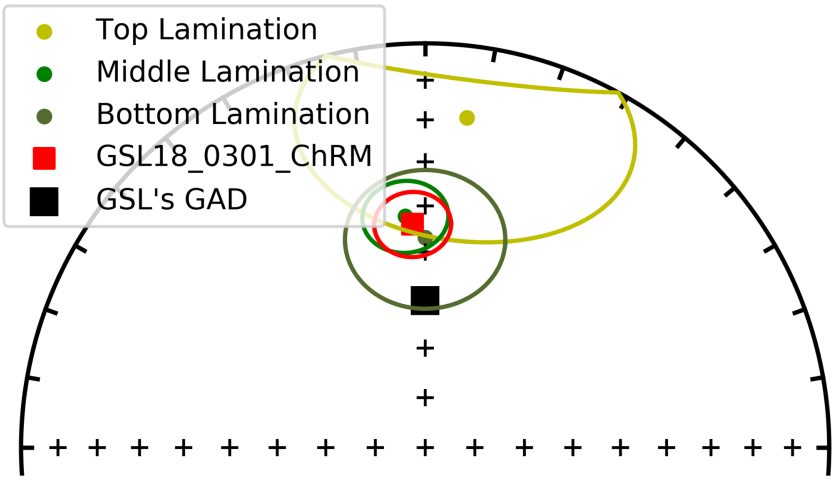

	Top L	Medium L	Bottom L	Mean
D	7.2	355.1	360.0	356.8
I	18.9	42.1	46.9	43.9
N *	7	16	10	26
N	19	19	17	55
R	5.9	15.3	9.2	24.5
k	5.5	22.9	11.4	16.9
α95	34.4	7.9	15.0	7.1

Figure 4.1. Equal area stereographic projection of magnetization components observed from the sample GSL18_0301. The mean declination and inclination with α_{95} ellipses of selected (MAD <10) ChRM of outer, medium, inner laminations are plotted with yellow, green, dark green circles and red square, respectively. The GSL's GAD is plotted with a large black square. The bottom chart shows Fisher statistics of different layers. D, mean declination; I, mean inclination; N*, number of specimens passed MAD<10, N, number of specimens; R, the length of the resultant vector; k, the precision parameter; α_{95}, the circle of 95% confidence angle about the mean.

GSL19_Site 1, Lakeside Site 1: The same criteria were applied on specimens of the sample GSL19_0103. All AF-demagnetized specimens (Figure 4.2.A) and 8 of 10 thermally-demagnetized specimens (Figure 4.2.B) displayed stable demagnetization patterns and passed MAD <10. ChRM directions isolated from different demagnetization methods are similar. NRM and ChRM directions were also very close (Figure 4.2.C and D), suggesting very little overprint. However, while the mean declination is close to north (4.1°), the inclination is about 20° shallower

than GAD or anything predicted by models over the past 10 kyr (Constable et al., 2016). In addition, two surface drill core samples from Lakeside Site 1 also have shallow NRM inclinations of 31.5°and 34.2° (star symbols in Figure 4.3).

In the field, some cliff rocks had fallen onto the monk's head structure microbialites. The shallow inclinations from the Lakeside Site 1 might be interpreted as the combination of disturbance by rearrangement due to cliff rocks or surface contamination, but the directions are also very close to those observed from Antelope Island (Fig. 4.3). Specimens from the inside of the structure displayed steeper inclination (41.8°) compared with the mean inclination from the surface part of the sample (30.7°), but it is still shallow compared to expected field directions. Sample GSL19_0104 which was highly disturbed by the cliff rocks was not used for directional analysis.

GSL19_Site 2, Lakeside Site 2: All specimens subsampled from the hand sample GSL19_0202 were AF demagnetized, but only eight out of twenty-three have MAD values <10. Unlike sample GSL19_0103, the mean ChRM directions were steeper than the NRM inclination (NRM inc:75.2°, ChRM inc: 64.0°). This ChRM is closer to the expected current GAD, IGRF, and paleosecular variations value (Figure 4.3). Likewise, while the mean NRM inclination (72.7°) of GSL19_0201 is steeper than any expected field inclination, the ChRM direction is expected to be shallower, although this sample was not AF demagnetized. A conglomerate unit stratigraphically above (but not covering) the microbialite layer has undergone slumping. Rotation associated with slumping about an axis roughly parallel to the shoreline (NW/SE) would result in a steepening of the paleomagnetic vector. However, it does not appear that the microbialite layer has undergone any rotation/slumping.

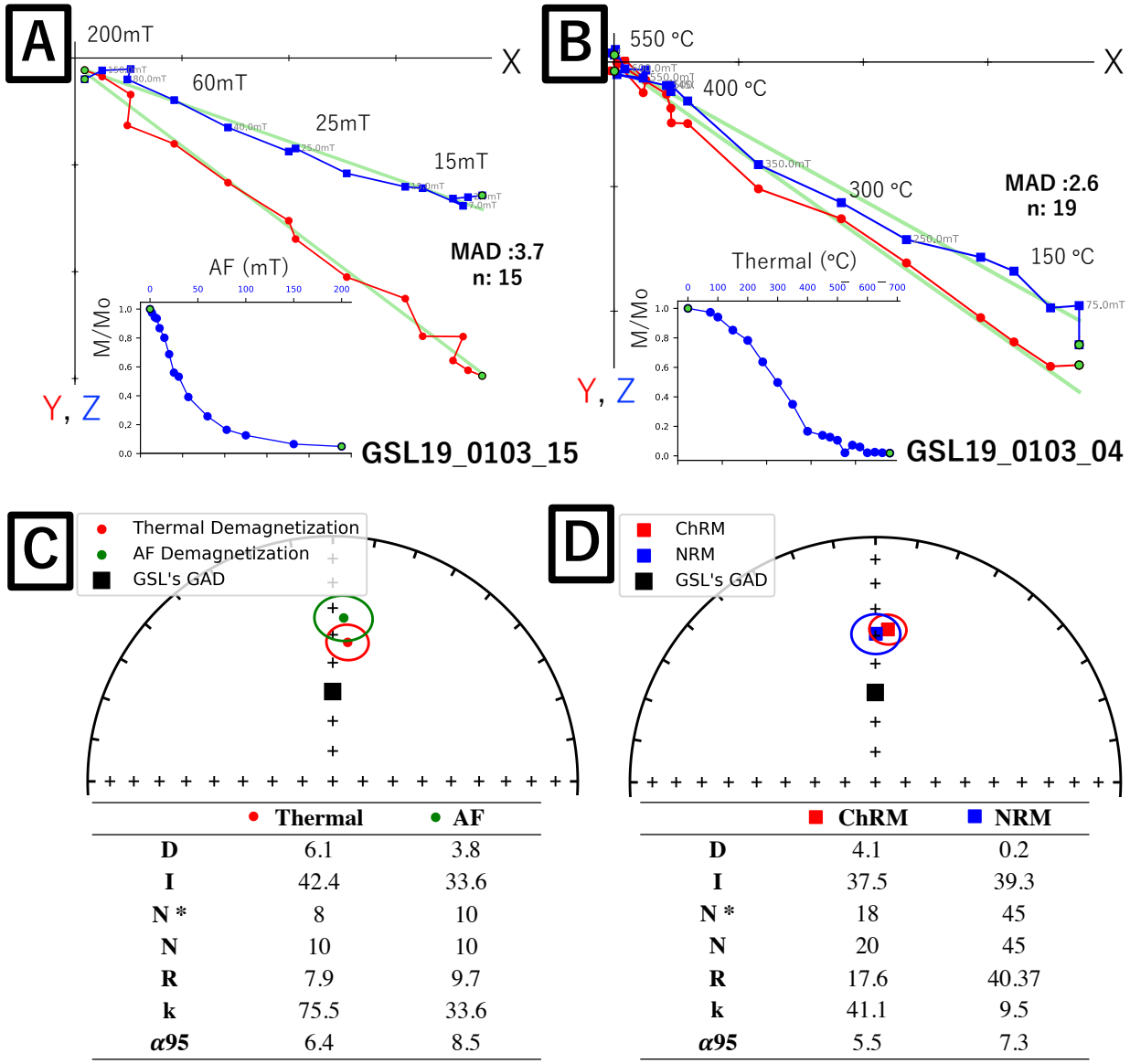

	Thermal	AF
D	6.1	3.8
I	42.4	33.6
N *	8	10
N	10	10
R	7.9	9.7
k	75.5	33.6
α95	6.4	8.5

	ChRM	NRM
D	4.1	0.2
I	37.5	39.3
N *	18	45
N	20	45
R	17.6	40.37
k	41.1	9.5
α95	5.5	7.3

Figure 4.2. Example demagnetization patterns and equal area stereographic projection of mean magnetization components observed from the Lakeside sample GSL19_0103.(a) Vector endpoint diagrams showing AF demagnetization of specimen GSL19_0103_15 and (b) Thermal demagnetization of specimen GSL19_0103_04, and associated magnetization intensity normalized to initial step (M/M_0) as a function of AF or temperature step. (c) The mean declination and inclination with α_{95} ellipses of ChRM of thermally and AF demagnetized specimens plotted with red and green circle symbols, respectively. (d) The mean declination and inclination with α_{95} ellipses of ChRM and NRM plotted with red and blue square symbols, respectively. The bottom charts show Fisher statistics of directions separated by different demagnetization methods of selected data. D, mean declination; I, mean inclination; N*, number of specimens passed MAD<10, N, number of specimens measured; R, the length of the resultant vector; k, the precision parameter; α_{95}, the circle of 95% confidence angle about the mean.

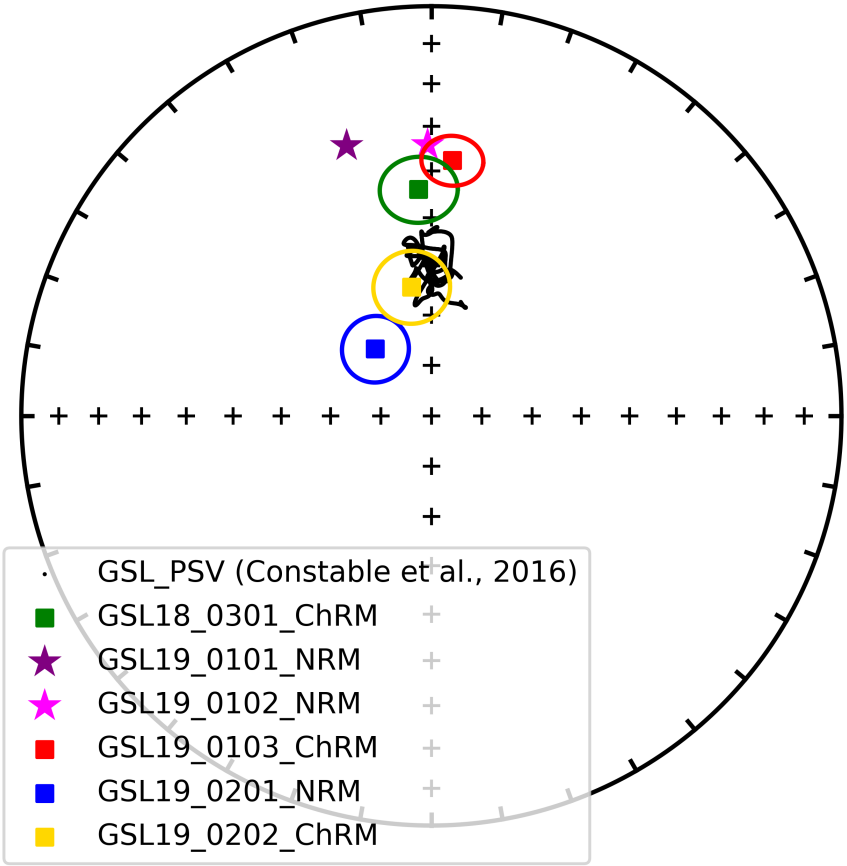

	GSL18_0301	GSL19_0103	GSL19_0201	GSL19_0202
D	356.8	4.1	320.0	351.3
I	43.9	37.5	72.7	64.0
N *	26	18	42	8
N	55	20	42	23
R	24.5	17.6	38.62	7.88
k	16.9	41.1	12.1	57.2
***α*95**	7.1	5.5	6.6	7.4

Figure 4.3. Equal area stereographic projection of magnetization components observed from all GSL samples. The mean declination and inclination with α_{95} ellipses of NRM or ChRM of hand samples or drilled core samples. Each sample site can be found on Figure 2.3. The mean declination and inclination with α_{95} ellipses of ChRM of AF demagnetized specimens from sample GSL18_0301 is plotted with green square symbol. NRM declination and inclination drilled core samples from Lakeside Site 1 are symbolized in purple and pink stars. Mean NRM direction of GSL19_0201 is marked with a blue square, and the combined thermally and AF demagnetized ChRM mean direction of GSL19_0202 is marked with a yellow square. The black line represents the CALSk10.2 model based on latitude and longitude of GSL sampling site from 10ka to present (Constable et al., 2016). The bottom chart shows Fisher statistics of the samples. D, mean declination; I, mean inclination; N*, number of specimens passed MAD<10, N, number of specimens; R, the length of the vector sum; k, the precision parameter; α_{95}, the circle of 95% confidence angle about the mean.

4.3.2. Laguna Bacalar

LB Site 1 – Living unlithified microbialite with cyanobacteria layer: The majority of NRM declinations of LB19_0101 and LB19_0102 specimens point roughly north with inclinations in the range of 20-40° (The GAD of LB: 33.94°) (Figure 4.5. left). However, due to the small number of data, the mean declination and inclination values have high uncertainties (Figure 4.4. right). In addition, none of the AF demagnetized LB19_0101 specimens passed MAD <10 and exhibited noisy demagnetization behavior. This should not result from mobilization of sediments within the sample cubes, as the specimens were kept frozen in the ice box during AF-demagnetization.

LB push core samples (LB19_0103 and LB19_0104) were not demagnetized because they dried out, disaggregated, and altered prior to demagnetization. NRM directions, however, point towards the southeast at the bottom (30 cm) of the core and rotate progressively towards north moving up core for sample LB19_0104. The NRM declination of sample LB19_0103 is to the southwest at the bottom (15cm) and directions also rotate towards north moving up. This likely reflects the fact that the core sample was twisted to the right for the case of LB19_0104 and to the left for the case of LB19_0103 during coring in the field. While the GSL statistics were calculated based on both inclination and declination, the LB core sample statistics were estimated based on inclination only data due to the core twisting effect during sampling. The mean inclinations of LB19_0103 and LB19_0104 were 29.6° and 36.8°.

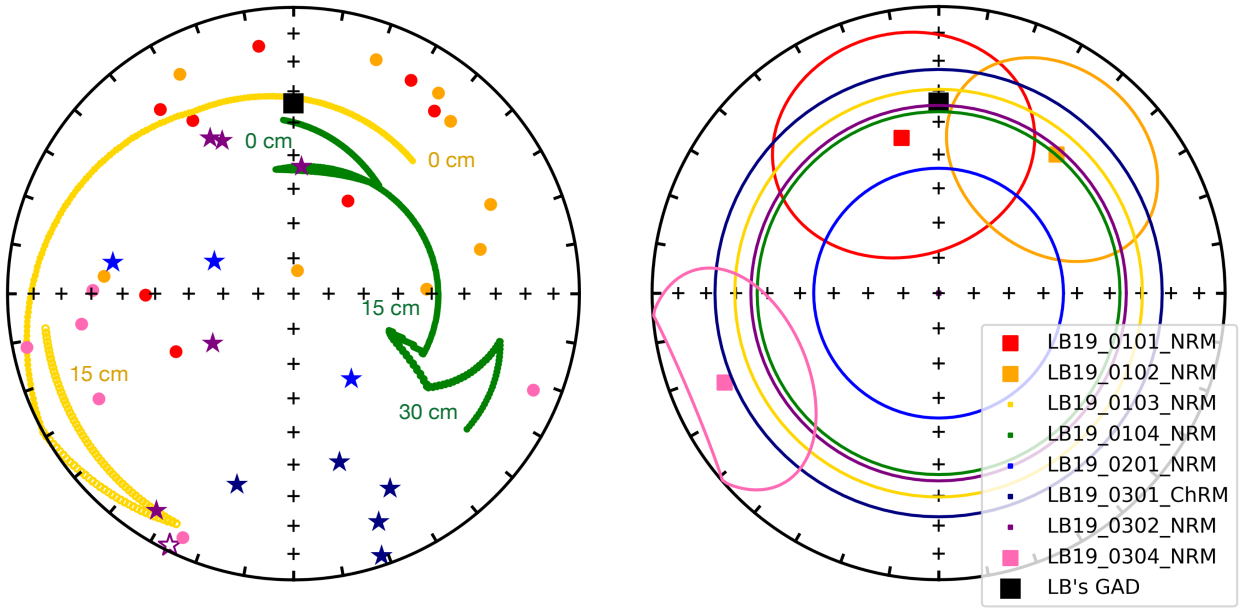

	D	I	N	k	α95
LB19_0101	346.6	43.6	8	3.5	34.9
LB19_0102	40.4	36.6	8	4.5	29.3
LB19_0103	n/a	29.6	8	n/a	n/a
LB19_0104	n/a	36.8	36	7.8	0.0
LB19_0201	n/a	56.4	3	12.9	45.57
LB19_0301	n/a	23.0	5	n/a	n/a
LB19_0302	n/a	38.4	6	5.9	25.84
LB19_0304	247.3	20.2	6	8.9	27.1

Figure 4.4. Equal area stereographic projection of magnetization components observed from the LB samples. The left plot displays the declination and inclination of cube specimens (circle), subsampled specimens from hand samples (circle) or push cores (line) or drilled core specimens. Subsamples of LB19_0101, 0102, 0103, 0104, 0201, 0301, 0302, 0304 are shown by red, orange, yellow, green, blue, navy, purple, pink. LB's GAD (0, 33.94°) is displayed as black square. Opened and closed symbols represent upper and lower hemisphere projections, respectively. The mean directions calculated from specimens from each level in push cores LB19_0103 and 0104 were linearly interpolated; depth from surface indicated in cm. Each sample site can be found on Figure 2.4. The right plot exhibits the Fisher mean declination and inclination (square) with α95 ellipses of NRM of subsamples (LB19_0101,0102, 0304). Where declination was not available (LB19_0103, 0104, 0201, 0301, 0302) mean inclination is shown as a circle around the center. The right bottom chart shows Fisher statistics of each sample. D, Fisher mean declination; I, Fisher mean inclination; N, number of specimens; R, the length of the vector sum; k, the precision parameter; α95; the circle of 95% confidence angle about the mean. The Fisher statistics of calculated by PmagPy software (Tauxe et al., 2016) using 'gofish' (specimens that have both declination and inclination data) and 'incfish' (specimens where only inclination data are available)

LB Site 2 (East Shore): Drilled core samples from LB Site 2 were porous and easily broken during sampling, and therefore the azimuthal orientation was not maintained. However, cores were drilled vertically, and the inclination information of three specimens from the LB19_0201 drilled core sample were available. The NRM mean inclination of 54.1° is steeper than the GAD inclination for LB (33.94°).

LB Site 3 (Rapids): Six cube specimens from living cyanobacteria layers (~2cm) (LB19_0304) and specimens from five azimuthally-oriented drill core specimens of lithified microbialites underneath (LB19_0301) were AF- demagnetized. The layer of living microbial communities displayed unstable demagnetization patterns on vector endpoint diagrams and the magnetization intensity did not decay monotonically (Figure 4.5.A). Compared with cyanobacteria layers, the lithified cores presented more stable demagnetization patterns (Figure 4.5.B).

The NRM intensity of cyanobacteria layers (1.00E-08 Am^2/kg) were roughly 10 times less than lithified microbialites (1.00E-07 Am^2/kg) and close to the magnetization value of the empty 2 cm^3 plastic cube (1.00E-09 to 1.00E-08 Am^2/kg). Hence, the low-quality results might represent the effect of a low signal:noise ratio.

With the exception of one specimen, however, the NRM declinations from the cyanobacteria layer point southwest with inclinations of around 20° (Figure 4.4. pink). The mean inclination of drilled core samples LB19_0301 and 0302 were 23.0° and 38.4°, respectively (Figure 4.4. right). The moderate current at the Site 3 sampling area was to the south, and this might cause directional error (see Section 4.4.1, Water Current).

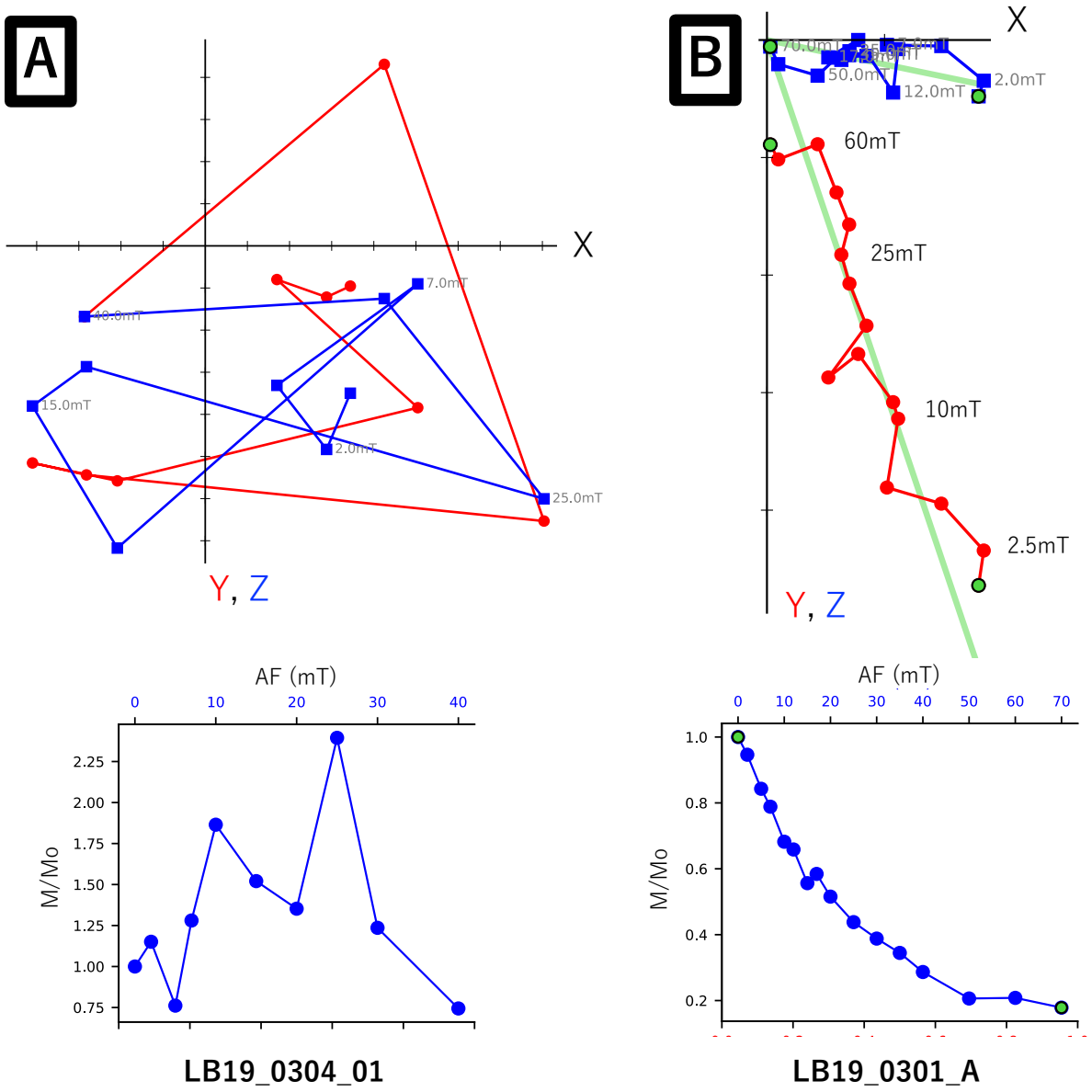

Figure 4.5. AF-demagnetization pattern of representative specimens of the living microbial communities LB19_0304_01) and lithified microbialites LB19_0301_A from the Rapid microbialites (LB19 Site3) (a) Vector endpoint diagrams showing AF demagnetization of specimen LB19_030401 and (b) LB19_0301_A and associated magnetization intensity normalized to initial step (M/M_0) as a function of AF demagnetization step.

4.3.3. Green River Formation

All 103 specimens of Green River Formation microbialite sample (GR18_0101) were AF demagnetized. However, while weakly magnetized specimens (NRM < 1.00E-06 Am^2/kg) displayed unstable AF-demagnetization patterns with high MAD values, specimens with strong NRM intensity (NRM > 1.00E-05 Am^2/kg) have similar ChRM directions and low MAD values (Figure 4.6.A).

ChRM directions (MAD <10, NRM > 5.00E-06 Am^2/kg) of specimens from the microbialite's internal structure plotted in Figure 4.6.B. The Fisher mean declination and inclination are 99.4° and -29.8°, which is not close to the expected APWP direction (Declination: 345.2°, Inclination: 62.2°) or to paleomagnetic directions (Declination: 234°, Inclination: 73°) obtained from the Green River sediments (Strangway, 1973).

The ChRM directions were regrouped by the left and right side of the highly magnetized spots (Figure 4.6). While the majority of the specimens from the right side point northeast (mean declination: 60.7 °, mean inclination: -12.1 °), the specimens from the left side show southeasterly directions (mean declination: 128.2 °, Mean inclination: -30.0 °). This unusual directional distribution implies the sample was not magnetized by the global core dynamo, but perhaps by a small scale induced magnetization such as an IRM produced by lightning strikes. However, the spatial scale associated with lightning-induced IRM is typically meters as opposed to centimeters.

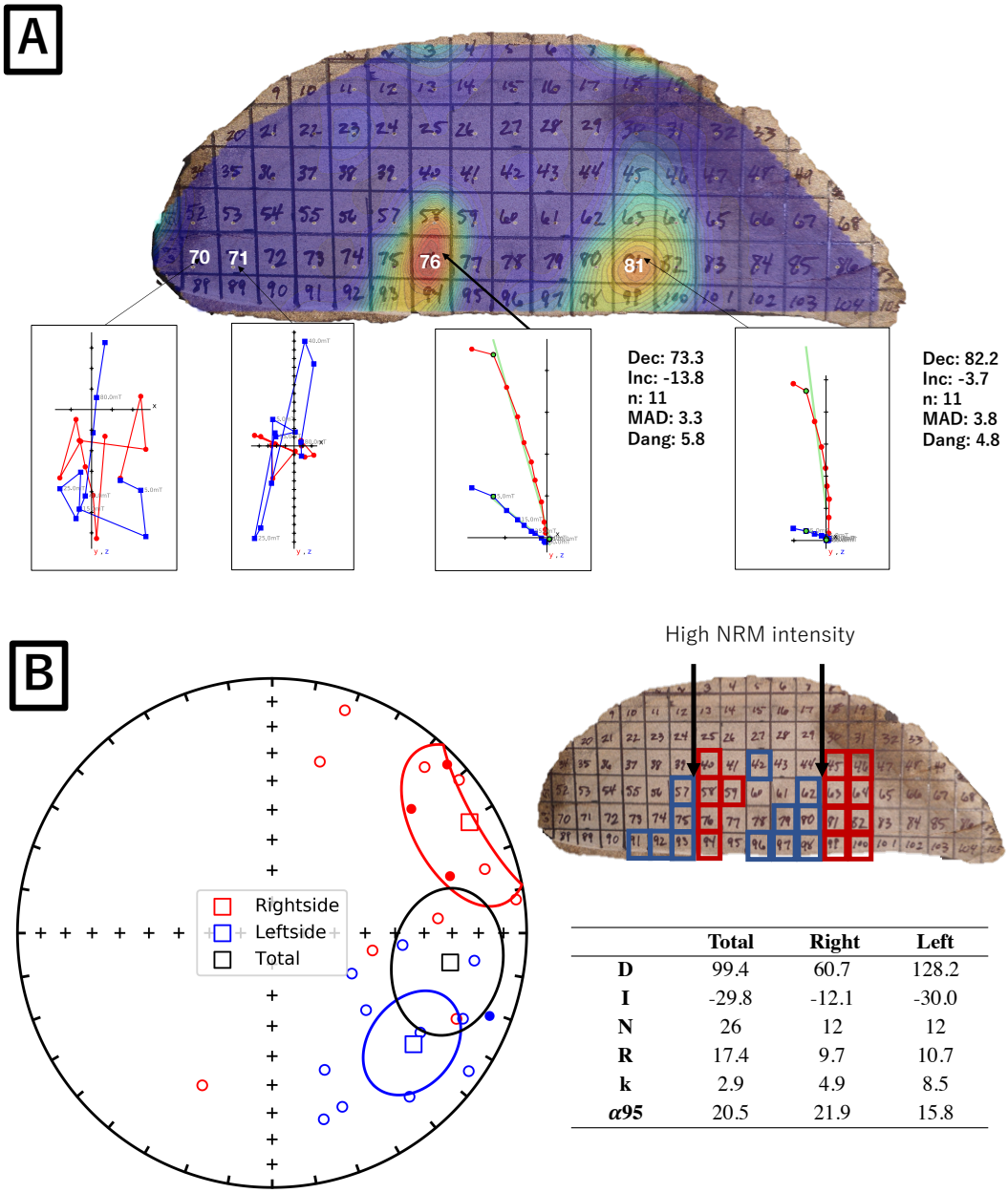

	Total	Right	Left
D	99.4	60.7	128.2
I	-29.8	-12.1	-30.0
N	26	12	12
R	17.4	9.7	10.7
k	2.9	4.9	8.5
α95	20.5	21.9	15.8

Figure 4.6. (a) Examples of AF demagnetization of GR specimens. Vector-endpoint diagrams of two weakly magnetized specimens (GR18_0101_70 and 71) and two highly magnetized specimens (GR18_0101_76 and 81). Background displays the NRM intensity mapping. (b) Equal area stereographic projection of magnetization components of right side (red circle) and left side (blue circle) of the highly magnetized spots (MAD <10, NRM > 5.00E-06 Am^2/kg). The Fisher mean declination and inclination of total, right side and left side with α_{95} ellipses are shown as black, red, and blue squares. Opened and closed symbols represent upper and lower hemisphere projections, respectively. Image to right shows where right side (red squares) and left side (blue squares) specimens were located in the structure. Black arrows point to highly magnetized spots. The right bottom chart shows Fisher statistics. D, mean declination; I, mean inclination; N, number of specimens; R, the length of the vector sum; k, the precision parameter; α_{95}, the circle of 95% confidence angle about the mean.

4.3.4. Bayan Gol Formation

The Cambrian microbialite from the Bayan Gol Formation (BG14_0101) was both AF (37 specimens) and thermally (10 specimens) demagnetized. AF cleaning was more effective in extracting the stable magnetizations, and none of the thermally processed samples had a useful coherent demagnetization pattern. Figure 4.7 shows AF-demagnetized (A) and thermally demagnetized (B) specimens which have the smallest MAD values.

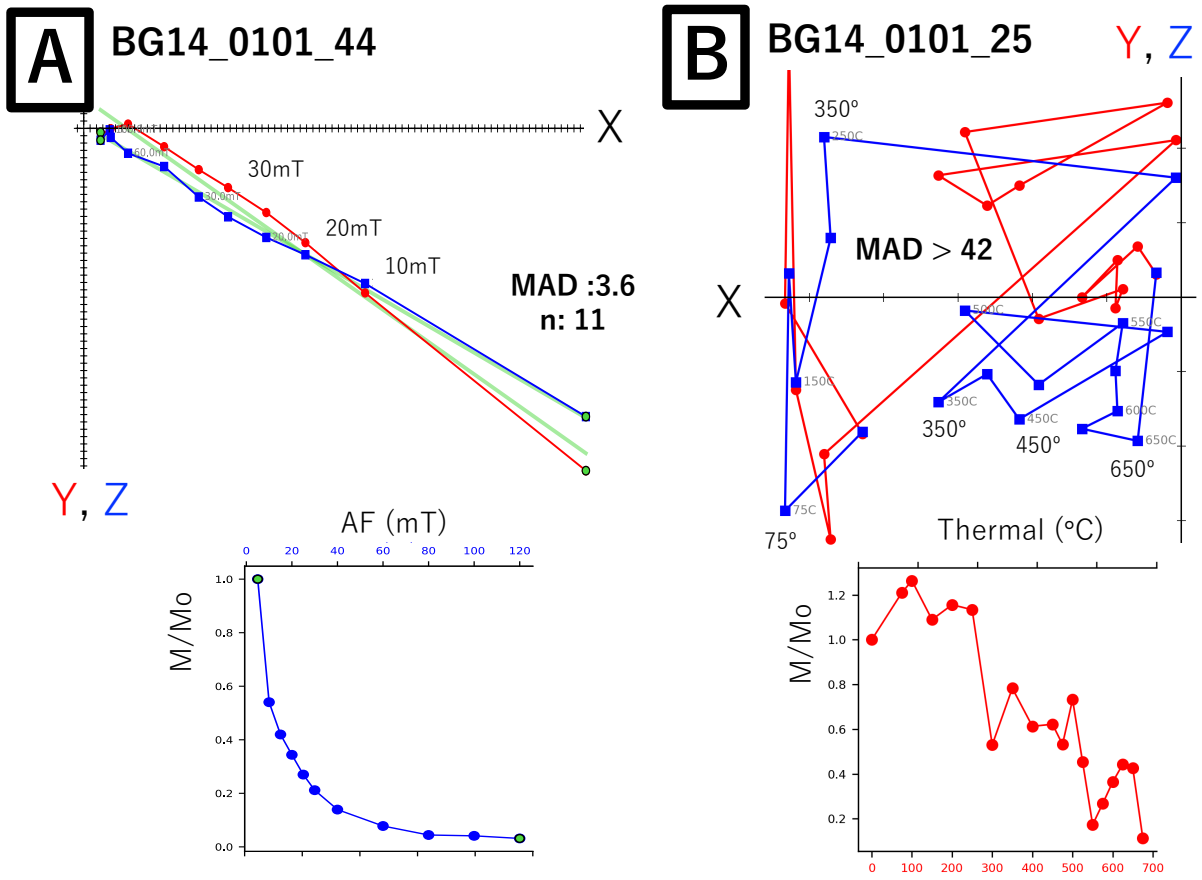

Figure 4.7. Examples of AF-demagnetization (A) and thermal-demagnetization processed BG14_0101 samples (B). Vector endpoint diagrams showing demagnetization of specimen (top graphs), and associated magnetization intensity normalized to initial step (M/Mo) as a function of AF or thermal demagnetization step.

The ChRM directions of 22 out of 37 AF-demagnetized specimens (MAD<10), were plotted on Figure 4.8.A. The sample was only oriented with respect to up in the field, so declinations are

unknown, but inclination is accurate, and specimens were mutually oriented. The mean ChRM has a high precision parameter value (k:81.7) and low alpha 95 value (a95:3.5). The only independent information on the expected inclination comes from paleomagnetic directions obtained from the same sedimentary bed (-62 ± 4°) (Evans et al., 1996). This result overlaps the calculated stromatolite inclination (-66.3°±3.5°). There are variations in the inclination, however, associated with bedding/lamination slopes of the microbialite (see Section 4.4.1, Deposition on a sloping bed). While the inclinations from the right arms of the structure have inclinations of -75.0° to -65.0°, the inclinations from the left side are -65.0° to -55.0° (Figure 4.8.B).

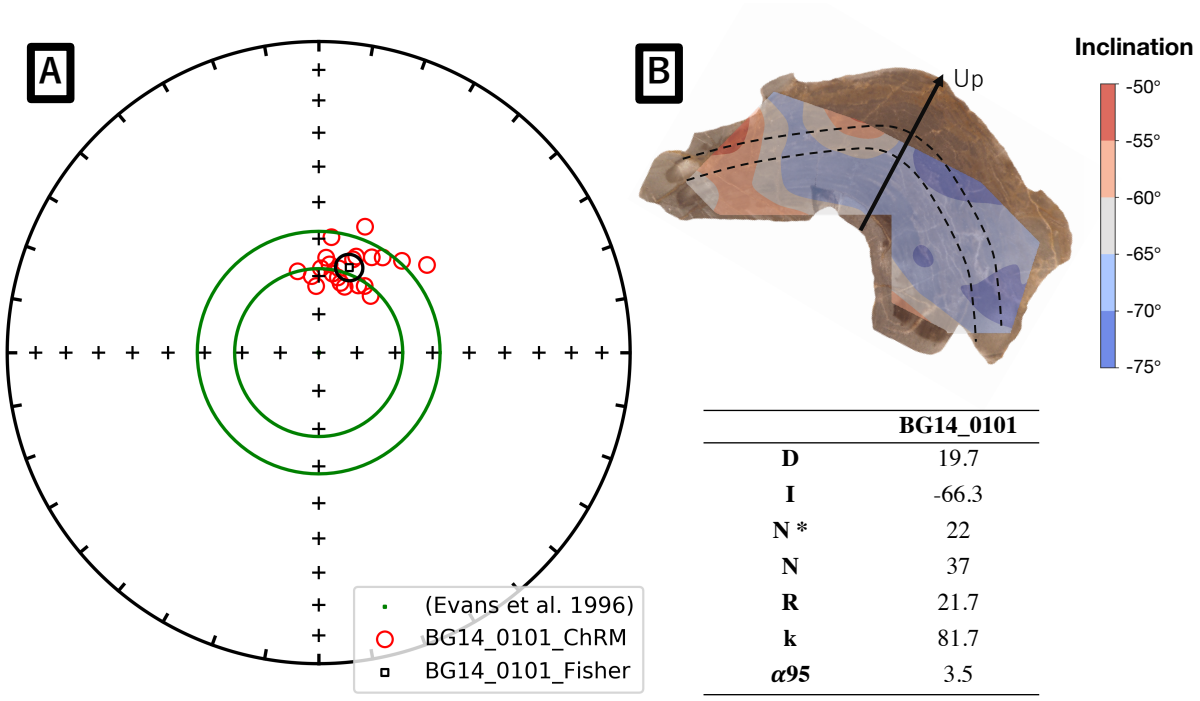

	BG14_0101
D	19.7
I	-66.3
N *	22
N	37
R	21.7
k	81.7
α95	3.5

Figure 4.8. (a) Equal area stereographic projection of ChRM directions (red circle) (MAD < 10) from BG14_0101 sample magnetization and calculated Fisher mean direction (black square) with a $\alpha 95$ ellipse. Opened and closed symbols represent direction in the upper and lower hemisphere, respectively. The green circles represent the expected inclination range derived from sedimentary beds in the same formation (-62± 4°) (Evans et al., 1996) (b) Inclination mapping by cubic interpolation on the sample slice. The black arrow and dash lines represent up directions and laminations. The left bottom chart shows Fisher statistics of each sample. D, mean declination; I, mean inclination; N, number of specimens; R, the length of the vector sum; k, the precision parameter; $\alpha 95$; the circle of 95% confidence angle about the mean.

4.4 Discussion

4.4.1. Is a Microbialite Capable of Recording Earth's Magnetic Field Direction?

The results show that, with the exception of the microbialite sample from the Green River Formation (GR18_0101), the ChRMs of other microbialites (M >1.00E-07 Am^2/kg) appear to record directions close to the expected field. The directional information from microbialites magnetized less than 1.00E-07 Am^2/kg are unreliable due to the sensitivity of the magnetometers (1.00E-12 to 1.00E-03 Am^2) and the magnetization of the sample containers (1.00E-12 to 1.00E-10 Am^2). It is possible that more sensitive instrumentation would allow reliable information to be extracted from these weakly magnetic samples.

The deviation away from expected values (declination $\pm$ 10°, inclination $\pm$ 20°) most likely results from the effects of 1) deposition on sloping beds and 2) water current (see below). Deposition under moving water or deposition on a sloping surface can create bedding error (Kodama, 2012), and burial compaction after DRM formation can cause inclination shallowing (Kodama, 2012; Tauxe et al., 2008). However, the effect of burial compaction is not applicable for the living or lithified microbialites on the surface, because it is typically caused by dewatering effects at depths >10 m sediment column.

4.4.2. Deposition on a Sloping Bed

King (1955) and Kodama (2012) have proposed that when the bed dips in the same direction as the magnetic field, the magnetization vector would be steeper by the degree of dip gradient (Figure 4.9). If the bedding slope is opposite to the Earth's magnetic field, however, the inclination can be shallower. Many microbialites have domal internal structures, hence, magnetic directions

recorded by different parts of the structure might be disturbed by the effect of deposition on a sloping bed.

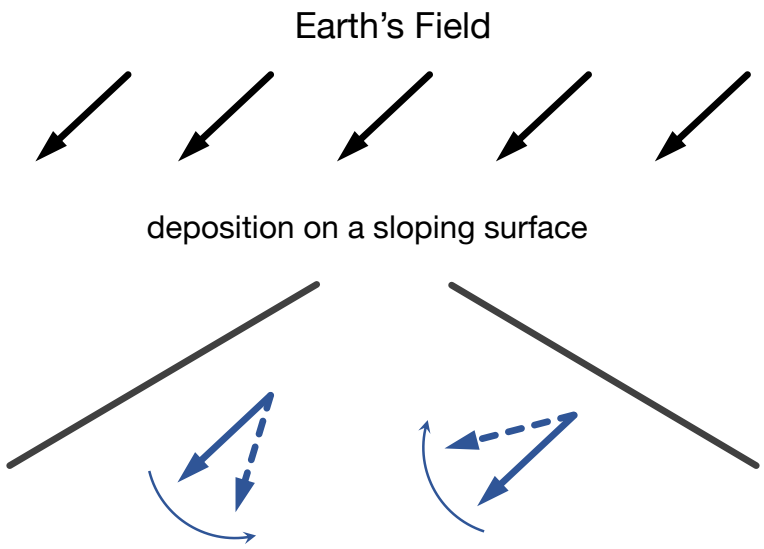

Figure 4.9. Diagrams illustrate a deposition on a sloping surface. The solid dark blue arrows represent an accurate DRM direction based on the Earth's field direction (solid black arrows) and the dashed dark blue arrow show the resultant of DRM deposition. (Modified from Kodama, 2012)

The GSL18_0101 hand sample was from the steep side of the columnar mound structure, and the sample was positioned opposite to the magnetic field. The sample's Fisher mean inclination of 43.9° is 16.1° shallower than the GAD inclination, and the magnetic vectors may have experienced a bedding-related shallowing. For sample BG14_0101, inclinations from one arm of the structure are -75.0° to -65.0°, while the specimens from the other side are -65.0° to -55.0° (Figure 4.5.B). These variations correspond to the structure's bedding slopes based on the laminations. The push core sample LB19_0104, however, was from the middle of the structure, and here the Fisher mean inclination of 36.8° is very close to the expected GAD inclination of 33.94°.

4.4.3. Water Current

Deposition from moving water may also result in directional error in the microbialites. If there is no water current, the detrital magnetic particles will be deposited aligning with the ambient magnetic field without significant inclination or declination deviations. However, if deposition occurs under a moving water current, the DRM vector rotates into the current direction about a horizontal axis perpendicular to the current direction (Kodama, 2012). In a turbulent current, one might expect that the DRM be more dispersed and randomized.

Errors in magnetic inclinations and declination of LB19 samples might be explained by the effect of water current. The whole water body of Laguna Bacalar flows form SW to NE, but current strength was different at each site. The water was stagnant for LB19 Site 1, and the samples (M >1.00E-07 Am^2/kg) from this site (LB19_0101, 0102, 0103, 0104) displayed magnetic inclination range of 30° to 44°. This is a close value to LB's GAD (33.94°) and the present IGRF (47.5°). The water was gently flowing south at LB19 Site 3. The samples from Site 3 (LB19_0301,0302,0304) exhibit shallower magnetic inclination range of 20° to 38° compared to Site 1. At Site 2, the water was turbulent, and this might have caused the errors in magnetic directions. Even though the sample LB19_0201 was collected from the middle of the structure, the inclinations were too steep (GAD ＋20°).

4.4.4. Timing of Magnetization

In the light of these two effects, we can assess the timing of the magnetization. The change of the magnetization over time in living LB and magnetic susceptibility of GSL microbialites (Chapter 3) would seem to call into question of the timing of the magnetization in the ancient microbialites. Does the original DRM get modified as the microbialites are buried and/or the lakes

dry up? However, the lithified GSL and BG samples show inclination variations correlated with bedding slopes and lithified and unlithified LB samples show directional variations that correlate with changes in water current. These cases suggest that the timing of sediment deposition and acquisitions of magnetization of the microbialites samples are close.

4.5 Conclusion

Microbialites that have magnetization intensity more than 1.00E-07Am^2/kg are shown to be plausible paleomagnetic recorders. To reduce the effects of sloping beds, for large domal structures, samples should be collected avoiding steep sides or by sampling all sides. For smaller scale hand samples (< 50 cm), the sample slice should be cut parallel to the expected direction of the magnetic declination. Then, specimens from different lamination angles should be collected to be average out the deviations generated by sloping beds. For future studies, improvements in magnetometer sensitivity or scanning magnetic microscopy may allow recovering magnetic directions recorded in the microbialites with at a higher temporal resolution.

Chapter 5: Magnetic properties of Microbialites

5.1 Introduction

Although magnetic carriers in microbialites appeared to record geomagnetic field (Chapter 4), the properties of the magnetic carriers (e.g., magnetic mineralogy and domain state) are important to distinguish possible secondary magnetizations and to understand the primary magnetization processes (see Chapter 6). Samples that have been remagnetized by secondary magnetization (e.g., VRM, CRM) should be excluded before the reconstruction of the magnetic field. The magnetization processes of the primary magnetization should be considered because different magnetization processes and mineralogies may result in deviations of magnetic directions (e.g., DRM's bedding slope error).

Previous studies observed various mineralogies that carry remanant magnetization in microbialites. For a microbialite to acquire DRM, it must incorporate ferromagnetic minerals in the structure from nearby sources. Thin section photomicrographs of coral reef samples displayed titanomagnetite grains bound within microbialites. These grains originated from the Tahiti volcanic edifice and were determined to carry the magnetization (Lund et al., 2010). In addition, unique mineral morphologies or magnetic properties have been used to infer biomineralization processes in microbialitic environments. The presence of magnetotactic bacteria (MTB) has been shown in ancient (Chang & Stolz, 1989) and modern stromatlitic environments (Stolz et al., 1987) by using rock magnetic techniques (e.g., Lowrie-Fuller test) and transmission electron microscopy to detect single domain magnetite unique crystal structures created by MTB. Mixtures of different types of minerals or grain sizes can also be found in microbialite. Hysteresis loops of Jurassic stromatolites from Poland were wasp-waisted, which may result from a mixture of magnetic components of

contrasting coercivities (Muraszko, 2014). It was interpreted as either the presence of a high coercivity component such as goethite and hematite mixed with a low coercivity component such as magnetite, or as a bimodal distribution of magnetic grain sizes. Other magnetic measurements (i.e., 3D IRM and Curie temperature) suggested the presence of single-domain grains, as well as goethite, hematite, and magnetite.

The main aim of this chapter is the identification of magnetic minerals and magnetic domain states of GSL, LB, GR, BG microbialites. This was analyzed by seven different rock magnetism experiments: 1) S-ratio, 2) IRM Unmixing, 3) Lowrie-Fuller Test, 4) 3D IRM technique, 5) Curie points, 6) hysteresis loop, and 7) FORC. With the exception of Curie point analysis, these experiments are based on determining a sample's coercivity distribution.

5.2 Background and Methods

5.2.1. S-ratio

Thomspon and Oldfield (1986) defined the classical S-ratio as:

$$S_{ratio} = -\left(\frac{IRM_{-0.3T}}{IRM_{\ 1T}}\right)$$

where a sample is magnetized in a 1T field (IRM_{1T}) and then a "backfield" IRM is applied in a 300 mT field in the opposite direction ($IRM_{-0.3T}$) The idea is that low coercivity minerals such as magnetite will be remagnetized by the 300 mT field, but the high coercivity minerals such as hematite will remain magnetized in the original direction. If only low-coercivity minerals are present, the S ratio will be 1. However, when both high and low coercivity phases coexist, the S ratio will decrease, and if only minerals with coercivities > 300 mT are present, the S ratio will be -1.

In this study, specimens were fully AF-demagnetized (to 200 mT). The 1000 mT IRM was acquired and measured on the fully demagnetized specimens. Then, the 300 mT IRM was acquired in the opposite direction. The S-ratio was calculated using the above equation. The S-ratio of two slices (A, B) of the lithified GSL18_0301 hand sample from Antelope Island; five specimens of lithified drill core sample LB19_0301; 32 specimens of the GR18_0101 sample; and 35 specimens of the BG14 _0101 sample were evaluated.

5.2.2. IRM Unmixing

The IRM unmixing method originally assumed that any mineral population has a log-normal distribution of grain size and hence coercivity (e.g., Robertson & France, 1994). In this experiment, there were two different setups for IRM acquisition: 1) IRM is acquired in steps between 0 mT and 1000 mT on a fully demagnetized specimen, and/or 2) a 1000 mT IRM is first acquired, then IRM is acquired in the opposite direction in steps between 0 mT and 1000 mT. Here, these two methods are symbolized as IRM_{0mT} for the first case and $IRM_{-1000mT}$ for the second case. The first derivative of this acquisition curve provides the coercivity spectrum, and it can be mathematically "unmixed" to estimate different magnetic mineral populations. Specimens descriptions and experimental setup type are listed in Table. 5.1.

The fitting technique has been updated to allow for distributions that deviate from normality, a condition often found in natural samples. Egli (2003) uses a skew generalized Gaussian (SGG) function to allow for non-normality, and these SGG functions are incorporated into the MaxUnmix (Maxbauer et al., 2016) online software that was used to fit a series of functions to the measured coercivity distribution. The starting fit is guided by the user, and the program then optimizes the fits. 95% confidence intervals are calculated using a resampling algorithm with N = 300. Individual

components are described by their mean coercivity and a dispersion parameter (DP). Here, a smoothing factor of 0.4 is applied to the data prior to fitting.

Table 5.1. IRM unmixing sample ID, specimen ID, IRM acquisition setup, and types and description of microbialite sample. CB layer, cyanobacteria layer; LM, lithified microbialites; UL deposits; unlithified sedimentary deposits

Sample ID	Specimen ID	Acquisition Setup	Type and Description
GSL18_0101	GSL18_0101_00	IRM_{0mT}	Living CB layer + porous LM
	GSL18_0101_01	IRM_{0mT}	Living CB layer + porous LM
GSL18_0301	GSL18_0301_A01	$IRM_{-1000mT}$, IRM_{0mT}	porous LM
	GSL18_0301_A02	$IRM_{-1000mT}$, IRM_{0mT}	porous LM
	GSL18_0301_B01	$IRM_{-1000mT}$	porous LM
	GSL18_0301_B03	$IRM_{-1000mT}$	porous LM
GSL19_0202	GSL19_0202_A03	$IRM_{-1000mT}$	LM with interbedded pebbles
	GSL19_0202_A04	$IRM_{-1000mT}$	LM with interbedded pebbles
	GSL19_0202_A05	$IRM_{-1000mT}$	LM with interbedded pebbles
	GSL19_0202_A10	$IRM_{-1000mT}$	LM with interbedded pebbles
	GSL19_0202_A11	$IRM_{-1000mT}$	LM with interbedded pebbles
	GSL19_0202_A12	$IRM_{-1000mT}$	LM with interbedded pebbles
LB19_0102	LB19_0102_03	IRM_{0mT}	Living CB layer +UL deposits
LB19_0301	LB19_0301_A	$IRM_{-1000mT}$, IRM_{0mT}	porous LM
	LB19_0301_B	IRM_{0mT}	porous LM
	LB19_0301_C	$IRM_{-1000mT}$, IRM_{0mT}	porous LM
	LB19_0301_D	$IRM_{-1000mT}$	porous LM
	LB19_0301_E	$IRM_{-1000mT}$	porous LM
LB19_0304	LB19_0304_02	IRM_{0mT}	Living CB layer
	LB19_0304_05	IRM_{0mT}	Living CB layer
GR18_0101	GR18_0101_A70	IRM_{0mT}	Eocene dense microbialite
	GR18_0101_A71	IRM_{0mT}	Eocene dense microbialite
	GR18_0101_A76	IRM_{0mT}	Eocene dense microbialite
	GR18_0101_A81	IRM_{0mT}	Eocene dense microbialite
BG14_0101	BG14_0101_A05	$IRM_{-1000mT}$	Cambrian dense stromatolite
	BG14_0101_A08	IRM_{0mT}	Cambrian dense stromatolite
	BG14_0101_A12	$IRM_{-1000mT}$	Cambrian dense stromatolite
	BG14_0101_A38	$IRM_{-1000mT}$	Cambrian dense stromatolite
	BG14_0101_A70	IRM_{0mT}	Cambrian dense stromatolite

Acquisition Setup	IRM acquisition step (mT)
$IRM_{-1000mT}$	-1000.0, 3.0, 5.0, 7.5, 10.0, 12.5, 15.0, 20.0, 25.0, 30.0, 35.0, 40.0, 50.0, 60.0, 70.0, 80.0, 100.0, 125.0, 150.0, 175.0, 200.0, 250.0, 300.0, 350.0, 400.0, 500.0, 600.0, 625.0, 800.0, 1000.0
IRM_{0mT}	0.0, 3.0, 5.0, 7.5, 10.0, 12.5, 15.0, 20.0, 25.0, 30.0, 35.0, 40.0, 50.0, 60.0, 70.0, 80.0, 100.0, 125.0, 150.0, 175.0, 200.0, 250.0, 300.0, 350.0, 400.0, 500.0, 600.0, 625.0, 800.0, 1000.0

5.2.3. Lowrie-Fuller Test

The so-called 'Lowrie-Fuller' test (Lowrie and Fuller, 1971) compares the AF demagnetization spectra of ARM and IRM to estimate the average domain state. The median destructive field (MDF) is the field at which 50% of the NRM is removed when a specimen is exposed to an alternating field. Assuming that the major remanence carrier of a rock is magnetite, the domain state can be estimated by comparing the MDF of the saturated isothermal remanence magnetization (sIRM) (i.e., 1000 mT IRM) and the MDF of the ARM (Johnson et al., 1975). When the MDF of the sIRM is greater than MDF of the ARM, it may be considered as MD. In contrast, when the MDF of sIRM is less than the MDF of ARM, it may be considered SD. Also, conventionally, the intersection point of the IRM acquisition and IRM demagnetization curve is taken as an estimate of the average coercivity of a sample. There are many caveats to this method (see, e.g., Dunlop and Özdemir, 1997), including effects of particle interactions, internal stress, and the presence of grains not saturated in a 1000 mT field. Lowrie-Fuller tests on stromatolites have been previously used (Chang & Stolz, 1989; Stolz et al., 1987) in order to search for single-domain biogenic magnetite in ancient and modern microbialites.

Two specimens subsampled from a living GSL18 microbialite collected from Site 1, Antelope Island, GSL (GSL18_0101_00, 01); two specimens subsampled from a lithified microbialite collected from Site 3, Antelope Island, GSL (GSL18_0301_A01, 02); six specimens subsampled from a lithified modern collected from Site 2, Lakeside, GSL (GSL19_0202_A03, 04, 05, 10, 11, 12); five specimens subsampled from a lithified porous microbialite collected from Site 3, the rapids, LB (LB19_0301_A, B, C, D, E); and four specimens subsampled from lithified Eocene microbialite collected from Site 1, Green River Formation (GR18_0101_A70, 71, 76, 81) were subjected to the Lowrie-Fuller test. ARM was acquired at 150 mT AF with a 0.05 mT bias field,

and AF-demagnetization steps are given in Table 4.1. Stepwise IRM was acquired in steps given in Table 5.1 and was AF demagnetized at the same steps as the ARM. The AFD_03 demagnetization step was used for all samples' ARM and IRM demagnetization, with the exception of sample GSL19_0202 where ARM was demagnetized according to AFD_05 and IRM was demagnetized according to AFD_03. The MDF of each specimen's IRM acquisition or IRM and ARM decay curves were calculated and compared. ARM and IRM were normalized by the initial value and plotted on a log scale, and the MDF of ARM and IRM decay were calculated based on linear interpolation. The intersections between IRM acquisition and decay were estimated by finding a field point of the least absolute value of subtraction of IRM acquisition from IRM decay.

5.2.4. 3D IRM Technique

The 3D IRM technique (i.e., Lowrie test; Lowrie, 1990) is a method that uses thermal demagnetization of specimen's triaxial IRM, which provides simultaneous information on coercivities and unblocking temperatures (T_b). In this test, three sequential IRMs (1000, 300, and 100 mT) are applied along the three orthogonal axes to separate the hard, medium, and soft coercivity fractions. The specimen is then subjected to thermal demagnetization in order to obtain the unblocking temperature distribution of each coercivity fraction. This method is useful in constraining the ferromagnetic minerals present.

Four specimens subsampled from a lithified microbialite collected from Site 3, Antelope Island, GSL (GSL18_0301_A01, 02, B01, B03); five specimens subsampled from a lithified modern collected from Site 2, Lakeside, GSL (GSL19_0202_A03, A04, A05, A10, A11); four specimens subsampled from a lithified porous microbialite collected from Site 3, the rapids, LB

(LB19_0301_A, B, C, E); and five specimens subsampled from lithified Cambrian stromatolite collected from Site 1, Bayan Gol Formation (BG14_0101_A05, A08, A12, A38, A70) were evaluated by the 3D IRM technique. All samples were placed in plastic cubes and were magnetized at 1000 mT along the z-axis, 300 mT along the y-axis, and finally 100 mT along the x-axis (Figure 5.1). Then, the samples were taken out from the cubes and were thermally demagnetized in zero applied field (using steps indicated in Table 4.1.). In order to measure the magnetic remanence after each demagnetization step, samples were placed back in the same cube placed at the same location inside the cube and fixed with the same amount of kimwipes to reduce noises in the data.

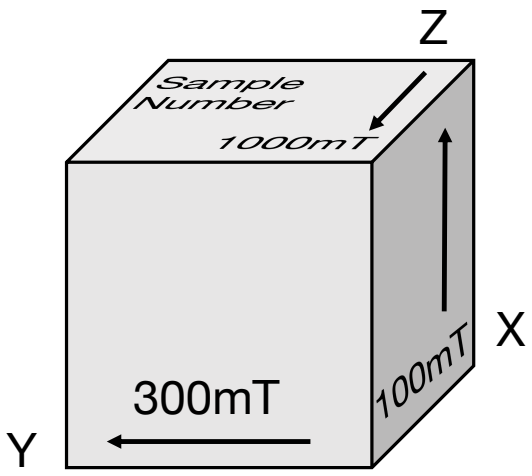

Figure 5.1. Diagram indicating IRM acquisition directions for the Lowrie 3D IRM test. 1000 mT, 300 mT, and 100 mT field are applied to the Z-axis, Y-axis, and X-axis to separate hard, medium, and soft coercivity minerals.

5.2.5. Curie Temperature

Curie point (T_c) is a temperature above which ferromagnets behave as paramagnets (no remanence). T_c is generally considered to be a physical property of magnetic minerals related to mineral composition. For example, magnetite has a T_c of 580℃, and hematite has a T_c of 675℃. T_c is measured by heating the sample, and this heating can sometimes alter magnetic minerals,

making interpretation difficult. In the present study, T_c was measured by heating and cooling the sample to 700°C while measuring susceptibility.

The Curie temperature was measured for five specimens subsampled from microbialites collected from Site 1, 2, 3, and 4, Antelope Island, GSL (GSL18_0101_00, 01, GSL18_0202_02, GSL18_0301_A02, GSL18_0402); two specimens subsampled from microbialite collected from Site 1 and 2, LB (LB19_0103, LB19_0201); four specimens subsampled from dense Eocene microbialites collected from Green River formation (GR18_0101A70, 71, 76, 81); and five specimens subsampled from lithified Cambrian stromatolite collected from Bayan Gol Formation (BG14_0101_A08, A24, A34, A40, A70). All samples were powdered and dried before prior to measurement.

Since the bulk magnetic susceptibility of microbialites is relatively low, the magnetic susceptibility of the empty furnace assembly (plastic, ceramic, and water – all diamagnetic) can affect the total bulk susceptibility. It was therefore necessary to subtract the signature of the empty furnace. A linear interpolation was used to resample furnace data at each measurement point. The empty furnace results were subtracted from actual raw measurements, and the Curie temperature may be estimated from a minimum in the first derivative. The first derivative of the heating and cooling curve can be calculated with different degrees of smoothing, and here a moving average is used with different window sizes.

5.2.6. Hysteresis Loops and Day Plot

Measuring magnetization (M) in the presence of a changing applied field (H) provides important information on magnetic mineralogy and domain state. Because ferromagnetic materials have magnetic remanence (magnetic “memory”), the M(H) function is typically characterized by

hysteresis (e.g., Fig. 1.1C). Hysteresis loop data are often summarized by extracting several useful parameters. Saturation magnetization (M_s) is the maximum magnetization achieved in a high field. If the measurement field is strong enough, the hysteresis loop will plateau at high fields, and this value is M_s (Figure 5.2). A saturation remanant magnetization (M_r) is the remanant magnetization in the absence of a field, following saturation. M_r can be obtained by finding the intercept between the loop and vertical axis. Coercivity (H_c) is measured in the presence of a field and is found from the hysteresis loop where M=0 (Figure 5.2. left). Coercivity of remanence (H_{cr}) is measured in zero field and is not taken from the hysteresis loop; instead it is found from the backfield remanence curve where M=0 (Figure 5.2. right).

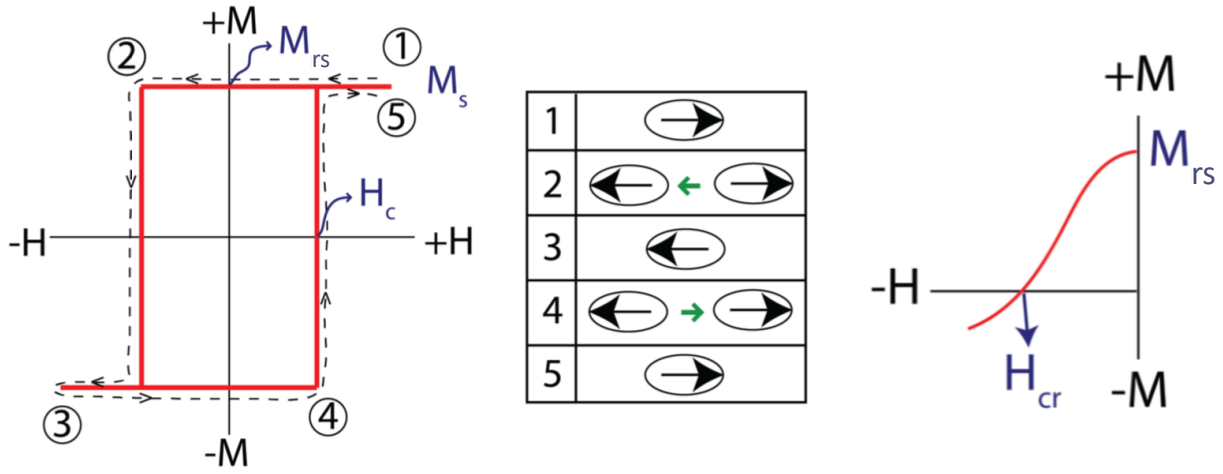

Figure 5.2 (left) Illustration of a hysteresis loop for a single, uniaxial, single-domain crystal where applied field is parallel to the direction of grain elongation. Characteristic parameters are shown: saturation remanant magnetization (M_{rs}), saturation magnetization (M_s), coercivity (H_c). (middle) Illustration of the change of SD magnetic direction as a function of magnetic field. (right) Backfield remanence curves, showing coercivity of remanence (H_{cr}). Note that loops for an assemblage of randomly oriented SD crystals will be similar to Fig. 1.1.C. (Figure courtesy of J. Bowles.)

The shape of the hysteresis loop is related to domain state. The square loop shown in Figure 5.2 is the special case for a single, uniaxial, SD grain where the field is applied parallel to the grain's long axis. The more typical case of an assemblage of many, randomly oriented, SD grains is shown in (Figure 1.1.C). As grain size increases from SD to PSD to MD, loops typically become

more closed, the ratio of M_r/M_s decreases, and H_c and H_{cr} decrease. SP grains exhibit closed loops very similar to MD grains. A mixture of two different domain states or coercivities results in a loop that is 'wasp-waisted' or constricted in the middle.

Before this information can be extracted from the ferromagnetic loop, one or more corrections are typically applied. As induced magnetization may contain contributions from paramagnetic and diamagnetic materials, a correction is applied to approximate and remove these contributions from the hysteresis loop. First, assuming that a ferromagnetic material is saturated in high fields, any linear variations in M(H) at high fields are interpreted to be generated by diamagnetic (negative gradient) and paramagnetic (positive gradient) minerals. Typically, a linear fit to data at fields > 70% of the maximum applied field is subtracted from the bulk measurements to isolate the ferromagnetic signal. If the ferromagnetic component is not saturated at the measured fields, a more complicated approach to saturation fit can be used (Jackson and Solheid, 2010).

The ideal hysteresis loop should display perfect inversion symmetry, which allows for the assessment of experimental error because the upper and lower branches of the loop can be treated as replicates. Deviations from symmetry can be due to noise, drift, and instrumental problems. Figures in Section 5.3.6 show the ferromagnetic loops, as well as two additional derived parameters which can be used to assess noise and error. 'M_{rh}' is is defined as:

$$M_{rh} = \frac{M^{+}(H) + M^{-}(H)}{2}$$

where $M^{+}(H)$ and $M^{-}(H)$ are the upper and lower branches of the hysteresis loop. With some rare exceptions (i.e., inhomogeneous interacting materials), the M_{rh} curve has even symmetry. The error curve, err(H), can be used to assess drift and noise and is calculated as:

$$\mathrm{err}(H) = M^{+}(H) - M^{-}_{inv}(H)$$

where M_{inv}^{-} is the inverted lower branch of the hysteresis loop. Because the two branches should have inversion symmetry, err(H) ≈ 0 for a loop with no noise or drift problems.

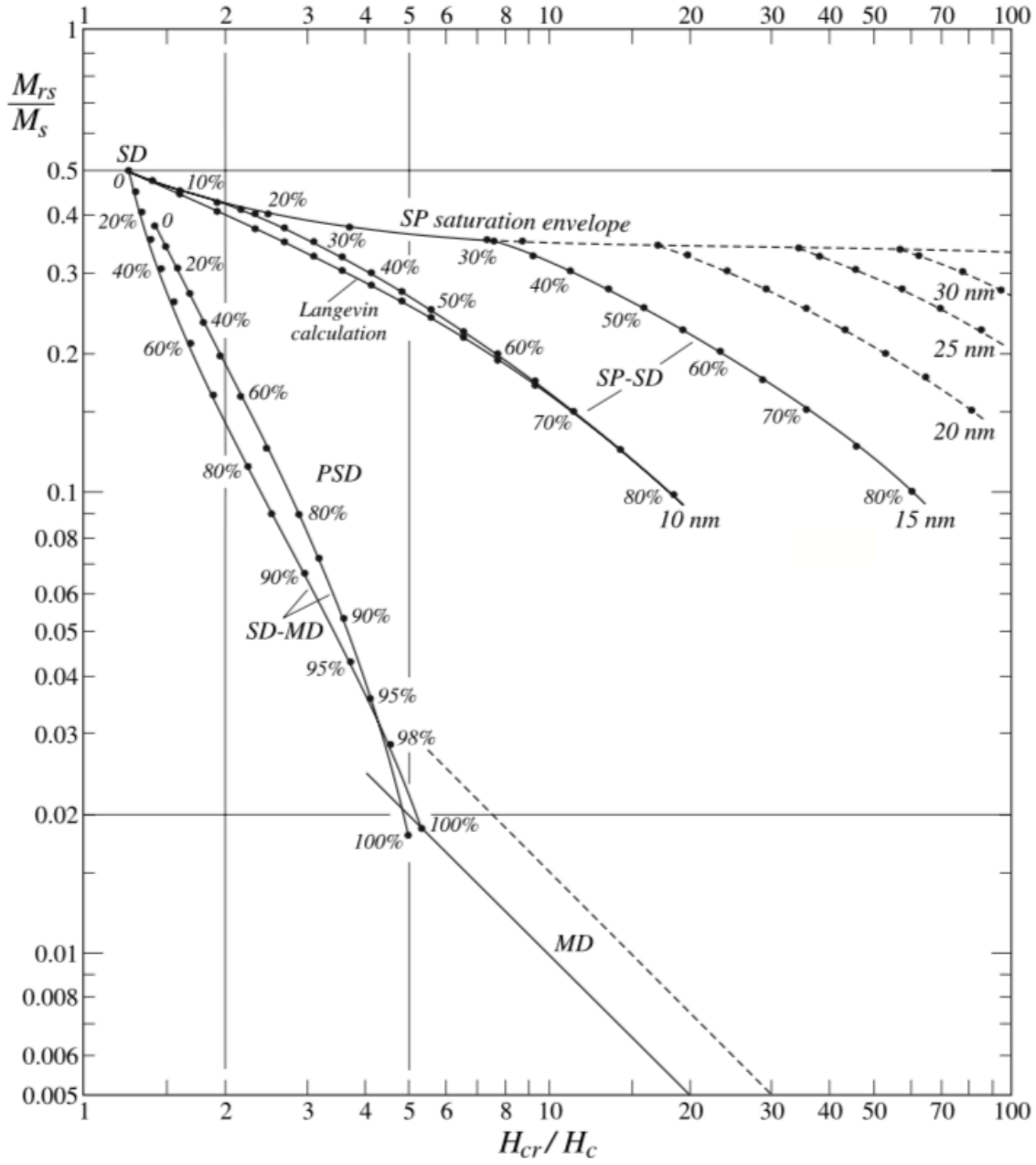

Figure 5.3. Theoretical Day plot representing SD, PSD, SP, and MD limits and mixing curves calculated for magnetite (From Dunlop et al., 2002).

Hysteresis data are often summarized on the Day plot (Day et al., 1977), a graph of M_{rs}/M_s as a function of H_{cr}/H_c (Figure 5.3). Although there can be a lot of ambiguity in interpreting the Day plot, it is useful in examining variations in the domain state and grain size of samples. For magnetite, SD grains plot in the upper left with M_{rs}/M_s near 0.5, and MD specimens plot in the lower right with M_{rs}/M_s below 0.02. PSD specimens fall in between, but specimens with a mixture SD and MD also fall in the "PSD" region (Figure 5.3). A specimen which is a mixture of SD and SP magnetite will typically fall to the right of the SP-MD mixing line.

Magnetic hysteresis loops, M(H), were collected with a maximum applied field, field increment, measurement averaging time of 1 T, 10 mT, and 500 ms. After each loop, a backfield remanence curve was acquired with an initial field, final field, and total number of points of 100 μT, 1T, and 120. Measurements were made on three living Great Salt Lake microbialites (GSL18_0101_00, GSL18_0101_01, GSL18_0202_02) and two GSL18 lithified microbialites (GSL18_0301_A01, GSL18_0301_A02); three drilled core microbialite specimens from Laguna Bacalar (LB19_0301_A, LB19_0301_B, LB19_0302_D); three Green River Formation microbialite specimens (GR18_0101_A70, GR18_0101_A76, GR18_0101_081); and four Bayam Gol stromatolite specimens (BG14_0101_A03, BG14_0101_A10, BG14_0101_A22, BG14_0101_A34).

Hysteresis loops and backfield remanence data were processed and parameters calculated in the IRM database using the methodology of Jackson & Solheid (2010). Ferromagnetic hysteresis loops are displayed (blue loops) with associated Mrh (green) and err(H) (brown) curves plotted by IRM database software. The hysteresis parameters are presented in a standard Day plot (Day et al., 1977; Dunlop, 2002).

5.2.7. First-Order Reversal Curves (FORC)

A standard hysteresis loop provides useful information on the average, or bulk, domain-state properties of a sample, including bulk coercivity. For more detailed information on the complete coercivity distribution and magnetic interaction, first order reversal curves (FORC) may be measured. The measurement protocol for a single FORC involves 1) saturating the sample in a strong field (e.g., 1 T), 2) decreasing the field to the reversal point, H_a, then 3) measuring M as a function of increasing field, H_b. This process is repeated for decreasing values of H_a until a set of FORCs is assembled. The FORC distribution is then calculated as the mixed second derivative (Pike et al., 1999)

$$\rho(H_a, H_b) = \left(\frac{\delta^2 M(H_a, H_b)}{\delta H_a, \delta H_b}\right)$$

A FORC density distribution $\rho(H_a, H_b)$ is typically plotted using a coordinate system rotated by 45° counterclockwise. The x-axis is then coercivity (H_c) and the y-axis is bias field (H_u), and is a measure of magnetic interactions. This coordinate system is defined as:

$$H_c = \frac{H_a - H_b}{2}, \qquad H_u = \frac{H_a + H_b}{2}$$

The results can provide for a more sophisticated analysis of the domain state(s) present in a sample. If the particles are SD, a distribution with a narrow positive ridge along the horizontal axis can be identified. The presence of magnetosome chains (i.e., SD magnetite) produced by MTB has been inferred by an exceptionally narrow central horizontal ridge (Heslop et al., 2014). When a density distribution is clustered near the origin of the $H_c = 0$ and $H_u = 0$, the domain state might be interpreted as PSD grains. MD signatures are characterized as a vertical ridge along H_u.

The FORC analyses were conducted on one living GSL18 microbialite specimen (GSL18_0101_00) and one LB19 drilled core microbialite specimen (LB19_0302_D); two GR

microbialite specimens (GR18_0101_A70, GR18_0101_081); and four BG stromatolite specimens (BG14_0101_A03, BG14_0101_A10, BG14_0101_A22, BG14_0101_A34). FORCs were collected with a saturating field of 1 T, field increment of 5.19 mT, and the number of FORCs of 100. For two specimens (BG14_0101_A03 and A34), the FORC measurements were repeated four times, and the results were stacked in an effort to increase the signal:noise ratio. The FORCs were processed and plotted with FORCinel (Harrison & Feinberg, 2008), which uses a locally weighted regression smoothing. Prior to processing, first and last points of each FORC were replaced to deal with an instrumental artifact. Smoothing factors of 4, 7, 3, and 7 were applied to the vertical ridge (S_c0), horizontal smooth (S_c1), Central ridge (S_b0), and vertical smooth (S_b1), respectively.

5.3. Results

5.3.1. S-ratio

GSL18: The S-ratio range was 0.92 to 1.06 and the average was 0.95. Since the S-ratio cannot be more than 1, this shows a possible error range of ~ ±0.06. Thus, the values just under 1 indicate a dominance of lower coercivity contributions, and there may or may not also be a small contribution from higher coercivity minerals (see also Section 4.6.).

Table 5.2. 1000 mT IRM, 300 mT IRM, and S-ratios for GSL18_0301(hand sample collected from Antelope Island Site 3, GSL). Units of acquired IRM are Am^2/kg, and S-ratio values are calculated based on Thomspon and Oldfield (1986).

Specimen ID	1000mT (Am^2/kg)	300mT (Am^2/kg)	S-ratio	Specimen ID	1000mT (Am^2/kg)	300mT (Am^2/kg)	S-ratio
GSL18_0301A_01	-5.95E-05	5.69E-05	0.96	**GSL18_0301B_02**	-2.95E-04	2.81E-04	0.95
GSL18_0301A_02	-3.82E-05	3.60E-05	0.94	**GSL18_0301B_03**	-1.45E-04	1.40E-04	0.97
GSL18_0301A_03	-7.40E-05	7.84E-05	1.06	**GSL18_0301B_04**	-6.71E-05	6.26E-05	0.93
GSL18_0301A_04	-4.72E-05	4.75E-05	1.01	**GSL18_0301B_05**	-1.01E-04	9.63E-05	0.95
GSL18_0301A_05	-6.58E-05	6.12E-05	0.93	**GSL18_0301B_06**	-1.21E-04	1.16E-04	0.96
GSL18_0301A_06	-6.42E-05	5.92E-05	0.92	**GSL18_0301B_07**	-5.64E-05	5.49E-05	0.97
GSL18_0301A_07	-4.68E-05	4.43E-05	0.95	**GSL18_0301B_08**	-7.78E-05	7.38E-05	0.95
GSL18_0301A_08	-5.28E-05	5.12E-05	0.97	**GSL18_0301B_09**	-1.02E-04	9.70E-05	0.96
GSL18_0301A_09	-5.59E-05	5.18E-05	0.93	**GSL18_0301B_10**	-1.27E-04	1.19E-04	0.94
GSL18_0301B_01	-1.22E-04	1.14E-04	0.93	**Mean**	-9.05E-05	8.64E-05	0.95

LB19: The S-ratio range was 0.99 to 1.05, and the mean S-ratio value was 1.02. Assuming a possible error range of ~ ±0.05, results indicate that there is no high coercivity contribution in LB samples.

Table 5.3. 1000mT IRM, 300mT IRM, and S-ratios for LB19_0301 (drilled core sample collected from Site 3-the Rapids, LB). Units of acquired IRM are Am^2/kg, and S-ratio values are calculated based on Thomspon and Oldfield (1986).

Specimen ID	1000mT (Am^2/kg)	300mT (Am^2/kg)	S-ratio	Specimen ID	1000mT (Am^2/kg)	300mT (Am^2/kg)	S-ratio
LB19_0301_A	-1.38E-05	1.43E-05	1.03	**LB19_0301_D**	-8.60E-06	8.87E-06	1.03
LB19_0301_B	-1.50E-05	1.51E-05	1.00	**LB19_0301_E**	-1.07E-05	1.13E-05	1.05
LB19_0301_C	-8.37E-06	8.30E-06	0.99	**Mean**	-1.13E-05	1.16E-05	1.02

GR18: Specimens of GR are from two lamination sections that show the most variation in NRM intensities (From GR18_0101_51 to GR18_0101_85) in order to test whether the variation in NRM intensity might be explained by a chemical alteration along the lamination. With the exception of four specimens (S-ratio > 0.87), the range of S-ratios of the GR microbialite lamination was relatively constant between 0.80 to 0.84 and the average was 0.84. This homogeneous distribution implies that the NRM intensity variations did not result variations in magnetic mineralogy, such as might arise from chemical alteration. One noteworthy point is that the GR18_0101 S-ratio values suggest a significant contribution from high coercivity minerals compared to the GSL18_0301 microbialite (S-ratio of 0.95). This implies the presence of high coercivity minerals like hematite and/or goethite.

Table 5.4. 1000mT IRM, 300mT IRM, and S-ratios for GR18_0101 (Eocene Microbialite from Green River Formation). Units of acquired IRM are Am^2/kg, and S-ratio values are calculated based on Thomspon and Oldfield (1986).

Specimen ID	1000mT (Am^2/kg)	300mT (Am^2/kg)	S-ratio	Specimen ID	1000mT (Am^2/kg)	300mT (Am^2/kg)	S-ratio
GR18_0101_A51	2.82E-04	-2.50E-04	0.88	**GR18_0101_A67**	1.08E-04	-8.92E-05	0.83
GR18_0101_A52	1.38E-04	-1.15E-04	0.83	**GR18_0101_A68**	1.40E-04	-1.18E-04	0.84
GR18_0101_A53	1.24E-04	-1.03E-04	0.83	**GR18_0101_A70**	9.43E-05	-8.91E-05	0.94
GR18_0101_A54	1.06E-04	-8.79E-05	0.83	**GR18_0101_A71**	7.37E-05	-6.71E-05	0.91
GR18_0101_A55	1.06E-04	-8.88E-05	0.84	**GR18_0101_A72**	1.12E-04	-9.07E-05	0.81
GR18_0101_A56	1.22E-04	-1.02E-04	0.84	**GR18_0101_A73**	1.03E-04	-8.29E-05	0.80
GR18_0101_A57	1.12E-04	-9.32E-05	0.84	**GR18_0101_A74**	1.14E-04	-9.09E-05	0.80
GR18_0101_A58	1.00E-04	-8.22E-05	0.82	**GR18_0101_A75**	1.11E-04	-8.98E-05	0.81
GR18_0101_A59	1.04E-04	-8.53E-05	0.82	**GR18_0101_A76**	6.69E-05	-5.47E-05	0.82
GR18_0101_A60	1.13E-04	-9.58E-05	0.85	**GR18_0101_A77**	1.28E-04	-1.06E-04	0.82
GR18_0101_A61	1.10E-04	-9.15E-05	0.83	**GR18_0101_A80**	1.05E-04	-8.57E-05	0.82
GR18_0101_A62	1.09E-04	-9.08E-05	0.83	**GR18_0101_A81**	7.22E-05	-6.05E-05	0.84
GR18_0101_A63	9.56E-05	-7.88E-05	0.82	**GR18_0101_A82**	1.07E-04	-8.94E-05	0.83
GR18_0101_A64	1.03E-04	-9.57E-05	0.93	**GR18_0101_A83**	1.02E-04	-8.18E-05	0.80
GR18_0101_A65	1.05E-04	-8.72E-05	0.83	**GR18_0101_A84**	1.12E-04	-9.32E-05	0.83
GR18_0101_A66	1.04E-04	-8.54E-05	0.82	**GR18_0101_A85**	1.05E-04	-8.53E-05	0.82

BG14: Unlike the GSL, LB, and GR samples, the BG stromatolite shows a large range in S-ratio from 0.42 to 0.95. Low coercivity (high S-ratio) minerals are located on the bottom of the

sample and high coercivity (low S-ratio) minerals are more concentrated on the top part on the stromatolite except two points the left top (Figure 5.4). However, the mineralogy distribution based on variations in S-ratio do not follow laminations.

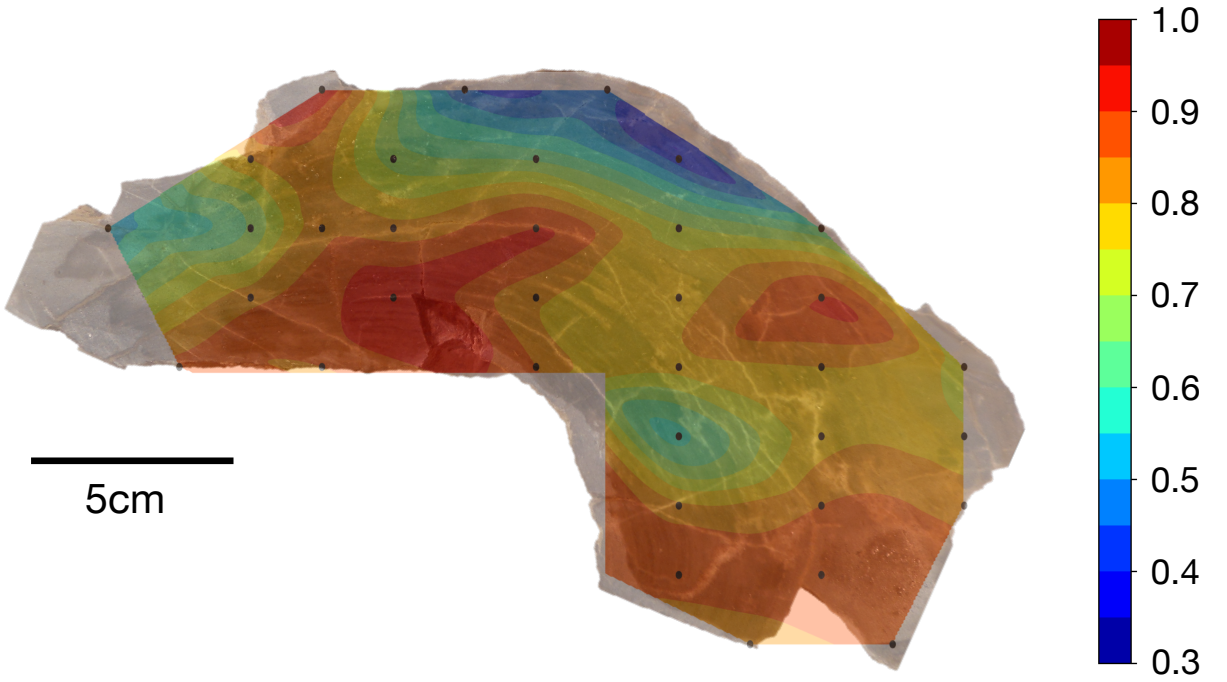

Figure 5.4. The mapping of S-ratio of BG14_0101 stromatolite slice A based on 35 specimens. Black dots are measurement positions. Reddish colors imply higher S-ratio, indicating lower coercivity magnetic compositions in their mineralogy.

Table 5.5. 1000mT IRM, 300mT IRM, and S-ratios for BG14_0101 (Cambrian stromatolite from Bayan Gol formation, Mongolia). Units of acquired IRM are Am^2/kg, and S-ratio values are calculated based on Thomspon and Oldfield (1986).

Specimen ID	1000mT (Am^2/kg)	300mT (Am^2/kg)	S-ratio	Specimen ID	1000mT (Am^2/kg)	300mT (Am^2/kg)	S-ratio
BG14_0101_A01	2.27E-05	-2.16E-05	0.95	**BG14_0101_A40**	1.21E-05	-1.09E-05	0.90
BG14_0101_A03	3.89E-05	-1.80E-05	0.46	**BG14_0101_A44**	3.77E-05	-3.26E-05	0.87
BG14_0101_A05	4.35E-05	-2.00E-05	0.46	**BG14_0101_A46**	6.09E-05	-5.18E-05	0.85
BG14_0101_A08	1.10E-05	-8.72E-06	0.80	**BG14_0101_A48**	3.42E-05	-2.90E-05	0.85
BG14_0101_A10	2.07E-05	-1.42E-05	0.68	**BG14_0101_A50**	2.34E-05	-1.80E-05	0.77
BG14_0101_A12	2.22E-05	-1.42E-05	0.64	**BG14_0101_A52**	2.68E-05	-2.14E-05	0.80
BG14_0101_A14	3.83E-05	-1.62E-05	0.42	**BG14_0101_A54**	6.69E-05	-4.79E-05	0.72
BG14_0101_A18	7.84E-05	-4.02E-05	0.51	**BG14_0101_A56**	2.05E-05	-1.20E-05	0.59
BG14_0101_A20	2.62E-05	-1.72E-05	0.66	**BG14_0101_A58**	2.21E-05	-1.72E-05	0.78
BG14_0101_A21	2.40E-05	-1.98E-05	0.83	**BG14_0101_A60**	3.60E-05	-2.73E-05	0.76
BG14_0101_A22	1.82E-05	-1.49E-05	0.82	**BG14_0101_A62**	1.83E-05	-1.48E-05	0.81
BG14_0101_A24	8.71E-06	-7.81E-06	0.90	**BG14_0101_A64**	2.35E-05	-2.00E-05	0.85

BG14_0101_A26	2.39E-05	-1.70E-05	0.71	**BG14_0101_A66**	3.95E-05	-3.27E-05	0.83
BG14_0101_A28	1.24E-05	-7.47E-06	0.60	**BG14_0101_A68**	2.18E-05	-1.89E-05	0.87
BG14_0101_A32	2.28E-05	-1.90E-05	0.83	**BG14_0101_A70**	1.74E-05	-1.55E-05	0.89
BG14_0101_A34	1.10E-05	-1.04E-05	0.94	**BG14_0101_A74**	2.48E-05	-2.02E-05	0.81
BG14_0101_A36	1.86E-05	-1.50E-05	0.81	**BG14_0101_A76**	2.84E-05	-2.47E-05	0.87
BG14_0101_A38	2.08E-05	-1.61E-05	0.78	**Mean**	2.79E-05	-2.04E-05	0.76

5.3.2. IRM Unmixing

GSL18: At least two magnetic components are required to fit the data for all GSL18 specimens. Results from living microbialite specimens GSL18_0101_00 and from Site 1 and lithified microbialite specimen GSL18_0301_A02 are shown in Figure 5.5 For specimens where IRM is acquired after full demagnetization (IRM_{0mT}), the dominant magnetic component mean coercivity is ~48 mT with a DP of ~2.3 (Table 5.6). The mean coercivity of specimens where IRM is acquired starting at -1000 mT ($IRM_{-1000mT}$) is ~40.5 mT, about 7-11 mT lower than the other ones, but with a similar dispersion value. A smaller, high-coercivity fraction is harder to fit, but the GSL living and fossilized microbialite samples have at least small amount of high coercivity materials. The mean coercivity of this secondary component for IRM_{0mT} specimens was ~ 300 mT, and for $IRM_{-1000mT}$ specimens it was ~100 mT. All $IRM_{-1000mT}$ specimens also contain a third low coercivity component less than 11 mT. However, it might be experimental error because similar components were not shown in the same IRM_{0mT} specimens. Additional IRM unmixing curves of GSL18 specimens are included in Appendix C (Figure C.1).

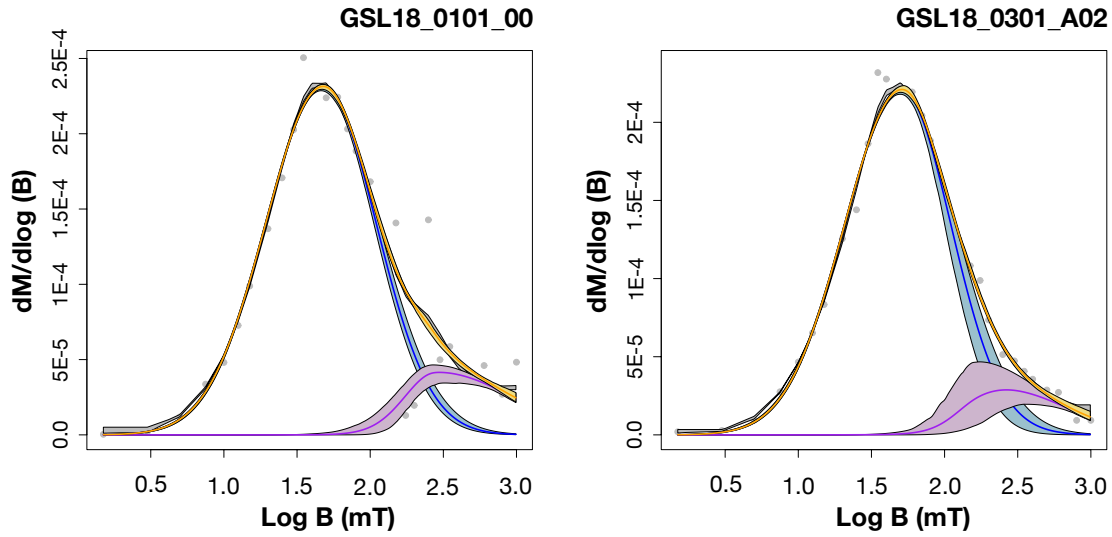

Figure 5.5. IRM unmixing curves of GSL18_0101_00 and GSL18_0301_A02 specimens plotted through the MaxUnmix online software (Maxbauer et al., 2016) in a log scale. Gray dots represent actual data, and yellow lines represents total IRM best-fit based on real data. Colored lines (blue and purple) represent different coercivity components. The shadings represent 95% confidence intervals calculated using a resampling algorithm with N = 300

Table 5.6. IRM unmixing statistics of GSL specimens. MC: Mean Coercivity (mT); MC.sd: Mean coercivity standard deviation (mT); DP: dispersion (mT); DP.sd: dispersion standard deviation (mT); P: relative proportion; P.sd: relative proportion standard deviation; S: skewness; S.sd: standard deviation of skewness. Note that '*' means specimens subjected to -1000mT before the stepwise IRM acquisition.

Component 1	MC	MC.sd	DP	DP.sd	P	P.sd	S	S.sd
GSL18_0101_00	45.21	1.01	2.39	1.01	0.99	0.01	0.96	0.02
GSL18_0101_01	42.92	1.02	2.2	1.01	0.97	0.01	0.89	0.03
GSL18_0301_A01	56.74	1.03	2.3	1.02	0.83	0.06	1.04	0.03
GSL18_0301_A02	46.23	1.04	2.33	1.02	0.98	0.01	0.93	0.04
GSL18_0301_A01*	46.94	1.06	2.01	1.04	0.90	0.05	1.23	0.08
GSL18_0301_A02*	37.89	1.04	2.16	1.02	0.76	0.04	0.98	0.03
GSL18_0301_B01*	38.38	1.04	2.07	1.03	0.98	0.01	1.05	0.04
GSL18_0301_B03*	37.37	1.04	2.07	1.03	0.96	0.02	1.04	0.04

Component 2	MC	MC.sd	DP	DP.sd	P	P.sd	S	S.sd
GSL18_0101_00	502.78	1.17	2.45	1.1	0.18	0.01	1.57	0.22
GSL18_0101_01	389.84	1.21	2.51	1.14	0.18	0.02	1.66	0.33
GSL18_0301_A01	65.76	1.15	4.98	1.23	0.17	0.06	1.07	0.18
GSL18_0301_A02	363.19	1.21	2.21	1.08	0.13	0.03	1.4	0.24
GSL18_0301_A01*	161.48	1.63	5.36	1.87	0.11	0.02	1.12	0.24
GSL18_0301_A02*	128.05	1.12	3.08	1.09	0.24	0.03	1.10	0.09
GSL18_0301_B01*	189.34	1.12	1.98	1.03	0.17	0.04	1.32	0.09
GSL18_0301_B03*	176.05	1.10	2.05	1.03	0.19	0.03	1.35	0.09

Component 3	MC	MC.sd	DP	DP.sd	P	P.sd	S	S.sd
GSL18_0101_00	n.a.	n.a.	n.a.	n.a.	n.a.	n.a.	n.a.	n.a.
GSL18_0101_01	n.a.	n.a.	n.a.	n.a.	n.a.	n.a.	n.a.	n.a.
GSL18_0301_A01	n.a.	n.a.	n.a.	n.a.	n.a.	n.a.	n.a.	n.a.
GSL18_0301_A02	n.a.	n.a.	n.a.	n.a.	n.a.	n.a.	n.a.	n.a.
GSL18_0301_A01*	10.26	1.17	1.68	1.14	0.32	0.05	0.85	0.18
GSL18_0301_A02*	8.40	1.16	3.18	1.11	0.20	0.02	0.91	0.06
GSL18_0301_B01*	5.39	1.19	2.35	1.14	0.14	0.02	0.57	0.08
GSL18_0301_B03*	7.65	1.13	2.09	1.07	0.19	0.03	0.76	0.08

GSL19: All IRM$_{-1000mT}$ GSL19 specimens possess at least three components, with a dominant mean coercivity of 35 mT and dispersion of 2.24. The mean coercivity of additional low coercivity and high coercivity components were 7.4 mT (dispersion:7.5) and 280 mT (dispersion 2.7). Specimens that have high NRM intensity (e.g. GSL19_0202_03, 04, 05) have a high relative proportion of the dominant coercivity component (>0.9), but weakly magnetized specimens (e.g. GSL19_0202_10,11,12) have a relatively low proportion (Table 5.7). This might indicate that the dominant component (blue shading lines in Figure 5.6) carries the NRM in the microbialites.

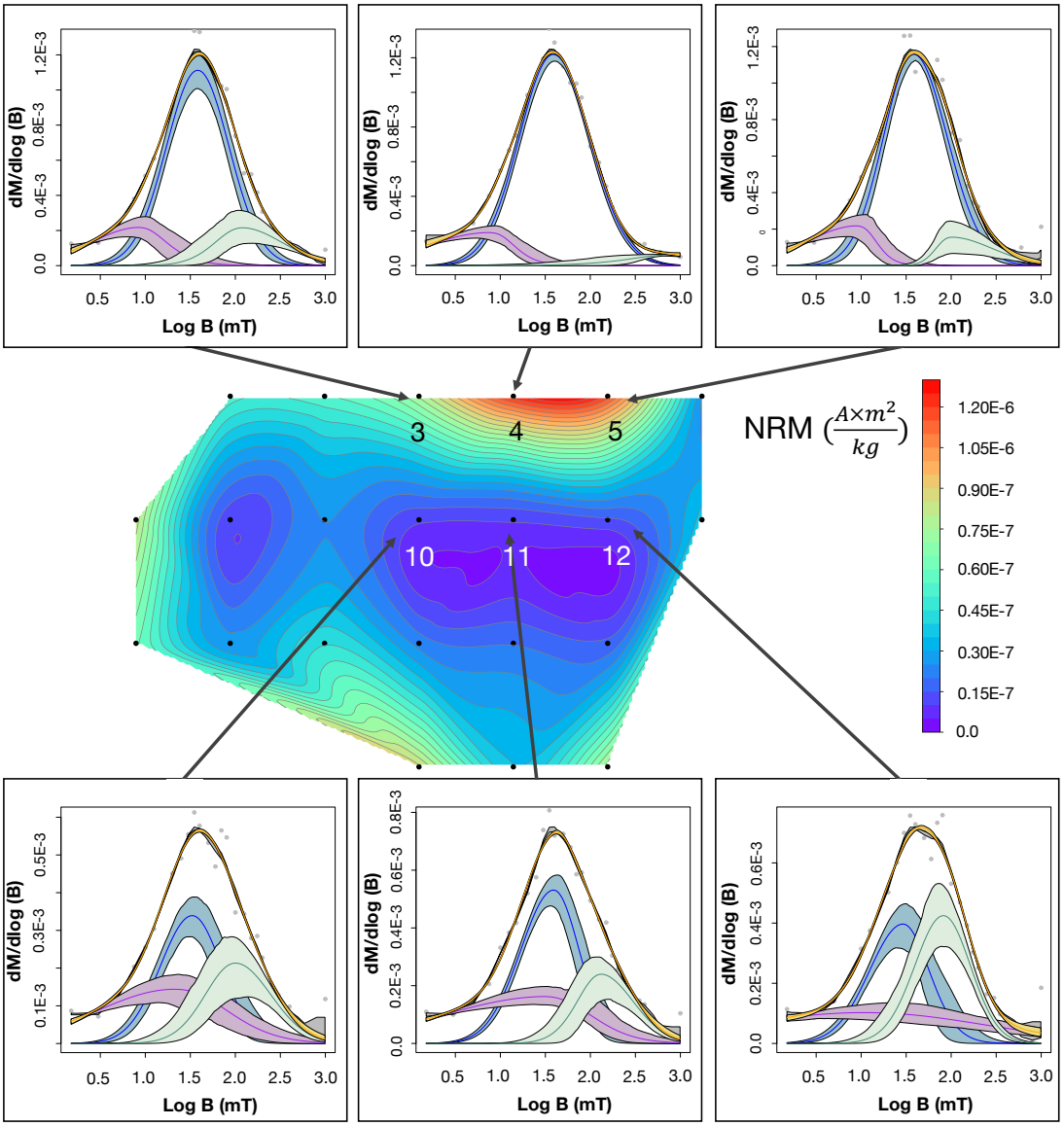

Figure 5.6. IRM unmixing curves of GSL19_0202 specimens plotted using MaxUnmix online software (Maxbauer et al., 2016) on a log scale. Gray dots represent actual data, and gray lines are smoothed data. Colored lines (blue, purple, green) represent different coercivity components and yellow lines are the sum of these (total best fit). The shadings represent 95% confidence intervals calculated using a resampling algorithm with N = 300.

Table 5.7. IRM unmixing statistics of GSL19_0202 specimens MC: Mean Coercivity (mT); MC.sd: Mean coercivity standard deviation (mT); DP: dispersion (mT); DP.sd: dispersion standard deviation (mT); P: relative proportion; P.sd: relative proportion standard deviation; S: skewness; S.sd: standard deviation of skewness. Note that '*' means specimens subjected to -1000mT before the stepwise IRM acquisition.

Component 1	MC	MC.sd	DP	DP.sd	P	P.sd	S	S.sd
GSL19_0202_A03*	38.19	1.04	2.24	1.04	0.91	0.04	1.00	0.04
GSL19_0202_A04*	40.56	1.03	2.46	1.02	0.98	0.01	1.03	0.03
GSL19_0202_A05*	41.18	1.04	2.27	1.03	0.98	0.01	1.06	0.05

GSL19_0202_A10*	31.58	1.10	2.19	1.05	0.59	0.05	0.96	0.05
GSL19_0202_A11*	33.50	1.07	2.12	1.03	0.71	0.04	0.87	0.04
GSL19_0202_A12*	25.26	1.10	2.17	1.06	0.55	0.05	0.88	0.06

Component 2	MC	MC.sd	DP	DP.sd	P	P.sd	S	S.sd
GSL19_0202_A03*	5.56	1.24	2.76	1.12	0.18	0.02	0.74	0.10
GSL19_0202_A04*	3.31	1.26	3.36	1.15	0.15	0.02	0.60	0.09
GSL19_0202_A05*	4.51	1.20	2.60	1.09	0.19	0.03	0.57	0.08
GSL19_0202_A10*	12.22	1.21	5.36	1.17	0.25	0.03	0.80	0.10
GSL19_0202_A11*	9.12	1.23	7.37	1.22	0.22	0.02	0.63	0.07
GSL19_0202_A12*	9.78	1.52	23.34	1.60	0.15	0.02	1.02	0.14

Component 3	MC	MC.sd	DP	DP.sd	P	P.sd	S	S.sd
GSL19_0202_A03*	158.73	1.17	2.44	1.12	0.18	0.04	1.27	0.12
GSL19_0202_A04*	999.44	1.33	3.73	1.45	0.05	0.00	1.18	0.17
GSL19_0202_A05*	175.46	1.14	2.17	1.09	0.13	0.04	1.71	0.16
GSL19_0202_A10*	112.52	1.12	2.32	1.07	0.38	0.07	1.09	0.08
GSL19_0202_A11*	156.78	1.14	2.06	1.06	0.33	0.05	1.19	0.11
GSL19_0202_A12*	79.05	1.07	2.05	1.05	0.59	0.07	0.97	0.05

LB19: All LB19 microbialites specimens including both IRM_{0mT} and $IRM_{-1000mT}$ specimens displayed no more than three components, and the mean coercivity of the dominant component was 30-50 mT with a dispersion of 2.1-2.6. Results show that living and lithified microbialite samples have no major differences in terms of component numbers, major mean coercivity, or dispersion (Table 5.8). However, the IRM unmixing data of living microbialites are more noisy than lithified ones (Figure 5.7. gray dots). Apart from the 30-50 mT dominant component, a smaller secondary component has high coercivity (>120 mT) for all living, unlithified microbialites with cyanobacteria layers (LB19_0102 and LB19_0304) and (when present) has low coercivity (<32mT) for lithified microbialites (LB19_0301). This high coercivity component found in the cyanobacteria layer might indicate the single domain magnetite generated by biomagnetism. Additional IRM unmixing curves of LB19 specimens are included in Appendix C (Figure C.2).

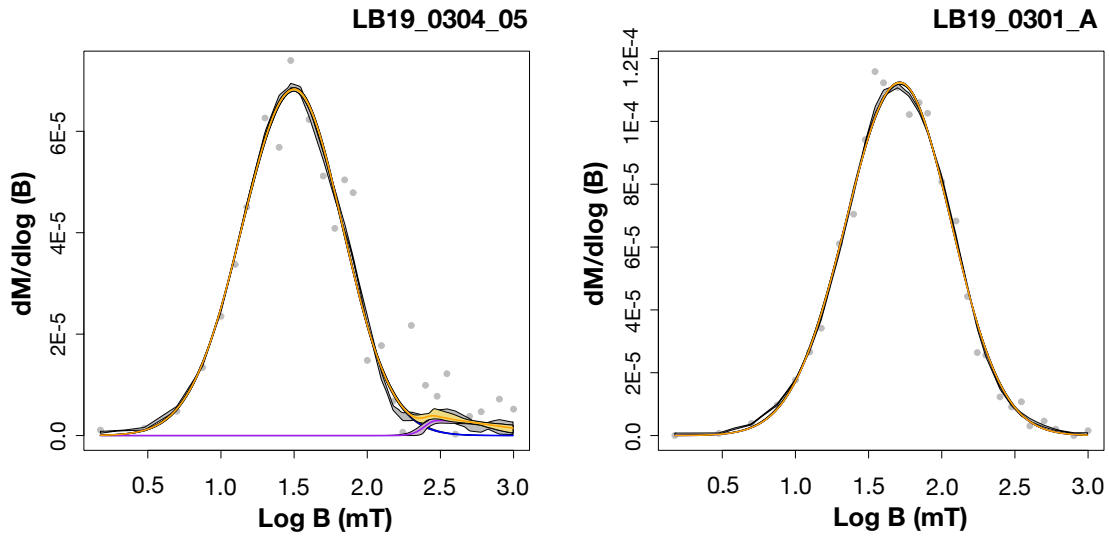

Figure 5.7. IRM unmixing curve of LB19 specimens plotted through the MaxUnmix online software (Maxbauer et al., 2016) in a log scale: (left) LB19_0304_05 (living unlithified microbialite with cyanobacteria layer); and (right) LB19_0301_A (lithified porous microbialite). Gray dots represent actual data, and yellow lines represents total IRM best-fit based on real data. Colored lines (blue and purple) represents different coercivity components. The shadings represent 95% confidence intervals calculated using a resampling algorithm with N = 300.

Table 5.8. IRM unmixing statistics of LB specimens. MC: Mean Coercivity (mT); MC.sd: Mean coercivity standard deviation (mT); DP: dispersion (mT); DP.sd: dispersion standard deviation (mT); P: relative proportion; P.sd: relative proportion standard deviation; S: skewness; S.sd: standard deviation of skewness. Note that '*' means specimens subjected to -1000mT before the stepwise IRM acquisition.

Component 1	MC	MC.sd	DP	DP.sd	P	P.sd	S	S.sd
LB19_0102_03	47.58	1.01	2.21	1.01	0.94	0.01	1.03	0.02
LB19_0301_A	49.94	1.00	2.29	1.00	1.01	0.00	0.97	0.00
LB19_0301_B	31.71	1.02	2.56	1.02	0.92	0.03	0.82	0.02
LB19_0301_A*	32.96	1.06	2.35	1.04	0.84	0.04	0.81	0.04
LB19_0301_B*	38.84	1.05	2.31	1.02	0.94	0.04	1.02	0.06
LB19_0301_C*	34.10	1.05	2.21	1.02	0.85	0.06	0.95	0.04
LB19_0301_D*	34.11	1.08	2.11	1.04	0.78	0.06	0.94	0.07
LB19_0301_E*	38.27	1.05	2.15	1.03	0.91	0.06	1.07	0.05
LB19_0304_02	44.33	1.03	2.07	1.01	0.87	0.03	0.84	0.02
LB19_0304_05	30.3	1.00	2.20	1.00	0.99	0.00	0.97	0.01

Component 2	MC	MC.sd	DP	DP.sd	P	P.sd	S	S.sd
LB19_0102_03	128.22	1.68	5.6	1.46	0.07	0.01	0.32	0.16
LB19_0301_A	n.a.	n.a.	n.a.	n.a.	n.a.	n.a.	n.a.	n.a.
LB19_0301_B	2.26	3.64	11.24	1.86	0.11	0.01	1.36	0.55
LB19_0301_A*	32.05	3.37	29.29	6.34	0.14	0.05	1.15	0.55
LB19_0301_B*	3.17	2.04	4.19	2.43	0.18	0.02	0.70	0.17
LB19_0301_C*	8.62	1.50	5.23	1.46	0.16	0.05	0.90	0.18
LB19_0301_D*	11.29	1.67	7.34	1.73	0.20	0.05	0.95	0.24
LB19_0301_E*	8.80	1.44	2.41	1.46	0.18	0.05	0.93	0.17

LB19_0304_02	224.18	1.31	8.20	1.26	0.15	0.02	1.41	0.14
LB19_0304_05	593.89	1.17	1.99	1.13	0.04	0.01	2.38	0.23

GR18: Four specimens of GR18_0101 were subjected to the IRM unmixing procedure, starting at IRM_{0mT}. All four specimens were from the same lamination, but two had high NRM (GR18_0101_A76, GR18_0101_A81) and two had low NRM (GR18_0101_A70, GR18_0101_A71) (Figure 5.8). All four specimens have a major component at ~47 mT with a mean dispersion of ~2.1 (blue shading lines in Figure 5.8) and have at least two additional high coercivity components (Table 5.9). This result suggests that the NRM differences are not from variations in magnetic mineralogy, such as might arise from chemical alteration, but could be an IRM such as from a lightning strike. The second coercivity component (purple shading lines in Figure 5.8) could be the signature of biominerals which have more SD magnetite. The highest coercivity component (green shading lines in Figure 5.8) from all four specimens could be high coercivity minerals such as hematite and/or goethite.

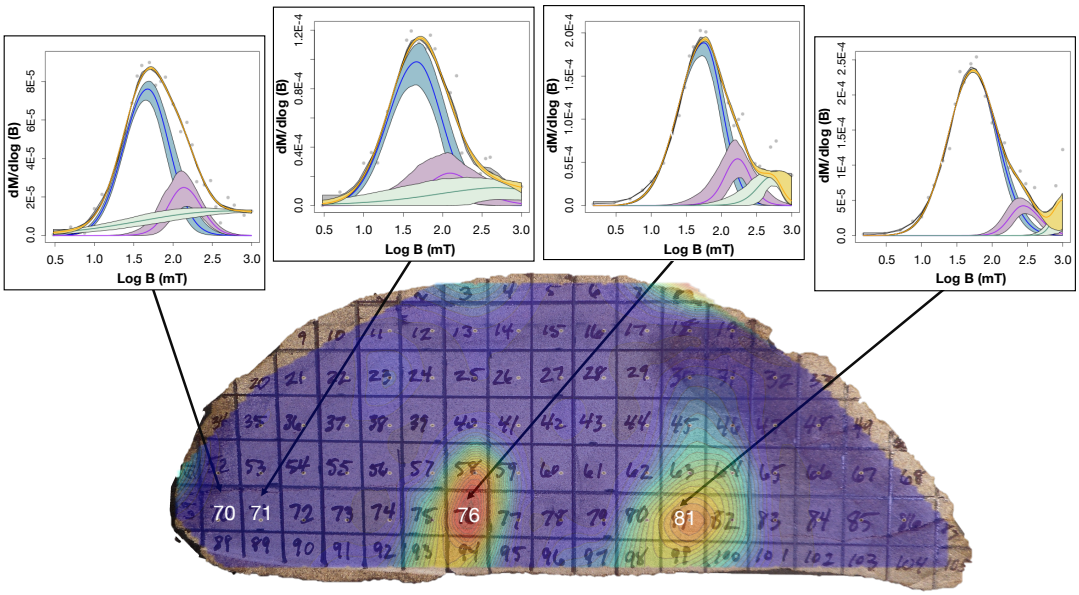

Figure 5.8. IRM unmixing curve of GR specimens plotted through the MaxUnmix online software (Maxbauer et al., 2016) in a log scale. Gray dots represent actual data, and yellow lines represents total IRM best-fit based on real data. Colored lines (blue and purple) represents different coercivity components. The shadings represent 95% confidence intervals calculated using a resampling algorithm with N = 300. The colormap image is showing NRM intensity.

Table 5.9. IRM unmixing statistics of GR specimens MC: Mean Coercivity (mT); MC.sd: Mean coercivity standard deviation (mT); DP: dispersion (mT); DP.sd: dispersion standard deviation (mT); P: relative proportion; P.sd: relative proportion standard deviation; S: skewness; S.sd: standard deviation of skewness

Component 1	MC	MC.sd	DP	DP.sd	P	P.sd	S	S.sd
GR18_0101_A70	44.93	1.04	1.96	1.03	0.87	0.03	0.95	0.04
GR18_0101_A71	43.08	1.06	2.19	1.04	0.86	0.06	0.94	0.05
GR18_0101_A76	46.58	1.04	2.06	1.02	0.97	0.03	0.84	0.04
GR18_0101_A81	52.63	1.03	2.23	1.02	0.98	0	0.98	0.03

Component 2	MC	MC.sd	DP	DP.sd	P	P.sd	S	S.sd
GR18_0101_A70	142.3	1.08	1.63	1.05	0.29	0.05	1.06	0.1
GR18_0101_A71	131.57	1.25	2.17	1.22	0.2	0.07	1.12	0.16
GR18_0101_A76	167	1.13	1.55	1.1	0.28	0.06	0.99	0.16
GR18_0101_A81	300.38	1.08	1.63	1.1	0.18	0.02	1.14	0.14

Component 3	MC	MC.sd	DP	DP.sd	P	P.sd	S	S.sd
GR18_0101_A70	619.68	1.31	13.42	1.21	0.15	0.01	1.04	0.15
GR18_0101_A71	509.94	1.56	6.59	2	0.11	0.03	1.06	0.25
GR18_0101_A76	458.47	1.13	1.52	1.13	0.28	0.02	0.85	0.16
GR18_0101_A81	1212.92	1.17	1.48	1.11	0.18	0.04	1.24	0.24

BG14: While the GSL18, GSL19, LB19, and GR18 IRM unmixing curves are all similar within each site, BG14's IRM unmixing curves show much more heterogeneity (Table 5.10). Figure 5.9 shows S-ratio variations for the whole sample slice and IRM unmixing results for 5 of these specimens. High coercivity minerals (low S-ratio) are mostly located on the top of the sample (see Section 5.3.1), and these specimens (specimen BG14_0101_A05, BG14_0101_A12) have unmixing curves with a large relative proportion of high coercivity minerals (purple shading lines in Figure 5.9) compared to specimens with high S-ratio fractions (specimen BG17_0101_A70). The combined result from the IRM unmixing and S-ratio experiments indicates that high coercivity minerals such as hematite make up a significant fraction of the magnetic mineral population, in addition to lower coercivity magnetite particles (coercivity less than 300 mT). Note that BG14_0101_A05, A12, and A38 were $IRM_{-1000mT}$ specimens, and BG14_0101_A08, A70 were IRM_{0mT} specimens.

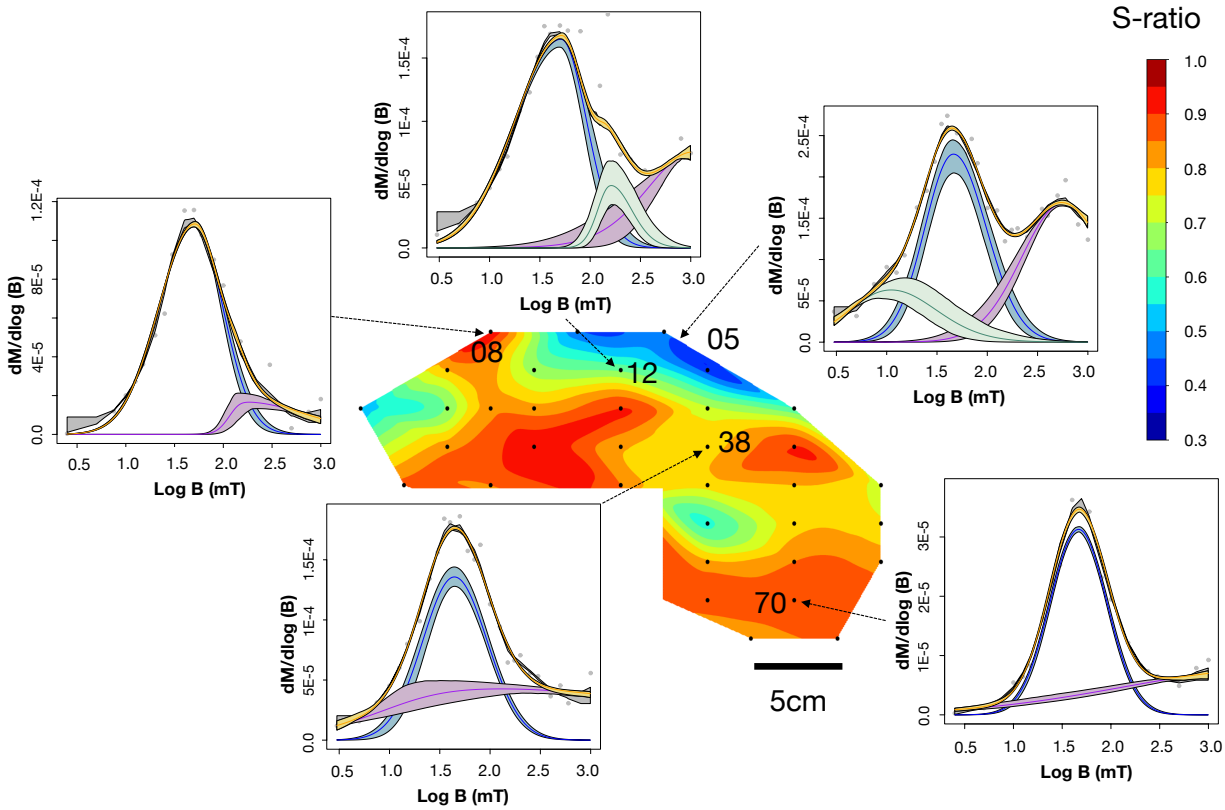

Figure 5.9. IRM unmixing curve of BG14_0101 specimens plotted through the MaxUnmix online software (Maxbauer et al., 2016) on a log scale. The background colormap is the S-ratio mapping of the stromatolite. Gray dots represent actual data, and yellow lines represents total IRM best-fit based on real data. Colored lines (blue, green, purple) represent different coercivity components. The shadings represent 95% confidence intervals calculated using a resampling algorithm with N = 300.

Table 5.10. IRM unmixing statistics of BG14_0101 specimens. MC: Mean Coercivity (mT); MC.sd: Mean coercivity standard deviation (mT); DP: dispersion (mT); DP.sd: dispersion standard deviation (mT); P: relative proportion; P.sd: relative proportion standard deviation; S: skewness; S.sd: standard deviation of skewness. Note that specimens 05, 12, and 38's IRM acquisitions are collected starting with -1000 mT, and specimens 08 and 70's IRM acquisitions are collected starting with no additional applied field.

BG14_0101_A05*	MC	MC.sd	DP	DP.sd	P	P.sd	S	S.sd
Component 1	49.87	1.05	2.03	1.02	0.87	0.04	1.07	0.04
Component 2	612.16	1.09	2.74	1.08	0.64	0.01	1.06	0.07
Component 3	12	1.17	2.72	1.1	0.25	0.02	1.06	0.1

BG14_0101_A08	MC	MC.sd	DP	DP.sd	P	P.sd	S	S.sd
Component 1	46.48	1.01	1.96	1.01	0.87	0.01	1	0.01
Component 2	980.67	1.73	14.39	1.23	0.19	0.01	0.55	0.25

BG14_0101_A12*	MC	MC.sd	DP	DP.sd	P	P.sd	S	S.sd
Component 1	35.42	1.04	2.31	1.02	0.97	0.02	0.75	0.04
Component 2	711.37	1.16	2.43	1.21	0.45	0.01	0.68	0.15

Component 3	186.36	1.07	1.49	1.04	0.29	0.05	1.29	0.13

BG14_0101_A38*	MC	MC.sd	DP	DP.sd	P	P.sd	S	S.sd
Component 1	45.13	1.03	2.1	1.02	0.77	0.03	1.02	0.03
Component 2	1108.33	1.62	48.4	1.45	0.24	0.01	1.61	0.26

BG14_0101_A70	MC	MC.sd	DP	DP.sd	P	P.sd	S	S.sd
Component 1	44.03	1.02	2.13	1.02	0.98	0.01	0.89	0.03
Component 2	433.31	1.18	2.74	1.1	0.15	0.02	2.22	0.14

5.3.3. Lowrie-Fuller test

GSL18 and 19: ARM MDF values of GSL18 and 19 specimens were lower than IRM MDF, and the intersection of the IRM acquisition and demagnetization curves provides a rough estimate for the average coercivity of ~ 15-17 mT and 18-23 mT for GSL18 (very young microbialites from Antelope Island) and GSL19 (modern microbialites from Lakeside) (Figure 5.10). This might indicate MD magnetite or maghemite. Compared with the dominant coercivity component of 47.78 mT extracted from the IRM unmixing curve, the estimated coercivity here is lower.

LB19: ARM MDF values of LB were higher than IRM MDF, suggesting single domain behavior. However, the intersection of IRM acquisition and demagnetization curves is at low coercivity values around 13-14 mT. Compared to the dominant magnetic component mean coercivity of ~48 mT from IRM unmixing curve, the coercivity value is lower.

GR18: Similar to GSL18 and 19 specimens, all four specimens of GR18 showed ARM MDF < IRM MDF, and low coercivity within the range of 18 to 22 mT. This value is still lower than major coercivity component from IRM unmixing (46.81 mT). Chang & Stolz (1989) find an intersection at approximately 40-45 mT on a GR stromatolite, and the ARM MDF was lower than IRM MDF, which they interpreted as multi-domain magnetite or maghemite as the major remanence carriers.

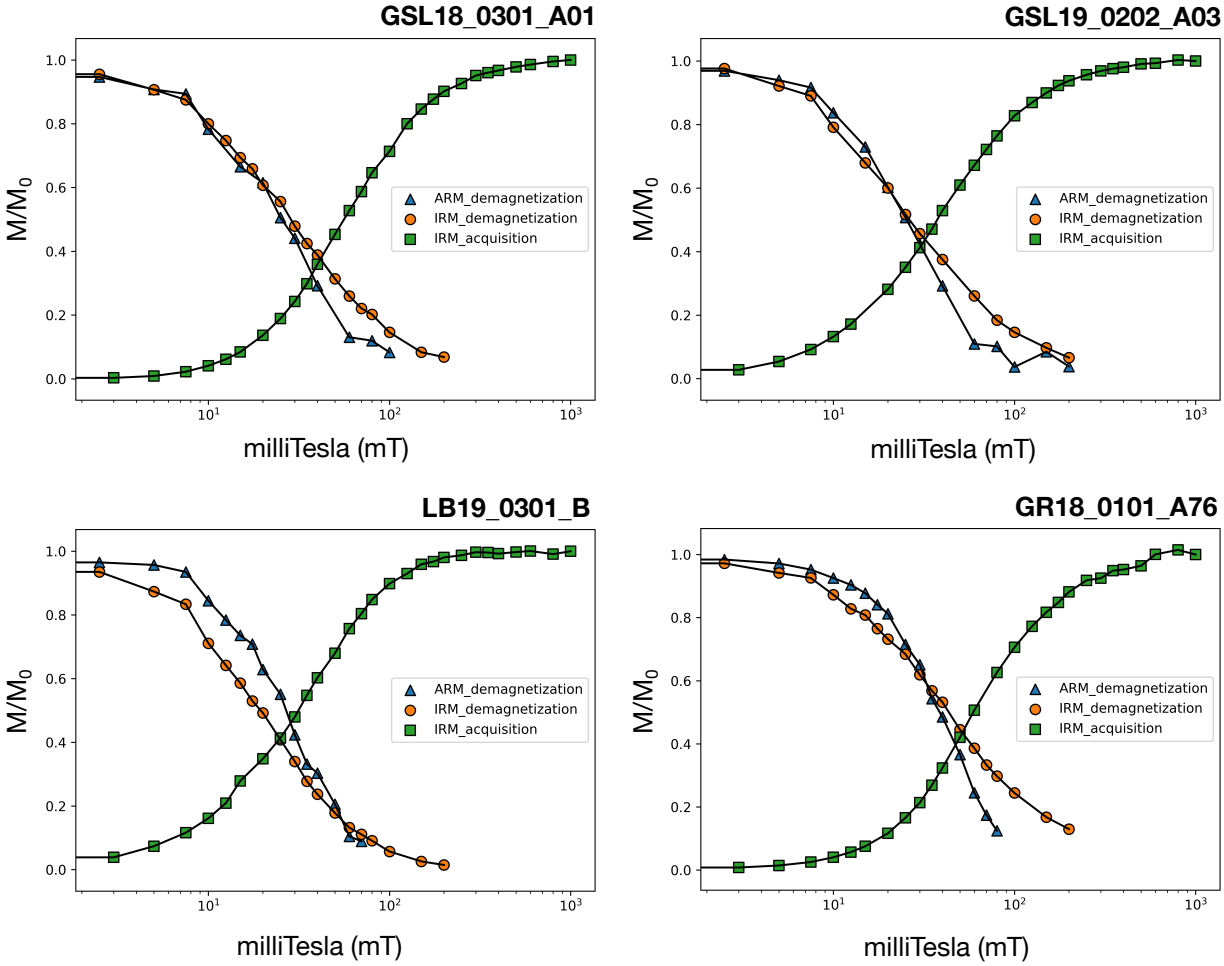

Figure 5.10. IRM acquisition (green squares), IRM demagnetization (orange circles) and ARM demagnetization (blue circles) normalized by the starting (or ending) values. (top left) The lithified GSL18 microbialite from Antelope Island; (top right) lithified GSL19 microbialite from Lakeside; (bottom left) lithified porous microbialites from Site 3-rapid; (bottom right) dense Eocene microbialite from Green River formation. ARM and IRM were applied along the sample z-axis. Additional IRM acquisition, IRM demagnetization and ARM demagnetization plots of GSL18, GSL19, LB19, and GR18 specimens are included in Appendix D.

Table 5.11. The specimens subjected to the Lowrie-Fuller test and calculated parameters. From left to right: ARM demagnetization MDF, IRM demagnetization MDF, IRM acquisition MDF and rough intersection field value of IRM demagnetization and IRM acquisition of GSL (top) and GR (bottom) microbialite samples.

Specimen ID	ARM_demag_MDF	IRM_demag_MDF	IRM_acquisition_MDF	IRM_Intersection
GSL18_0101_00	32.75 mT	33.63 mT	61.88 mT	15.82 mT
GSL18_0101_01	29.07 mT	35.43 mT	55.89 mT	15.42 mT
GSL18_0301_A01	38.76 mT	43.64 mT	50.06 mT	17.02 mT
GSL18_0301_A02	36.44 mT	43.44 mT	60.06 mT	15.22 mT

Specimen ID	ARM_demag_MDF	IRM_demag_MDF	IRM_acquisition_MDF	IRM_Intersection
GSL19_0202_A03	25.43 mT	26.43 mT	77.01 mT	18.82 mT
GSL19_0202_A04	24.42 mT	25.43 mT	72.07 mT	17.82 mT
GSL19_0202_A05	25.63 mT	27.63 mT	75.08 mT	18.62 mT

GSL19_0202_A10	23.82 mT	33.03 mT	84.08 mT	21.62 mT
GSL19_0202_A11	22.02 mT	33.43 mT	88.08 mT	22.62 mT

Specimen ID	ARM_demag_MDF	IRM_demag_MDF	IRM_acquisition_MDF	IRM_Intersection
LB19_0301_A	24.73 mT	20.42 mT	50.05 mT	13.21 mT
LB19_0301_B	27.26 mT	19.42 mT	59.06 mT	14.01 mT
LB19_0301_C	19.90 mT	19.62 mT	55.06 mT	13.81 mT
LB19_0301_D	23.89 mT	19.22 mT	55.06 mT	13.61 mT
LB19_0301_E	22.07 mT	21.82 mT	57.05 mT	14.41 mT

Specimen ID	ARM_demag_MDF	IRM_demag_MDF	IRM_acquisition_MDF	IRM_Intersection
GR18_0101_A70	32.75 mT	33.63 mT	61.88 mT	19.22 mT
GR18_0101_A71	29.07 mT	35.43 mT	55.89 mT	17.82 mT
GR18_0101_A76	38.76 mT	43.64 mT	50.06 mT	21.22 mT
GR18_0101_A81	36.44 mT	43.44 mT	60.06 mT	21.82 mT

5.3.4. Lowrie Test ("3D IRM" Technique)

GSL18 and 19: GSL18 and 19 samples (Figure 5.11. top left; Figure E.1 and 2 from Appendix E) possess a high soft coercivity fraction (≤ 100 mT) and a very small but recognizable medium coercivity fraction (> 100 mT and ≤ 300 mT). The soft fraction of all samples gradually decreases and flattens out after 575°C to 620 °C, indicating PSD and/or MD magnetite. The medium coercivity fraction displays a similar pattern, but some specimens from Lakeside (e.g. GSL19_0202_A04 and 05) showed a more rapid decrease around 350 °C. This might be the signature of thermally unstable maghemite (maximum coercivity: 0.3 T, maximum unblocking temperature: 350 °C), pyrrhotite (maximum coercivity: 0.5-1T, maximum unblocking temperature: 325 °C), and/or titanomagnetite. The very low hard coercivity fractions were hard to be identify for GSL18 (Antelope Island) specimens, but the magnetization of hard minerals in GSL19 (Lakeside) specimens gradually decreased to >670°C, representing PSD or MD hematite. Other specimens' unblocking temperature values by coercivity fraction are given in Table 5.12.

LB19: Soft coercivity minerals accounted for the highest proportions of IRM for LB19 specimens, and there were no hard coercivity fractions (Figure 5.11. top right; Figure E.3 from

Appendix E). Similar to GSL samples, the soft minerals gradually decreased and flattened out after 575°C to 600 °C, indicating PSD and/ or MD magnetite. With the exception of one sample (LB19_0301_C), the medium coercivity component had maximum unblocking temperatures of 550°C, which might represent titanomagnetite.

GR18: The results (Figure 5.11. left bottom; Figure E.4 from Appendix E) show that the GR18 sample has identifiable soft, medium, and hard fractions. The soft fraction is the largest and gradually decreases and flattens out after 620 °C, which might indicate mixture of multidomain magnetite with other high coercivity mineral such as (titano)hematite. The medium fraction gradually decreases to more maximum unblocking temperatures of 650 to 670 °C, which might represent high coercivity minerals, high-T_c minerals such as hematite.

BG14: The BG14 results (Figure 5.11. right bottom; Figure E.5 from Appendix E) show that the soft fraction is the largest, and there are approximately equal hard and medium fractions. The soft fraction gradually decreases and flattens out after 575°C to 600 °C, which might indicate multidomain magnetite. Medium fractions decreased to around 350 °C and then plateau, decreasing again between about 400 – 500 °C for BG14_0101_A12 and 500 – 600 °C for BG14_0101_A38. Hard fractions decreased to around 300 – 400 °C, near the maximum unblocking temperature of maghemite and/or pyrrhotite. The hard fractions decrease around 625 to 675 °C, which might indicate hematite.

Table 5.12. Lists of maximum unblocking temperature of soft (100mT) , medium (300mT), and hard (1000mT) coercivity minerals observed in 3D IRM technique plots.

GSL18_Specimen ID	Soft	Medium	Hard
GSL18_0301_A01	580°C	600°C	n.a.
GSL18_0301_A02	600°C	600°C	n.a.
GSL18_0301_B01	600°C	n.a.	n.a.
GSL18_0301_B03	620°C	620°C	300°C

GSL19_Specimen ID	Soft	Medium	Hard
GSL19_0202_A03	600°C	620°C	>675°C
GSL19_0202_A04	600°C	350°C, >675°C	>675°C
GSL19_0202_A05	600°C	350°C, >675°C	>675°C
GSL19_0202_A10	580°C	575°C	>675°C
GSL19_0202_A11	580°C	620°C	>675°C

LB19_Specimen ID	Soft	Medium	Hard
LB19_0301_A	580°C	550°C	n.a.
LB19_0301_B	580°C	550°C	n.a.
LB19_0301_C	580°C	620°C	n.a.
LB19_0301_E	620°C	550°C	n.a.

GR18_Specimen ID	Soft	Medium	Hard
GR18_0101_A70	620°C	675°C	n.a.
GR18_0101_A71	620°C	n.a.	n.a.
GR18_0101_A76	620°C	650°C	500°C
GR18_0101_A81	620°C	650°C	620°C

BG14_Specimen ID	Soft	Medium	Hard
BG14_0101_A05	600°C	300°C	>675°C
BG14_0101_A08	620°C	n.a.	>675°C
BG14_0101_A12	600°C	500°C	>675°C
BG14_0101_A38	600°C	350°C, >675°C	>675°C
BG14_0101_A70	620°C	300°C	n.a.

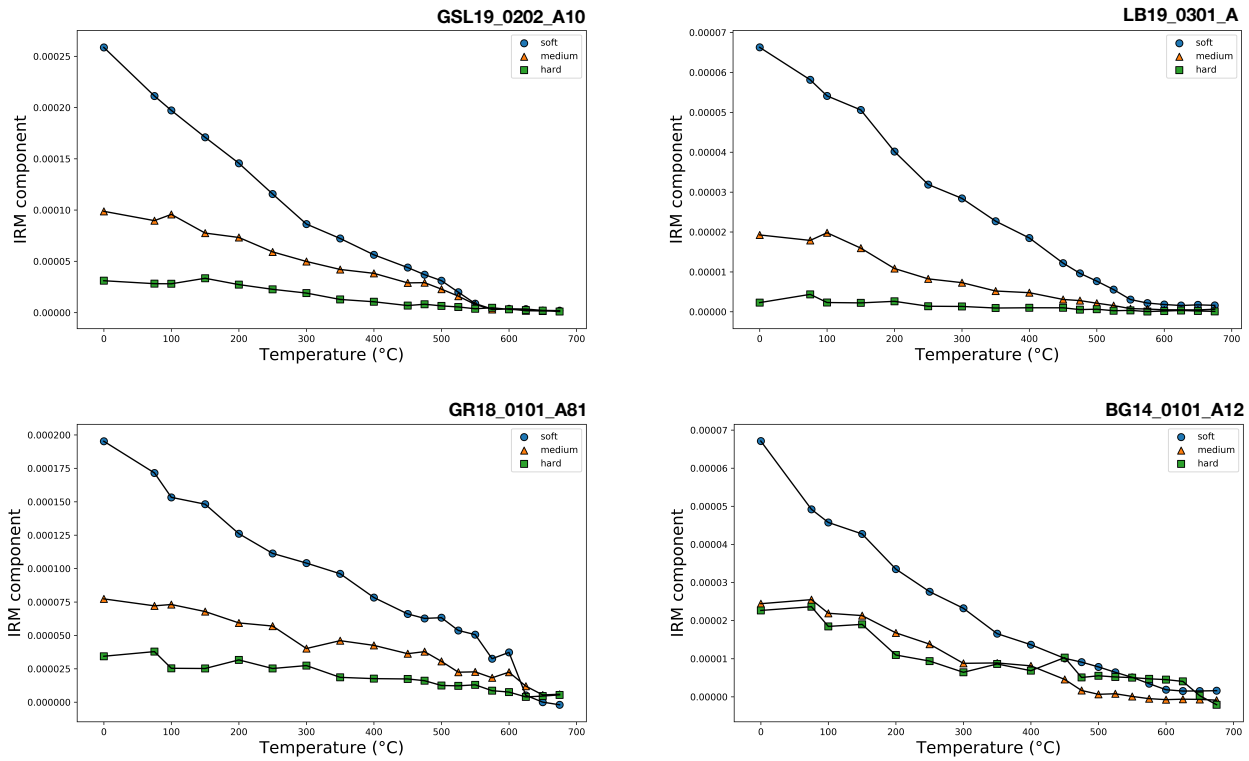

Figure 5.11. 3D IRM technique plots of GSL18 (top left); LB19 (top right); GR18 (bottom left); and BG14 (bottom right) microbialites. Thermal demagnetization of a three-component IRM produced by 100mT (x-axis), 300mT (y-axis) and 1000mT (z-axis). Soft, medium, and hard fractions are shown as blue circle, orange triangle, and green square respectively. Additional 3D IRM technique plots of GLS18, GLS19, LB19, GR18, and BG 14 specimens are included in Appendix E.

5.3.5. Curie Temperature

GSL18: Four living microbialite specimens and one lithified microbialite specimen were measured. The living microbialites' heating curves from Site 1 (GSL18_0101_00, GSL18_0101_02) are very similar to the empty furnace heating curve, which means there was almost no measurable magnetic signature. However, once the samples were heated over 520°C, susceptibility increased. This implies that non-magnetic Fe-bearing minerals reacted during heating and created new ferromagnetic mineral(s) with a Curie point around 520°C. Alternatively, weakly magnetic minerals such as hematite may have reduced to more magnetic forms such as magnetite. The samples from Site 2 (GSL18_0202_02) (Figure 5.12) and 4 (GSL_18_0402_02)

had higher susceptibility compared to the empty furnace and were more easily evaluated. These two heating curves shows relatively clear Curie points around 550 °C, which indicates the signature of magnetite. Once these samples were heated over the Curie temperature of magnetite, these samples also increased in magnetic susceptibility. The cooling curve has a Curie point of 520°C, which would be the T_c of the combined original magnetite and any newly formed magnetic minerals. One lithified microbialite specimen (GSL18_0301_A02) from Site 3 also shows a similar χ(T) pattern with a slightly higher susceptibility. Heating and cooling T_c values are given in Table 5.13. Appendix F (Figure F.1) includes additional Curie point graphs of GSL18 specimens.

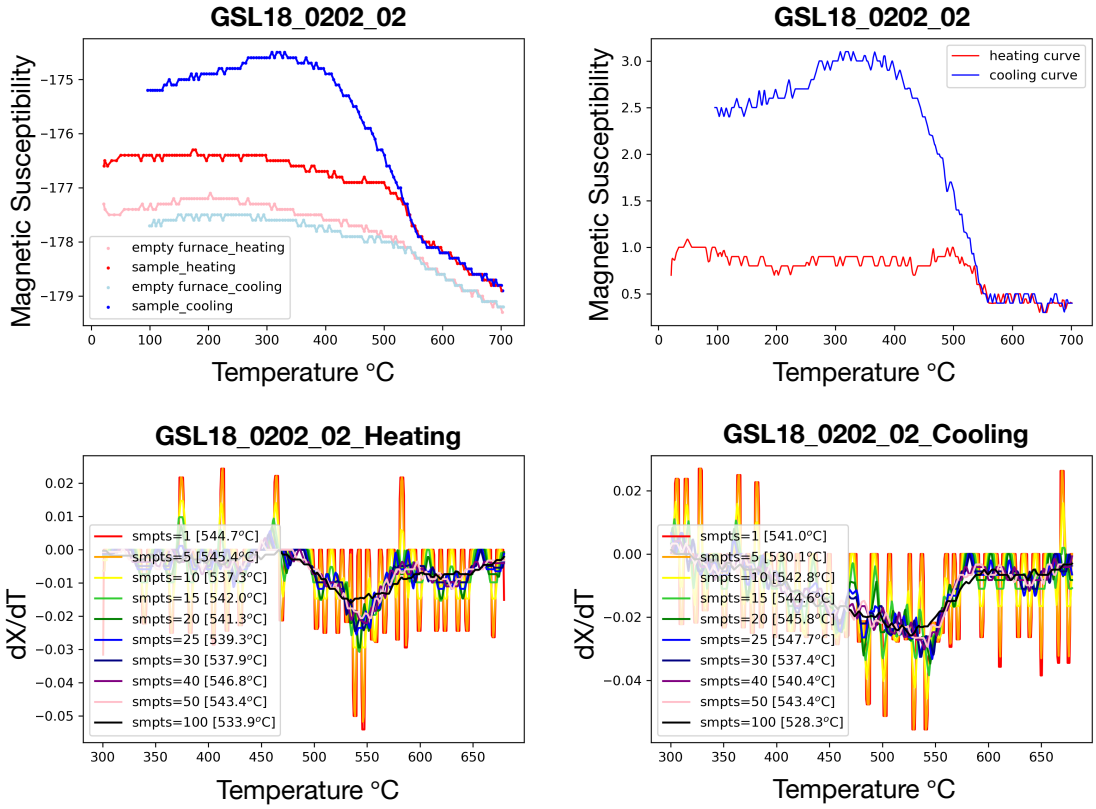

Figure 5.12. The Curie point graphs of specimen GSL18_0202_02. (Top left) Raw susceptibility data for heating (red) and cooling curve (blue) versus temperature, and empty furnace data for heating (light pink) and cooling curve (light blue). (Top right) Measured sample data with furnace component subtracted. The first derivative of the heating curve (bottom left) and cooling curve (bottom right) are plotted based on smoothing point numbers ('smpts' on the legend is the width of the moving average window) and the temperature where the minimum is identified ('[ ]' on the legend).

Table 5.13. GSL samples' Curie points based on heating (top chart) and cooling (bottom chart) curve smoothing points.

Specimen ID	Width of Smoothing Window									
T_C_Heating	**1**	**5**	**10**	**15**	**20**	**25**	**30**	**40**	**50**	**100**
GSL18_0101_00	565.5	566.2	507	464.8	525.4	559.4	558.7	562.8	560.1	590
GSL18_0101_01	642.3	642.3	643.7	558.1	556.8	554.7	553.4	550	539.9	529.8
GSL18_0202_02	544.7	545.4	537.3	542	541.3	539.3	537.9	546.8	543.4	533.9
GSL18_0402_02	536.3	537.6	539	539.7	539	530.8	530.8	532.9	537.6	554.7
GSL18_0301_A02	555	553.7	552.3	506.2	536.7	511	509.6	561.8	566.6	534.7

T_C_Cooling	**1**	**5**	**10**	**15**	**20**	**25**	**30**	**40**	**50**	**100**
GSL18_0101_00	434.3	433.7	434.3	488.6	440.9	448.2	440.9	452.4	447	462.1
GSL18_0101_01	601.4	600.8	538	538.6	565.8	564.6	565.8	561	549.5	548.3
GSL18_0202_02	541	530.1	542.8	544.6	545.8	547.7	537.4	540.4	543.4	528.3
GSL18_0402_02	553.3	552.1	485.4	533.9	533.9	535.7	536.9	541.8	542.4	477.6
GSL18_0301_A02	445.4	444.8	444.8	446.6	440.6	439.4	437.6	434.6	438.8	448.4

LB19: The Curie temperatures of the lithified drill core sample from Site 2 (LB19_0201) (Figure 5.13) and living sample from Site 1 (LB19_0103) were measured. Although the specimen LB19_0201 has a lot of noise, it shows a Curie point of around 550-580°C, indicating magnetite. Unfortunately, the reduction in susceptibility observed when LB19_0103 dried out at room temperature (Section 3.4.2.2) resulted in an extremely noisy χ (T) curve, and the Curie point could not be determined. Appendix F (Figure F.2) includes additional Curie point graphs of LB19 specimens.

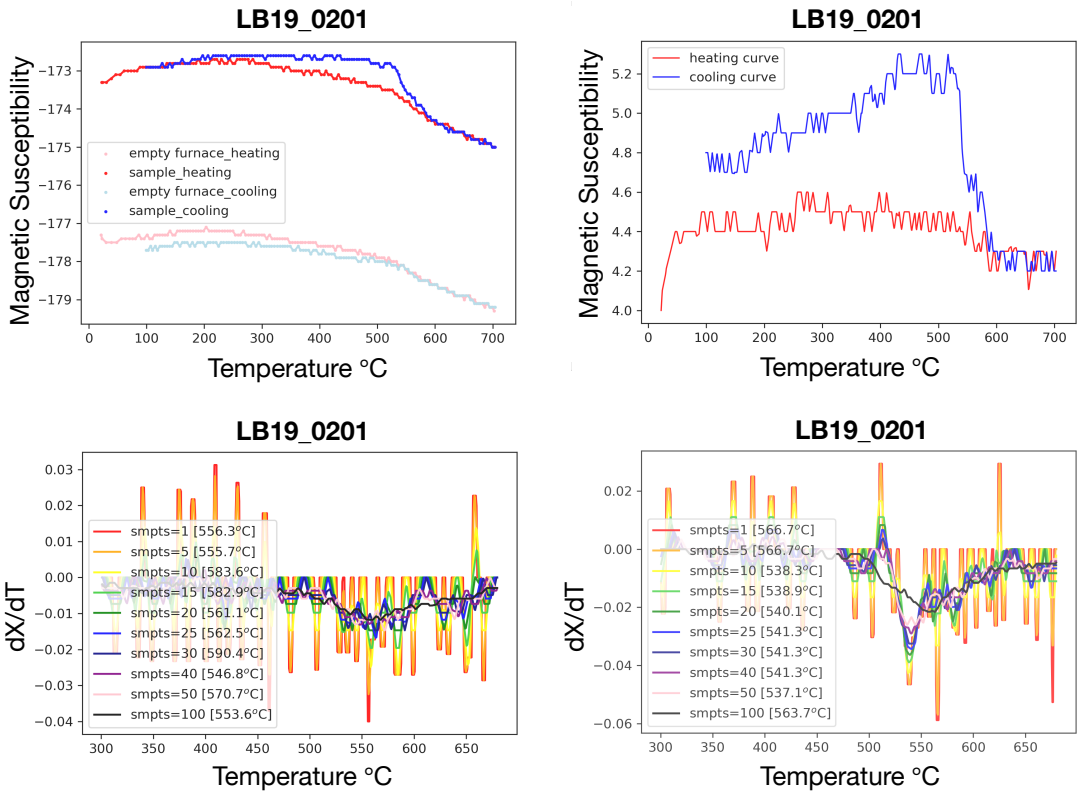

Figure 5.13. The Curie point graphs of specimen LB19_0201 (Top left) Raw susceptibility data plots of heating (red) and cooling curve (blue) versus temperature, and empty furnace data plot of heating (light pink) and cooling curve (light blue). (Top right) The subtraction plot of linearly interpolated empty furnace susceptibility data from raw susceptibility data. The first derivative graph of the heating curve (bottom left) and cooling curve (bottom right) are plotted based on smoothing point numbers ('smpts' on the legend). The temperature corresponding to the minimum in the derivative is indicated by '[ ]'.

GR18: Specimens 70 and 71 have relatively low NRM intensity values (2.68E-07 and 6.03E-07 Am^3/kg) compared with specimens 76 and 81 (2.35E-05 and 1.88E-05 Am^3/kg), but they have similar magnetic susceptibility values (Section 3.4.1.3), IRM unmixing distributions (Figure 5.8), and S-ratios (Table 5.4). The Curie temperatures from the heating curves are found to be the range of 535°C to 554°C. However, the increase in susceptibility around 400 to 500°C on the heating curve and drastic increase in susceptibility on the cooling curve might result from the chemical alteration of other minerals at high temperature (Figure 5.14. Table 5.14). For example, siderite can decompose in a reaction that produces magnetite and results in a thermomagnetic signal similar

to what we observe here (Pan et al., 2000). Appendix F (Figure F.3) includes additional Curie point graphs of GR18 specimens.

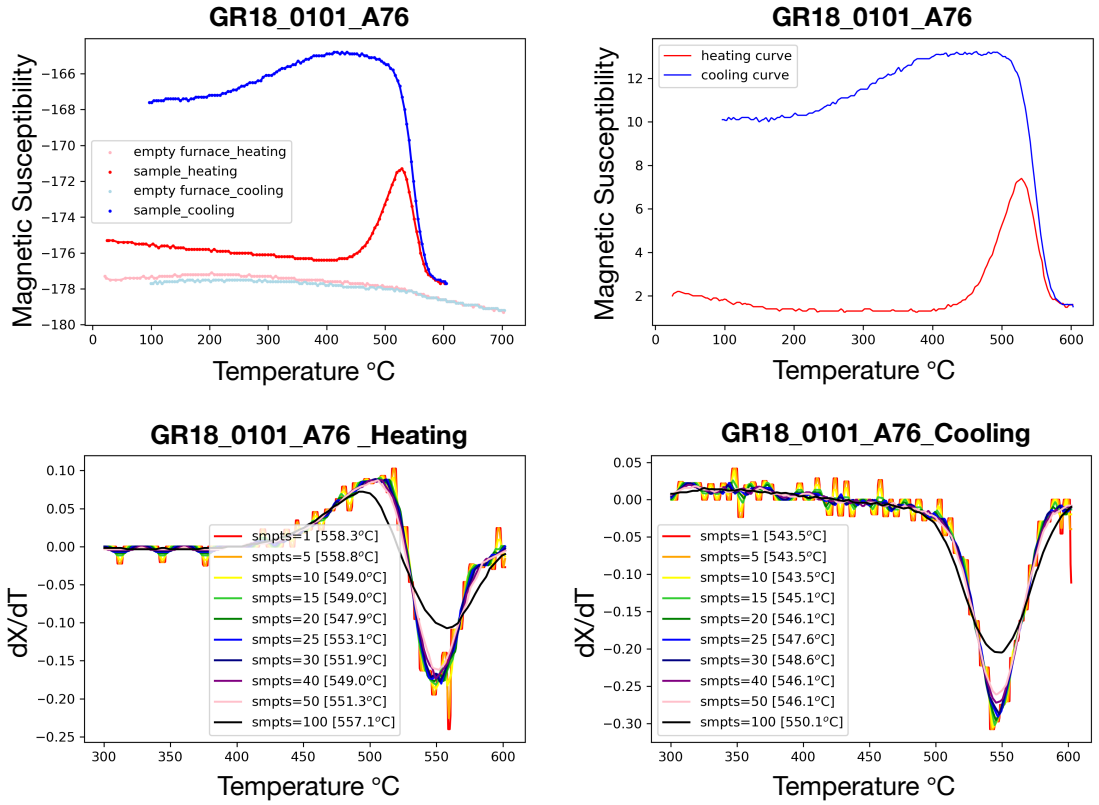

Figure 5.14. The Curie point graphs of specimen GR18_0101_A76. (Top left) Raw susceptibility data plots of heating (red) and cooling curve (blue) versus temperature, and empty furnace data plot of heating (light pink) and cooling curve (light blue). (Top right) The subtraction plot of linearly interpolated empty furnace susceptibility data from raw susceptibility data. The first derivative graph of the heating curve (bottom left) and cooling curve (bottom right) are plotted based on smoothing point numbers ('smpts' on the legend) and the temperature where the smallest value of derivative value ('[ ]' on the legend).

Table 5.14. The total GR18_0101 sample' Curie points based on heating (top chart) and cooling (bottom chart) curve smoothing points

Specimen ID	**Width of Smoothing Window**									
T_C_Heating	**1**	**5**	**10**	**15**	**20**	**25**	**30**	**40**	**50**	**100**
GR18_0101_A70	532.9	534.2	536.3	537	539	539.7	538.3	539	536.3	551.2
GR18_0101_A71	548.3	548.3	548.3	547.2	548.3	549.5	550.7	550.1	553	560
GR18_0101_A76	558.3	558.8	549	549	547.9	553.1	551.9	549	551.3	557.1
GR18_0101_A81	545.2	546.4	545.8	544.6	543.5	544	545.8	549.8	551.6	562

T_C_Cooling	**1**	**5**	**10**	**15**	**20**	**25**	**30**	**40**	**50**	**100**
GR18_0101_A70	541.3	540.7	541.3	543.1	543.7	542.5	543.1	541.3	541.3	530.4
GR18_0101_A71	553.4	552.9	551.3	550.8	551.8	551.3	550.8	551.3	551.3	548.3
GR18_0101_A76	543.5	543.5	543.5	545.1	546.1	547.6	548.6	546.1	546.1	550.1

GR18_0101_A81	551.3	552.3	550.8	549.8	548.3	548.8	549.8	548.3	550.8	551.8

BG14: The Curie temperatures of specimens BG14_0101_A08, 24, 34, 40, and 70 were measured. However, the susceptibility of all heating curves was lower than that of the empty furnace. This negative susceptibility indicates a low proportion of ferromagnetic and paramagnetic minerals compared to diamagnetic minerals. Although the signal was small, all heating curves show peaks around 450-500 °C. This could be interpreted as the effect of chemical alteration during heating such as decomposition of siderite to magnetite. The rough range of the Curie points from the heating and cooling curves are 500-550 °C and 520-560 °C, respectively (Figure 5.15, Table 5.15). Appendix F (Figure F.4) includes additional Curie point graphs of BG14 specimens.

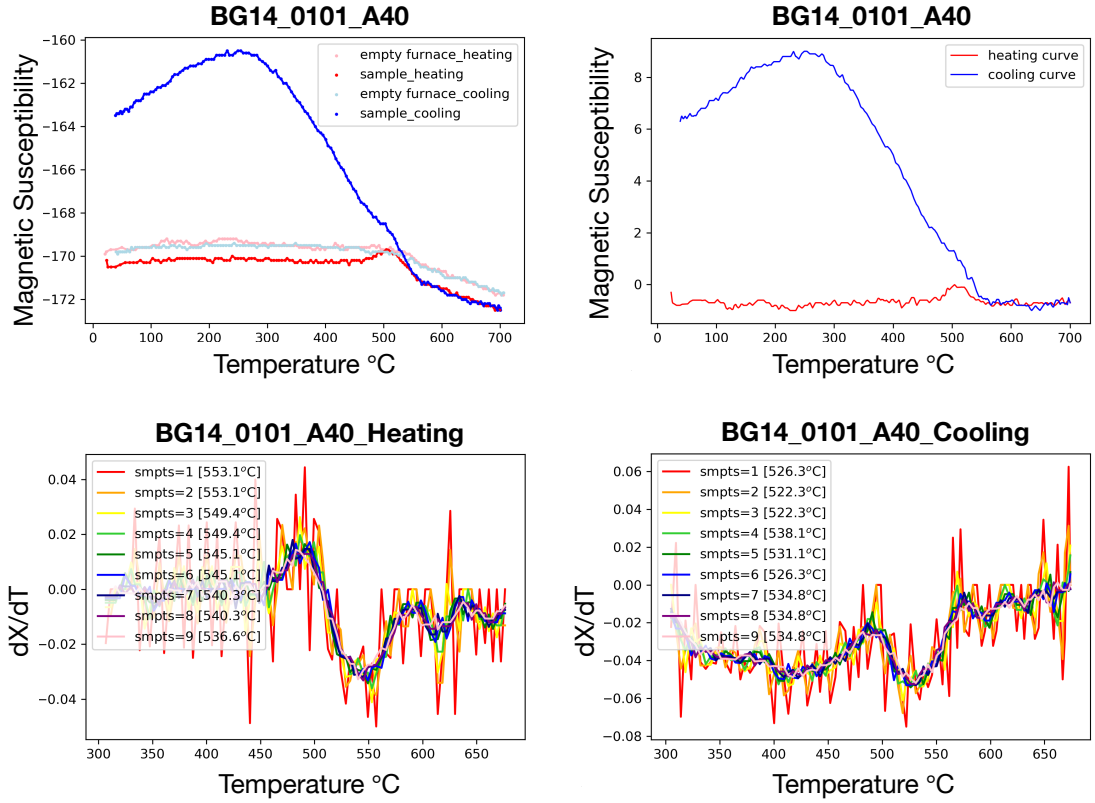

Figure 5.15. The Curie point graphs of specimen BG14_0101_A40. (Top left) Raw susceptibility data plots of heating (red) and cooling curve (blue) versus temperature, and empty furnace data plot of heating (light pink) and cooling curve (light blue). (Top right) The subtraction plot of linearly interpolated empty furnace susceptibility data from raw susceptibility data. The first derivative graph of the heating curve (bottom left) and cooling curve (bottom right) are plotted based on smoothing point numbers ('smpts' on the legend) and the temperature where the smallest value of derivative value ('[ ]' on the legend).

Table 5.15. The total BG18_0101 sample' Curie points based on heating (top chart) and cooling (bottom chart) curve smoothing points

Specimen ID	Width of Smoothing Window									
T_C_Heating	1	5	10	15	20	25	30	40	50	100
BG14_0101_A08	612.6	478.1	506.1	547.8	549.8	500.6	553.2	505.4	509.5	497.2
BG14_0101_A24	495.8	497.1	499.2	499.8	539.3	540	534.5	535.2	533.3	529.8
BG14_0101_A34	658.7	660	550.4	548.4	547	553.8	555.8	540.2	536.8	550.4
BG14_0101_A40	554.8	554.8	553.4	551.4	550.7	548	546.6	543.3	539.9	538.5
BG14_0101_A70	490.5	490.5	489.2	490.5	491.9	496.6	498.7	502.7	506.1	521.7

T_C_Cooling	1	5	10	15	20	25	30	40	50	100
BG14_0101_A08	521.1	520.5	533.7	532.4	532.4	534.4	528.4	524.4	527.8	531.7
BG14_0101_A24	525.1	523.8	525.1	527.1	527.7	529.7	531.1	534.4	537.7	534.4
BG14_0101_A34	348.4	347.1	550.4	549.7	548.4	543.7	544.4	541.1	537.8	543.1
BG14_0101_A40	523.5	524.8	533.8	521.5	520.1	540	528.8	532.1	533.4	428.1
BG14_0101_A70	527.7	527.7	528.4	530.3	531.7	533.6	535	523.7	526.4	522.4

5.3.6. Hysteresis Loops and Day Plot

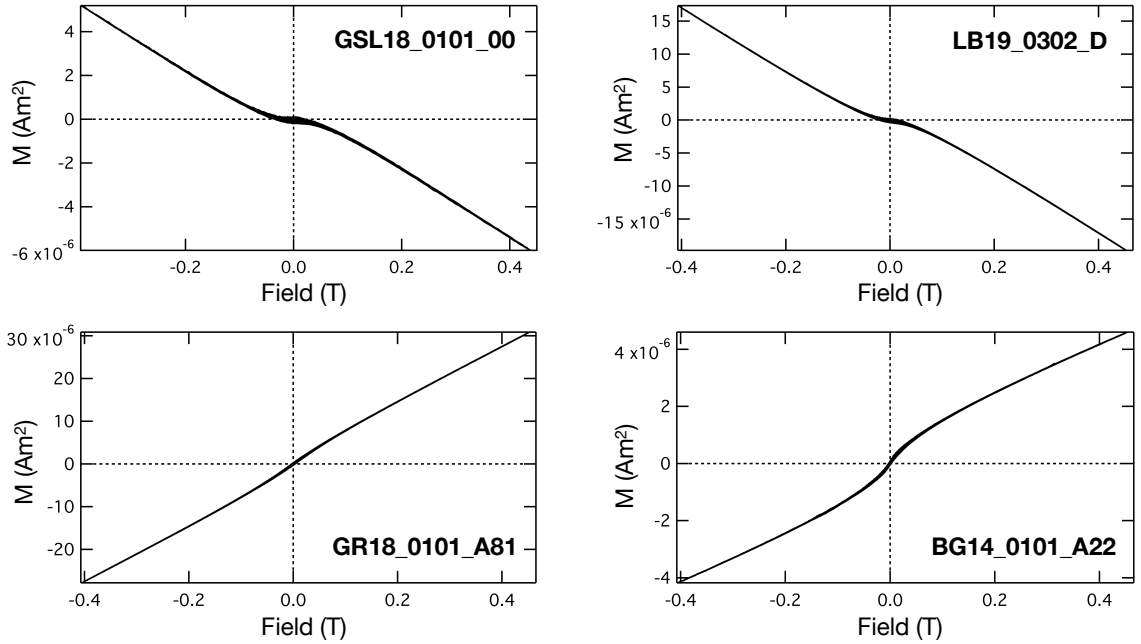

Figure 5.16. Magnetization (M, y-axis) as a function of applied field (x-axis) of GSL, LB, GR and BG microbialites before slope correction. While GSL18_0101_00 and LB19_0302_D specimens have negative slope (diamagnetic), GR18_0101_A81 and BG14_0101_A22 specimens have positive slope (paramagnetic).

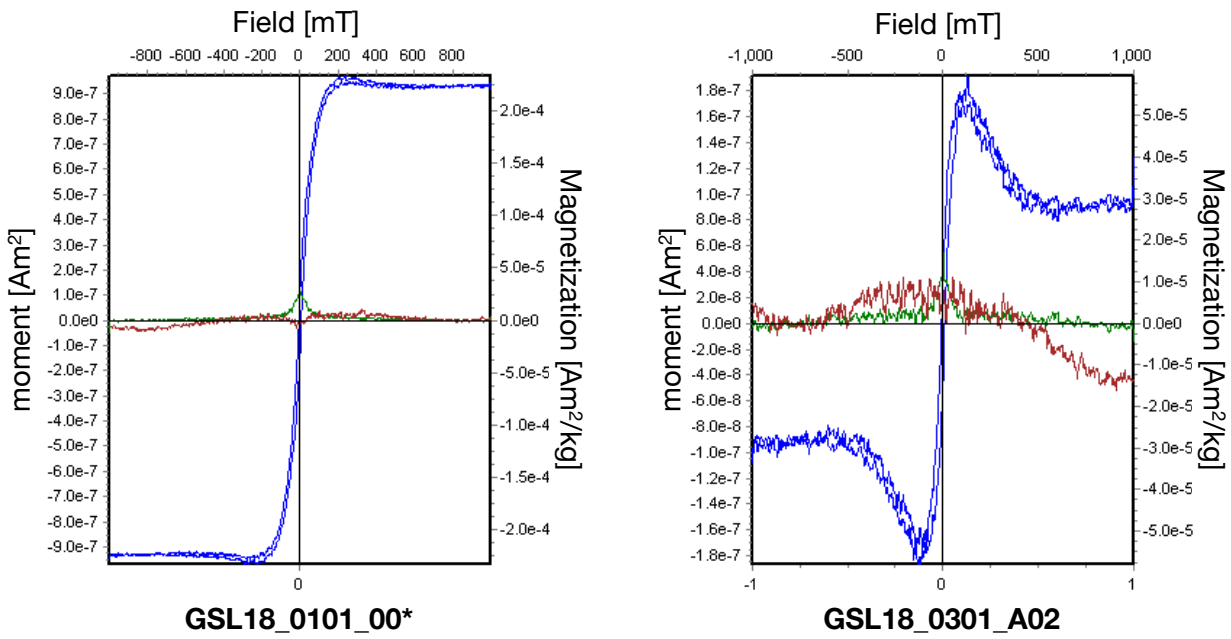

Figure. 5.17. Hysteresis loops of GSL18 specimens collected from Antelope Island: GSL18_0101_00* - lithified microbialite with a cyanobacteria layer (left) and GSL18_0301_A02 -lithified young microbialite (right). Blue is slope and error corrected loop; brown shows err(H); green is $M_{rh}(H)$. The unit of moment and magnetization are Am^2 and Am^2/kg respectively. The image is created using IRM database software (Jackson & Solheid, 2010).

GSL18: All microbialite samples collected from Antelope Island, GSL display large negative diamagnetic slopes (Figure 5.16; Table 5.16, X_{hf}). Once this signal is removed, the ferromagnetic loop can be seen (blue loops on Figure 5.17), but the extremely low ferromagnetic:diamagnetic ratio means that the loops are noisy and often have physically-implausible characteristics (see brown error curves). Nevertheless, approximate values of M_r, M_s, and H_{cr} are extracted from the loops. A porous microbialite with dried cyanobacteria layer shows a closed loop characteristic of SP or MD grains (Figure 5.17. Left). The lithified sample GSL18_0301 was more noisy than other samples with high err(H) and physically-unrealistic maxima at ~ ±125 mT, but it also displayed a closed loop, also representing SP or MD grains.

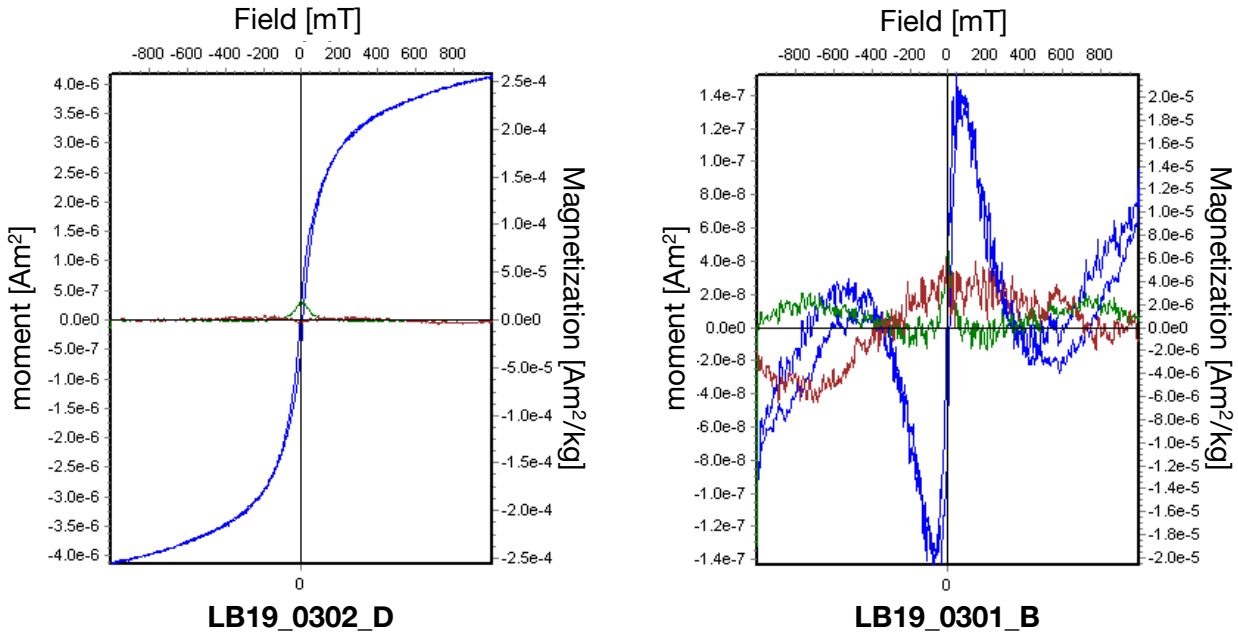

Figure. 5.18. Hysteresis loops of LB19's lithified very porous microbialite specimens (LB19_0302_D (left) and LB19_0301_B (right)) collected from Site 3- Rapids. Blue is slope and error corrected loop; brown shows err(H); green is $M_{rh}(H)$. The unit of moment and magnetization are Am^2 and Am^2/kg, respectively. The image is created by using software IRM database (Jackson & Solheid, 2010).

LB19: Microbialite drill core samples collected from Site 3 (Rapids) also are dominated by a negative diamagnetic slope (Figure 5.16; Table 5.16. X_{hf}), and the resulting corrected loop has high noise. With the exception of specimen LB19_0302_D, all the other specimens displayed poor-quality hysteresis loops that were impossible to interpret (e.g., Figure 5.18. right). Specimen LB19_0302_D shows a closed loop representing SP or MD grains (Figure 5.18. Left). However, there was no saturated magnetization plateau, which can arise from insufficient diamagnetic/paramagnetic correction and/or the presence of high-coercivity ferromagnetic minerals.

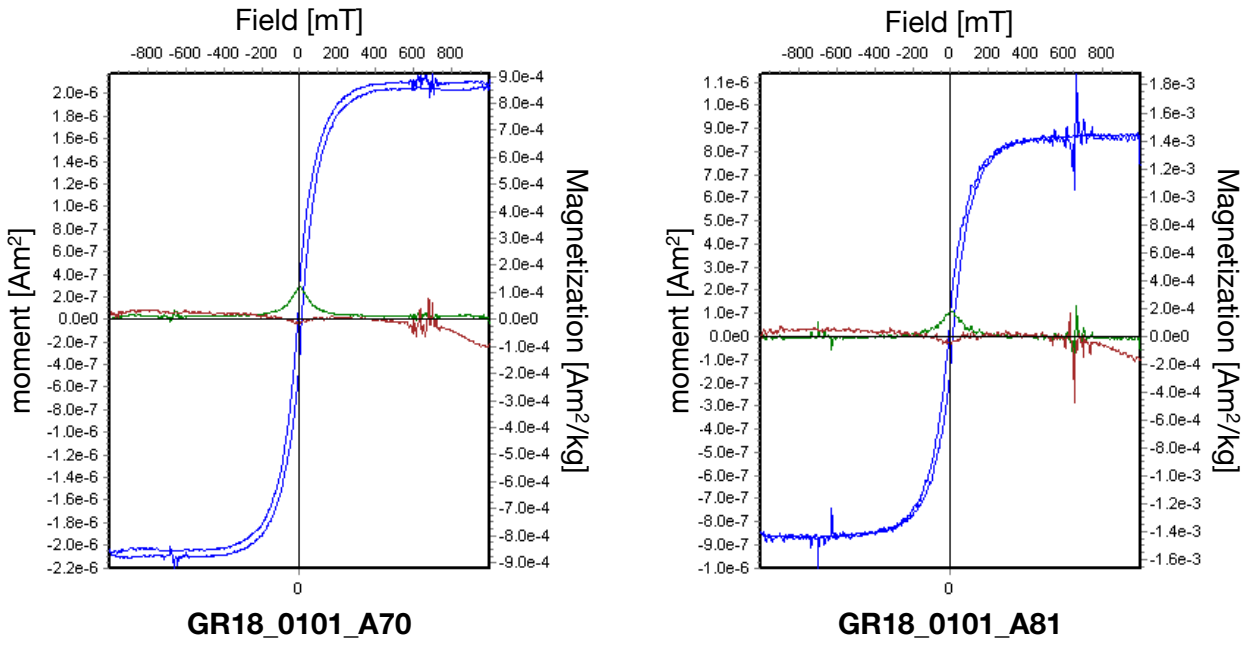

Figure 5.19. Hysteresis loops of dense Eocene Green Formation microbialites: (left) lowly magnetized specimen (GR18_0101_A70) and (right) highly magnetized specimen (GR18_0101_A81). Blue is slope and error corrected loop; brown shows err(H); green is $M_{rh}(H)$. The unit of moment and magnetization are Am^2 and Am^2/kg, respectively. The image is created by using software IRM database (Jackson & Solheid, 2010).

GR18: Magnetic hysteresis loops of specimens with low (Figure 5.19. GR18_0101_A70) and high NRM (Figure 5.19. GR18_0101_A81) are assessed. Both hysteresis loops are very similar, again showing that there is no mineral or grainsize/domain difference between the high and low NRM regions. Loops are almost but not completely closed like GSL or LB samples. This might indicate that the sample contains some SD and/or PSD material.

BG14: Magnetic hysteresis loops were obtained on Cambrian Bayan Gol Formation stromatolite specimens with different S-ratios (Figure 5.20). The S-ratio of specimens BG14_0101_A03, 10, 22, and 34 were 0.46, 0.68, 0.82, 0.94, respectively. Overall, specimens with low S-ratio (high coercivity) displayed open loops with wasp-waisted configuration, representing two different compositions (e.g. magnetite and hematite) or two different grain sizes (e.g. SD +

PSD or SD +MD). However, high S-ratio specimens exhibited a similar closed loop (MD or PSD) feature with other microbialites from GSL, LB and GR.

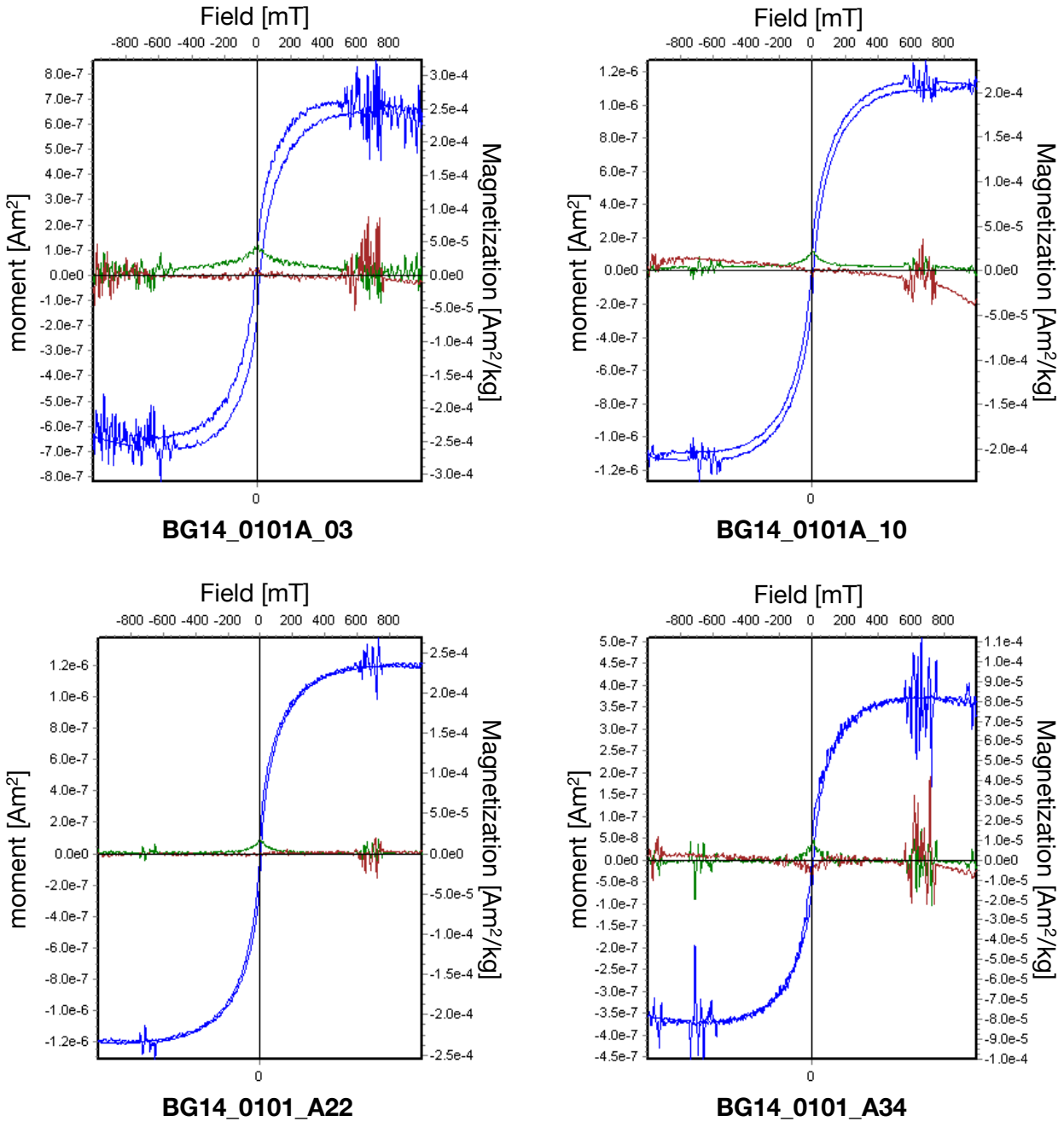

Figure 5.20. Hysteresis loops of Cambrian Bayan Gol Formation stromatolite: (left top) BG14_0101_A03 (s-ratio: 0.46); BG14_0101_A10 (s-ratio: 0.68); BG14_0101_A22 (s-ratio: 0.82); and BG14_0101_A34 (s-ratio: 0.94). Blue is slope and error corrected loop; brown shows err(H); green is $M_{rh}(H)$. The unit of moment and magnetization are Am^2 and Am^2/kg, respectively. The image is created by using software IRM database (Jackson & Solheid, 2010).

Day plot: Hysteresis data are summarized in a standard Day plot (Figure 5.21), with the exception of GSL (GSL18_0301_A01*) and LB (LB19_0102_03) specimens, which were weakly magnetic and extremely noisy. Most specimens plotted in the PSD ($0.02 < M_r/M_{rs} < 0.5$, $2 < H_{cr}/H_c < 5$) region. The trend of all specimens is similar to the magnetite SD-MD mixture curves (Dunlop, 2002). Also, there was no correlation between placement on plot and S-ratio (e.g. BG14 specimens).

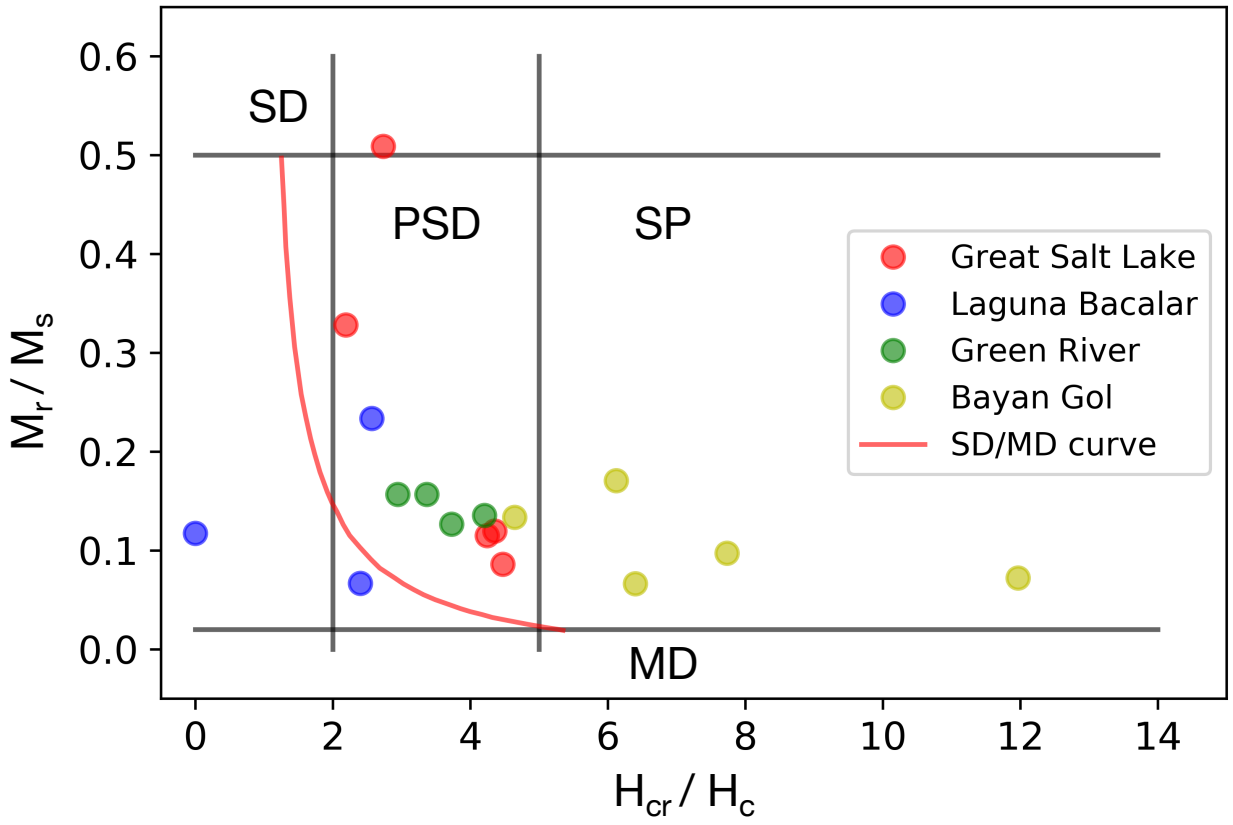

Figure 5.21. Day plot of microbialite specimens collected from four different locations. Red, blue, green, and. yellow circles represent specimens from Great Salt Lake, Laguna Bacalar, Green River and Bayan Gol Formation. Magnetite SD-MD mixing curve for reference (Dunlop, 2002)

Table 5.16. List of parameters of specimens measured by hysteresis loops and backfield remanence curves. M_{rs}, saturation magnetization; M_r, remanent magnetization; H_c, coercivity; H_{cr}, remanence coercivity; X_{hf}, high-field susceptibility (paramagnetic/diamagnetic contribution).

Specimen	M_{rs}[Am^2/kg]	M_r[Am^2/kg]	H_c[mT]	H_{cr}[mT]	X_{hf}[m^3/kg]
GSL18_0101_00	2.30E-04	1.97E-05	6.29E+00	2.81E+01	-4.64E-09
GSL18_0101_00*	2.24E-04	2.67E-05	6.46E+00	2.81E+01	-4.61E-09
GSL18_0101_01	1.00E-04	3.29E-05	9.55E+00	2.09E+01	-1.19E-08

GSL18_0202_A01	2.29E-04	2.63E-05	6.83E+00	2.90E+01	-6.46E-09
GSL18_0301_A02	2.82E-05	1.44E-05	9.11E+00	2.49E+01	-6.86E-09
LB19_0301_A	8.16E-06	1.01E-05	1.27E+01	8.36E+00	-6.18E-09
LB19_0301_B	2.61E-05	6.11E-06	8.73E+00	2.24E+01	-6.46E-09
LB19_0302_D	4.64E-06	3.10E-07	7.37E+00	1.77E+01	-6.48E-11
GR18_0101_A70	1.43E-03	1.81E-04	1.12E+01	4.16E+01	3.78E-08
GR18_0101_A76	8.98E-04	1.41E-04	1.54E+01	4.53E+01	3.30E-08
GR18_0101_A76*	8.98E-04	1.41E-04	1.54E+01	5.18E+01	3.30E-08
GR18_0101_A81	8.77E-04	1.19E-04	1.11E+01	4.68E+01	3.33E-08
BG14_0101_A03	2.51E-04	4.28E-05	1.36E+01	8.32E+01	7.33E-09
BG14_0101_A10	2.10E-04	2.04E-05	6.66E+00	5.15E+01	7.89E-09
BG14_0101_A10*	2.17E-04	1.44E-05	8.05E+00	5.15E+01	7.90E-09
BG14_0101_A22	2.35E-04	1.69E-05	4.06E+00	4.86E+01	1.91E-09
BG14_0101_A34	8.01E-05	1.07E-05	7.43E+00	3.45E+01	1.10E-09

5.3.7. First Order Reversal Curves (FORC)

GSL18 and LB19: The FORC diagram of modern microbialites from GSL and LB reveal a peak in the FORC distribution around H_u=0 and H_c=0, which might represent PSD grains (Figure 5.22). There are also weak signatures along the horizontal axis, which might be SD grains, but the signature decreased as a smoothing factor increased.

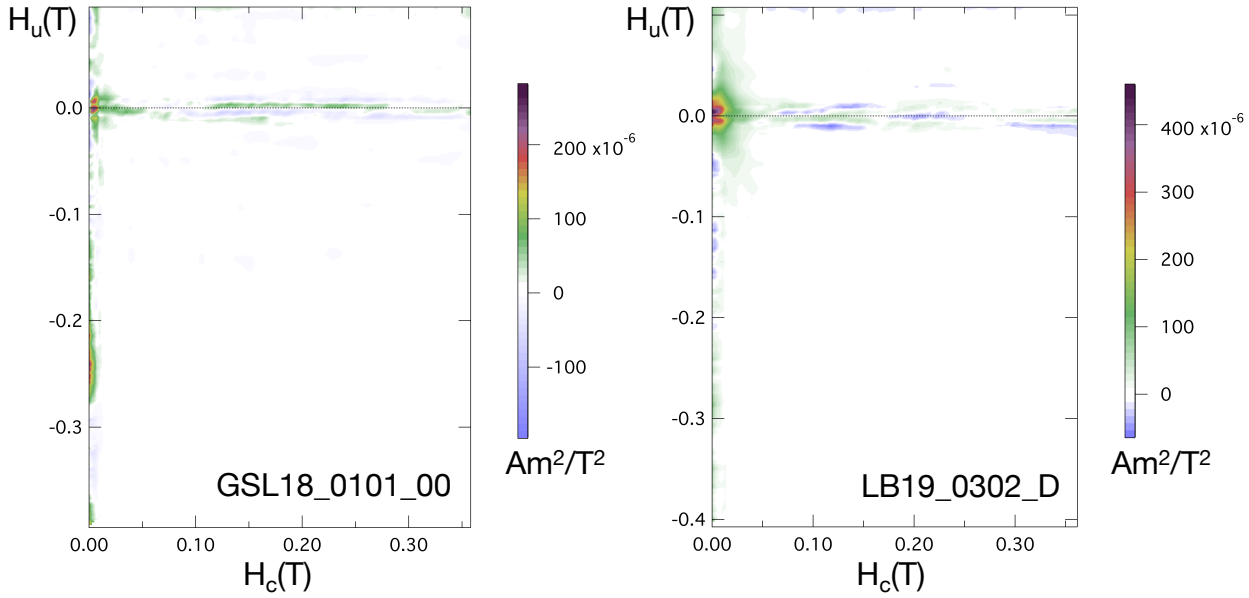

Figure 5.22. FORC distribution of specimens GSL18_0101_00 (left) and LB19_0302_D (right) made with FORCinel (Harrison & Feinberg, 2008). Vertical ridge (S_c0) =4; Horizontal smooth (S_c1)=7; Central ridge (S_b0)=3; Vertical smooth (S_b1) =7

GR18: The FORC diagram of both ancient GR microbialite specimens from high NRM (GR18_0101_A81) and low NRM (GR18_0101_A70) display central ridges along the horizontal axes and vertical signatures (Figure 5.23). These signatures remain as the smoothing factor increases, suggesting they are real features. Thus, the magnetic domain of the GR18 microbialite might be interpreted as the mixture of SD and MD, which is also shown from the Day plot (green circles on Figure 5.21).

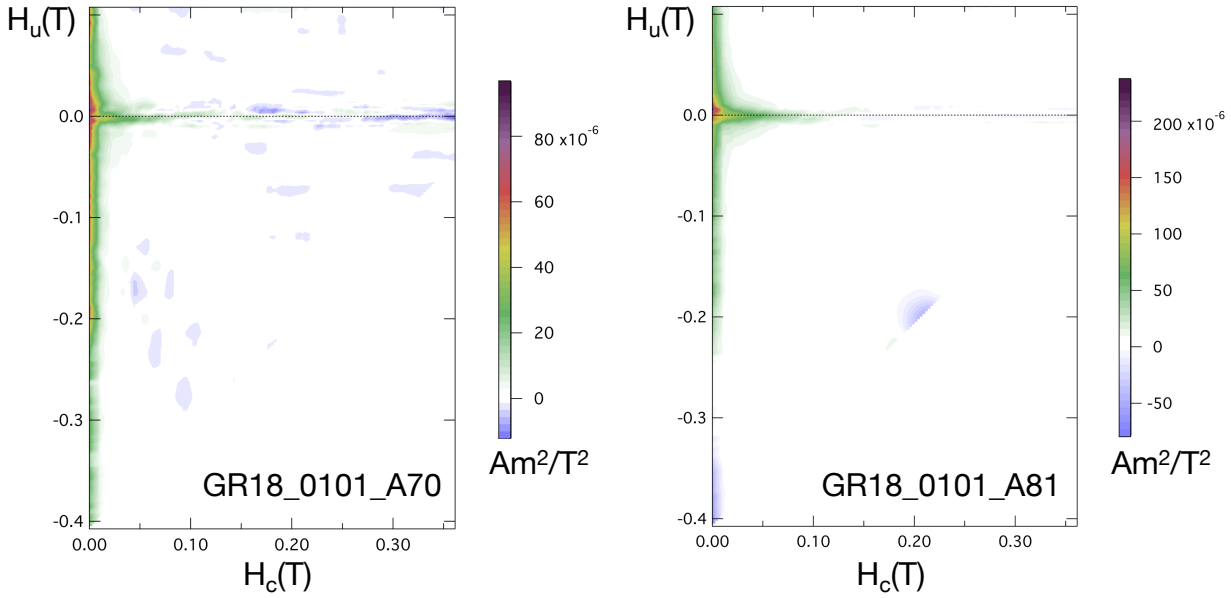

Figure 5.23. FORC distribution of specimens GR18_0101_A70 (left) and GR18_0101_A81 (right) made with FORCinel (Harrison & Feinberg, 2008). Vertical ridge (S_c0) =4; Horizontal smooth (S_c1)=7; Central ridge (S_b0)=3; Vertical smooth (S_b1) =7.

BG14: The stacked FORC diagrams of ancient BG stromatolite specimens from low S-ratio (0.46; BG14_0101_A03) and high S-ratio (0.94, BG14_0101_A34) regions are shown in Figure 5.24. In spite of the stacking, the signal:noise ratio is low. Specimen BG14_0101_A03 has the most density distribution on the vertical axis and small signature along the horizontal axis. Specimen BG14_0101_A34 also contains a signature form vertical axis but a more significant signature from central ridges around H_c above 0.11(T). The magnetic domains of the BG14's other

specimens exhibit similar density distributions, consistent with a mixture of SD and MD, also supported by the Day plot (yellow circles on Figure 5.21). Appendix G includes additional FORC diagrams of BG14 specimens.

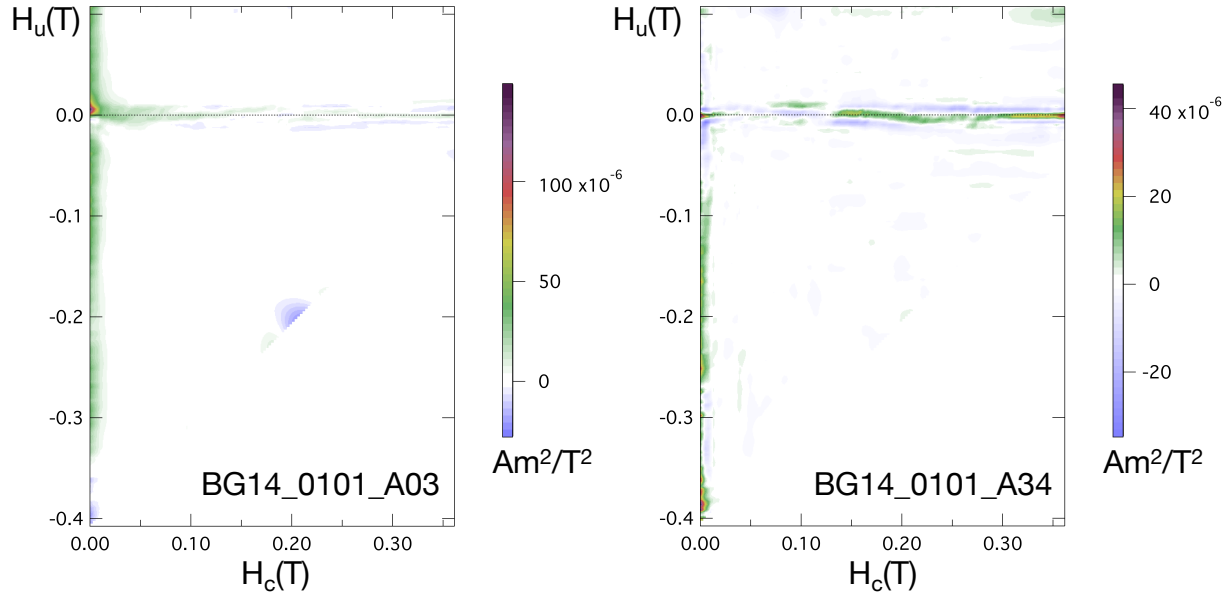

Figure 5.24 FORC distribution of specimens BG14_0101_A03 (left) and BG14_0101_A34 (right) made with FORCinel (Harrison & Feinberg, 2008). Both FORC diagrams were obtained by stacking 4 FORCs. Vertical ridge (S_c0) =4; Horizontal smooth (S_c1)=7; Central ridge (S_b0)=3; Vertical smooth (S_b1) =7.

5.4. Summary/Discussion

Combining all rock magnetic results, the dominant coercivity component is inferred to be PSD to MD magnetite for all microbialites. Samples also contain some other high coercivity minerals such as hematite. The complete summary is listed in Table 5.17.

5.4.1. Great Salt Lake

GSL18 – living or very young microbialites: Based on S-ratio (0.95) and Curie temperature (500°C), the major mineralogy of GSL18 specimens is magnetite or titanomagnetite. IRM unmixing curves reveal that a higher coercivity fraction (> 150 mT) is also found in addition to the major coercivity component at ~ 40.5 mT. The results from the 3D-IRM technique exhibit unblocking temperature of the soft (100mT) and medium (300mT) minerals of 580°C - 620°C and 600°C - 620°C, consistent with magnetite and/or slightly oxidized magnetite (maghemite). The domain state obtained by hysteresis loops, Day plot, and FORCs represents a mixture of SD + MD or PSD.

GSL19 – Pleistocene microbialites: GSL19 samples have similar magnetic mineralogy and coercivity to GSL18 samples but more complex mineralogy, including higher-coercivity and higher T_b minerals. In addition to magnetite (T_b = 575 - 600 °C) from the soft minerals, the 3D-IRM technique shows a high coercivity component with an average T_b of 675°C (hematite). Medium coercivity components show a lower average T_b of 350°C (maghemite or pyrrhotite). However, a comparison of IRM unmixing results with the NRM coercivity distribution suggests that the NRM is carried predominantly by the magnetite fraction.

5.4.2. Laguna Bacalar

LB19– living or very young microbialites: LB19 samples have an S-ratio of 1 (magnetite) and a low coercivity based on IRM unmixing (IRM_{0mT} :30 – 50 mT, $IRM_{-1000mT}$:33 – 39 mT) and Lowrie-Fuller (18 - 23 mT) test. Based on the T_b of soft and medium fractions (580 - 620 °C) and the T_c (550 °C), the major mineralogy can be interpreted as magnetite. While the dominant domain state is inferred to be SD based on the Lowrie-Fuller test, hysteresis and FORC results suggest PSD or an SD+MD mixture.

5.4.3. Green River Formation

GR18 – Eocene microbialites: The T_c of GR18 specimens is 500-550°C, consistent with magnetite or low-Ti titanomagnetite. However, the average S-ratio of 0.84, shows that some high coercivity minerals are present in addition to (titano)magnetite. This also can be seen from IRM unmixing curves, which have a high-coercivity component in addition to the presumed magnetite component. The 3D-IRM technique reveals that the medium coercivity fraction has a maximum T_b of 650 - 675 °C, consistent with hematite. The domain states appear to be SD+MD or PSD based on hysteresis loops and FORCs. GR18 specimens do not show any mineralogical differences in the structure, and therefore the unusual NRM intensity distribution and directions are unlikely to arise from a CRM and are more likely to represent IRM.

5.4.4. Bayan Gol Formation

BG14- Lower Cambrian Stromatolite: Magnetite or titanomagnetite are identified as the major magnetic mineral in the BG14 stromatolite, based on T_c (500°C) and IRM unmixing. However, specimens show variable relative contributions from higher coercivity minerals in the

structure, which supports the results of BG14's susceptibility and NRM intensity mapping from Chapter 3. The proportion of high-coercivity magnetic minerals appears to be approximately continuous along laminations, similar to magnetic susceptibility variations. However, NRM signatures were fully AF- demagnetized after 200 mT, showing that high coercivity materials do not significantly contribute to NRM, so the NRM variations are less continuous along laminations. The S-ratio of the outer layers was lower than the inner layers. This is also shown in IRM unmixing curves, 3D-IRM technique, and hysteresis loops. Outer layers exhibit significantly higher coercivity distributions in IRM unmixing curves, and these high coercivity minerals can be identified as hematite (T_b = 650 - 675 °C) according to the 3D-IRM technique. While hysteresis loops of inner layers show closed loops (PSD or MD), outer layers have a wasp-waisted configuration, which might represent two different minerals (magnetite + hematite) or domain states (SD + MD). Domain states are identified as SD+MD or PSD by Day plot results and SD+MD by FORC measurements.

5.4.5. Ancient vs Modern Microbialites

Mineralogy: While the high S-ratio values of all modern microbialites (i.e., GSL18, LB19) is consistent with a high concentration of magnetite, ancient samples (i.e., GR18, BG14) have lower values indicating the presence of additional high coercivity materials. IRM unmixing results show that all modern samples which had living cyanobacteria layers possess a very small proportion of high coercivity material (e.g., GSL18 >300 mT, LB19 >100mT), which might be an indication of biogenic magnetite or just result from experimental noise. One of the interesting features found with ancient microbialites is that they have a high relative proportion of very high coercivity minerals (e.g., GR18 >100mT and 300mT, BG14 > 150 – 1000 mT), consistent with

hematite and/or goethite. However, this high-coercivity contribution does not contribute to the NRM. These high coercivity minerals might result from post-deposition of hematite

Domain states: Magnetic domain tests show a PSD and/or SD+MD mixture in modern and ancient microbialite samples. However, FORCs of modern microbialites (i.e., GSL18, LB19) show more PSD signatures compared to ancient samples (i.e., GR18, BG14). This might indicate that the growth of grain size of magnetic minerals over time, which may result in the change of PSD domain to MD behavior.

Diamagnetic vs Paramagnetic: Magnetization versus applied field shows negative high-field slopes (diamagnetic) for modern microbialites but positive (paramagnetic) for ancient microbialites. Ancient microbialites might contains paramagnetic materials such as siderite. The Curie points for the modern microbialites (i.e., GSL18, LB19) cannot be precisely defined (500 - 580°C) because they are strongly diamagnetic and have a very low c(T) signal:noise ratio. However, c(T) data from the two ancient microbialites (i.e., GR18, BG14) are more easily interpreted with a clear Curie temperature (550°C). The incorporation of paramagnetic material will increases overall susceptibility and thus increases signal:noise ratio.

Table 5.17 Summary of the magnetic properties' experiments on GSl18, GSL19, LB19, GR18, BG14 microbialites.

Samples	GSL18	GSL19	LB19	GR18	BG14
S-ratio	0.95	n.a.	> 0.99	0.84	0.42 - 0.95
$N_{components}$	2 or 3	3	1 or 2	3	2 or 3
$H_{cr_IRM\ unmixing}$	40.5, 48 mT	35 mT	30 - 50 mT	47 mT	35 - 50 mT
$H_{cr\ _Lowrie\text{-}Fuller}$	15 - 17 mT	18 - 23 mT	13 - 14 mT	18 - 22 mT	n.a.
T_b_soft	580 - 620 °C	580 - 600 °C	580 - 620 °C	620 °C	600 - 620 °C
T_b_medium	600 - 620 °C	350, 575 - 675 °C	550, 620 °C	650 - 675 °C	300, 500 - 675°C
T_b_hard	n.a.	> 675 °C	n.a.	n.a.	675°C
T_c_heating	520 - 560 °C	550 - 580 °C	550 °C	500 - 550 °C	520 - 560 °C
T_c_cooling	440 - 570 °C	580 °C	550 °C	520 - 560 °C,	440 - 570 °C
T_h_heating	500 °C	n.a	500 - 540 °C	480 - 530 °C	500 °C
T_h_cooling	300 - 400 °C	450 - 550 °C	n.a.	400 - 500 °C	300 - 400 °C
Domain$_{LF}$	MD	MD	SD	MD	n.a.
Domain$_{hys}$	PSD or MD	n.a.	PSD + MD	SD + MD or PSD	SD + MD or PSD
Domain$_{dayplot}$	PSD or SD + MD	n.a.	PSD or SD + MD	SD + MD or PSD	SD + MD or PSD
Domain$_{FORC}$	PSD + SD	n.a.	PSD + SD	SD + MD	SD + MD
Mineralogy 1	Magnetite or Titanomagnetite	Magnetite or Titanomagnetite	Magnetite or Titanomagnetite	Magnetite or Titanomagnetite	Magnetite or Titanomagnetite
Mineralogy 2	n.a.	Maghemite Pyrrhotite Hematite	n.a.	Hematite	Maghemite Pyrrhotite Hematite

S-ratio: the sample average S-ratio; **$N_{components}$**: number of observed components through IRM unmixing; **$H_{cr\ _IRM\ unmixing}$**: the major coercivity/dispersion extracted from IRM unmixing data; **$H_{cr_Lowrie\text{-}Fuller}$**: the coercivity defined by the intersection of IRM acquisition and decay (Lowrie-Fuller test); **T_b_soft**: the unblocking temperature (°C) of soft fragment (Coercivity >100mT) identified by 3D IRM technique; **T_b_medium**: the unblocking temperature (°C) of medium fragment (Coercivity >300mT) identified by 3D IRM technique; **T_b_hard**: the unblocking temperature (°C) of medium fragment (Coercivity >1T) identified by 3D IRM technique; **T_c_heating**: the Curie point from heating curve; **T_c _cooling**: the Curie point from cooling curve; **T_h_heating**: the Hopkinson peak observed from the susceptibility heating curve; **T_h_cooling**: the Hopkinson peak observed from the susceptibility cooling curve; **Domain$_{LF}$**: magnetic domain identified by Lowrie-Fuller test; **Domain$_{hys}$**: magnetic domain identified by hysteresis loops; **Domain$_{dayplot}$**: magnetic domain identified by dayplot; **Domain$_{FORC}$**: magnetic domain identified by First Order Reversal Curves (FORC). **Mineralogy 1**: Dominant mineralogy based on the seven experiments; **Mineralogy 2**: Additionl mineralogy based on the seven experiments.

Chapter 6: Microbialite Magnetization Processes

6.1. Introduction

There might be three possible ways for microbialites to incorporate magnetic particles and (in theory) accurately record the magnetic field: 1) a DRM (abiogenic); 2) biologically controlled minerals produced by magnetotactic bacteria living within the microbial mat (biogenic); and 3) biologically induced biomineralization (biogenic) (Figure 6.1).

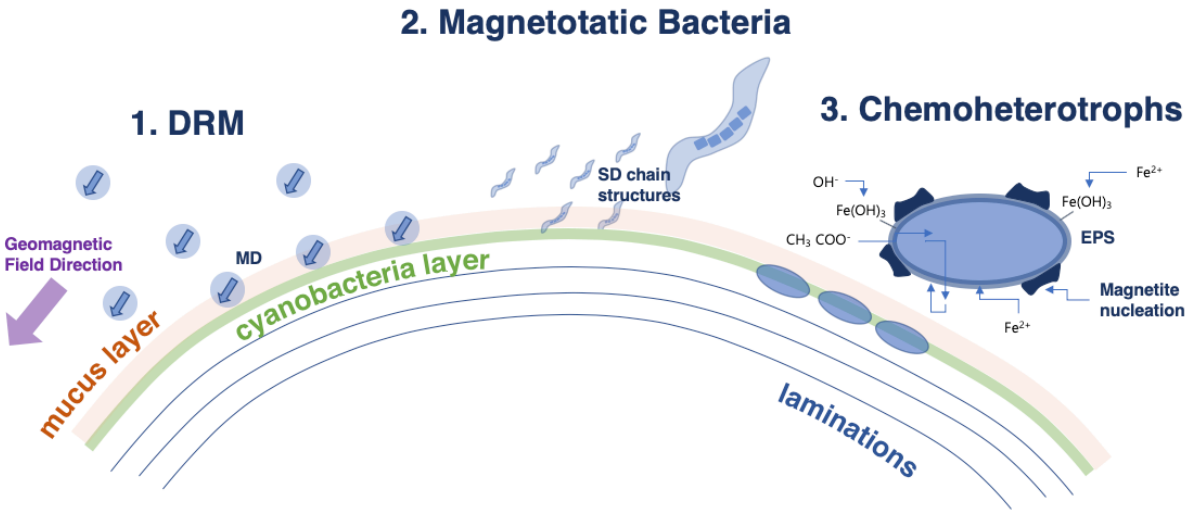

Figure 6.1. Diagram showing plausible magnetization processes for microbial mats, 1. Detrital remanent magnetization; 2. Biomagnetization by magnetotactic bacteria and 3. magnetite formed by iron-reducing bacteria

Detrital sediments would be trapped in the microbialite matrix, and if deposited magnetic particles are aligned to the field direction, this type of magnetization will be similar to magnetization in normal lakes or marine sediments (DRM). In the case of DRM, the magnetic domains will most likely have a wide variety of types from single-domain (SD) to multidomain (MD), depending on their source materials. A DRM may also be biomediated in that the "sticky" microbial mat may play a role in particle retention and immobilization. A recent study used bulk

magnetic susceptibility to differentiate between stromatolites that are biogenic or abiogenic in origin (Petryshyn et al., 2016). When magnetic particles are deposited on a sticky mucus created by microbial filaments, magnetic particles will be distributed uniformly, independent of lamination slope. However, we can expect higher bulk susceptibilities on the top and lower value on the sloping sides if the stromatolites went through a completely abiogenic growth process and DRM mechanism. It is also demonstrated that cyanobacterial mats trap and bind grains more readily than abiogenic carbonate precipitates.

The other potential sources of magnetic particles are magnetic minerals grown by iron biomineralization. Iron biomineralization can be either biologically controlled biomineralization (BCM) or biologically induced biomineralization (BIM). Magnetotactic bacteria (MTB) produce single-domain (SD) magnetosomes in chains by a BCM (matrix mediated) process. It is believed these chains are used to find the oxic-anoxic interface or transition zone (OATZ), aligning them to the Earth's magnetic field. Since a BCM process does not require a thermodynamically suitable environment for precipitating minerals, they are widely distributed and ubiquitous in most aquatic environments (Bazylinski, 2007; Bazylinski et al., 2007), but in general, they are absent in highly acidic or aerated environments. The OATZ zones are usually located at the sediment-water interface in many freshwater settings, and in the water column in some marine systems (Bazylinski, 2007; Bazylinski et al., 2007). Magnetite chains (and sometimes greigite) created by MTB have readily distinguishable crystal features (e.g., hexagonal prism, cuboid and teardrop) compared with minerals formed by BIM processes (e.g., amorphous and/or octahedral crystal magnetite). The magnetic domain state of magnetosomes should be predominantly single domain or pseudo-single domain. Previous studies documented the presence of MTB in ancient (Chang & Stolz, 1989) and modern stromatlitic environments (Stolz et al., 1987) by using rock magnetic

techniques and transmission electron microscopy to detect single domain magnetite unique crystal structures created by MTB.

Biogenic magnetite might be also produced extracellularly (BIM) thorough biomineralization by iron reducing bacteria (Konhauser et al., 2011). For example, chemoautotrophs convert amorphous ferric oxide to different types of iron-bearing minerals (e.g. magnetite) by coupling iron reduction to the oxidation of organic compounds. The magnetite formed by BIM process can occur as tiny (10-50 nm), rounded, poorly crystalline particles on cell surfaces (Konhauser & Riding, 2012). These particles would be SD if isolated, but they could approach PSD behavior if they are clustered. Under low oxygen and neutral pH settings, chemoheterotrophs reduce ferric iron to ferrous iron (coupling iron reduction) and may precipitate different types of iron-bearing minerals such as siderite, vivianite and pyrite if abundant ferric iron is present. Photoautotrophs and chemolithoautotrophs also produce ferric hydroxide minerals extracellularly by oxidizing ferrous iron (BIM) under certain conditions (Kendall et al., 2012).

To date, most paleomagnetic works on microbialites have either assumed a detrital origin or focused on documenting the presence of individual occurrences of magnetotactic bacteria or chemoautotrophs, not the complex system of microbialite magnetism including the DRM process. In this chapter, magnetization processes of microbialite samples are identified focusing on DRM and biomagnetism.

6.2. Methods

6.2.1. ARM vs NRM

An ARM produced in the laboratory tends to have very similar properties to and magnetizes the same grains as a TRM. These are relatively efficient methods of magnetizing a rock, in that a

relatively high degree of magnetic alignment is achieved in a relatively weak Earth-like field. This is in contrast to a typical DRM, which is relatively inefficient. By comparing ARM with NRM, we may therefore learn something about the magnetization process (Tauxe et al., 2010; Kodama, 2012). Since DRM is not an efficient way to record a magnetic moment, the ARM of materials that went through DRM processes is usually higher than NRM. This is because when magnetic particles are deposited in water, the particles are typically incorporated into larger sediment flocs such that the net vector magnetization is low compared to the saturation value. The aligning torque is also insufficient to fully align these larger flocs. The NRM intensity of materials which went through a TRM mechanism is similar to its ARM intensity, and when a specimen's NRM value is significantly higher than ARM, it can be an indication of IRM processes. Biomagnetization by microbial communities growing magnetic minerals aligning to the magnetic field might be similar to CRM processes and results in similar intensity value of NRM to ARM.

Living microbialite samples with cyanobacteria layer from Antelope Island (GSL18_0101, 0102, 0104, 0201, 0401, 0402) and LB (LB19_0101, LB19_0102, LB19_0304) were subjected to this experiment. In addition, the NRM/ARM ratio of lithified samples from GSL (GSL18_0301, GSL19_0202), LB (LB19_0301), GR (GR18_0101) and BG (BG14_0101) were calculated and GSL, GR and BG slices' NRM/ARM ratio were mapped out. ARM was acquired at 150 mT AF with a 0.05 mT bias field.

6.2.2. Anisotropy of Magnetic Susceptibility (AMS)

Magnetic anisotropy is a measure of the preferred alignment of magnetic particles or minerals in a rock, and the total anisotropy of a rock depends on the magnetic anisotropy of individual grains and their preferred orientation in a rock. Most individual magnetic particles have an energetically

preferred direction of magnetization related to magnetocrystalline or shape anisotropy. For example, while the easy magnetic axes for hematite are perpendicular to the crystallographic c-axis, equant magnetite particles have an easy axis along the cubic body diagonal (Kodama, 2012). Elongated magnetite particles have stronger magnetic susceptibility along the axis of elongation in order to reduce the energy (i.e. shape anisotropy).

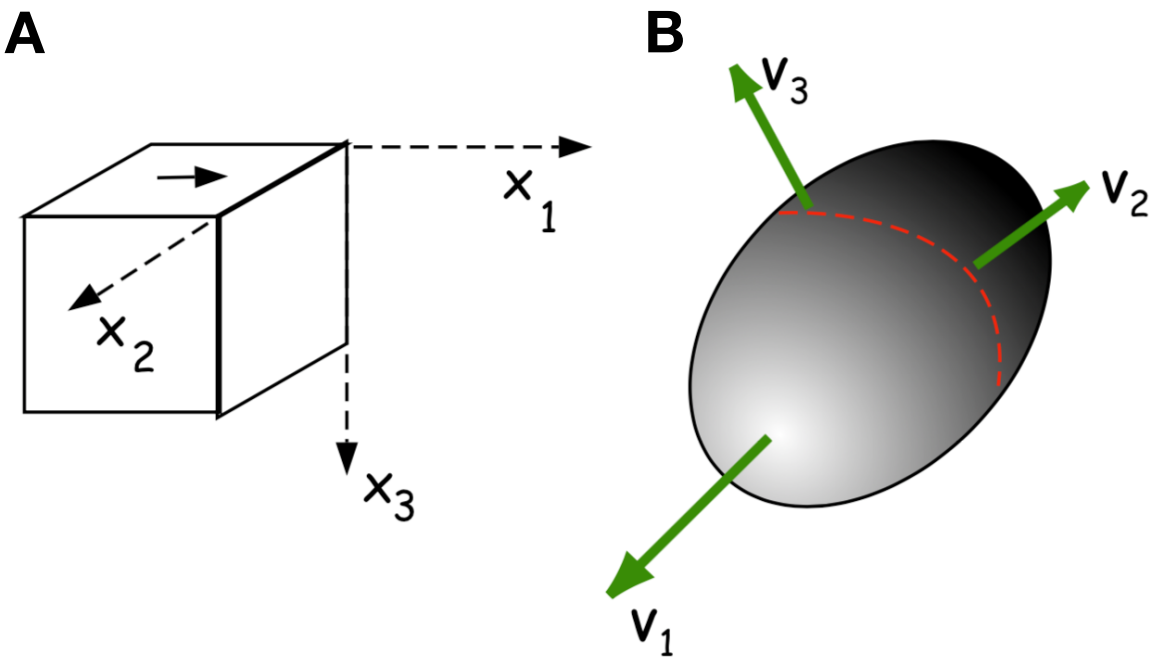

Figure 6.2. (A) Specimen coordinate system when measuring AMS. (B) Results can be visualized in terms of an anisotropy ellipsoid. The eigenvectors define the directions of maximum (V_1), intermediate (V_2) and minimum (V_3) susceptibility. The eigenvalues describe the lengths of each of these axes (From Tauxe et al., 2010).

Anisotropy of magnetic susceptibility (AMS) is a technique to detect geometrically preferred magnetic orientations in a rock. AMS is represented as an ellipsoid with the easy, intermediate, and hard directions of susceptibility represented by the maximum (V_1), intermediate (V_2) and minimum (V_3) ellipsoid axes (Figure 6.2.B). The AMS of a specimen (Figure 6.2.A) can be measured by rotating it about three orthogonal axes (i.e. X_1, X_2, X_3) under an applied alternating

field. Induced magnetism of the specimen in a coordinate system (M_i) is a function of applied field (H_i) on each axis, and this can be denoted as:

$$M_1 = \chi_{11}H_1 + \chi_{12}H_2 + \chi_{13}H_3$$
$$M_2 = \chi_{21}H_1 + \chi_{22}H_2 + \chi_{23}H_3$$
$$M_3 = \chi_{31}H_1 + \chi_{32}H_2 + \chi_{33}H_3$$

Numerically, AMS is represented by a second-order tensor (χ_{ij}) with 6 independent matrix elements because the matrix is symmetric (i.e., $\chi_{ij}=\chi_{ji}$), and the orientations of the ellipsoid axes are described by the tensor eigenvectors (V_1, V_2, and V_3). The lengths of the maximum (τ_1), intermediate (τ_2), and minimum (τ_3) axes are represented by the eigenvalues. The eigenvectors are plotted on a lower hemisphere stereonet as red squares (V_1), blue triangles (V_2) and black circles (V_3) respectively.

AMS may be used to interpret the direction of sediment transportation and/or deformation. It has also been used to determine flow direction in igneous rocks. Likewise, it might be also useful to understand whether microbialites' magnetic particles are created through biomagnetism or DRM processes. The assumption is that the magnetic fabrics would have a similar AMS to a sedimentary rock if DRM was a dominant magnetization processes, but if the magnetic fabrics of microbialites are biogenically created, AMS directions will be more randomized. In general, a typical sedimentary fabric in a quiet water environment has a minimum axis perpendicular to the bedding and displays oblate AMS ellipsoid with no preferred orientation within the bedding plate (Figure 6.3. B, F). Under weak and moderate flow conditions, the long axis is aligned with the flow (e.g., Figure 6.3. C, G). However, when sediments are deposited under high current flow, the maximum axis would be perpendicular to the flow direction and create a prolate or triaxial fabric (Tauxe, 2010).

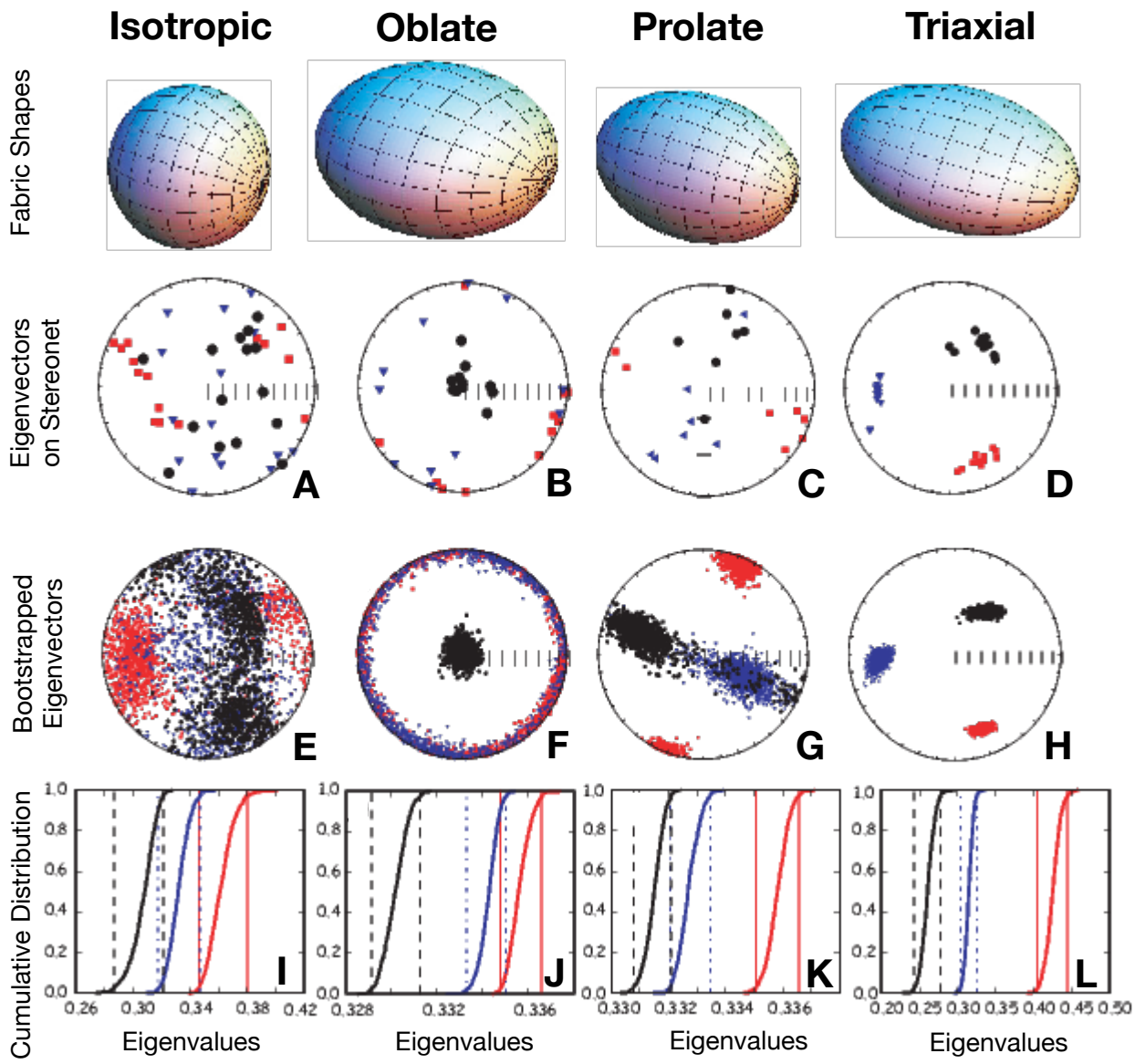

Figure 6.3. Classification of AMS fabric using bootstrap confidence ellipses. (Top) From left to right the shapes are defined as sphere/isotropic ($\tau_1 \cong \tau_2 \cong \tau_3$), oblate ($\tau_1 \cong \tau_2 > \tau_3$), prolate ($\tau_1 > \tau_2 \cong \tau_3$), and triaxial ($\tau_1 > \tau_2 > \tau_3$). Measured data sets plotted as eigenvectors from each specimen on stereonet (A-D), bootstrapped eigenvectors (E-H), and bootstrapped eigenvalue cumulative distribution graphs (I-L). (From Tauxe et al., 2010)

To assess uncertainty in the data, a bootstrap method is used (Constable & Tauxe, 1990; Tauxe et al., 2016) The bootstrap analysis is a resampling method where many paradata sets are created and used to calculate the mean and standard deviation. The bootstrapped eigenvectors can be plotted, and surfaces enclosing 95% of the bootstrapped eigenvectors provide 95% confidence

bounds on the directions. Cumulative distributions of the bootstrapped eigenvalues can be used to describe the shape of the magnetic fabric as (Figure 6.3): spherical ($\tau_1 \cong \tau_2 \cong \tau_3$), oblate ($\tau_1 \cong \tau_2 > \tau_3$), prolate ($\tau_1 > \tau_2 \cong \tau_3$), or triaxial ($\tau_1 > \tau_2 > \tau_3$).

The above describes the fabric of an assemblage of specimens. However, if an individual specimen is not anisotropic or is otherwise problematic, it may be inappropriate to include in the sample analysis. Specimens were therefore subjected several criteria before incorporation into sample-level fabric analysis. First, specimen-level results with negative eigenvalues were excluded because negative eigenvalues are physically unmeaningful and likely result from a low signal:noise ratio and/or low ferromagneic:diamagnetic ratio. Second, specimens were subjected to an F-test (Hext, 1963) to determine whether or not they are statistically anisotropic. F-test statistics compare the variation between eigenvalues to a measure of the data misfit. Three parameters F, F_{12}, and F_{13}, and can be calculated as:

$$F = 0.4\frac{(\tau_1^2 + \tau_2^2 + \tau_3^2 - 3\chi_b^2)}{\sigma^2}$$

$$F_{12} = 0.5\left(\frac{\tau_1 - \tau_2}{\sigma^2}\right)^2$$

$$F_{23} = 0.5\left(\frac{\tau_2 - \tau_3}{\sigma^2}\right)^2$$

where the χ_b and σ^2 are the bulk susceptibility and estimated variance. σ^2 is defined as the square root of the residual sum of squares over the number of degrees of freedom and is a measure of misfit between the data and the best fit tensor. A specimen can be tested whether it is isotropic ($\tau_1 \cong \tau_2 \cong \tau_3$) (F), oblate ($\tau_1 \cong \tau_2$) ($F_{12}$), or prolate ($\tau_2 \cong \tau_3$) ($F_{23}$). If the calculated F values exceed critical values of 3.4817, 4.2565, and 4.2565 for F, F_{12}, and F_{23}, respectively, the specimen is considered anisotropic at the 95% confidence level. Specimens that failed the F test ($F < 3.4817$) were excluded from analysis. If a sample has many isotropic specimens, that might be interpreted

to results from CRM by biomagnetism (amorphous magnetite created by BIM or randomized growth of magnetic minerals). The specimens that passed the F-test have high similar susceptibility values compared to specimens of $F < 3.48$. This eliminates the possibility of F-test failure that caused by a low signal:noise ratio.

AMS measurements of GSL18_0301 (20 specimens), GSL19_0202 (6 specimens), GR18_0101 (103 specimens), and BG14_0101 (27 specimens) were conducted. Only specimens which have positive susceptibility and pass the F test were used for fabric analysis. To analyze uncertainty in principal mean orientations, 95% confidence ellipses were created using a bootstrap method for paleomagnetic tensors by using PmaPy software (Tauxe et al., 2016).

6.2.3. Low-temperature test for biogenic magnetite

Moskowitz (1993) defined a diagnostic rock magnetic criteria for the detection of biogenic magnetite. The Verwey transition (T_V) is a crystallographic phase transition of magnetite at 120K, where magnetite transforms from cubic at $T > 120$ K to monoclinic at $T < 120$K. This crystallographic transformation results in a rotation of the magnetic remanence and typically a sharp decrease magnetization. The test makes use of T_V by measuring the difference in remanence lost on warming through T_V after cooling in a strong field versus cooling in zero field. Moskowitz (1993) found that the chains of SD magnetite found in MTB have a diagnostic signature (Figure 6.4).

This experiment was carried out at the Institute for Rock Magnetism using the Magnetic Properties Measurement System (MPMS). Four living microbialites specimens of LB19_0305 were measured. A sample is first cooled in a 2.5 T field (field cooled, FC) from room temperature to 20 K. The field is turned off, and the remanence is measured during warming back to room

temperature. The sample is then cooled back to 20 K in zero field (zero field cooled, ZFC). At 20 K, a 2.5 T IRM is imparted, the field is then turned off, and the sample is again measured on warming back to room temperature.

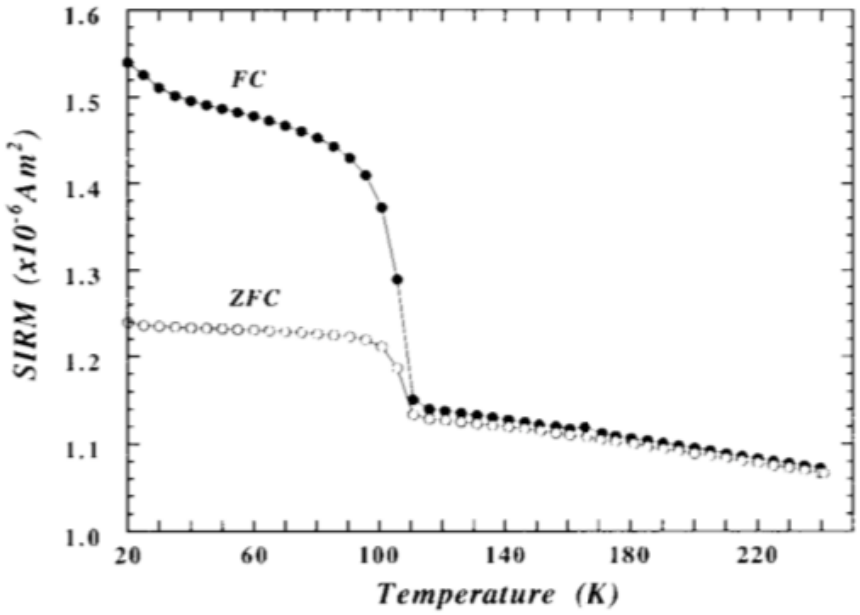

Figure 6.4. A comparison of 2.5 T IRMs of FC (closed circles) and ZFC (opened circles) treatments of a biogenic magnetite. The Verwey transition at 100K is more conspicuous after FC treatment than ZFC, and initial IRM intensity at 20 K is 25-30 % greater (From Moskowitz et al, 1993).

6.3. Results

6.3.1. ARM vs NRM

Of the measured microbialites, most ARM intensities are higher than NRM, as expected for DRM (Figure 6.5). The x-axis and y-axis of the figure represent the intensity of NRM and ARM (Am^2/kg), and the black line has a gradient of 1. Specimens that plot on the left side of the black line have NRM<ARM, which is consistent with a DRM origin. Specimens which have NRM>>ARM (right side of the black line), in contrast, may have been exposed to high fields and have an IRM. Specimens with NRM intensity values similar to ARM intensity (± 10%) may imply biogenic, chemical, or thermal magnetization processes.

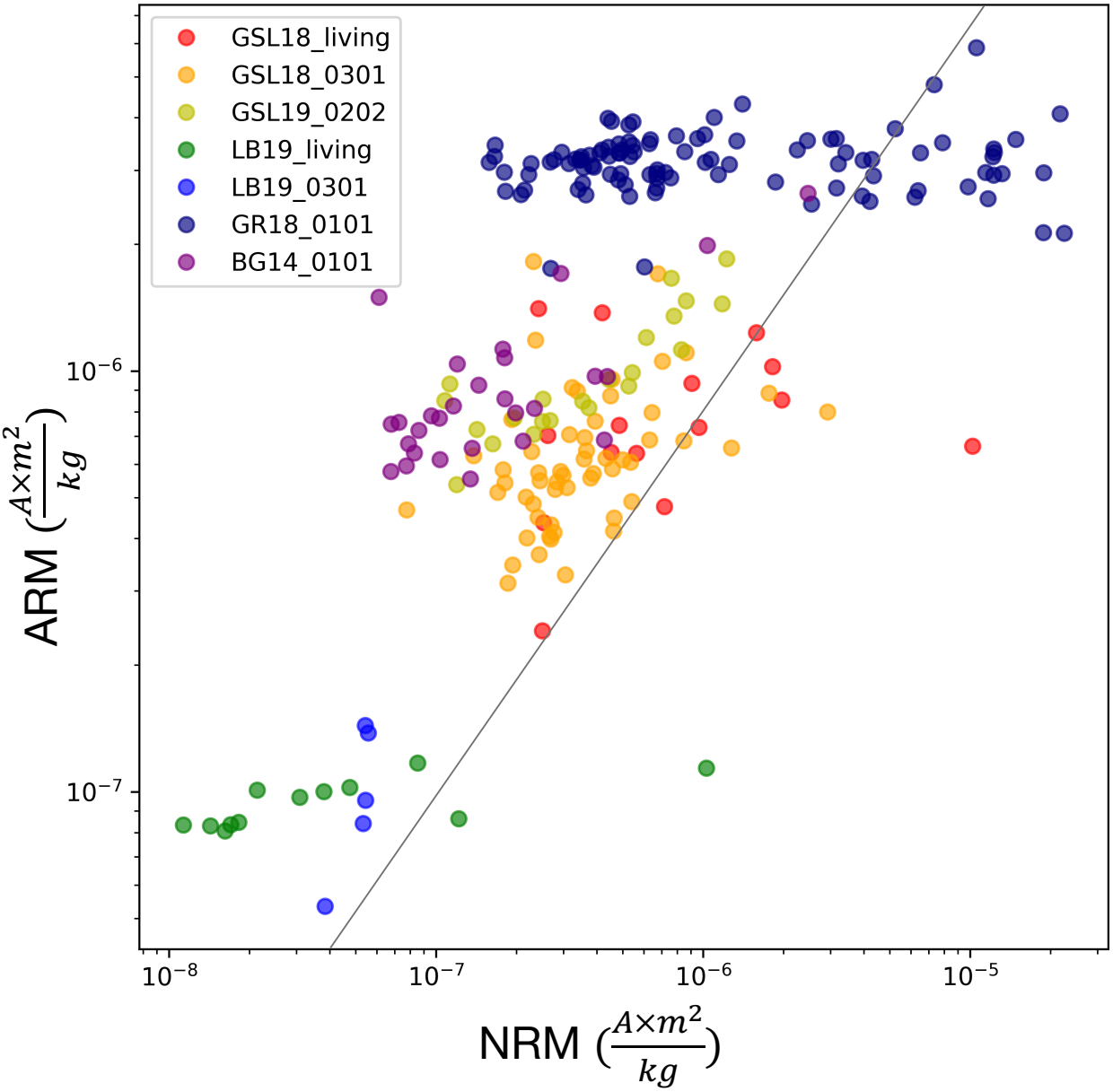

Figure 6.5. NRM intensity (x-axis) versus ARM intensity (y-axis) of microbialites on log scales. The sample group of GSL18_living (GSL18 living microbialites with cyanobacteria layer collected from Antelope Island Site 1,2 and 4), GSL18_0301 (lithified microbialite from Antelope Island Site 3), GSL19_0202 (lithified modern microbialite from Lakeside Site 2), LB19_living (surface living microbialite samples collected from LB19 Site 1 and 3), LB19_0301 (lithified porous microbialite sample from LB19 Site 3), GR18_0101 (Eocene Green River formation microbialite), BG14_0101 (Cambrian Bayan Gol formation stromatolite) are shown with red, orange, yellow, green, blue, navy, and purple circles. The black line represents y=x. Left of the black line (ARM>>NRM), is consistent with a DRM origin. Right of the black line (ARM<<NRM), may indicate magnetization via an IRM. Specimens near the black line (ARM≈NRM) may have an NRM resulting from biogenic processes.

GSL: The majority of GSL lithified and living samples have NRM < ARM. Of the Antelope Island specimens subsampled from living microbialites with cyanobacteria layers (GSL18_0101, 0102, 0104, 0201, 0202, 0401, 0402; red circles on Figure 6.5), 6 out of 15 have NRM/ARM > 1. Three specimens display ARM value close to NRM (NRM/ARM: 0.90 to 1.1). The lithified microbialite sample from Antelope Island (GSL18_0301; orange circles on Figure 6.5) shows that 4 out of 55 specimens have NRM > ARM intensity, 4 specimens have NRM/ARM ratio in the range of 0.90 and 1.1, and the remainder have NRM < ARM. However, none of the 22 specimens from the Pleistocene lithified microbialite from Lakeside (GSL19_0202) have NRM > ARM (yellow circles on Figure 6.5). The geometric mean of the NRM/ARM of GSL18_living, GSL18_0301, GSL19_0202 are 0.98, 0.57, and 0.37, respectively. The NRM/ARM intensity of GSL18_0301 A, B, C, D, E and GSL19_0202 were mapped out (Figure 6.6). While GSL19_0301 shows dispersed spots where NRM > ARM, GSL19_0202_A has a ratio less than 1 and a pattern very similar to the NRM intensity mapping (Figure 5.4), showing very low NRM/ARM ratio in the middle of the structure.

LB: LB samples exhibit low intensity in both NRM and ARM results compared to other microbialites. The results show that 2 out of 13 specimens from the LB surface living cyanobacteria layer (LB19_0101, LB19_0102, LB19_0304) show NRM > ARM (green circles on Figure 6.5). No specimens from the porous but lithified LB microbialite (LB19_0301) have NRM > ARM (blue circles on Figure 6.5).

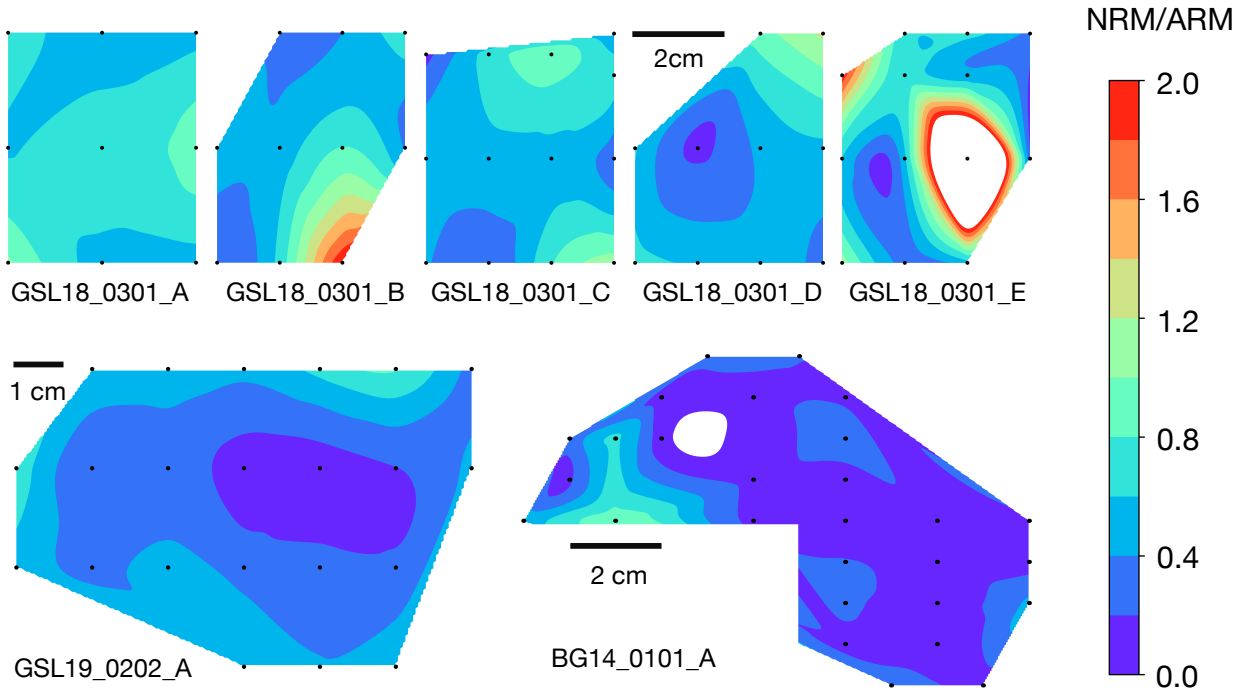

Figure 6.6. Mapping of NRM intensity /ARM intensity ratio of GSL18_0301 A, B, C, D, E slices (Top); slice A of GSL19_0202 sample (Bottom left); and slice A of BG14_0101sample. Black dots represent actual measurement positions, and the NRM/ARM ratio is mapped out with cubic interpolation (refer color bar on the right). Values less than one (NRM < ARM) are consistent with magnetization by DRM processes. A value close to 1 or significantly more than 1 might represent biogenic processes and IRM processes, respectively.

GR: The GR microbialite sample (GR18_0101) displays high values in both ARM and NRM intensity with a wide range of NRM/ARM ratios (navy circles in Figure 6.5), and the geometric mean of the NRM/ARM ratio is 0.36. NRM/ARM for highly magnetized specimens are more than 1 and some specimens are even more than 12. The distribution of the mapping is displayed in Figure 6.7. The mapping shows a similar pattern with NRM intensity mapping (Figure 3.5), showing the two highly magnetized spots at the bottom. In consideration of results from sections in previous chapters (See Section 3.4.1.3 spatial variation mapping; Section 4.3.3 directional analysis; Section 5.3.1 S-ratio; and Section. 5.3.2 IRM Unmixing), this result also supports the interpretation of an IRM process in the GR microbialite.

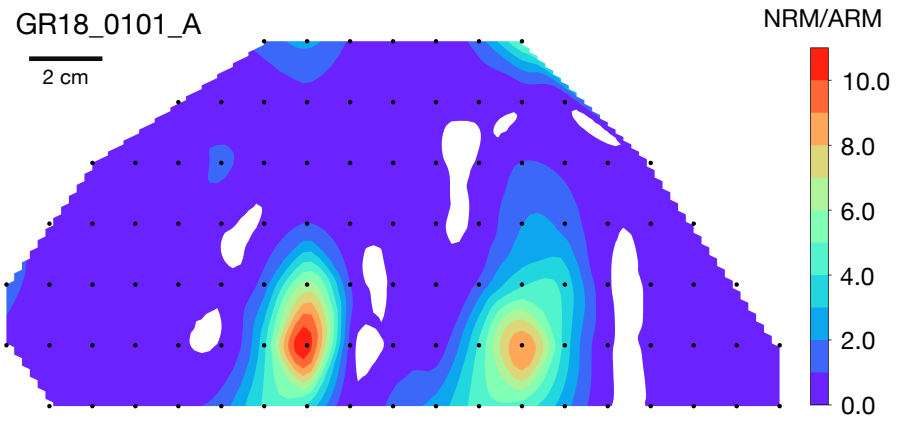

Figure 6.7. Mapping of NRM intensity/ARM intensity ratio the slice A of the GR18_0101 sample. Black dots represent actual measurement positions, and the NRM/ARM ratio are mapped out with cubic interpolation (refer color bar on the right). Values less than one (ARM > NRM) are consistent with magnetization by DRM processes. The ratio value more than 1 might represent IRM process.

BG: The Cambrian Bayan Gol formation stromatolite has no specimens where NRM > ARM and has a geometric mean NRM/ARM ratio of 0.19. The spatial variations in the NRM to ARM intensity ratio does not correlate with any of NRM intensity, susceptibility, S-ratio or IRM unmixing. It might demonstrate that the origin of the BG is mostly DRM.

6.3.2. Anisotropy of Magnetic Susceptibility (AMS)

GSL: The lithified microbialites from Antelope Island (GSL18_0301) and from Lakeside (GSL19_0202) were subjected to AMS tests. Only 4 out of 20 specimens from GSL18_0301 have positive eigenvalues and pass the F-test for anisotropy. The eigenvectors of GSL18_0301 show the characteristics of triaxial fabric (Figure 6.8 bottom). GSL19_0202 specimens all have positive eigenvalues and 4 out of 6 specimens from GSL19_0202 pass the F-test. The GSL19_0202 sample also displays a triaxial fabric.

This might indicate that the magnetization process of GSL18_0301 and GSL19_0202 was mixture of two processes (i.e., DRM and Biomagnetization processes). Deposition of the magnetic particles under (non-turbulent) flowing water results in long axis aligned with the flow and results

in triaxial or prolate fabric. However, specimens or samples with isotropic fabrics might be explained by growth of new magnetic particles by biomagnetization processes after the physical deposition.

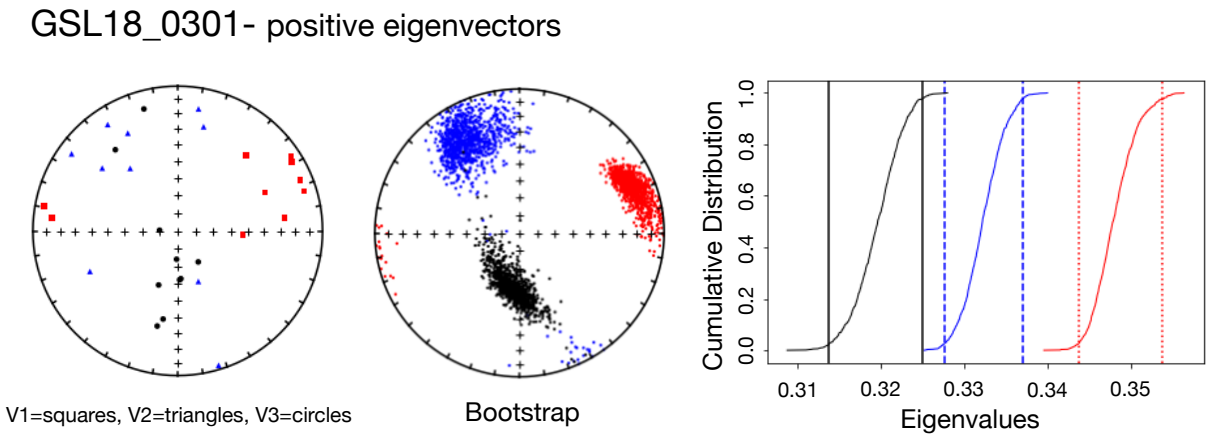

Figure 6.8. AMS results of GSL18_0301 specimens that have positive eigenvalues (top) and that have positive eigenvalues specimens and pass the F test (F > 3.481) (bottom). Measured data sets plotted as eigenvectors from each specimen (left). The maximum, intermediate, and minimum susceptibility are shown as red square, blue triangle and black circle, respectively. Bootstrapped eigenvectors with confidence ellipses (center), and bootstrapped eigenvalue cumulative distribution graphs (right).

GR: The AMS of 103 specimens of GR microbialite were measured, and 100 specimens have positive eigenvalues and pass the F-test for anisotropy (Figure 6.9). The eigenvectors show the characteristics of a horizontal oblate ellipsoid, which might indicate that the dominant

magnetization process was DRM. In a stagnant lacustrine environment, this fabric will occur when the platy magnetic particles or flakes are preferentially deposited horizontally and/or elongate magnetic particles are deposited with long axis randomly oriented within the bedding plane.

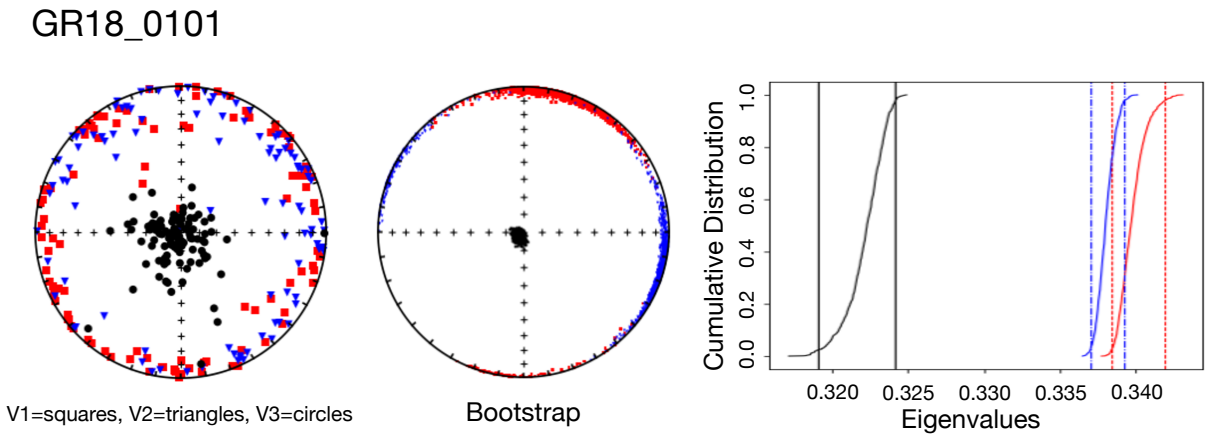

Figure 6.9. AMS results of GR18_0101 specimens. Measured data sets plotted as eigenvectors from each specimen (left). The maximum, intermediate, and minimum susceptibility are shown as red square, blue triangle and black circle, respectively. Bootstrapped eigenvectors with confidence ellipses (center), and bootstrapped eigenvalue cumulative distribution graphs (right).

BG: Out of the total of 26 specimens of BG14_0101, 20 have positive eigenvalues (Figure 6.10 top). Ten specimens which pass the F-test are plotted on bottom of the Figure 6.10. The eigenvectors show the characteristics of a triaxial fabric. This might indicate that the magnetization process was a DRM, with deposition of the magnetic particles under moderate flowing water. Similar to GSL results, isotropic specimens might reflect a greater magnetization contribution from biomagnetization after or during physical deposition.

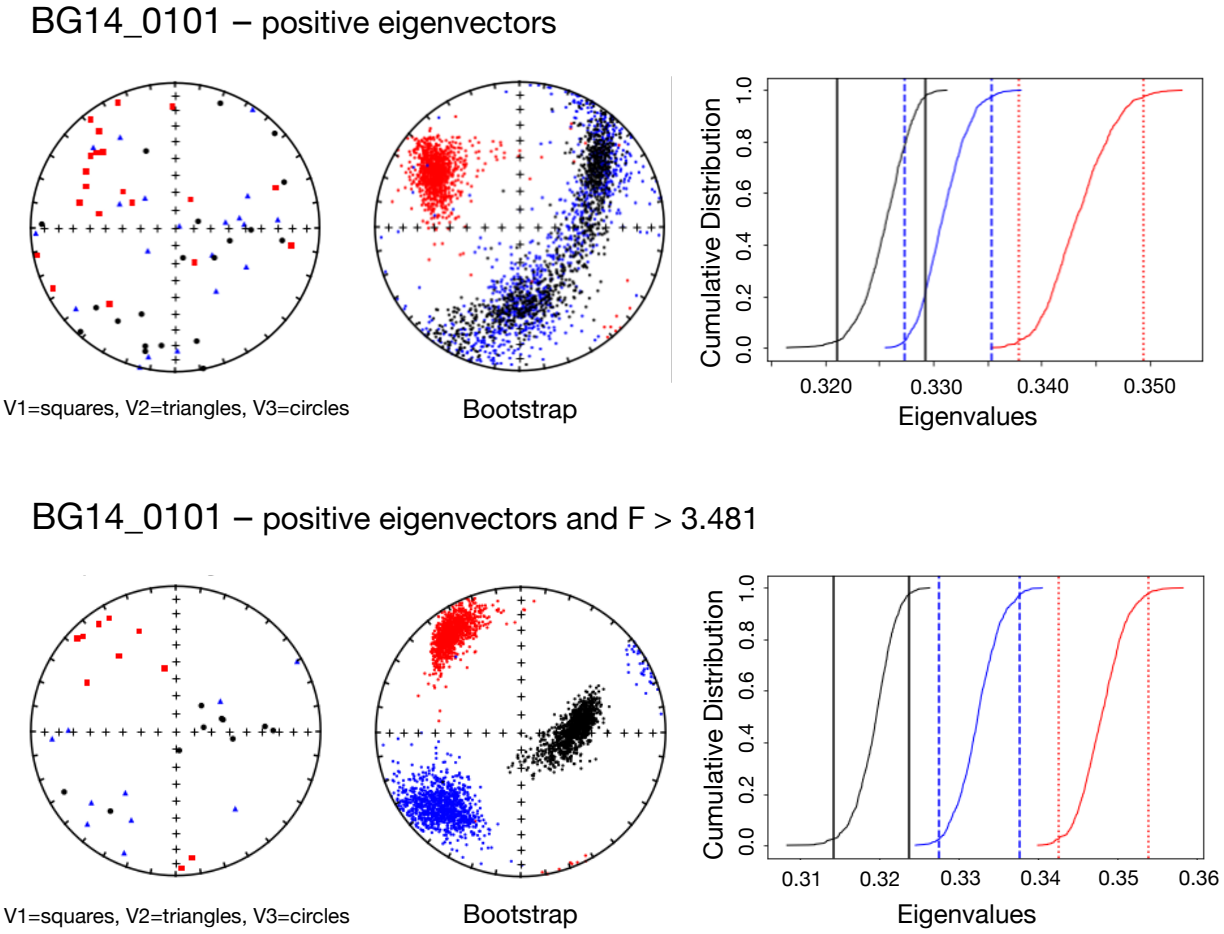

Figure 6.8. AMS results of BG14_0101 specimens that have positive eigenvalues (top) and that have positive eigenvalues specimens and pass the F test (F > 3.481) (bottom). Measured data sets plotted as eigenvectors from each specimen (left). The maximum, intermediate, and minimum susceptibility are shown as red square, blue triangle and black circle, respectively. Bootstrapped eigenvectors with confidence ellipses (center), and bootstrapped eigenvalue cumulative distribution graphs (right).

6.3.3. Low-temperature test for biogenic magnetite

MPMS results from four specimens from sample LB19_0305 show that a decrease of sIRM with increasing temperature, but there is no signature of the Verwey transition around 120 K in both curves (Figure 6.11: LB19_0305_04). The signature of biogenic or inorganic magnetite was not found in the specimens. Another possible explanation is the oxidation of magnetite to

maghemite before sample measurements. The Verwey transition is not present in maghemite. Appendix H includes additional MPMS measurements of LB19_0305_01 and LB19_0305_03.

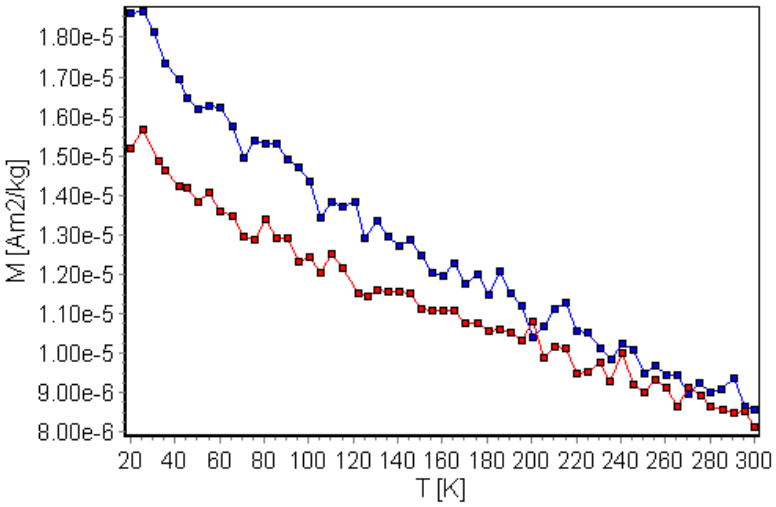

Figure 6.11. MPMS measurement of specimen LB19_0305_04. A 2.5 T IRM is measured on warming after cooling in zero field (ZFC; red) and after cooling in a 2.5 T field (FC; blue). There is no evidence for the Verwey transition, and the experiment therefore failed to detect biogenic magnetite.

6.4. Summary/ Discussion

The combined results suggest that the major magnetization process of microbialites is DRM but there may be a contribution of biogenic origin. Lithified GSL, LB, BG microbialites have a mixture of DRM and biomagnetization processes, and GSL18 and LB19 microbialites have a greater signature of biogenic origin. These primary magnetizations, however, can be overprinted by other processes. For example, the GR microbialite's primary magnetization was purely DRM, but the sample was remagnetized by an IRM.

6.4.1. DRM

Based on NRM/ARM intensity ratios less than 1, most of the samples may have been magnetized by DRM processes, but some of the specimens experienced other types of magnetism (NRM $\geq$ ARM). The AMS results of the GSL and BG microbialite display triaxial fabrics, and

the GR microbialite has an oblate fabric. The results are consistent with sedimentary deposition in a gentle water current (triaxial) for GSL and BG samples and a stagnant water environment (oblate) for GR samples.

6.4.2. Biomagnetism

With the exception of the GR microbialite (IRM processes), some of the microbialite specimens have NRM/ARM values close to 1. In particular, some living GSL and LB specimens which contain cyanobacteria layers shown NRM/ARM value close to 1. If microbial communities grow magnetic as either BCM or BIM, the minerals may be magnetized in alignment with the magnetic field, which might be a process similar to CRM. The ratio of CRM/ARM is normally higher than DRM, showing values close to 1, which might suggest some microbialites have a biogenic magnetization. AMS results of GSL and BG microbialites display a signature interpreted to arise from biomagnetism. Specimens which are isotropic (which do not pass the F test) might result from of magnetic mineral growth by BIM. The MPMS FC-ZFC experiment of the LB living microbialite was inconclusive in the test for biogenic magnetite chains (BCM). It did not show any magnetite phase transition, probably due to oxidation before measurement.

Chapter 7: Conclusions

7.1 General Observations and Summary

Do microbialites carry magnetization that is stable in time? Although microbialites possess a high proportion of diamagnetic minerals and relatively low concentration of ferromagnetic minerals, all microbialites have permanent magnetic signatures. The GSL18 and LB19 living microbialites show that magnetic mineralogy changes as the samples are removed from the environments based on the magnetic susceptibility measurement over time. However, the NRM intensity of the majority of GSL18 over time showed that living microbialites have stable NRM. The changes in susceptibility may therefore be associated mostly with changes in the paramagnetic and/or superparamagnetic fraction that does not carry remanence.

What are the spatial variations in magnetization within the microbialite structure? The implication of spatial variations is with respect to magnetization processes and the reliability of NRM. If a microbialite displays homogenous magnetization continuity along laminations, and variations across laminations, this suggests a magnetic concentration and magnetization distribution associated with primary deposition. If a microbialite has inhomogeneous magnetization distribution along laminations, it suggests a very heterogeneous incorporation detrital material and/or a different primary magnetization processes (biomagnetization) or a secondary magnetization. The NRM intensity mapping shows inhomogeneous magnetic distribution within microbialites, with the exception of GSL19 microbialites (from Lakeside). Magnetic susceptibility mappings of GSL18 and 19 microbialites are similar to NRM intensity mappings, but other microbialites display discrepancies. The susceptibility high in LB19 long core which is not accompanied by an NRM high might result from hurricane events or be related to the

change of growth structure mode. For the GR18 microbialite, IRM by lightening or possibly by some other artificial mechanism post-sampling may have overprinted the NRM distribution. The BG14 microbialite susceptibility, displays homogenous continuity along laminations and variations across laminations which are not as evident in the NRM. This discrepancy might represent an additional deposition of paramagnetic minerals or ferromagnetic materials that do not contribute to NRM.

Do microbialites accurately record Earth's magnetic field direction? The results show that, with the exception of the microbialite sample from the GR18 microbialite, the ChRMs of other microbialites (M >1.00E-07 Am^2/kg) appear to record directions close to the expected field. The deviation away from expected values (declination $\pm$ 10°, inclination $\pm$ 20°) most likely results from the effects of deposition on sloping beds (e.g., GSL18 and BG14) and water current (e.g., LB19).

What are the magnetic carriers in the microbialites? Combining all rock magnetic results, the dominant coercivity component that carries the NRM is inferred to be pseudo-single-domain to multi-domain magnetite for all microbialites. However, lithified microbialites (i.e., GSL19, GR18, and BG14) appear to contain some other high coercivity minerals, which might be hematite, but these minerals do not carry NRM. The specific magnetic properties of each microbialite are listed in Table 5.17.

What is the magnetization process or the origin of the magnetization? The combined results suggest that the major magnetization process of microbialites is DRM, but there may be a contribution of biogenic origin. Based on the NRM/ARM ratio, all microbialites present DRM as the main magnetization process, but GSL18 and LB19 living microbialites have a greater signature of biogenic origin. AMS results from GSL18, GSL19, and BG14 microbialites suggest a mixture

of DRM and biomagnetization processes. The GR18 microbialite has a typical sedimentary AMS fabric, but the primary magnetization appears to be overprinted by an IRM.

7.2. Assessment as a Paleomagnetic Recorder

In this study, microbialites are shown to have a high potential for paleomagnetic reconstructions. Microbialites contain ferromagnetic materials and record a stable NRM by DRM and/or biogenic processes. The timing of the microbialites' magnetization is inferred to be close to the physical deposition of magnetic minerals based on the directional variations associated with bedding slopes and water flow conditions. However, there are limitations for using a microbialite as a paleomagnetic recorder due to their relatively low magnetization and directional deviations caused by bedding slopes and water current. The time variations in magnetic susceptibility observed in living microbialites indicates the potential for diagenetic changes in the magnetic mineralogy and magnetization. However, the lack of clear, corresponding changes in NRM suggests that susceptibility changes may be limited to paramagnetic and/or superparamagnetic fractions. The implication for ancient samples is that a primary NRM is not necessarily overprinted by chemical changes as the microbialites become incorporated into the geologic record.

Suggestions for addressing some of the practical problems are below:

NRM intensity limit: Microbialites that have a magnetization intensity more than 1.00E-07Am^2/kg are shown to be plausible paleomagnetic recorders. The directional information from microbialites magnetized less than 1.00E-07 Am^2/kg are unreliable due to the moment sensitivity limit of the cryogenic SQUID magnetometers (1.00E-12 to 1.00E-03 Am^2) and the moment of the sample containers (1.00E-12 to 1.00E-10 Am^2). This also limits the spatial resolution at which

microbialite samples can be evaluated because smaller subsampling results in even weaker measured moments. Higher spatial resolution would theoretically translate to recovering magnetic directions at a higher temporal resolution that was possible in this study. It is possible that more sensitive instrumentation and/or preparation using containers that are more magnetically clean would allow reliable information to be extracted from these weakly magnetic samples.

Sample collection and preparation: To reduce the effects of sloping beds, samples should be collected avoiding steep sides or by sampling all sides for large domal structures. Sample slices should be cut parallel to the expected direction of the magnetic declination for smaller-scale hand samples. Then, specimens from different lamination angles should be collected to average out the deviations generated by sloping beds. The best sampling sites for living and unlithified microbialites would be stagnant water environment, and microbialites growing under turbulent water environment should be excluded.

Sample preservation for living microbialites: While lithified microbialites are shown to carry stable magnetization, living and modern microbialites displayed the reduction of magnetic susceptibility under artificial environmental settings. This can be explained by the destruction of paramagnetic or superparamagnetic, or transformation to a less magnetic form, but not the change of ferromagnetic particles. However, environmental and laboratory settings such as humidity, temperature, and pH conditions should be considered, and an effort made to keep similar environmental conditions to the sites before assessing the magnetic mineralogy of living and modern microbialites.

REFERENCES

Awramik, S. M., & Buchheim, P. H. (2015). Giant stromatolites of the eocene green river formation (Colorado, USA). *Geology, 43*(8), 691–694. doi:10.1130/G36793.1

Baskin, R. L. (2014). Occurrence and spatial distribution of microbial bioherms in Great Salt Lake, Utah, PhD dissertation, 203 pp, University of Utah.

Bazylinski, D. A. (2007). Magnetism and Biology: The Magnetotactic Bacteria. *Gravitational and Space Research, 17*(2), 115–126.

Bazylinski, Dennis A., Frankel, R. B., & Konhauser, K. O. (2007). Modes of biomineralization of magnetite by microbes. *Geomicrobiology Journal, 24*(6), 465–475. doi:10.1080/01490450701572259

Berelson, W. M., Corsetti, F. A., Pepe-Ranney, C., Hammond, D. E., Beaumont, W., & Spear, J. R. (2011). Hot spring siliceous stromatolites from Yellowstone National Park: Assessing growth rate and laminae formation. *Geobiology, 9*(5), 411–424. doi:10.1111/j.1472-4669.2011.00288.x

Besse, J. & Courtillot, V. (2002). Apparent and true polar wander and the geometry of the geomagnetic field over the last 200 Myr. *J. Geophys. Res*, *107*, doi:10.1029/2000JB000050

Bourne, M. D., Feinberg, J. M., Strauss, B. E., Hardt, B., Cheng, H., Rowe, H. D., Lawrence Edwards, R. (2015). Long-term changes in precipitation recorded by magnetic minerals in speleothems. *Geology, 43*(7), 595–598. doi:10.1130/G36695.1

Bouton, A., Vennin, E., Boulle, J., Pace, A., Bourillot, R., Thomazo, C., Visscher, P. T. (2016). Linking the distribution of microbial deposits from the Great Salt Lake (Utah, USA) to tectonic and climatic processes. *Biogeosciences, 13*(19), 5511–5526. doi:10.5194/bg-13-5511-2016

Brady, A. L., Slater, G., Laval, B., & Lim, D. S. (2009). Constraining carbon sources and growth rates of freshwater microbialites in Pavilion Lake using 14C analysis. *Geobiology, 7*(5), 544–555. doi:10.1111/j.1472-4669.2009.00215.x

Burns, B. P., Anitori, R., Butterworth, P., Henneberger, R., Goh, F., Allen, M. A., Neilan, B. A. (2009). Modern analogues and the early history of microbial life. *Precambrian Research, 173*(1–4), 10–18. doi:10.1016/j.precamres.2009.05.006

Burns, B. P., Goh, F., Allen, M., & Neilan, B. A. (2004). Microbial diversity of extant stromatolites in the hypersaline marine environment of Shark Bay, Australia. *Environmental Microbiology, 6*(10), 1096–1101. doi:10.1111/j.1462-2920.2004.00651.x

Butler, R. F. (1992). *Paleomagnetism: Magnetic Domains to Geologic Terranes*.Blackwell Scientific Publications, New Jersey.238 pp

Castro, S. I. (2014). Freshwater microbialites from Laguna Bacalar, Quintana Roo, Mexico: effects controlling their grow, M.S. thesis, 134 pp, University of Alberta.

Castro, S.I., Gingras, M.K, Pecoits, E., Aubet, N.R., Retrash, D., Castro,S. M., Konfuser,K.O. (2014). Textural and Geochemical Features of Freshwater Microbialites From Laguna Bacalar, Quintana Roo, Mexico. *Palaios, 29*(5), 192–209. doi: 10.2110/palo.2013.063

Chang, S.-B. R., & Stolz, J. F. (1989). Biogenic magnetite in stromatolites. II. Occurrence in ancient sedimentary environments. *Precambrian Research, 43*, 305–315. doi:10.1016/0301-9268(89)90061-2

Chivas, A. R. (1990). Growth rates and Holocene development of stromatolites from Shark Bay, Western Australia. *Australian Journal of Earth Sciences, 37*(37), 113–121. doi:10.1080/08120099008727913

Constable, C. & Tauxe, L. (1990). The bootstrap for magnetic susceptibility tensors. *J. Geophys. Res., 95*, 8383–8395. doi:10.1029/JB095iB06p08383

Constable, C., Korte, M., & Panovska, S. (2016). Persistent high paleosecular variation activity in southern hemisphere for at least 10 000 years. *Earth and Planetary Science Letters, 453*, 78–86. doi:10.1016/j.epsl.2016.08.015

Day, R., Fuller, M. D., & Schmidt, V. A. (1977). Hysteresis properties of titano- magnetites: grain size and composition dependence. *Phys. Earth Planet. Inter., 13*, 260–266. doi:10.1016/0031-9201(77)90108-X

Dunlop, D. (2002). Theory and application of the Day plot (Mrs/Ms versus Hcr/Hc) 2. Application to data for rocks, sediments, and soils. *J. Geophys. Res, 107,* doi:10.1029/2001JB000487.

Edgcomb, V. P., Bernhard, J. M., Summons, R. E., Orsi, W., Beaudoin, D., & Visscher, P. T. (2014). Active eukaryotes in microbialites from Highborne Cay, Bahamas, and Hamelin Pool (Shark Bay), Australia. *ISME Journal, 8*(2), 418–429. doi:10.1038/ismej.2013.130

Egli, R. (2003). Analysis of the field dependence of remanent magnetization curves. *J. Geophy. Res., 108*(B2) doi:10.1029/2002JB002023

Evans, D. A., Zhuravlev, A. Y., Budney, C. J., and Kirschvink, J. L. (1996). Palaeomagnetism of the Bayan Gol Formation, western Mongolia. *Geological Magazine, 133*(4), 487-496. doi:10.1017/S0016756800007615

Ferris, F. G., Thompson, J. B., Beveridge, T. J., Ferris, F. G., & Thompson, J. B. (2016). Modern Freshwater Microbialites from Kelly Lake, British Columbia, Canada . *Palaios 12*(3),213-219. doi:10.2307/3515423

Fisher, R. A. (1953). Dispersion on a sphere. *Proc. Roy. Soc. London, Ser. A, 217*, 295–305. doi:10.1098/rspa.1953.0064

Frantz, C. M., Petryshyn, V. A., Marenco, P. J., Tripati, A., Berelson, W. M., & Corsetti, F. A. (2014). Dramatic local environmental change during the early eocene climatic optimum detected using high resolution chemical analyses of Green River Formation stromatolites. *Palaeogeography, Palaeoclimatology, Palaeoecology, 405*, 1–15. doi:10.1016/j.palaeo.2014.04.001

Gischler, E., Gibson, M. A., & Oschmann, W. (2008). Giant holocene freshwater microbialites, Laguna Bacalar, Quintana Roo, Mexico. *Sedimentology, 55*(5), 1293–1309. doi:10.1111/j.1365-3091.2007.00946.x

Godsey, H. S., Currey, D. R., & Chan, M. A. (2005). New evidence for an extended occupation of the Provo shoreline and implications for regional climate change, Pleistocene Lake Bonneville, Utah, USA. *Quaternary Research, 63*(2), 212–223. doi:10.1016/j.yqres.2005.01.002

Grotzinger, J. P., & Knoll, A. H. (2002).Stromatolites in Precambrian carbonates: Evolutionary Mileposts or Environmental Dipsticks? *Annual Review of Earth and Planetary Sciences, 27*(1), 313–358. doi:10.1146/annurev.earth.27.1.313

Halley, R. B. (1976). Textural Variation Within Great Salt Lake Algal Mounds. *Development in Sedimentology, 20*, 435–445.

Harrison, R. J., and J. M. Feinberg (2008), FORCinel: An improved algorithm for calculating first-order reversal curve distributions using locally weighted regression smoothing, *Geochem. Geophys. Geosyst., 9*, Q05016. doi:10.1029/2008GC001987

Hext, G. R. (1963). The estimation of second-order tensors, with related tests and designs. *Biometrika, 50*, 353–357.

Jackson, M., & P. Solheid (2010), On the quantitative analysis and evaluation of magnetic hysteresis data, *Geochem. Geophys. Geosyst., 11*, Q04Z15, https://doi.org/10.1029/2009GC002932.

Johnson, D. B., Beddows, P. A., Flynn, T. M., & Osburn, M. R. (2018). Microbial diversity and biomarker analysis of modern freshwater microbialites from Laguna Bacalar, Mexico. *Geobiology, 16*(3), 319–337. https://doi.org/10.1111/gbi.12283

Johnson, H. P., Lowrie, W., & Kent, D. V. (1975). Stability of ARM in fine and course grained magnetite and maghemite particles. *Geophys. J. R. Astron. Soc., 41*(108), 1–10.

Kendall, B., Anbar, A. D., Kappler, A., & Konhauser, K. O. (2012). The Global Iron Cycle. *Fundamentals of Geobiology,* 65–92. doi:10.1002/9781118280874.ch6

Kennard, J. M., & James, N. P. (2007). Thrombolites and Stromatolites: Two Distinct Types of Microbial Structures. *Palaios, 1*(5), 492. doi:10.2307/3514631

Khomentovsky, V. V., & Gibsher, A. S. (1996). The Neoproterozoic–lower Cambrian in northern Govi-Altay, western Mongolia: regional setting, lithostratigraphy and biostratigraphy. *Geological Magazine, 133*(4), 371–390. doi:10.1017/s001675680000755x

King, R. F. (1955). The remanent magnetism of artificially deposited sediments, Monthly Notices Roy. *Monthly Notices Roy. Astron. Soc., Geophys. Suppl., 7*(I), 115–134.

Kirschvink, J. (1980). The least-square line and plane and the analysis of paleomagnmetic data. *Geophysical Journal of the Royal Astronomical Society, 62*, 699–18.

Kodama, K. P. (2012). *Paleomagnetism of sedimentary Rocks: Process and Interpretation*, Blackwell Publishing Ltd. New Jersey, 156 pp.

Konhauser, K. O., Kappler, A., & Roden, E. E. (2011). Iron in microbial metabolisms. *Elements, 7*(2), 89–93. doi:10.2113/gselements.7.2.89

Konhauser, K., & Riding, R. (2012). Bacterial Biomineralization, *Fundamentals of Geobiology*. In Blackwell Publishing Ltd. doi:10.2465/gkk1952.20.93

Korte, M. & Constable, C. G. (2003). Continuous global geomagnetic field models for the past 3000 years. *Phys. Earth Planet. Inter., 140*, 73–89.

Lascu, I., & Feinberg, J. M. (2011). Speleothem magnetism. *Quaternary Science Reviews, 30*(23–24), 3306–3320. doi:10.1016/j.quascirev.2011.08.004

Lindsay, J. F., Brasier, M. D., Shields, G., Khommentovsky, V. V. & Bat-Ireedui. Y. A. (1996). Glacial facies asssociations in a Neoproterozoic back-arc setting. Zavkhan Basin. western Mongolia*. Geological Magazine 133*. 391-402.

Lowrie, W. (1990). Identification of ferromagnetic minerals in a rock by coercivity and unblocking temperature properties. *Geophys. Res. Lett., 17,* 159–162

Lowrie, W. & Fuller, M., (1971). On the alternating field demagnetization characteristics of multidomain thermoremanent magnetization in magnetite. *J. Geophys. Res., 76*: 6339-6349.

Lund, S.P., Platzman, E., Thouveny, N., Camoin, G., Corsetti, F., Berelson, W., 2010. Bi- ologic control of paleomagnetic remanence acquisition in carbonate framework rocks of the Tahiti coral reef. *Earth Planet. Sci. Lett. 298*, 14–22.

Maxbauer, D. P., Feinberg, J. M., & Fox, D. L. (2016). MAX UnMix: A web application for unmixing magnetic coercivity distributions. *Computers and Geosciences*, *95*, 140–145. doi:10.1016/j.cageo.2016.07.009

McFadden, P. L. & Reid, A. B. (1982). Analysis of paleomagnetic inclination data. *Geophys. J.R. Astr. Soc., 69*, 307–319.

Moskowitz, B. M., Frankel, R. B., & Bazylinski, D. A. (1993). Rock magnetic criteria for the detection of biogenic magnetite. *Earth and Planetary Science Letters, 120*(3-4)*,* 283–300. doi:10.1016/0012-821x(93)90245-5

Muraszko, J. R. (2014). Magnetic properties of Jurassic stromatolites from selected localities in Poland.M.S. Thesis, 10300, University of Warsaw, Poland

Newell, D. L., Jensen, J. L., Frantz, C. M., & Vanden Berg, M. D. (2017). Great Salt Lake (Utah) microbialite d13C, d18O, and d15N record fluctuations in lake biogeochemistry since the late Pleistocene. *Geochemistry, Geophysics, Geosystems, 18*, 3631–3645. doi:10.1002/2017GC007078

Pan, Y., Zhu, R., Banerjee, S. K., Gill, J., & Williams, Q. (2000). Rock magnetic properties related to thermal treatment of siderite: Behavior and interpretation. *Journal of Geophysical Research: Solid Earth*, *105*(B1), 783–794. doi: 10.1029/1999jb900358

Pedone, V. A., & Dickson, J. A. D. (2000). Replacement of aragonite by quasi-rhombohedral dolomite in a late Pleistocene tufa mound, Great Salt Lake, Utah, U.S.A. *Journal of Sedimentary Research, 70*(5), 1152–1159.

Pedone, V. A., & Folk, R. L. (1996). Formation of aragonite cement by nannobacteria in the Great Salt Lake, Utah. *Geology, 24*(8), 763–765. doi:10.1130/0091-7613(1996)024<0763:FOACBN>2.3.CO;2

Pepe-Ranney, C., Berelson, W. M., Corsetti, F. A., Treants, M., & Spear, J. R. (2012). Cyanobacterial construction of hot spring siliceous stromatolites in Yellowstone National Park. *Environmental Microbiology, 14*(5), 1182–1197. doi:10.1111/j.1462-2920.2012.02698.x

Petryshyn, V. A., Corsetti, F. A., Frantz, C. M., Lund, S. P., & Berelson, W. M. (2016). Magnetic susceptibility as a biosignature in stromatolites. *Earth and Planetary Science Letters, 437*, 66–75. doi:10.1016/j.epsl.2015.12.016

Pike, C.R., Roberts, A.P., and Verosub, K.L. (1999). Characterizing interactions in fine magnetic particle systems using first order reversal curves, *Journal of Applied Physics, 85*(9), 6660-6667.

Planavsky, N., and Ginsburg, R.N. (2009). Taphonomy of Modern Marine Bahamian Microbialites. *Palaios, 24*(1), 5–17. doi:10.2110/palo.2008.p08-001r

Rasmussen, K. A., Macintyre, I. G., & Prufert, L. (1993). Modern stromatolite reefs fringing a brackish coastline, Chetumal Bay, Belize. *Geology, 21*(3), 199–202. doi:10.1130/0091-7613(1993)021<0199:MSRFAB>2.3.CO;2

Riding, R. (2006). Microbial carbonate abundance compared with fluctuations in metazoan diversity over geological time. *Sedimentary Geology, 185*(3-4 SPEC. ISS.), 229–238. doi:10.1016/j.sedgeo.2005.12.015

Riding, R. (2011a). Microbialites , stromatolites , and thrombolites. In J . Reitner and V . Thiel (eds), *Encyclopedia of Geobiology, Encyclopedia of Earth Science Series*, Springer, Heidelberg, pp. 635-654.

Riding, R. (2011b). The Nature of Stromatolites: 3500 Million Years of History and a Century of Research, *Advances in Stromatolite Geobiology* (Vol. 131). doi:10.1007/978-3-642-10415-2

Robertson, D. J. & France, D. E. (1994). Discrimination of remanence-carrying miner- als in mixtures, using isothermal remanent magnetisation acquisition curves. *Phys. Earth Planet. Int., 82*(3-4), 223–234.

Rupke, A., & Mcdonald, A. (2012). Great Salt Lake brine chemistry database, 1966-2011: Utah Geological Survey Open-File Report 596. Retrieved from http://ugspub.nr.utah.gov/publications/open_file_reports/ofr-596/appa.xls

Ryan, W. B. F., S.M. Carbotte, J. Coplan, S. O'Hara, A. Melkonian, R. Arko, R.A. Weissel, V. Ferrini, A. Goodwillie, F. Nitsche, J. Bonczkowski, and R. Zemsky (2009). Global Multi-Resolution Topography (GMRT) synthesis data set, *Geochem. Geophys. Geosyst., 10*, Q03014, doi:10.1029/2008GC002332.

Seard, C., Camoin, G., Rouchy, J. M., & Virgone, A. (2013). Composition, structure and evolution of a lacustrine carbonate margin dominated by microbialites: Case study from the Green River formation (Eocene; Wyoming, USA). *Palaeogeography, Palaeoclimatology, Palaeoecology*, 381–382, 128–144. doi:10.1016/j.palaeo.2013.04.023

Smith,M.E., Carroll, A.R., Singer, B.S., (2008). Synoptic reconstruction of a major ancient lake system: Eocene Green River Formation, western United States. *Geol. Soc. Am. Bull. 120*, 54–84. doi:10.1130/B26073.1.

Stolz, J. F., Chang, S.-B. R., & Kirschvink, J. L. (1987). Biogenic magnetite in stromatolites. I. Occurrence in modern sedimentary environments. *Precambrian Research, 43*(4), 295–304. doi:10.1016/0301-9268(89)90061-2

Strangway, D. W., & Mcmahon, B. E. (1973). Paleomagnetism of annually banded Eocene Green River sediments. *Journal of Geophysical Research, 78*(23), 5237–5245. doi:10.1029/jb078i023p05237

Surdam, R.C., Stanley, K.O., and Buchheim, H.P. (1980). Depositional environment of the Laney Member of the Green River Formation, south- western Wyoming: Guidebook for SEPM Field Trip No. 5, Denver, Colorado: Denver, Rocky Mountain

Tarhan, L. G., Planavsky, N. J., Laumer, C. E., Stolz, J. F., & Reid, R. P. (2013). Microbial mat controls on infaunal abundance and diversity in modern marine microbialites. *Geobiology, 11*(5), 485–497. doi:10.1111/gbi.12049

Tauxe, L, Shaar, R., Jonestrask, L., Minnett, R., Koppers, A. A. P., Constable, C. G.,Sciences, P. (2016). PmagPy: Software package for paleomagnetic data analysis and a bridge to the Magnetics Information Consortium (MagIC) Database. *Geochemistry, Geophysics, Geosystems, 2450–2463*. doi:10.1002/2016GC006307

Tauxe, L., (2010). *Essentials of Rock and Paleomagnetism* (with contributions from R.F. Butler, R. Van der Voo, and S.K. Banerjee), University of California Press, Los Angeles, 489pp.

Tauxe, L., Kodama, K. P., & Kent, D. V. (2008). Testing corrections for paleomagnetic inclination error in sedimentary rocks: A comparative approach. *Physics of the Earth and Planetary Interiors, 169*(1–4), 152–165. doi:10.1016/j.pepi.2008.05.006

Tauxe, L., Steindorf, J. L., & Harris, A. (2006). Depositional remanent magnetization: Toward an improved theoretical and experimental foundation. *Earth and Planetary Science Letters, 244*(3–4), 515–529. doi:10.1016/j.epsl.2006.02.003

Thébault, E., Finlay, C.C., Beggan, C.D. et al. International Geomagnetic Reference Field: *the 12th generation. Earth Planet Sp 67, 79* (2015). doi:10.1186/s40623-015-0228-9

Thompson, R. & Oldfield, F. (1986) *Environmental Magnetism.* Allen & Unwin: Springer, London. doi:10.1007/978-94-011-8036-8

Trindade et al. (2018). Speleothem record of geomagnetic South Atlantic Anomaly recurrence, *PNAS, 115,* 13198-13203, doi:10.1073/pnas.1809197115

Vanyo, J. P., & Awramik,S.M., (1982). Length of Day and Obliquity of the Ecliptic 850 Ma ago: Preliminary result of a stromatolite growth model. *Geophysical Research Letters, 9*(10), 1125–1128.

Appendix A: Sample Photos and Coordinates

Appendix A is a supplementary material for Section 2.2: Laboratory Sample Preparation. Appendix A includes the photos of microbialite samples which were subjected to NRM intensity and susceptibility mappings (Samples: GSL18_0301_A, B, C, D, E (Figure A.1); GSL19_0103_A (Figure A.2); GSL19_0201_A (Figure A.3); GSL19_0202_A (Figure A.4); LB19_0104 (Figure A.5); GR18_0101_A (Figure A.6); BG14_0101_A (Figure A.7)). The associated grids and specimen names of final cuts are shown.

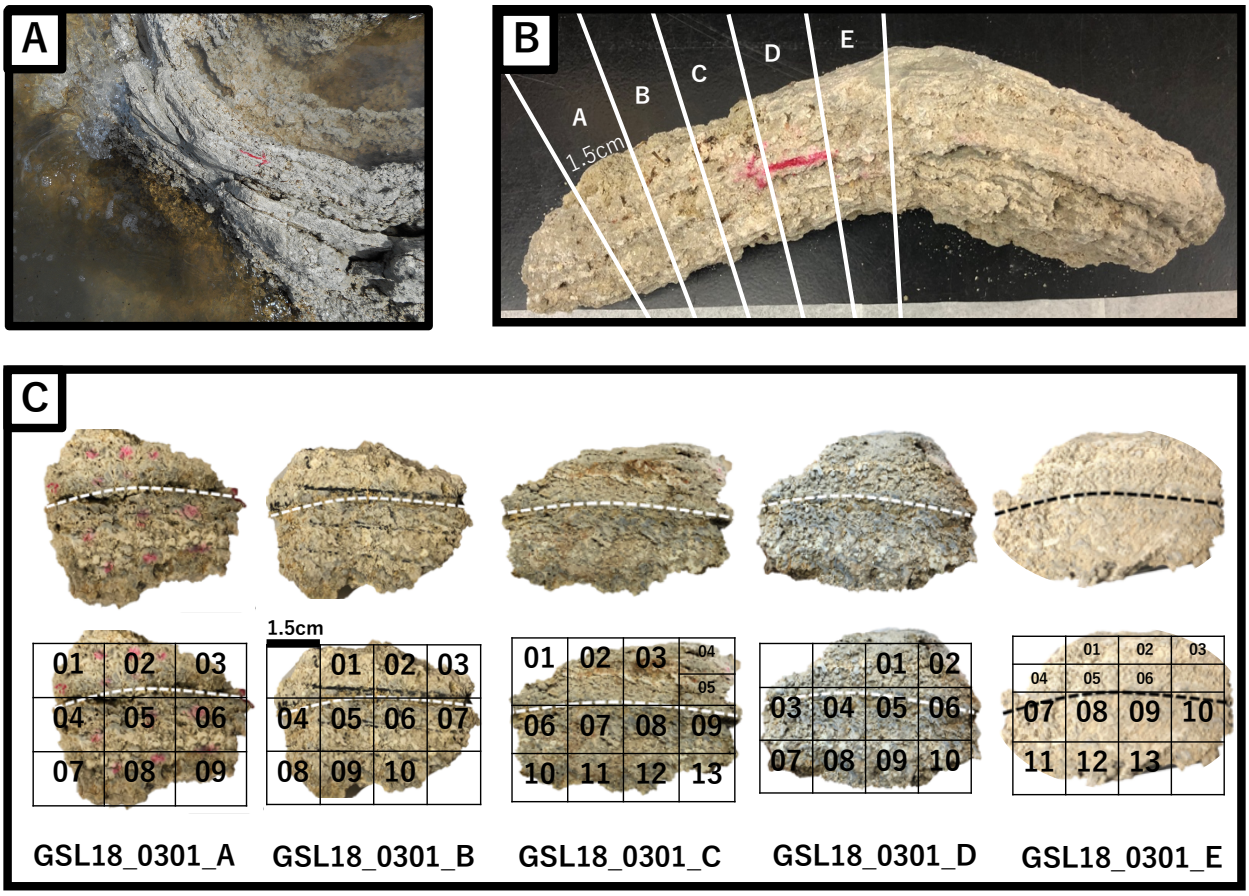

Figure A.1. (A) Field photo of the sample GSL18_0301 (collapsed dome structure lithified microbialite protruding above the waterline at Site 3; (B) 30 cm long microbialite collected at the side of the microbialite dome structure. Left half of this sample cut into 5 slices (GSL18_0301_A, B, C, D, E) and used for this study; (C) Image of the GSL18_0301 sample slices A, B, C, D, E at the top. Grid lines (bottom) created on the cut surface of the slice indicate where final cuts were made.

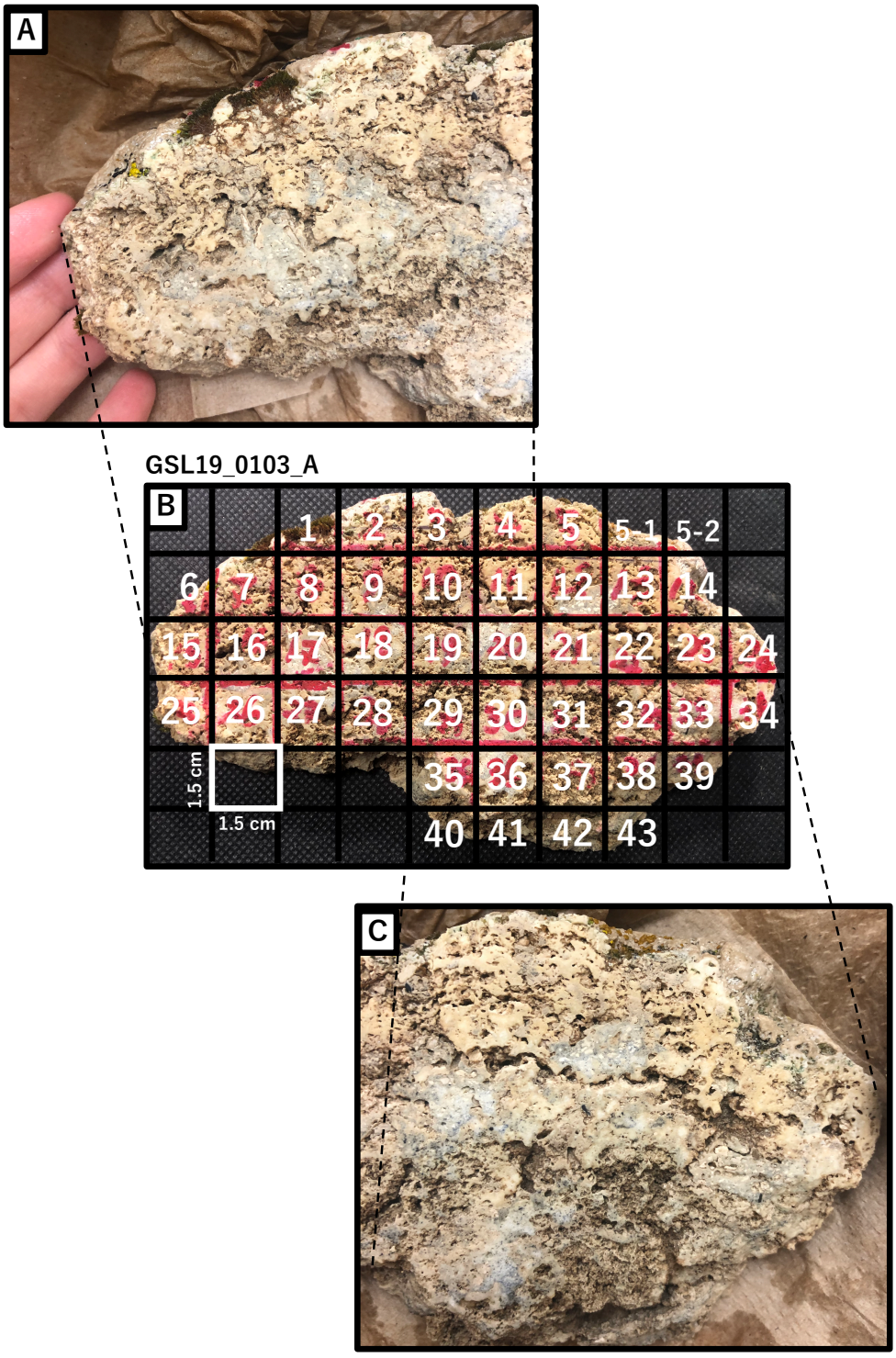

Figure A.2. (A) A closer look of the left side of the sample GSL19_0103 _A; (B) Grid lines created on the cut surface of the slice indicate where final cuts were made. The background is the image of the GSL19_0103 sample slice A**;** (C) A closer look of the right side of the sample GSL19_0103 _A;

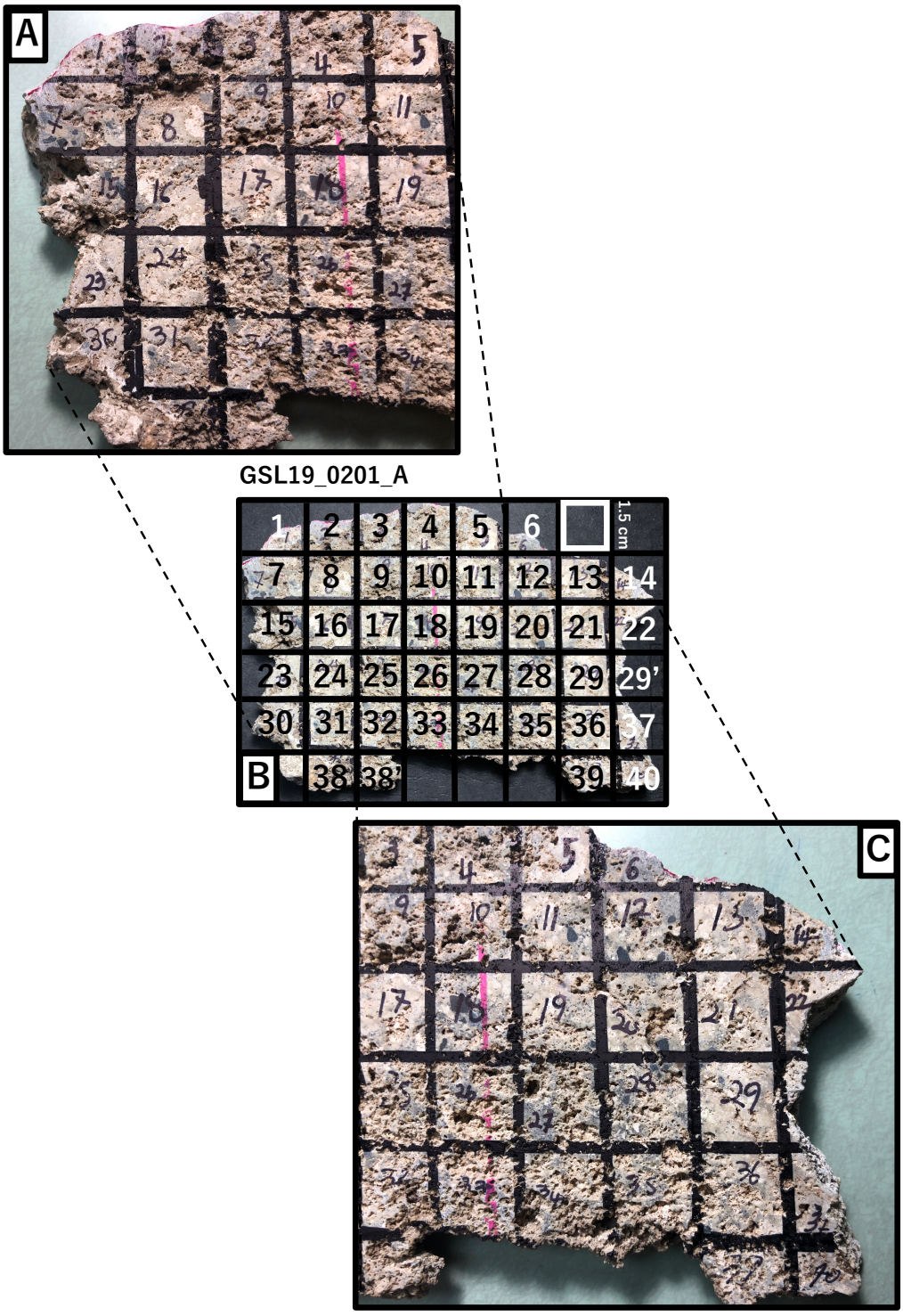

Figure A.3. (A) A closer look of the left side of the sample GSL19_0201 _A; (B) Grid lines created on the cut surface of the slice indicate where final cuts were made. The background is the image of the GSL19_0201 sample slice A**;** (C) A closer look of the right side of the sample GSL19_0201 _A;

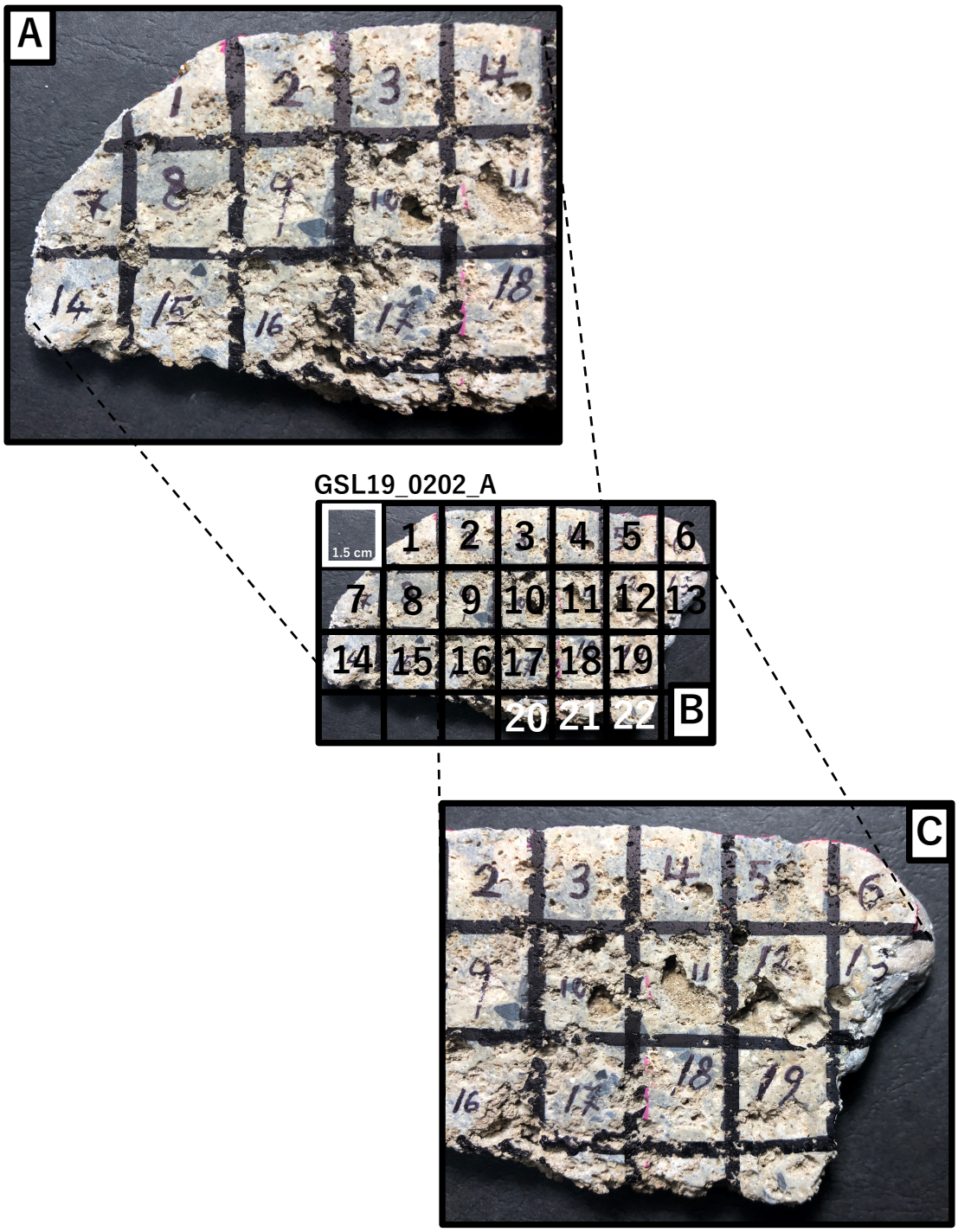

Figure A.4. (A) A closer look of the left side of the sample GSL19_0202 _A; (B) Grid lines created on the cut surface of the slice indicate where final cuts were made. The background is the image of the GSL19_0202 sample slice A**;** (C) A closer look of the right side of the sample GSL19_0202 _A.

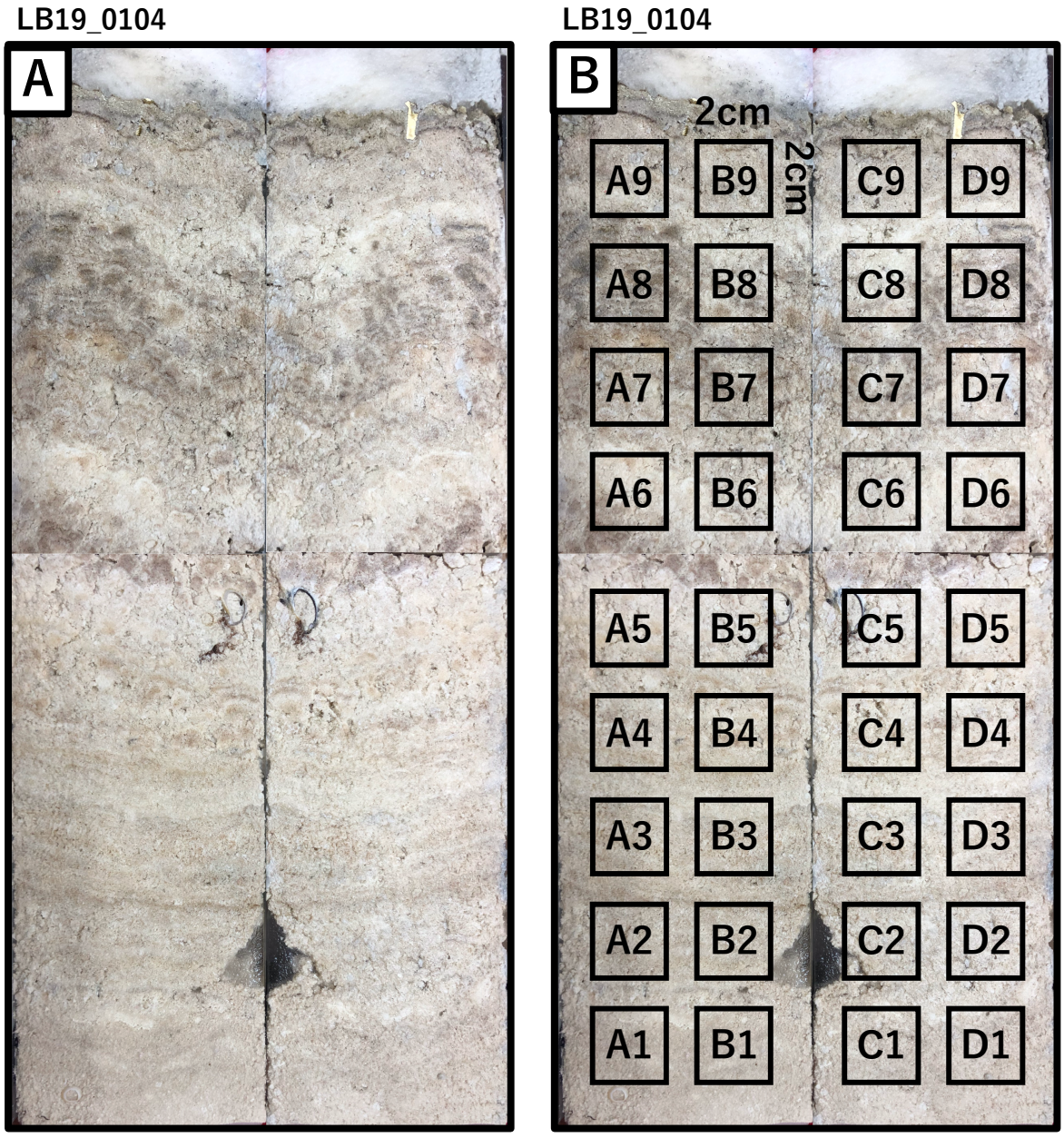

Figure A.5. (A) Photo of push core sample LB19_0104's transect profile; (B) Squares represent where the cube specimens (2x2x2 cm^3) were collected from the LB19_0104.

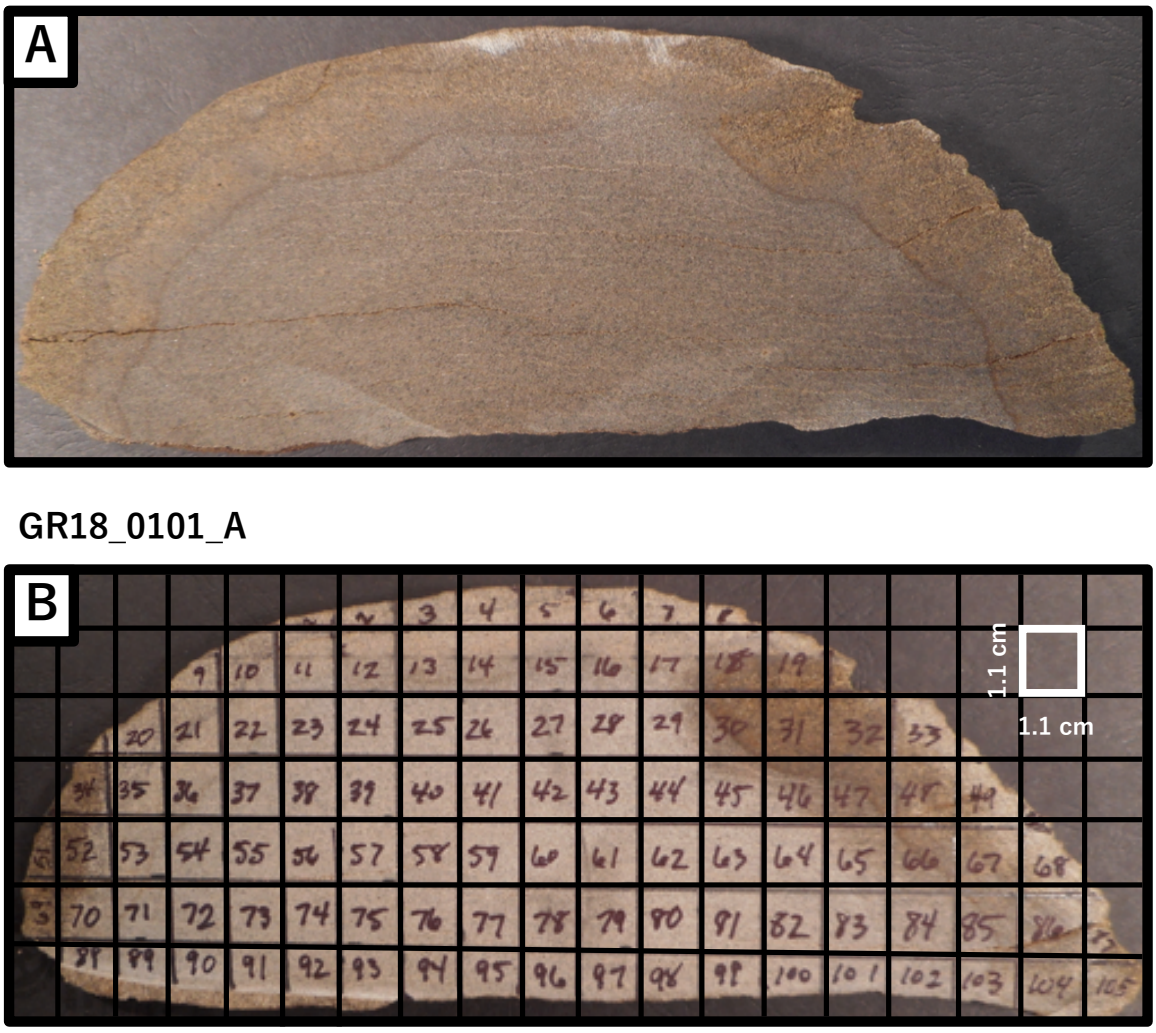

Figure A.6. (A) Photo of GR18_0101A sample slice prior to sub-sampling; (B) Grid lines created on the cut surface of the slice indicate where final cuts were made. The background is the image of the GR18_0101 sample slice A.

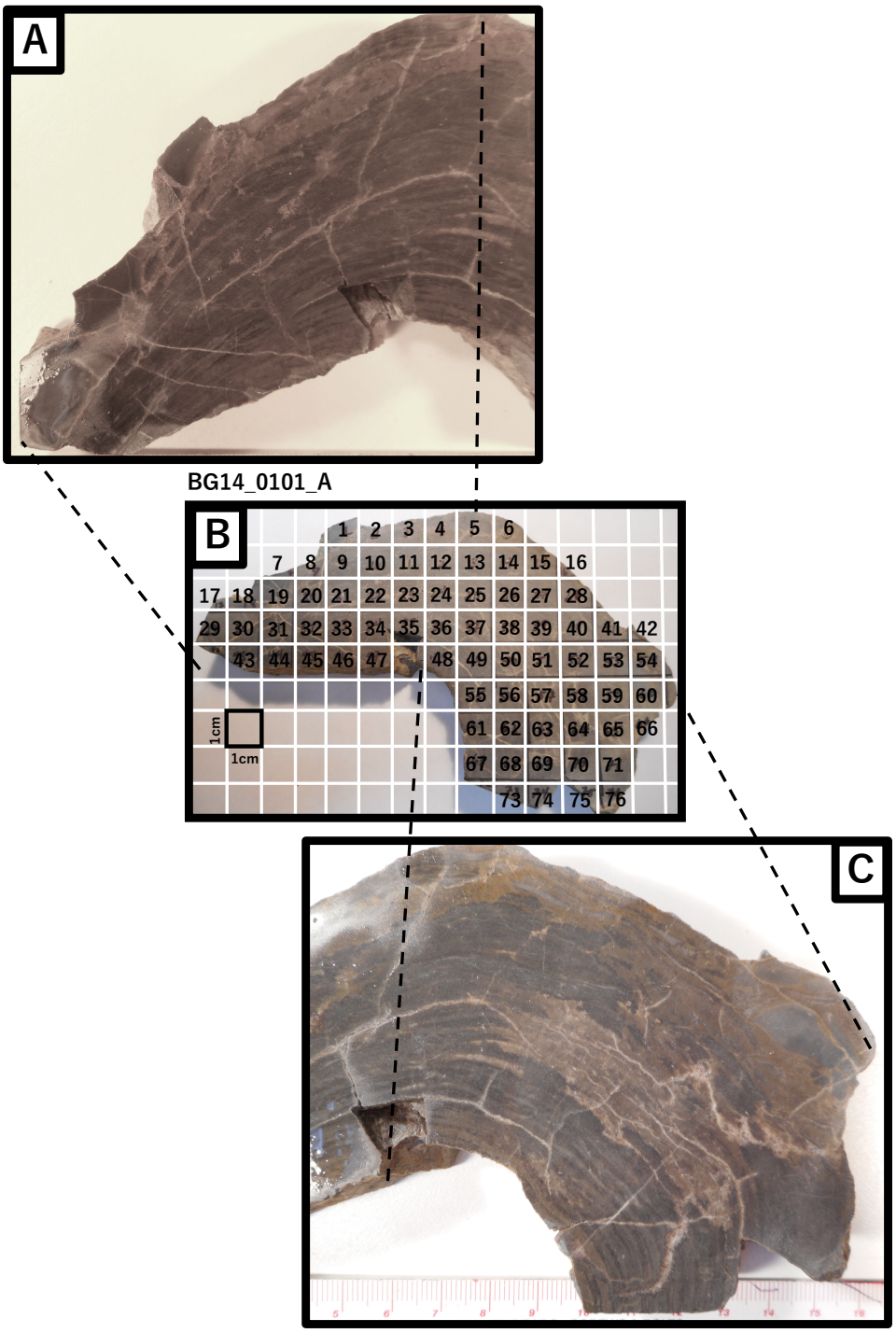

Figure A.7. (A) A closer look of the left side of the sample BG14_0101_A; (B) Grid lines created on the cut surface of the slice indicate where final cuts were made. The background is the image of the BG14_0101 sample slice A**;** (C) A closer look of the right side of the sample BG14_0101_A.

Appendix B: NRM intensity and Magnetic Susceptibility Mappings

Appendix B includes additional NRM intensity and magnetic susceptibility mapping of GSL19 microbialites collected from Lakeside (see Section 3.4.1. Spatial Variations).

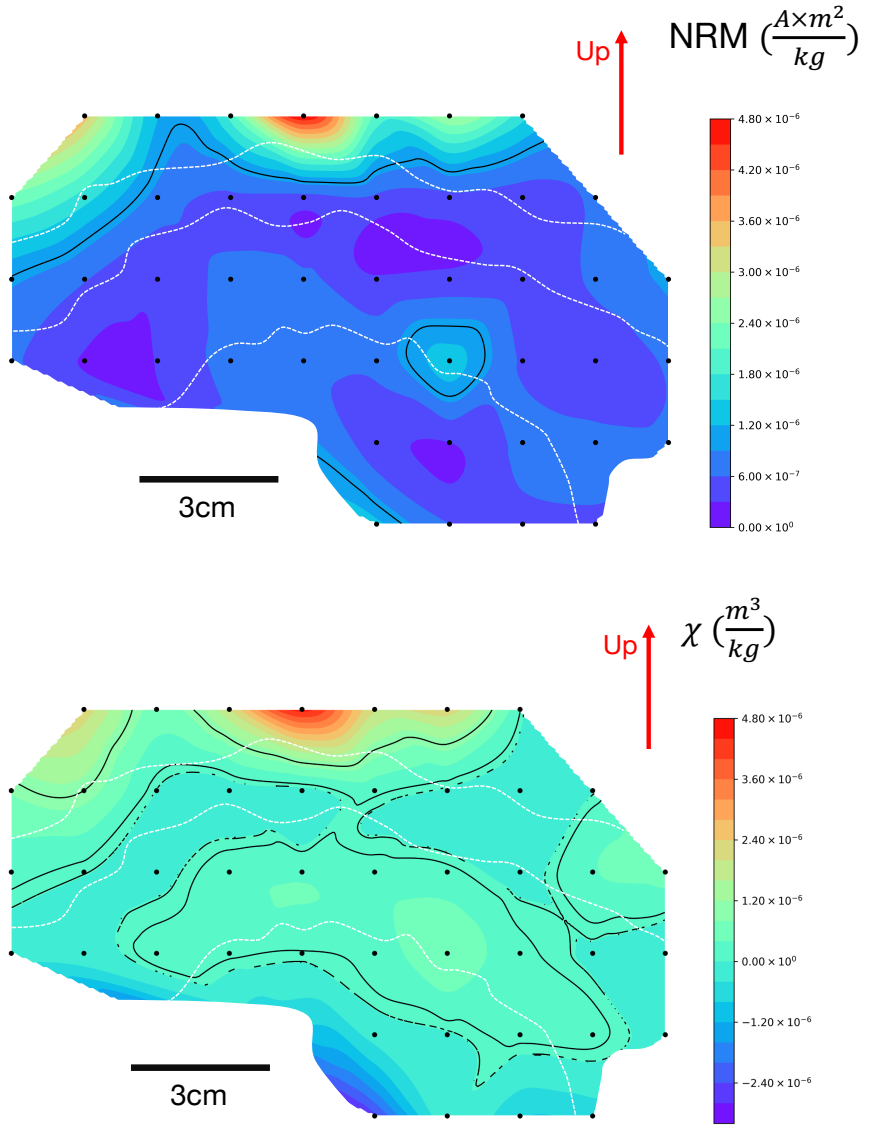

Figure B.1. NRM intensity mapping (top) and magnetic susceptibility mapping (bottom) of GSL19_0103A with cubic interpolation with the approximate 1.5 cm spatial resolution. Color contours are on a linear scale but labeled black contour lines show order of magnitude variations. Black dots are sample positions and the color bars represent NRM intensity (Am^2/kg) and magnetic susceptibility(m^3/kg) values in color range. Solid (up) red arrow indicates up in the field and is similar to the sample's growth direction. The white dashed lines roughly represent the locations of distinct laminations.

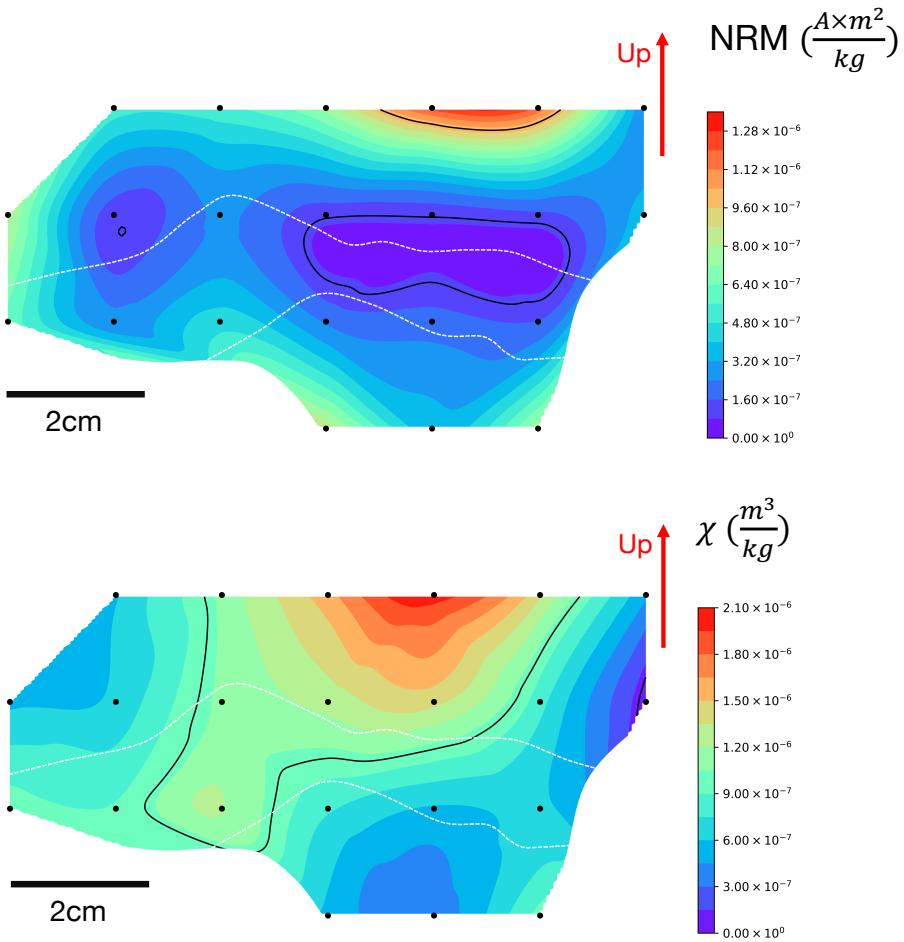

Figure B.1. NRM intensity mapping (top) and magnetic susceptibility mapping (bottom) of GSL19_0202A(bottom) with cubic interpolation with the approximate 1.5 cm spatial resolution. Color contours are on a linear scale but labeled black contour lines show order of magnitude variations. Black dots are sample positions and the color bars represent NRM intensity (Am^2/kg) and magnetic susceptibility(m^3/kg) values in color range. Solid (up) red arrow indicates up in the field and is similar to the sample's growth direction. The white dashed lines roughly represent the locations of distinct laminations.

Appendix C: IRM Unmixing Curves

Appendix C includes additional IRM unmixing results from GSL18 (Figure C.1) and LB19 (Figure C.2) microbialites, which are not shown in the main text (see Section 5.3.2. IRM Unmixing).

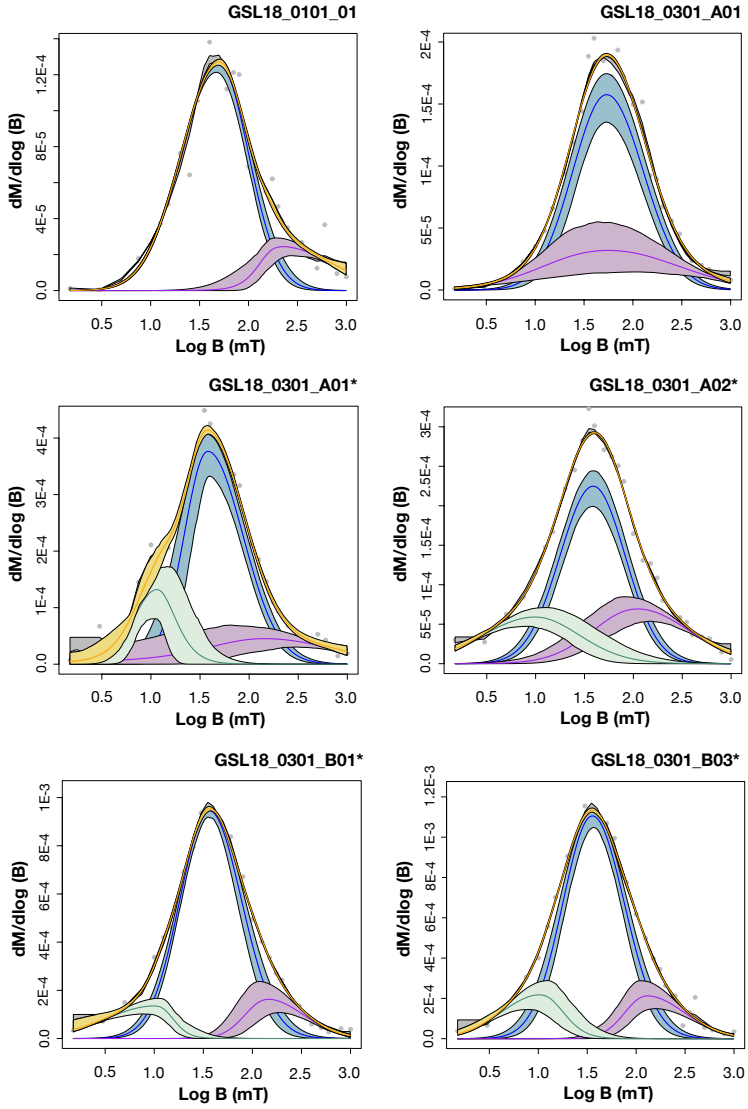

Figure C.1. IRM unmixing curves of GSL18_0101_01, GSL18_0301_A01, A01*, A02*, B01*, B03* specimens plotted through the MaxUnmix online software (Maxbauer et al., 2016) in a log scale. Gray dots represent actual data, and yellow lines represents total IRM best-fit based on real data. Colored lines (blue and purple) represent different coercivity components. The shadings represent 95% confidence intervals calculated using a resampling algorithm with N = 300 Note that '*' means specimens subjected to -1000mT before the stepwise IRM acquisition.

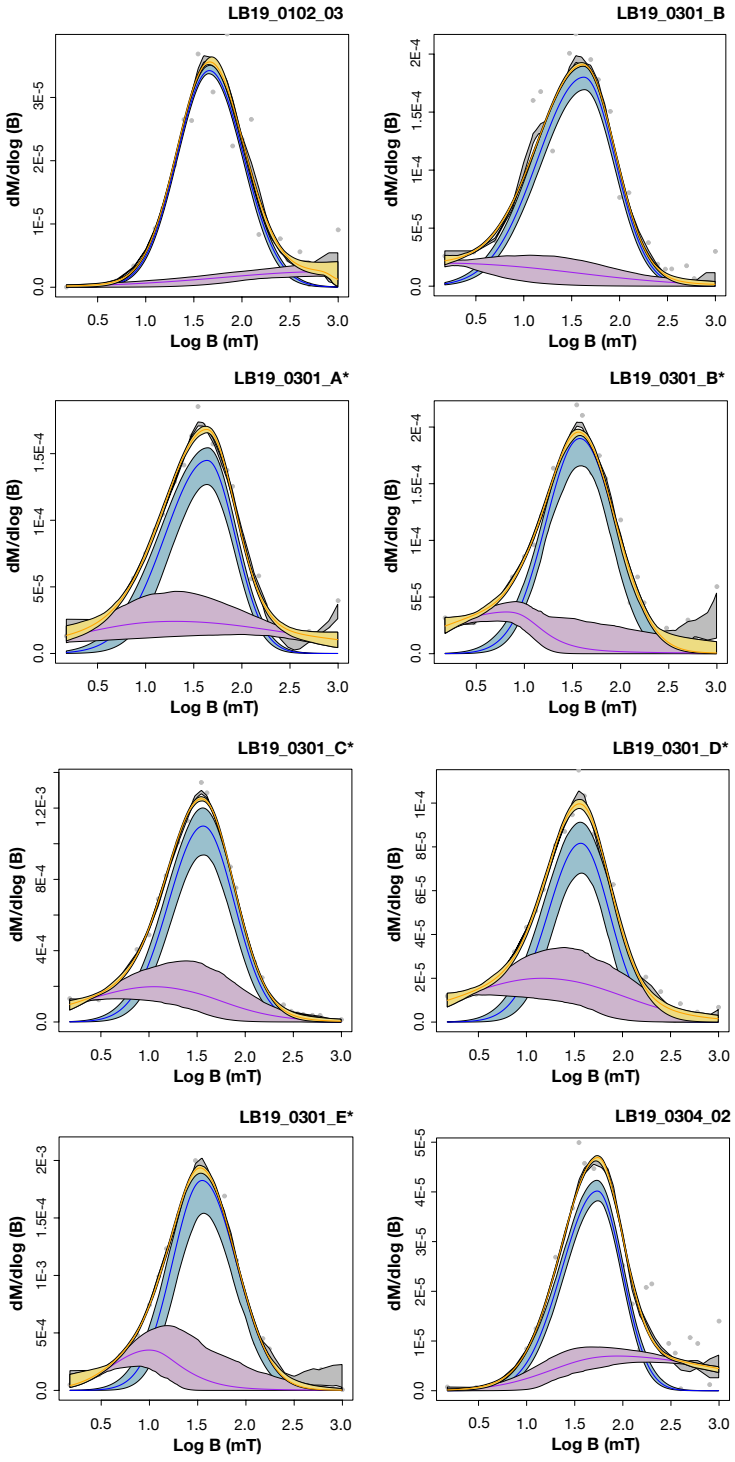

Figure C.2. IRM unmixing curves of LB19_0102_03, LB19_0301_B, A* ,B* ,C* ,D*, E*, LB19_0304_02 plotted through the MaxUnmix online software (Maxbauer et al., 2016) in a log scale. Gray dots represent actual data, and yellow lines represents total IRM best-fit based on real data. Colored lines (blue and purple) represent different coercivity components. The shadings represent 95% confidence intervals calculated using a resampling algorithm with N = 300 Note that '*' means specimens subjected to -1000mT before the stepwise IRM acquisition.

Appendix D: Lowrie-Fuller Tests

Appendix D includes additional ARM decay and IRM acquisition and decay plots of GSL18 (Figure D.1), GSL19 (Figure D.2), LB19 (Figure D.3), and GR18 (Figure D.4) microbialites, which are not displayed in the main text (see Section 5.3.3. Lowrie-Fuller Test).

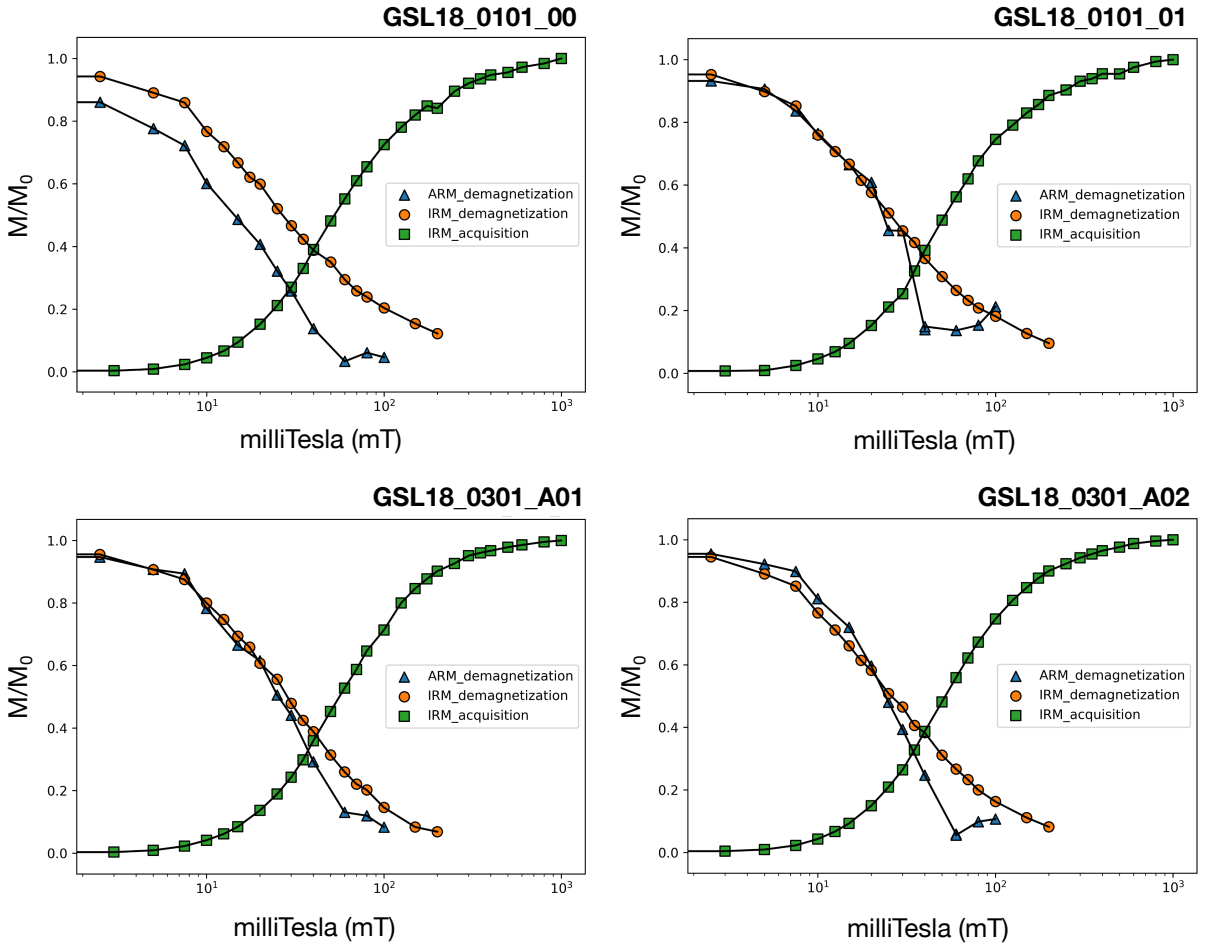

Figure D.1. IRM acquisition (green squares), IRM demagnetization (orange circles) and ARM demagnetization (blue circles) normalized by the starting (or ending) values of GSL18 microbialites from Antelope Island. (top) Living microbialites with cyanobacteria layers (GSL18_0101_00, GSL18_0101_01). (bottom) The lithified modern microbialite (GSL18_0301_A01, GSL18_0301_A02). ARM and IRM were applied along the sample z-axis.

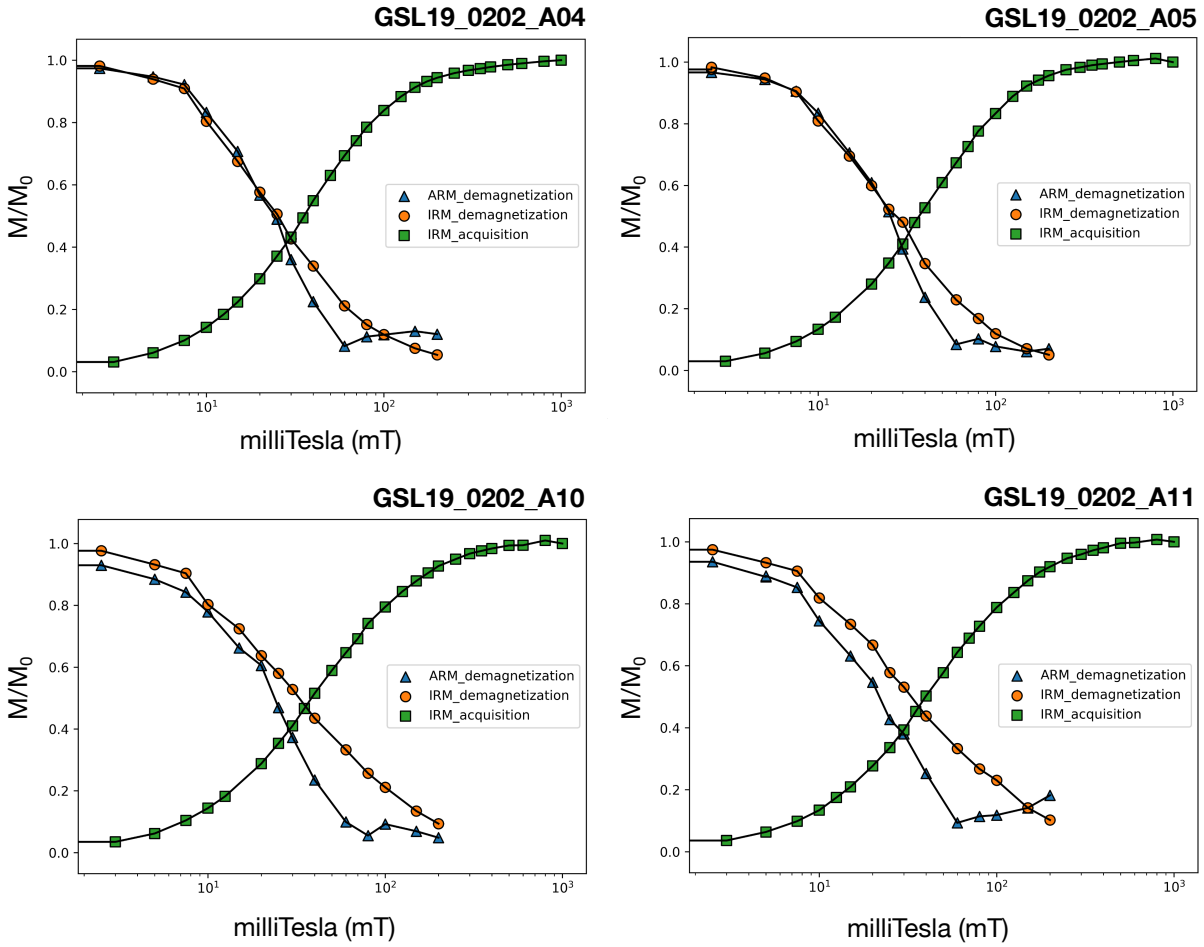

Figure D.2. IRM acquisition (green squares), IRM demagnetization (orange circles) and ARM demagnetization (blue circles) normalized by the starting (or ending) values of Pleistocene GSL19 microbialites from Lakeside. (top) Specimens from high NRM intensity (GSL19_0202_A04, GSL19_0202_A05). (bottom) Specimens from low NRM intensity (GSL19_0202_A10, GSL19_0202_A11). ARM and IRM were applied along the sample z-axis.

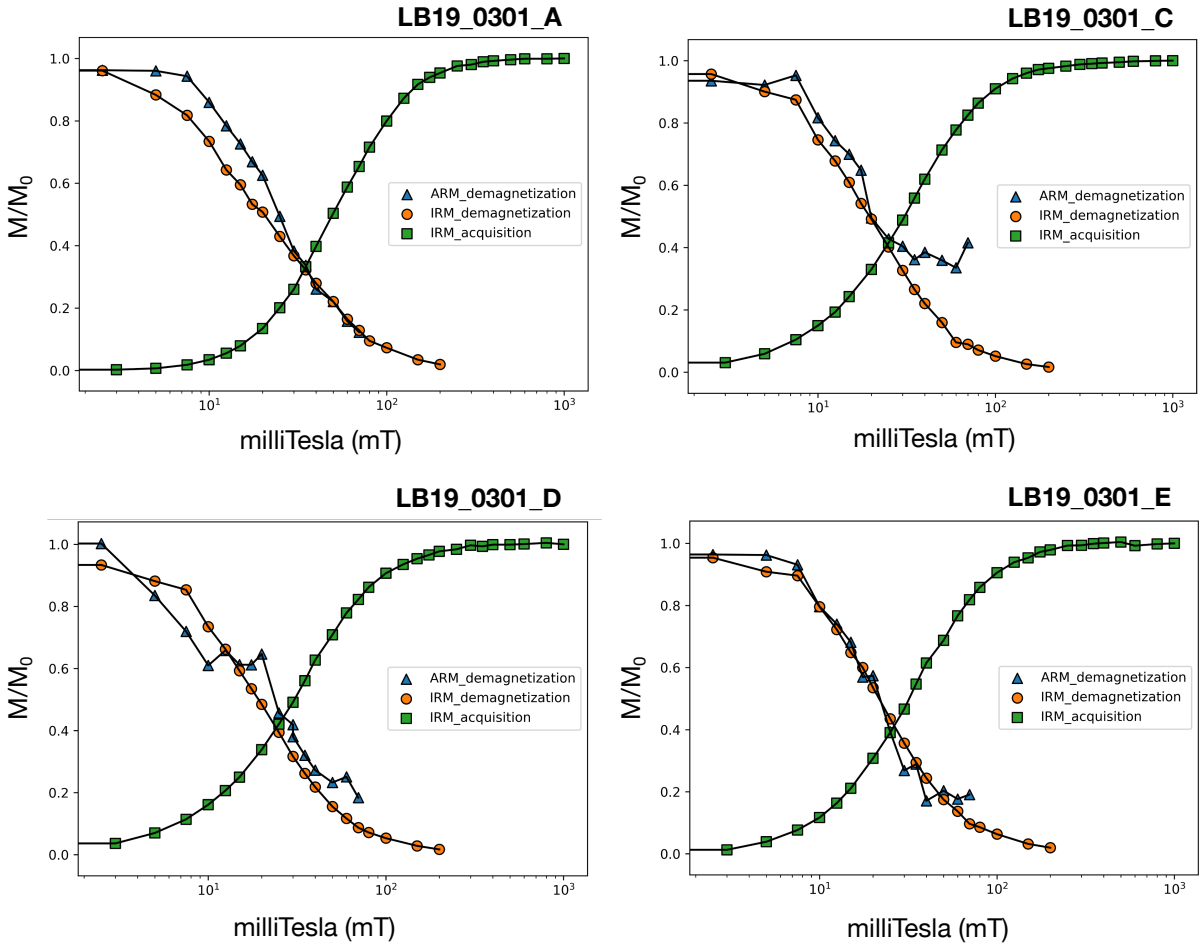

Figure D.3. IRM acquisition (green squares), IRM demagnetization (orange circles) and ARM demagnetization (blue circles) normalized by the starting (or ending) values of LB19 lithified drilled core specimens from rapid (Site 3) (LB19_0301A, C, D, E). ARM and IRM were applied along the sample z-axis.

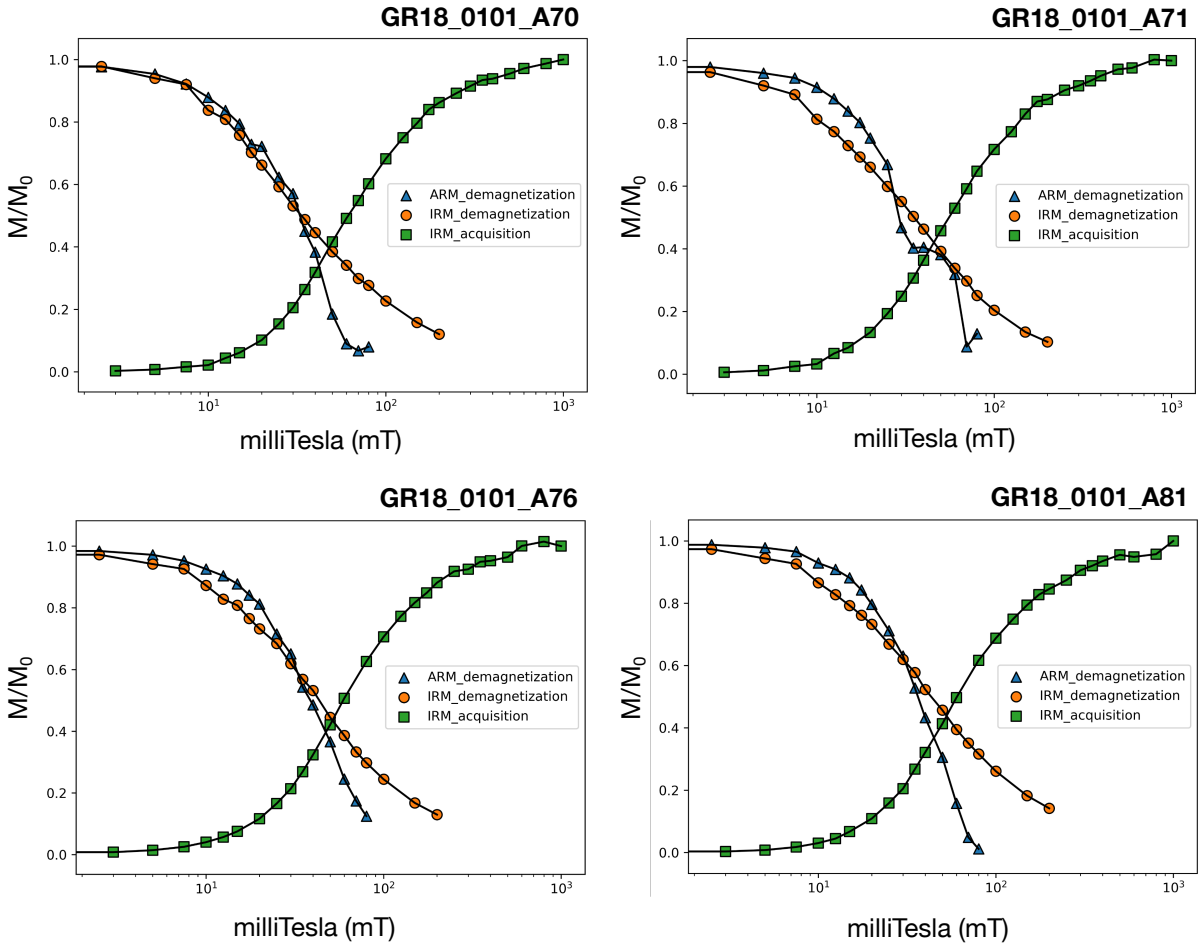

Figure D.4. IRM acquisition (green squares), IRM demagnetization (orange circles) and ARM demagnetization (blue circles) normalized by the starting (or ending) values of Eocene GR18 microbialite. (top) Specimens from low NRM intensity (GR18_0101_A70, GR18_0101_A71). (bottom) Specimens from high NRM intensity (GR18_0101_A76, GR18_0101_A81). ARM and IRM were applied along the sample z-axis.

Appendix E: 3D IRM Technique

Appendix E includes 3D IRM technique (Lowrie, 1990) results of GSL18 (Figure E.1), GSL19 (Figure E.2), LB19 (Figure E.3), GR18 (Figure E.4), BG14 (Figure E.5) microbialites, which are not displayed in the main text (see Section 5.3.4. 3D IRM Technique).

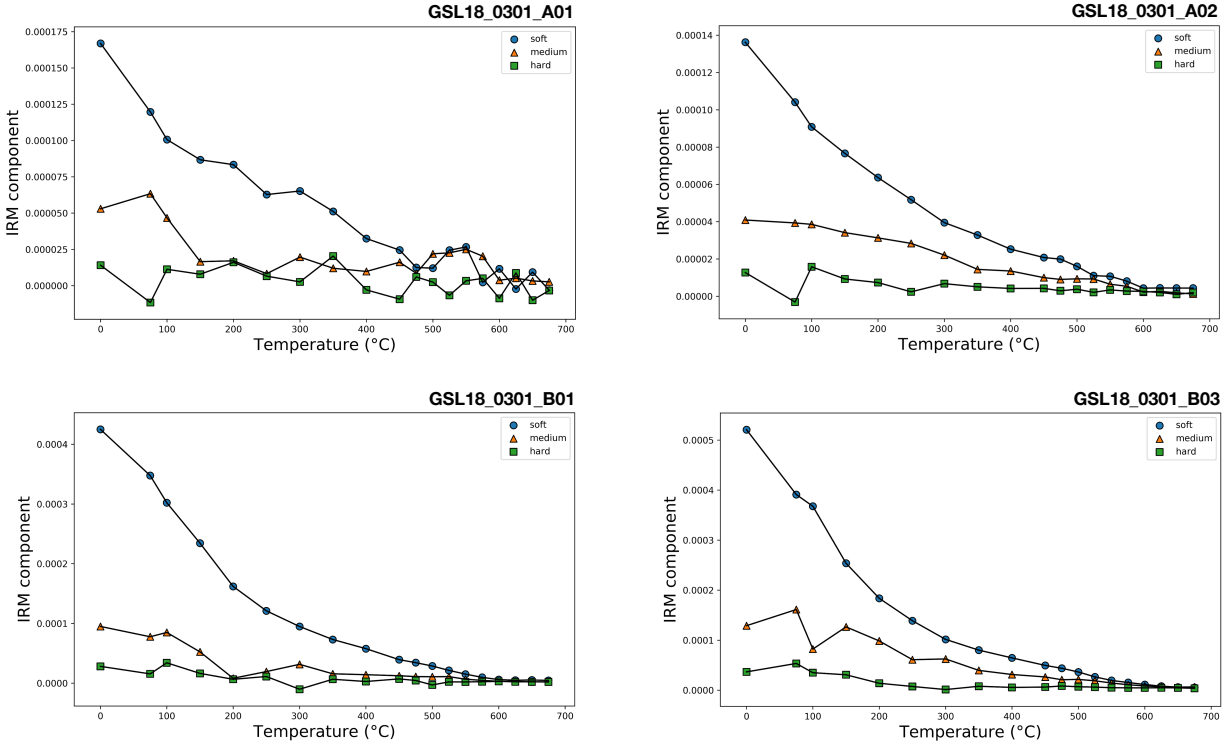

Figure E.1. 3D IRM technique plots of the lithified GSL18 microbialite (GSL18_0301) specimens collected from Antelope Island. Thermal demagnetization of a three-component IRM produced by 100mT (x-axis), 300mT (y-axis) and 1000mT (z-axis). Soft, medium, and hard fractions are shown as blue circle, orange triangle, and green square respectively.

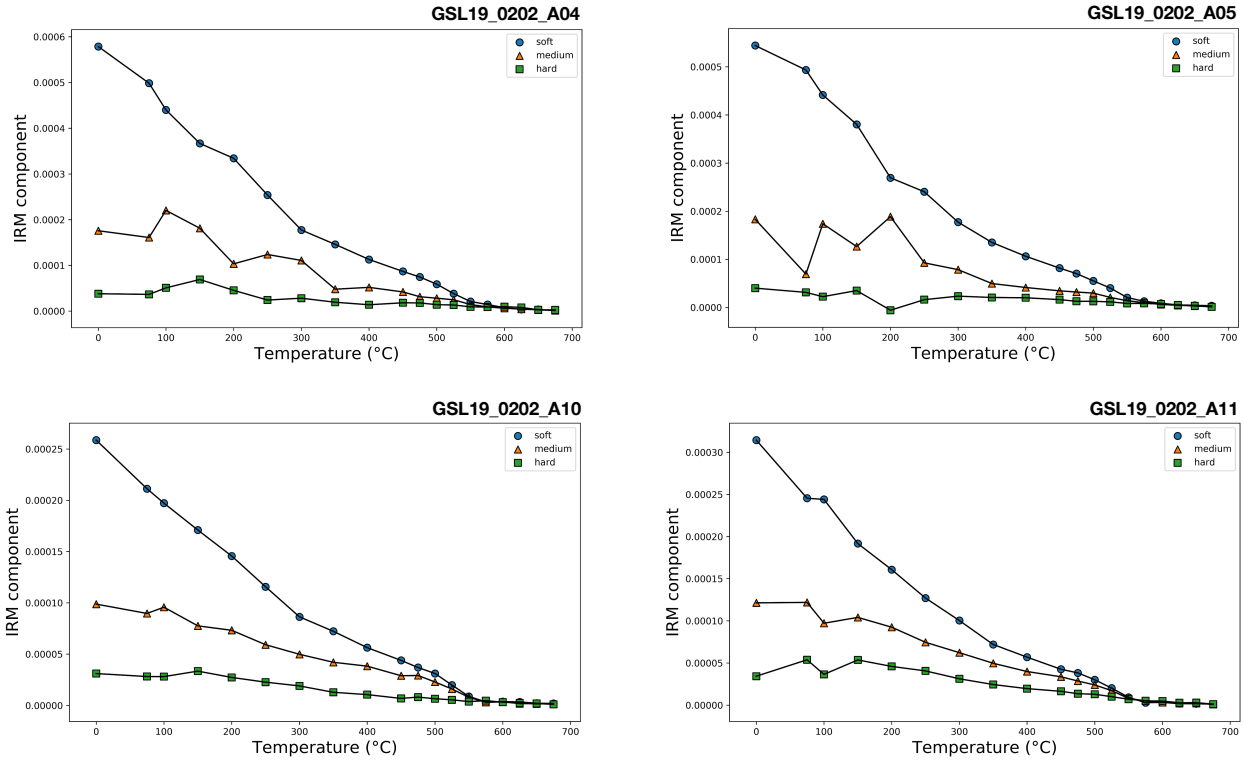

Figure E.2. 3D IRM technique plots of the Pleistocene GSL19 microbialite (GSL19_0202)'s high NRM intensity specimens (GSL19_0202_A04, GSL19_0202_A05) and low NRM intensity specimens (GSL19_0202_A10, GSL19_0202_A11) collected from Lakeside. Thermal demagnetization of a three-component IRM produced by 100mT (x-axis), 300mT (y-axis) and 1000mT (z-axis). Soft, medium, and hard fractions are shown as blue circle, orange triangle, and green square respectively.

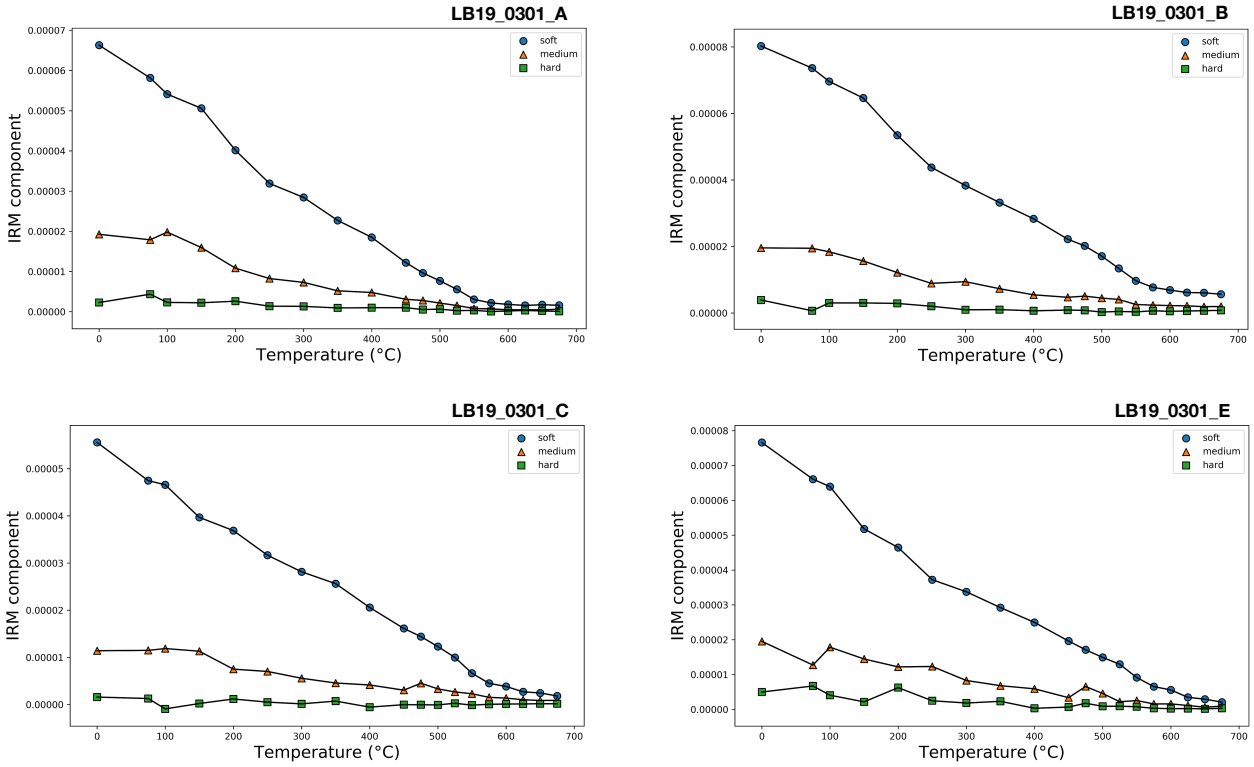

Figure E.3. 3D IRM technique plots of the modern LB19 microbialites collected from Rapids (Site 3). Thermal demagnetization of a three-component IRM produced by 100mT (x-axis), 300mT (y-axis) and 1000mT (z-axis). Soft, medium, and hard fractions are shown as blue circle, orange triangle, and green square respectively.

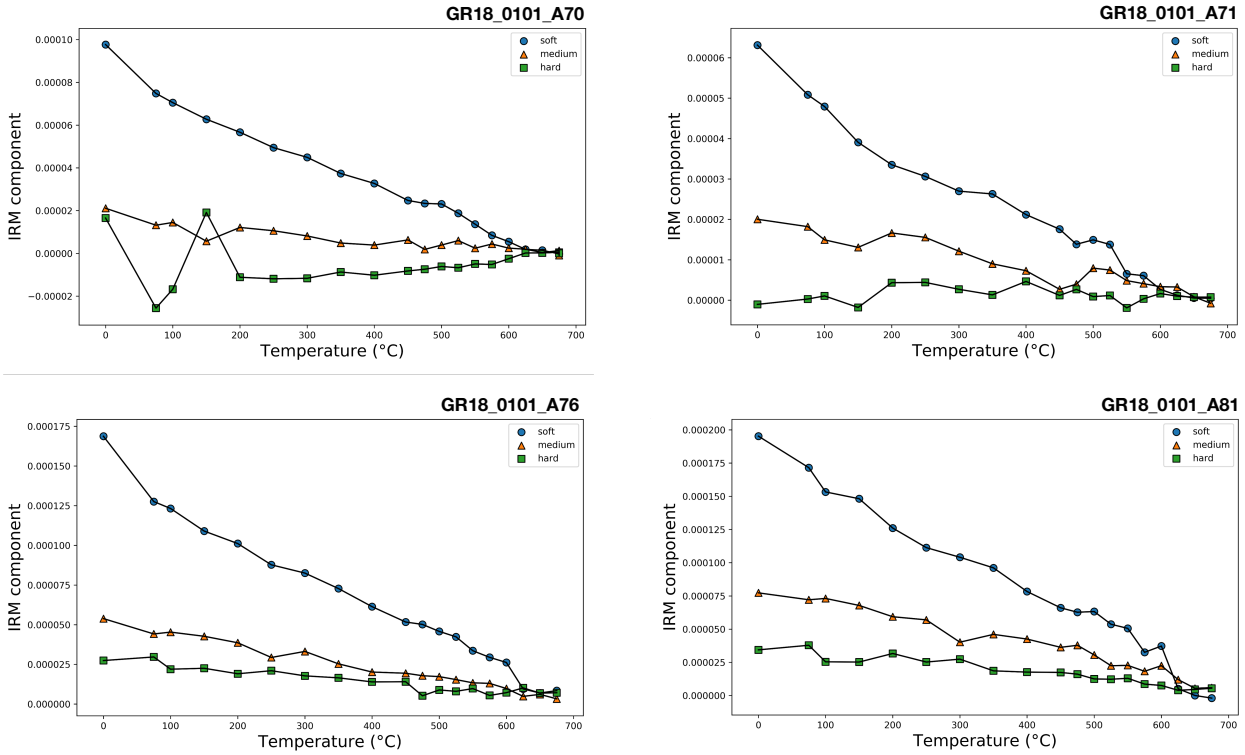

Figure E.4. 3D IRM technique plots of the Eocene GR18 microbialite (GR18_0101)'s low NRM intensity specimens (GR18_0101_A70, GR18_0101_A71) and high NRM intensity specimens (GR18_0101_A76, GR18_0101_A81). Thermal demagnetization of a three-component IRM produced by 100mT (x-axis), 300mT (y-axis) and 1000mT (z-axis). Soft, medium, and hard fractions are shown as blue circle, orange triangle, and green square respectively.

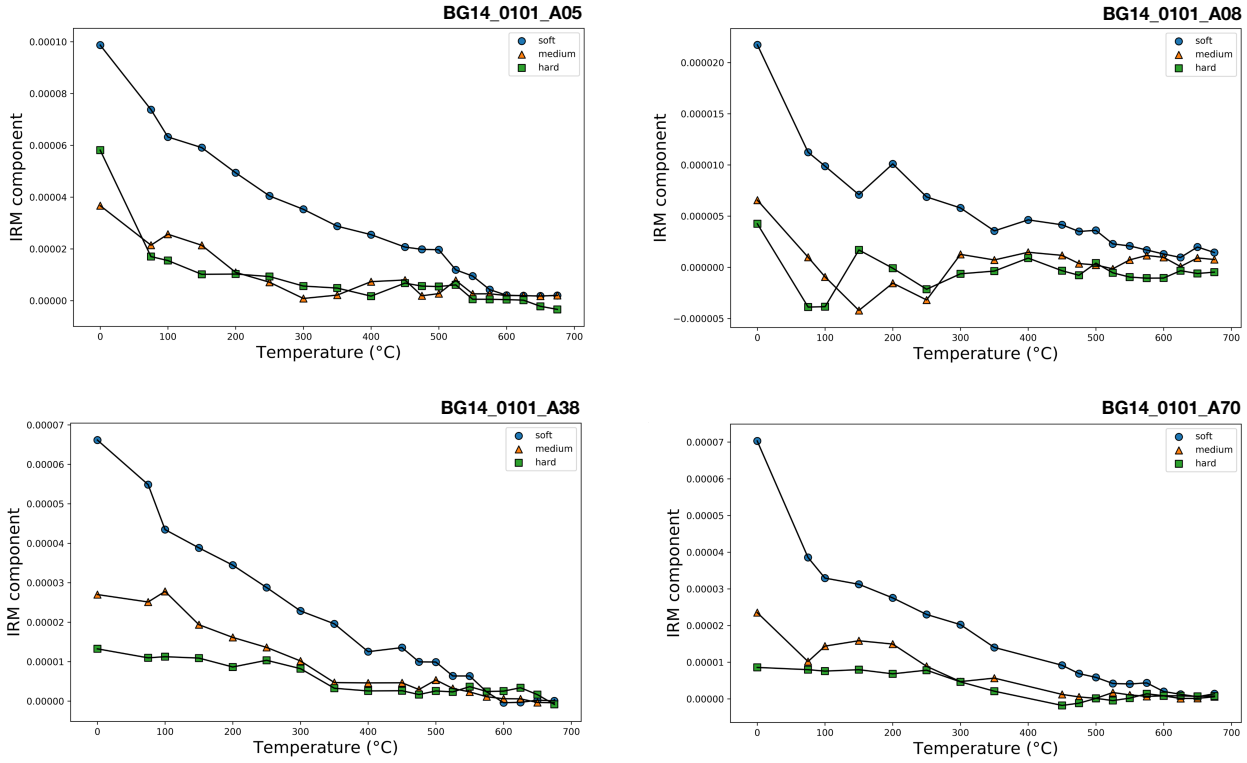

Figure E.5. 3D IRM technique plots of the Cambrian BG14 stromatolite (BG14_0101)'s low S-ratio specimens (BG14_0101_A05, BG14_0101_A05) and high S-ratio specimens (BG14_0101_A38, BG14_0101_A70). Thermal demagnetization of a three-component IRM produced by 100mT (x-axis), 300mT (y-axis) and 1000mT (z-axis). Soft, medium, and hard fractions are shown as blue circle, orange triangle, and green square respectively.

Appendix F: Curie Temperature

Appendix F includes magnetic susceptibility versus temperature plots of GSL18 (Figure F.1), LB19 (Figure F.2), GR18 (Figure F.3), BG14 (Figure F.4) microbialites, which are not displayed in the main text (see Section 5.3.5. Curie Temperature)

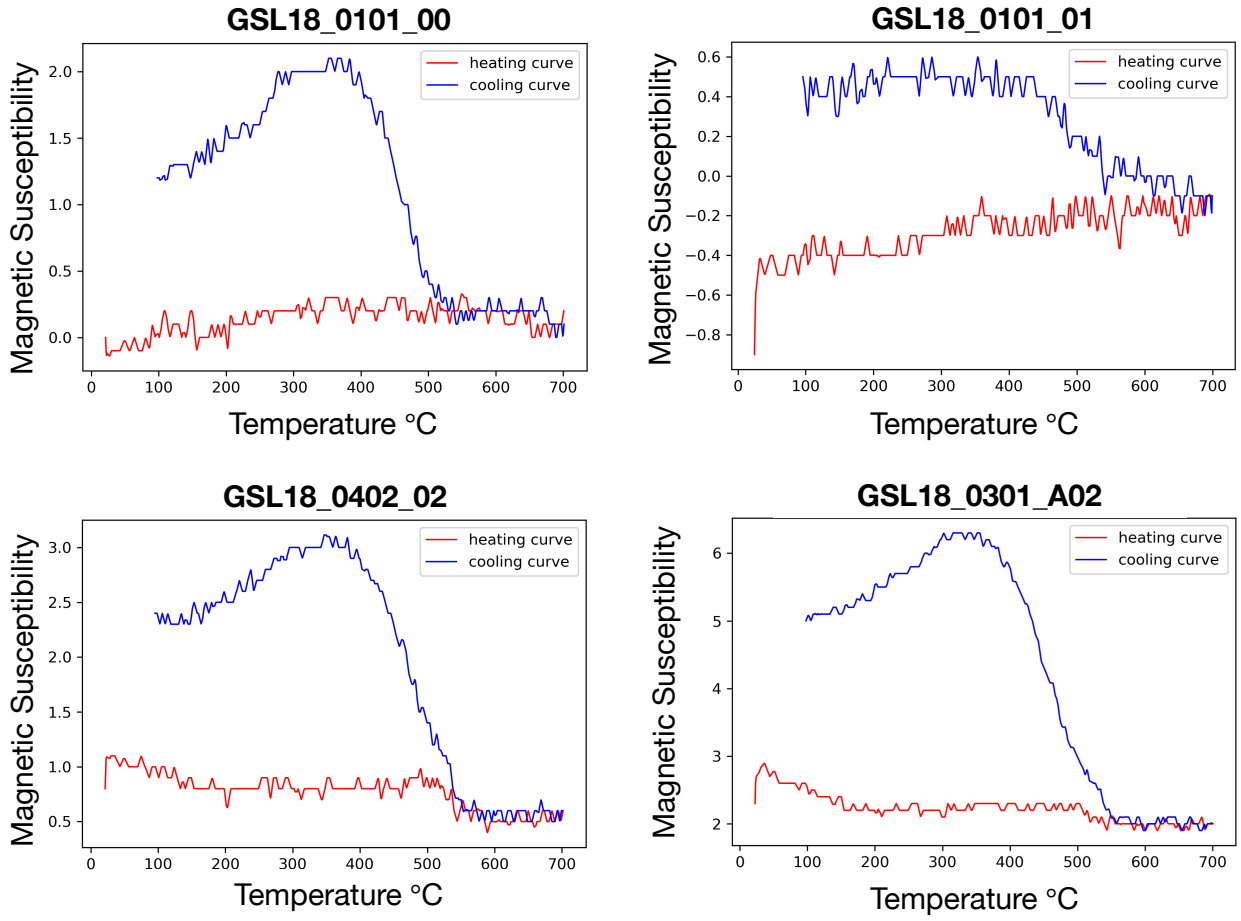

Figure F.1. The Curie point graphs of specimens GSL18_0101_00, GSL18_0101_01, GSL18_0402_02 (Living GSL18 microbialites with cyanobacteria bacteria) and GSl18_0301_A02 (Lithified modern microbialite) from Antelope Island. Linearly interpolated empty furnace susceptibility data were subtracted from raw susceptibility data. Heating and cooling curves are colored in red and blue, respectively.

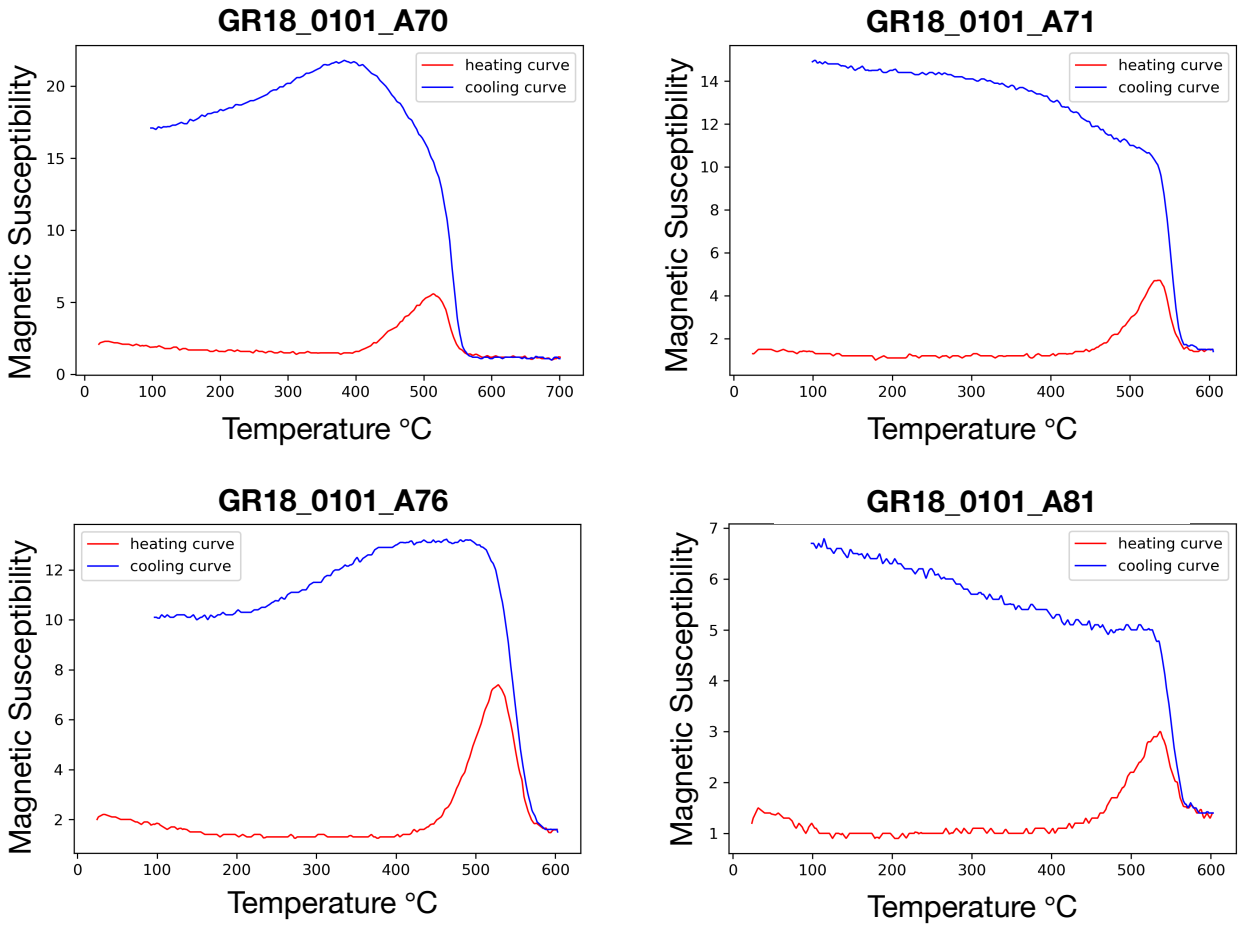

Figure F.2. The Curie point graphs of GR18_0101's specimens from low NRM intensity spots (GR18_0101_A70, GR18_0101_A71) and high NRM intensity spots (GR18_0101_A76, GR18_0101_A81). Linearly interpolated empty furnace susceptibility data were subtracted from raw susceptibility data. Heating and cooling curves are colored in red and blue, respectively.

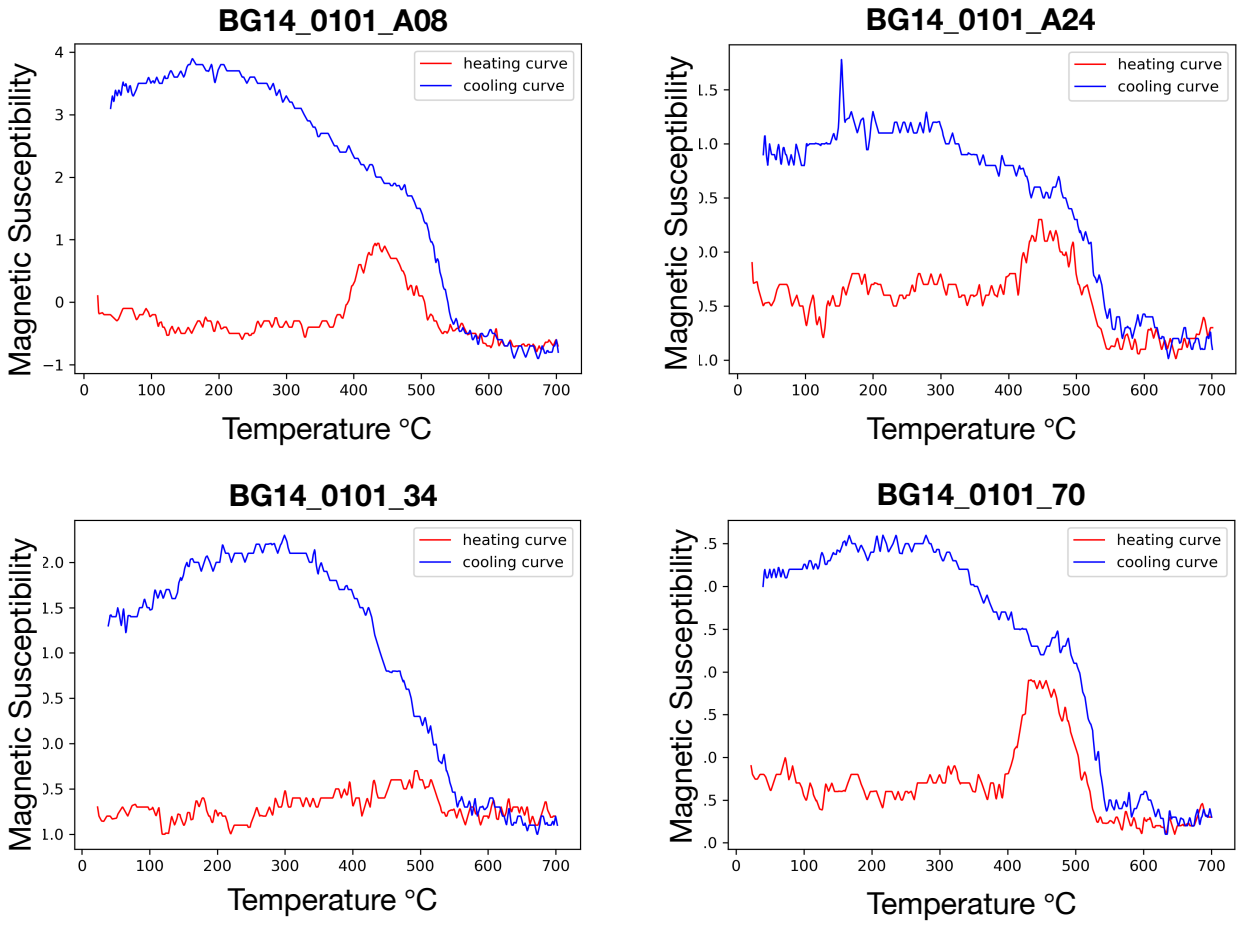

Figure F.3. The Curie point graphs of BG14_0101's specimens (BG14_010_A08, 24,34,70). Linearly interpolated empty furnace susceptibility data were subtracted from raw susceptibility data. Heating and cooling curves are colored in red and blue, respectively.

Appendix G: FORCs Measurements

Appendix G includes FORC diagrams of BG14 stromatolite, which are not displayed in the main text (see Section 5.3.7. First Order Reversal Curves (FORC)). Figure G.1. and Figure G.2. display the FORC diagrams of high coercivity and low coercivity specimens, respectively.

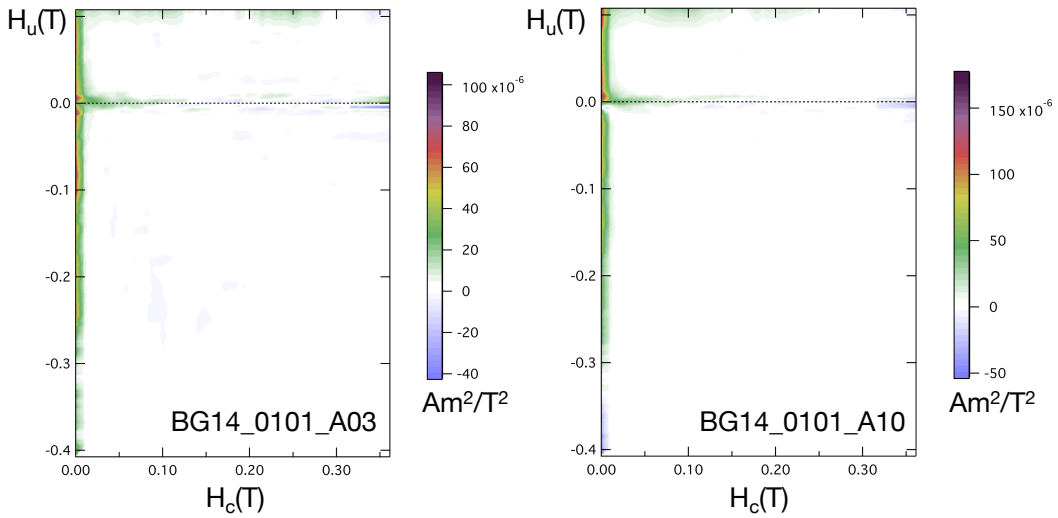

Figure G.1. FORC distribution of high coercivity specimens BG14_0101_A03 (S-ratio: 0.46) (left) and BG14_0101_A10 (S-ratio: 0.68) (right) made with FORCinel (Harrison & Feinberg, 2008). Vertical ridge (S_c0) =4; Horizontal smooth (S_c1)=7; Central ridge (S_b0)=3; Vertical smooth (S_b1) =7.

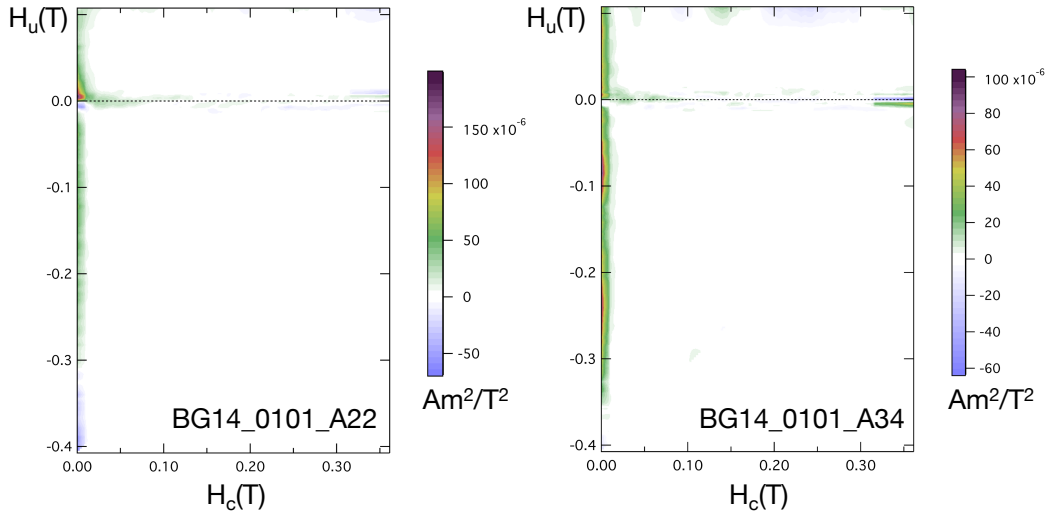

Figure G.2. FORC distribution of low coercivity specimens BG14_0101_A22 (S-ratio: 0.82) (left) and BG14_0101_A34 (S-ratio: 0.94) (right) made with FORCinel (Harrison & Feinberg, 2008). Vertical ridge (S_c0) =4; Horizontal smooth (S_c1)=7; Central ridge (S_b0)=3; Vertical smooth (S_b1) =7.

Appendix H: MPMS measurements

Appendix H includes additional MPMS measurements, which are not displayed on the main text (see Section 6.3.3. Low-temperature test for biogenic magnetite)

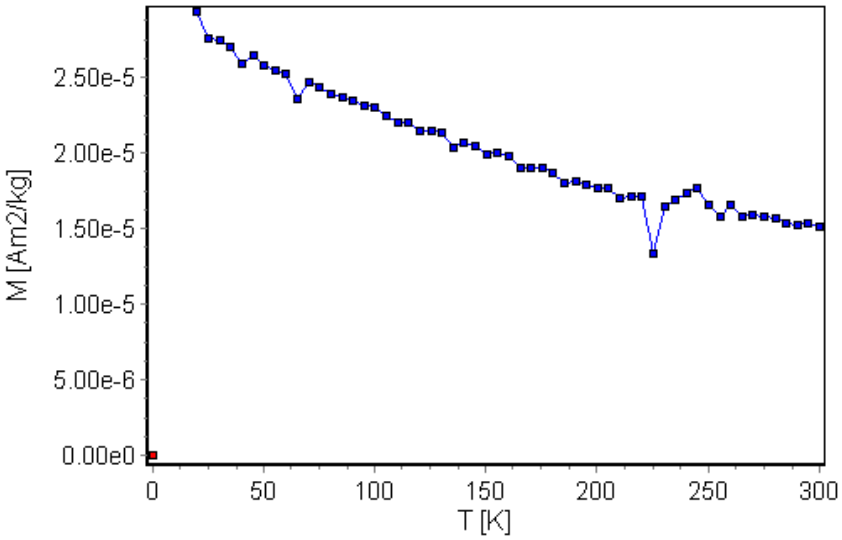

Figure H.1. MPMS measurement of specimen LB19_0305_01. A 2.5 T IRM is measured on warming after cooling in a 2.5 T field (FC; blue). There is no evidence for the Verwey transition, and the experiment therefore failed to detect biogenic magnetite.

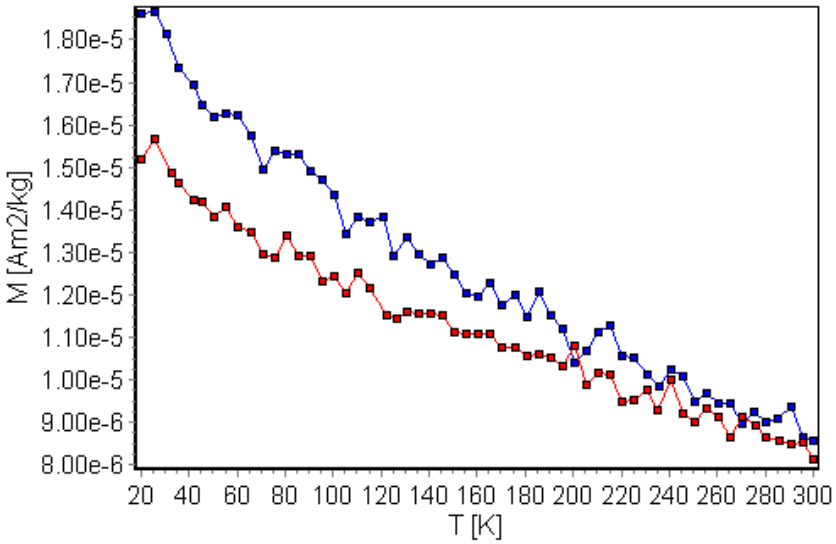

Figure H.1. MPMS measurement of specimen LB19_0305_03. A 2.5 T IRM is measured on warming after cooling in zero field (ZFC; red) and after cooling in a 2.5 T field (FC; blue). There is no evidence for the Verwey transition, and the experiment therefore failed to detect biogenic magnetite.